Photon and hadron interactions of radially excited states

Andrew Bradley

PHOTON AND HADRON INTERACTIONS OF RADIALLY EXCITED STATES

PHOTON AND HADRON INTERACTIONS OF RADIALLY EXCITED STATES

THESIS SUBMITTED TO
THE UNIVERSITY OF DURHAM

BY

ANDREW BRADLEY, B.Sc. (DURHAM)

FOR THE DEGREE OF DOCTOR OF PHILOSOPHY

DEPARTMENT OF PHYSICS
DURHAM UNIVERSITY

MARCH 1978

CONTENTS

ACKNOWLEDGEMENTS

I would like to thank Fred Gault for his prompting, advice and invaluable support throughout my research training here at Durham. My thanks to him also for reading the manuscript and for collaboration on some of the work.

I am grateful to the Science Research Council for financial support.

ABSTRACT

We review the development of the quark model with particular emphasis on the interpretation of quarks as dynamical, confined, hadronic constituents. This interpretation encompasses naturally the phenomenon of radially excited states. The simple vector dominance model is reviewed and an extended vector meson dominance model which includes both radial excitations of the vector mesons, and q^2- dependence of the photon-vector meson coupling is applied to radiative decays and photoproduction of the vector mesons. The parameters estimated from ψ radiative decay, define a phenomenological prescription in which the radial excitations play a minor role compared with the ground state vector mesons. The predictions of the model for various cross-sections and decay widths are presented and found to be in good agreement with experiment. However we predict a larger total cross-section, $\sigma_{tot}(\psi N)$ than has been recently measured and the suppression of the large phase space decays of excited states is not understood.

By re-identifying some of the vector meson states which have been more recently observed coupling to e^+e we show that in all flavour sectors the spectra of radial

excitations can be well described by a Klein-Gordon type wave equation employing a simple, linear $q\bar{q}$ potential. The wave-functions obtained by solving the equation are coupled with a quark pair creation hypothesis to predict a number of partial decay widths of the light quark, radially excited states. The suppression of large phase space decays of the excited states is then understood.

CHAPTER 1

RADIAL EXCITATIONS IN THE QUARK MODEL

1.1 Degrees of Freedom in a 2-body bound state

We will be dealing throughout this work with radial excitations of mesons - integer spin hadrons which appear in the quark model as bound states of one quark and one antiquark. To discuss the general nature of radially excited states, we consider, as an introductory example, the dynamical degrees of freedom of two spinless particles bound by a harmonic oscillator interaction. We suppose that the motion of the particles is non-relativistic and we choose this specific type of interaction because of the mathematical simplicity of the equations of motion.

The Hamiltonian in the centre of mass system of particles of equal mass (m) reads

$$H = \frac{p^2}{m} + m\omega^2 r^2 \qquad (1.1)$$

where r is $\sqrt{2}$ x particle separation and p is the particle s momenta. The usual quantum mechanical substitutions yield the Schrödinger equation

$$\nabla^2\psi(\underline{r}) + (mE - m^2\omega^2 r^2)\psi(\underline{r}) = 0 \qquad (1.2)$$

and this equation is separable in polar co-ordinates.

Writing

$$\psi(r) = \chi(\theta,\phi)\, R(r)/r \qquad (1.3)$$

the angular equations have solutions

$$\chi_l^m = e^{im\phi} P_l^m(\cos\theta) \quad , \quad (m = -l, \ldots, l : l \text{ integer}) \qquad (1.4)$$

where m, l are separation constants and the remaining radial equation is

$$\frac{d^2R}{dr^2} + \left(mE - \frac{l(l+1)}{r^2} - m^2\omega^2r^2\right)R = 0 \qquad (1.5)$$

The boundary conditions we must impose are $R \to 0$ as $r \to 0$ and R remains finite as $r \to \infty$. (1.5) can be transformed into a confluent hypergeometric equation[1], the solution to which is the hypergeometric series - a series that remains finite as $r \to \infty$ only for the energy eigenvvalues

$$E = \omega(2n + l + 3/2), \qquad n, l \in \{\mathbb{Z}^+, 0\} \qquad (1.6)$$

where n is the degree of radial excitation and l the degree of orbital excitation. The energy is independent of $m = -l, \ldots, l$ and this degeneracy is related to the fact that the original equation is separable in more than one co-ordinate system. The Schrödinger equation can be separated and solved in cylindrical and rectangular co-ordinates also, the latter method yielding the eigenvalue equation

$$E = \omega(p + q + r + 3/2) \qquad ,p,q,r \in \{Z^+,0\} \qquad (1.7)$$

and the equivalence of the degeneracies in each system is apparent, e.g.

$$E = 5/2\,\omega\,, \quad \left.\begin{matrix} n & l & m \\ 0 & 1 & +1 \\ 0 & 1 & 0 \\ 0 & 1 & -1 \end{matrix}\right\} \text{3-fold degenerate} \left\{\begin{matrix} p & q & r \\ 1 & 0 & 0 \\ 0 & 1 & 0 \\ 0 & 0 & 1 \end{matrix}\right. \qquad (1.8)$$

We see in (1.6) the two signatures of a harmonic oscillator interaction: integrally spaced energy levels and double spacing of the radial excitations (in covariant models there is the possibility that time-like excitations may effectively fill the gaps in this double spacing (2,3)): these points will be useful when we examine meson spectra in chapter four.

1.2 The Non-Relativistic Quark Model

As radially excited mesons arise naturally in the non-relativistic quark model we sketch briefly the development of this scheme.

The first advances in comprehensively classifying hadrons were group theoretical in nature. Mesons were found to fall into octets with the same spin and parity, while baryons fitted into octets and decuplets. All these states can be economically classified in terms of an SU(3) symmetry based on quarks, spin $\frac{1}{2}$ hadronic constituents hypothesised by Gell Mann and Zweig (4,5).

This quark triplet (u,d,s) consists of the $I=\frac{1}{2}$ doublet (u,d) and the I=0 singlet s, each quark has baryon number $B=\frac{1}{3}$ and a corresponding antiquark $\bar{q}$ with $B=-\frac{1}{3}$. The $(u,d,\bar{u},\bar{d})$ quarks have strangeness zero and the $s,\bar{s}$ quarks have strangeness ± 1 respectively.

The mesons have the structure $q\bar{q}$, and the baryons the structure qqq. These hadrons may be usefully classified in terms of a more restrictive symmetry than SU(3), namely the SU(6) symmetry whose transformations act in the space of $SU(3)\otimes SU(2)_{\sigma}$, where σ denotes Pauli spin. This possibility was first proposed by Gursey and Radicati[6] by analogy with the SU(4) symmetry, acting in the space $SU(2)\otimes SU(2)$, which has proved successful in nuclear physics, for the light nuclei. The mesons then appear in multiplets of

$$\underline{6}\otimes\bar{\underline{6}} = \underline{1} + \underline{35} \qquad (1.9)$$

and the $\underline{35}$ has the $SU(3)\text{-}SU(2)_{\sigma}$ content

$$\underline{35} = {}^{3}(\underline{8}+\underline{1}) + {}^{1}(\underline{8}) \qquad (1.10)$$

where the superfix is 2S+1. The nine triplet states of (1.10) are said to form a nonet and the singlet of (1.9) has the structure ${}^{1}(\underline{1})$.

The baryon states form multiples of

$$\underline{6}\otimes\underline{6}\otimes\underline{6} = \underline{20} + \underline{56} + \underline{70} + \underline{70} \qquad (1.11)$$

where the $\underline{56}$ is symmetric, the $\underline{20}$ antisymmetric and the $\underline{70}$'s are of mixed symmetry with respect to the quark flavour-spin labels. No example of a $\underline{20}$ representation is yet known.

Invariance under space rotations leads to an SU(6) x O(3) symmetry and the correct parity for the multiplets emerges. The symmetry is non-relativistic and works well in classifying practically all known hadrons.[7]

The group-theoretical quark content of hadrons described so far can be predictive when applied to hadron scattering. For low energy scattering in the s-channel the scattering amplitude can conveniently be written as a partial wave series and the various partial wave amplitudes are frequently dominated by resonance pole contributions. At high energies on the other hand it is very useful to work instead with the t-channel partial wave series, transformed via the Sommerfeld-Watson representation[8] into a sum of t-channel Regge poles (and cuts).

In the intermediate region, however, there are two possibilities. One might try adding the two contributions

$$A = A^{res} + A^{Regge} \qquad (1.12)$$

This is often called the interference model because of the oscillations of the amplitude as a function of **s**. However it leads to a double counting of resonance contributions and consequently it was suggested[9] that the average of the resonance contributions and the average of the Regge contributions are equivalent in the intermediate energy range. As **s** increases the density of resonances will increase, smoothing out the bumps,

until eventually there is "local duality":

$$A = A^{res} = A^{regge} \qquad (1.13)$$

This may be expressed in terms of quark diagrams if exotic exchanges and resonances are forbidden.[10,11] The rules for drawing a legal diagram are simple:

i) each quark has its own line and does not change its identity;

ii) every external baryon is represented by three lines running in the same direction;

iii) every external meson is represented by two lines running in opposite directions,

iv) the two ends of a single line cannot belong to the same particle;

v) in any of the s, t, u channels it is possible to cut the diagram in two by cutting only a non-exotic combination of lines.

(An exotic particle here is any combination other than $q\bar{q}$, qqq - for a more recent and topical treatment of exotics see ref. (12)).

Consider now as an (S-channel) example pp and $p\bar{p}$ scattering (p = proton). The six quarks from the incoming protons cannot combine non-exotically and at low energies the process can take place only through a non-resonating background, and, using two component duality,[13] that is by diffraction. On the other hand $p\bar{p}$ scattering has three incoming quarks and three

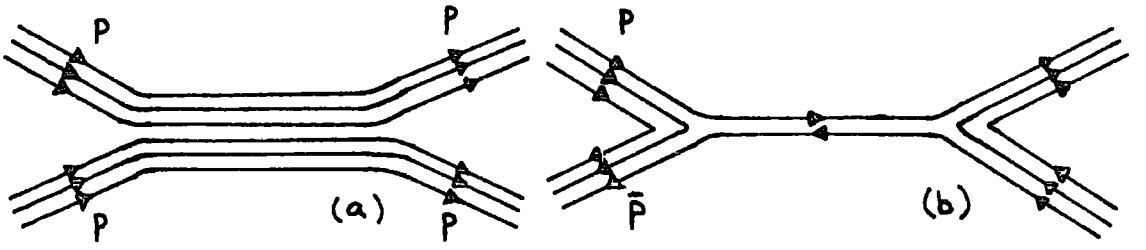

Fig. (1.1)
Quark diagrams for proton-proton(a) and proton antiproton(b) scattering

antiquarks which may form non-exotic combinations. Hence there is a resonance contribution and the cross-section should show resonance structure. Both these predictions are verified by experiment. Similar predictions can be made[10,11] for meson-meson and meson-baryon scattering.

A comparable quark philosophy applied to three-hadron vertices takes the form of the Zweig rule, which says simply that unconnected diagrams are suppressed.

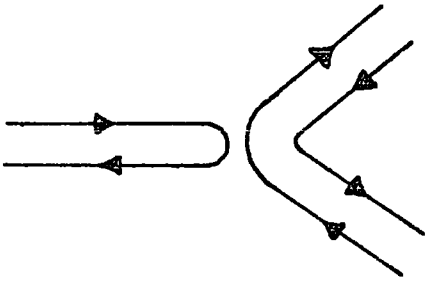

Fig.(1.2)
Zweig suppressed three meson vertex

The small branching ratio for $\phi \to \rho\pi$ and, as we shall see later, the narrowness of the ψ, ψ' are consistent with this rule.

1.3 Dynamical Quarks

A free quark has never been observed and for some time their physical relevance was denied, many people regarding them as only a useful mnemonic underlying the classification of hadrons. However it was eventually realised that the quark hypothesis presented for the first time a single and consistent way of calculating a large number of decay processes with very few assumptions.

The quark binding was assumed to result in non-relativistic quark motion within a hadron and the non-observation of free constituents suggested they were very heavy and tightly bound. Van Royen and Weisskopf[14] speculated on the nature of the deep binding potential-well arguing that there were two possibilities:

i) it may transform as the fourth component of a four-vector, like the Coulomb potential, or

ii) it may be a scalar potential.

The motion of a quark inside the well (of depth V_0) can be described by a Dirac equation

$$\left(\alpha_i \frac{\partial}{\partial x_i} + \beta M_q\right)\psi = (E + V_0)\,\psi \qquad (1.14a)$$

or

$$\left(\alpha_i \frac{\partial}{\partial x_i} + \beta(M_q - V_0)\right)\psi = E\psi \qquad (1.14b)$$

In the scalar case (1.14b) the Dirac magnetic moment of a bound quark would be

$$e/2M_{eff} \quad \text{Bohr Magnetons} \qquad (1.15)$$

where Meff = $M_q - V_o$. Now if the quarks move non-relativistically we expect

$$M_{eff} \simeq M_p/3 \simeq 0.3 \text{ GeV} \qquad (1.16)$$

which yields a value for the proton magnetic moment

$$\mu_p = \mu_q = \frac{e}{2M_{eff}} \simeq \frac{3e}{2M_p} \qquad (1.17)$$

in good agreement with the experimental value. (In fact $m_q = m_u = m_d = 336$ MeV reproduces the experimental value exactly.) The SU(6) prediction for the neutron magnetic moment is then[15]

$$\mu_n = -2/3\ \mu_p \qquad (1.18)$$

in good agreement with experiment (for a comparison of SU(6) predictions with "bag model" predictions for the $\frac{1}{2}^+$ baryons see ref.(16)).

In the vector case (1.14a) the quark magnetic moments would be much smaller ($\propto 1/M_q$) and one must then assume that most of the quark's magnetic moment is anomalous.

Relativistic generalisations of this naive heavy quark model were investigated by considering the Bethe-Salpeter equation[17] for the bound state of a fermion and anti-fermion. In the ladder approximation (when the interaction potential depends only on the quark-antiquark exchange momentum) the configuration space equation takes the form

$$\left(\not{p}/2 + i\not{\partial} - m_q\right)\psi(x)\left(\not{p}/2 - i\not{\partial} + m_q\right) = \lambda V(x)\psi(x) \qquad (1.19)$$

where $P = p_1 + p_2$. This equation is extremely complicated, however for massless bound states it becomes more tractable and can be solved analytically.[18] If the quark mass is large compared with low lying meson masses then a reasonable first approximation may be $m_{hadron} = 0$, followed by a perturbation expansion in m_{hadron}/m_{quark}. Bohm et al[18] inject a covariant oscillator interaction which, as always, simplifies the solution process and leads to linear Regge trajectories on the J vs. M^2_{hadron} plane. (Walters et al[19] take the $m_q \to \infty$ limit of the Bethe-Salpeter equation and demand that the squared equation has a harmonic oscillator form, obtaining similar results.) The model is applied to strong meson decays[20], the vertex calculation methods being motivated by duality diagrams (see Chapter Five), with predicted widths that are in reasonable agreement with experiment (~20%). Notably they predict the 2π branching ratio of the $\rho'(1600)$ regarding this state as the first radial excitation of the ρ. As we shall discuss in more detail later, the node in the wave-function of the ρ' is responsible for a suppressed partial width of

$$\Gamma(\rho' \to 2\pi) \sim 80 \text{ MeV} \qquad (1.20)$$

where the normalisation is on $\Gamma(\rho \to 2\pi) = 146$ MeV.

Although the philosophy of heavy quarks has recently become questionable, consideration of the properties of such four-dimensional theories deserve more attention at the present time.

A disguised heavy quark model was developed from the non-relativistic harmonic oscillator quark model[21] by Feynman, Kislinger and Ravndal(FKR)[22]. Spin is artificially introduced ($P_{quark} \rightarrow \not{P}_{quark}$) and relativity is introduced as simply as possible. The quark mass is disguised as follows.

Consider the non-relativistic harmonic oscillator quark model for mesons. The Hamiltonian in the rest frame is equation (1.1).

$$H = p^2/m_q + m_q\omega^2 r^2 \tag{1.21}$$

i.e.

$$m_q H = p^2 + \Omega^2 r^2 \tag{1.22}$$

where we have defined

$$\Omega = m_q\omega \tag{1.23}$$

Adding a constant $c/4 = m_q^2$ to both sides we can write

$$4m_q^2 + 4m_q H = 4p^2 + 4\Omega^2 x^2 + C \tag{1.24}$$

and if $m_q^2 \gg H^2$ the left hand side can be identified as the relativistic energy squared of the meson.

$$M^2_{meson} = (2m_q + H)^2 \approx 4m_q^2 + 4m_q H \tag{1.25}$$

and we obtain

$$M^2_{meson} = 4(p^2 + \Omega^2 x^2) + C \tag{1.26}$$

We see that the quark mass does not appear explicitly.

Relativity is introduced by writing down the most natural covariant form of (1.21)

$$K = -2\left[P_1^2 + P_2^2 + 2\Omega^2(x_1 - x_2)^2\right] \qquad (1.27)$$

where we are no longer in the c.of m. frame. When $P_\mu = P_{1\mu} + P_{2\mu}$, $2p_\mu = P_{1\mu} - P_{2\mu}$ and $x = x_1 - x_2$ we have the c.of m. equation

$$K = P^2 - 4(p^2 + \Omega^2 x^2) \qquad (1.28)$$

Comparing with equation (1.26), $K-P^2$ may be identified with the mass squared operator. This leads to straight line Regge trajectories of slope $1/8\Omega$ and meson excited states are generated by the action of creation operators on the oscillator vacuum state. Negative norm. time-like excitations are removed by an arbitrary subsiduary condition and an arbitrary correction factor must be introduced to account for the consequent unitarity violation.

Matrix elements are calculated by a minimal substitution of the electromagnetic current and the divergence of the axial current, the large number of predictions being mostly within 20% of the experimental data. The harmonic oscillator form of the interaction and wave-functions was not vigorously tested as data only existed for low lying states.

The discovery of the new particles in November 1974 gave a new dimension to the study of quark dynamics. It now seems clear that the new degree of hadronic

freedom responsible for those unexpected phenomena is charm, precisely in the sense of Bjorken and Glashow[23] and Glashow, Illiopoulos and Maiani[24].

Since the discovery of the ψ and ψ', the charmonium spectrum has filled out and charmed particles (D,F,...) have been isolated. Some of the lower charmonium levels are shown schematically in Figure (1.3). We see that the

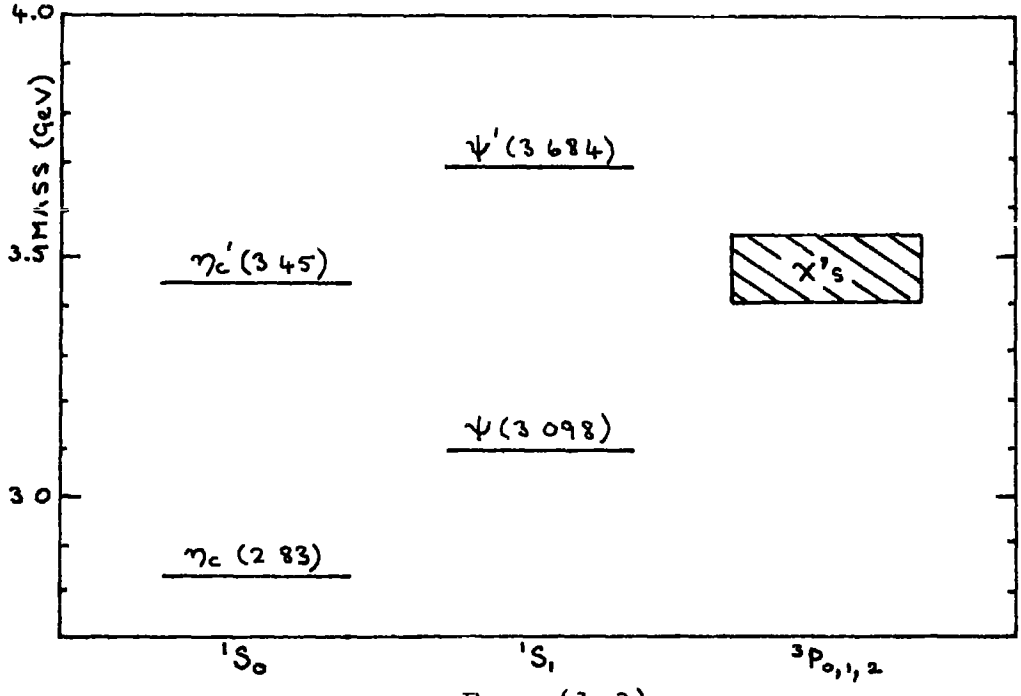

Fig. (1.3)
The lower levels of the charmonium spectrum

radial states are doubly spaced with respect to the orbital states suggesting a harmonic oscillator description which turns out to work well for the lower levels with a Regge slope of 1/2 GeV^{-2}. We can compare this with the Regge slope for the old mesons (= 1 GeV^{-2}) in terms of the FKR model and obtain information on the new charmed quark mass.

From (1.28) we saw that the Regge slope in this model is proportional to

$$1/\Omega = 1/m_q\omega \qquad (1.29)$$

where ω is constant. Hence from the observed slopes we have

$$\Omega_{charm} = 2\,\Omega_{old} \qquad (1.30)$$

or

$$m_c \simeq 2\,m_{u,d,s} \qquad (1.31)$$

and this indicates that the heavy quark model ($m_q >> m_{meson}$) described so far is incorrect - since relation (1.31) would not be possible with a small percentage mass difference between the quarks.

We are thus led (phenomenologically) to the hypothesis of light quarks, a hypothesis supported by the identification of quarks with the light, point-like partons seen in deep inelastic electron scattering experiments (see section 1.5).

The discovery of higher radially excited states in the charmonium spectrum will provide a more exacting test of our understanding of the spatial structure of hadron wave-functions - as will the recent discovery[25] of high mass (10 GeV) vector meson states which is heralding a repeat performance of the new particles show. A unified understanding of the quark dynamics of radially excited states from $m^2_\rho = 0.6$ GeV^2 to $m^2_{\Upsilon''} = 108$ GeV^2 is a problem we attempt to solve in Chapter Four.

1.4 Coloured Quarks

If we now assume that quarks are light then their conspicuous absence forces us to hypothesise that they are dynamically or statistically confined. This is sometimes (emptily) expressed by demanding that all hadrons have zero triality, defined as

$$t = \{n(q) - n(\bar{q})\} \text{ mod. } 3 \qquad (1.32)$$

One of the major problems with the quark hypothesis for many years was due to the Pauli exclusion principle. The lowest baryonic multiplets are the $\frac{1}{2}^+$ octet of states and the $\frac{3}{2}^+$ decuplet of states. Within an SU(6) symmetry, these receive a direct interpretation as the spin-SU(3) components of a $\underline{56}$ representation. However, as we have seen, this representation has even permutation symmetry with respect to the labels on the three quarks, whereas the spin-statistics theorem of Pauli, together with spin $\frac{1}{2}$ for quarks, requires that the complete wave-function should have odd symmetry. The spatial wave function cannot provide this anti-symmetry since the ground state wave-function is expected to be nodeless. We are forced to introduce another label called "colour"[26] so that each quark comes in red, yellow and blue. Now the wave-function can be antisymmetric in colour

$$\varepsilon_{ijk} \; q_i q_j q_k \qquad (1.33)$$

where ε_{ijk} is the completely antisymmetric tensor and

i,j,k go from one to three. With this extra degree of freedom the number of states proliferates - a problem we overcome by treating colour as a group, $SU(3)_{col.}$ in fact, and triality is replaced by postulating that the only allowed physical states are colour singlets. ($\underline{3} \otimes \bar{\underline{3}}$ and $\underline{3} \otimes \underline{3} \otimes \underline{3}$ yield singlets whilst $\underline{3} \otimes \underline{3}$ does not, hence mesons and baryons)

Other arguments for postulating colour in this way include the $\pi^0 \to \gamma\gamma$ decay rate calculation[27] and, as we discuss, in the next section, the experimental value for R in e^+e^- annihilation.

The emergence of colour gauge theories as possible candidates for the description of strong interactions gives colour its main theoretical significance. It was shown by Politzer[28] and Gross and Wilczek[29] that non-Abelian (Yang-Mills) gauge theories in which quarks are coupled to massless gauge vector gluons have a running coupling constant which approaches zero as the (momentum transfer)^2 approaches infinity. The colour SU(3) gauge group provides the non-Abelian character that is necessary for this phenomenon of 'asymptotic freedom', a phenomenon which helps us understand in a wider sense the successes of the parton model.

Asymptotic freedom has led to the conjecture that the forces between quarks resulting from such a colour gauge theory may reach the opposite extreme in the large distance, low energy regime, namely that they become strong enough to confine quarks and gluons until it

becomes energetically favourable to produce $q\bar{q}$ pairs. The pairs interact in a normal colourless way and only colour singlet states can ever be observed.

This is at present only a speculation, the technical problems of Yang-Mills theories are sufficiently great for there to be no general theory of quark confinement. However the phenomenological applications[30] of the view that there exist large distance confining forces together with simple gluon exchange forces at short distances have led to a quantitative understanding of many aspects of meson spectroscopy.

We will adopt these philosophies in our treatment of the radial excitation spectra, together with the indications[31] that the inter-quark forces may be independent of the separation and that the long range confining force is essentially spin-independent.

1.5 Partons and Quarks

The credibility of a physical basis for the quark model was boosted by the emergence of the parton model - a model designed to explain phenomena observed in the deep inelastic scattering of electrons off protons.

When an electron with four momentum k scatters from a target and produces in the final state an electron with momentum k' then the process may be represented by Fig. (1.4) in the one photon exchange approximation. The lab. energy of the photon is $\nu = E-E'$ and the mass-

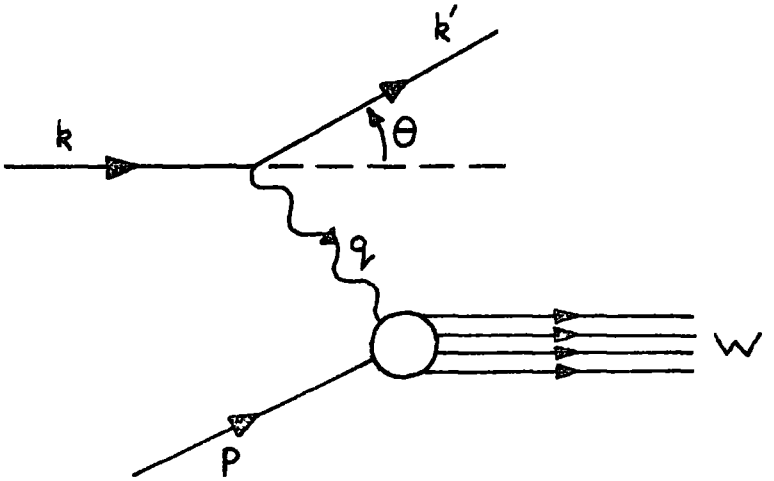

Fig. (1.4)
Electron-proton inelastic scattering in the one photon exchange approximation

squared of the photon can also be varied

$$q^2 = (k - k')^2 = -4EE' \sin^2\theta/2 \qquad (1.34)$$

The lepton-photon vertex is known from quantum-electro-dynamics (QED). Writing down the most general form[32] for the hadronic vertex which is consistent with gauge invariance we obtain for the differential cross-section

$$\frac{d^2\sigma}{d\Omega\, dE'} = \frac{4\alpha^2 E'^2}{q^4}\left\{\cos^2\frac{\theta}{2}\, W_2 + 2W_1 \sin^2\theta/2\right\} \qquad (1.35)$$

where $W_i(\nu, Q^2)$ are structure functions depending on the internal structure of the proton target. The data originally indicated[33] that in fact W_1 and W_2 are functions only of the ratio

$$\omega = \frac{2M\nu}{q^2} \qquad (1.36)$$

known as the Bjorken[34] scaling variable. The parton

model derivation of this scaling phenomenon begins with the assumption that the inelastic cross-section is the incoherent sum of elastic cross-sections from individual partons contained within the proton. For spin $\frac{1}{2}$ partons the structure functions take the form familiar from the QED description of electron-muon scattering

$$\left.\begin{aligned} W_1(\nu,Q^2) &= \frac{Q^2}{4m^2}\,\delta(Q^2/2m - \nu)\,e_i^2 \\ W_2(\nu,Q^2) &= \delta(Q^2/2m - \nu)\,e_i^2 \end{aligned}\right\} \quad (1.37)$$

where m is the parton mass and e_i is the ratio of the parton charge to the muon charge. Then if $f(x)dx$ is the probability that the fractional parton mass is between xM and (x + dx)M

$$W_i(\nu,Q^2) = \sum_i \int_0^1 dx\, f(x) e_i^2 \frac{Q^2}{4x\nu M^2}\,\delta(1/\omega - x) \quad (1.38)$$

where we have used the fact that

$$\delta\left(\frac{Q^2}{2xM} - \nu\right) = \frac{x}{\nu}\,\delta(1/\omega - x) \quad (1.39)$$

Evaluating the integral in (1.38) we obtain

$$W_i(\nu,Q^2) = \sum_i e_i^2/2M\, f(1/\omega) = W_i(\omega) \quad (1.40)$$

and a similar result obtains for W_2. Thus the structure functions have the desired property of scaling.

The experimental behaviour of the ratio of the transverse and scalar photon absorption cross-sections[22]

$$\sigma_S/\sigma_T = W_2/W_1\,(1 + \nu^2/Q^2) \quad (1.41)$$

rules out a spin 0 assignment for the partons and supports the spin $\frac{1}{2}$ assumption. We are led to the attractive proposition that these partons are the quarks of Gell-Mann and Zweig with the usual quantum numbers - a proposition which finds some experimental support[32] in the non-diffractive behaviour of νW_2 (nucleon).

In the parton model $e^+e^- \rightarrow$ hadrons takes place by $e^+e^- \rightarrow$ parton + antiparton and the partons then fragment into the observed hadrons. Then at large $S\ (= q^2)$[35].

$$\sigma(e^+e^- \rightarrow \text{hads}) = \sum_i \sigma(e^+e^- \rightarrow q_i \bar{q}_i)$$

$$= \sum_i e_i^2 \sigma(e^+e^- \rightarrow \mu^+\mu^-) \quad (1.42)$$

and the ratio

$$R = \frac{\sigma(e^+e^- \rightarrow \text{hads})}{\sigma(e^+e^- \rightarrow \mu^+\mu^-)} = \sum_i e_i^2 \quad (1.43)$$

should be constant with q^2 (scales) and its magnitude measures the sum of the squared charges of the fundamental fermion fields (q_i). Below charm threshold we have

$$R = 3(4/9 + 1/9 + 1/9) = 2 \quad (1.44)$$

where the (obviously essential) factor 3 is due to colour. The data do show scaling with a value of R which is roughly constant and between 2 and 3 for $\sqrt{q^2} <$ 3 GeV. The rise in R around 4 GeV would have been troublesome for this model until the discovery of charm

and a new heavy ($\sim$1.9 GeV) lepton[36]. The hadronic contribution to R is here given by

$$R = 3(4/9 + 1/9 + 1/9 + 4/9) = 3\tfrac{1}{3} \qquad (1.45)$$

whilst R settles down to around $5\frac{1}{2}$ after the 4 GeV structures. Subtracting one unit due to heavy lepton pair production there is still 1 missing unit.

This unit may be qualitatively provided by the predictions of non-Abelian gauge theories with asymptotic freedom briefly discussed in the preceding section. In these theories the asymptotic value of R should be approached slowly from above - thus explaining the discrepancies below 3 GeV and above 4 GeV. Small deviations from exact Bjorken scaling are also predicted by gauge theories and these violations have been found experimentally.

The question of additional structure in R, below 3 GeV and above the established ρ,ω,ϕ mesons is one we shall address in detail in what follows, as meson radial excitations are expected to appear in this region. The possible "duality" between the quark-parton model description of this area in R and the vector meson dominance description has been discussed in detail by Close[37] (it is well-known that scaling behaviour can be obtained in generalised vector dominance models[38], - we now proceed to discuss the effect of radial states observed in this region on specific vector dominance calculations.

Summary

We have reviewed the development of the quark model with particular emphasis on the interpretation of quarks as dynamical, confined, hadronic constituents. This interpretation encompasses naturally the phenomenon of radially excited states.

CHAPTER 2

RADIAL EXCITATIONS IN THE VECTOR DOMINANCE MODEL

2.1 Simple Vector-Dominance

The fundamental matrix element relationship of vector-dominance as first written down by Gell-Mann and Zacharaisen[39] reads

$$\langle B|\, j_\mu^3\, |A\rangle = \frac{m_\rho^2 f_\rho}{\sqrt{4\pi\alpha}} \frac{1}{q^2 + m_\rho^2} \langle B|\, J_\mu^{(\rho)}\, |A\rangle \qquad (2.1)$$

where j_μ^3 stands for the iso-vector part of the electromagnetic current and $J_\mu^{(\rho)}$ stands for the ρ-meson source. ($q^2 = (p_B - p_A)^2$). Fig. (2.1) represents a pictorial way

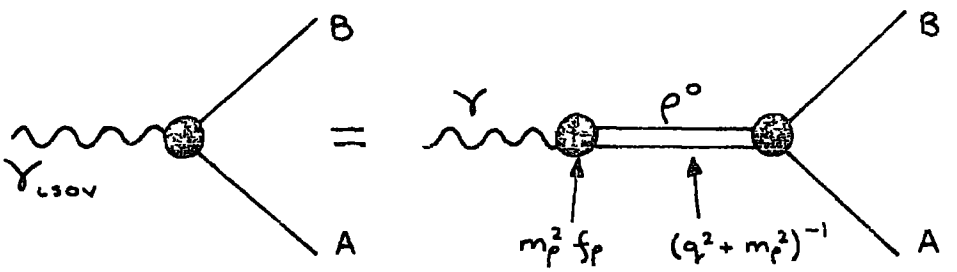

Fig. (2.1)
The rho-photon analogy

of interpreting this equation. The left hand side of (2.1) is directly measurable in photoproproduction, electro-production, e^+e^- experiments etc., since $e\langle B|\, j_\mu^3\, |A\rangle$ is just the amplitude for

$$\gamma_{isov} + A \longrightarrow B \qquad (2.1a)$$

In contrast $\langle B | J_\mu^{(r)} | A \rangle$ that appears on the right-hand side is not directly measurable without the additional hypothesis that the off-shell ρ-amplitudes with $(P_B - P_A)^2 = 0$ are not too different from on-shell ρ-amplitudes with $(P_B - P_A)^2 = -m_\rho^2$ ("smoothness hypothesis"). We must also assume that the photon-vector meson coupling constant fv does not vary in the trip from $q^2 = -m_v^2$ to $q^2 = 0$. At $q^2 = -m_\rho^2$ equation (2.1) is an exact but essentially trivial statement. It tells us only that whenever a ρ-meson is emitted in a hadronic process then an electron-positron pair is also produced with a branching ratio calculable from the γ-ρ coupling constant $m_\rho^2 f_\rho$

Vector-meson-dominance (VMD) then, is not a precisely defined hypothesis, however a great deal of early progress was made by putting faith in the smoothness statement. As a simple example let us consider the case where A,B are a single π^+ state and $q^2 = 0$. If the $\rho\pi\pi$ vertex and f_ρ vary little between $q^2 = -m_\rho^2$ and $q^2 = 0$ then the right-hand-side of equation (2.1) can be approximated by the on-shell $\rho \to \pi\pi$ matrix element. So

$$F_\pi(0)(P_A + P_B)_\mu = \frac{f_\rho}{\sqrt{4\pi\alpha}} g_{\rho\pi\pi} (P_A + P_B)_\mu \qquad (2.2)$$

or

$$\frac{f_\rho}{\sqrt{4\pi\alpha}} g_{\rho\pi\pi} = 1 \qquad (2.3)$$

$(F_\pi(0) = 1$, norm$^2)$

which is a special case of the 'Universality relation' proposed originally by Sakurai[40]. Numerically we have (see Table 2.1)

$$\frac{f_\rho}{\sqrt{4\pi\alpha}}\, g_{\rho\pi\pi} = 1.2 \pm 0.1 \qquad (2.3a)$$

which was an encouraging result for this most basic form of vector-dominance - the ρ-photon analogy.

The real photon in (2.1) with $q^2 = 0$ has only two (transverse) states of polarisation while the finite mass ρ has three. Intuitively it is reasonable that only the matrix elements for transversely polarised ρ's should be compared to photoproduction matrix elements. Hence people first wrote down

$$M(\gamma_{isov} + A \to B) = f_\rho M(\rho^0_{trans} + A \to B) \qquad (2.3)$$

however the notion of transverse polarisation is not covariant and the question was raised - in which frame does the vector-meson resemble the photon most closely? It would seem natural to apply the model to invariant amplitudes which are free from kinematical singularities and zeroes and this leads to non-trivial identities between longitudinal and transverse helicity amplitudes[41] which for certain accessible processes are not incompatible with experiment[42].

The model can of course be trivially extended to encompass the full electromagnetic current by the inclusion of identical terms for the iso-scalar ω and ϕ vector mesons in the right-hand-side of equation (2.1).

This simplest and most predictive form of the vector-dominance model leads to a host of relations which can be subjected to experimental tests (radiative decays, vector-meson photo-production and total cross-sections, Compton scattering ...). Before going on to discuss in detail the new dimension added to VMD by the consideration of radially excited (daughter) stated we examine some of the qualitative features of photon-induced reactions expected within this model.

Firstly total cross-sections in photon-nucleon collisions leading to purely hadronic final states are expected to exhibit the features of typical hadron-hadron cross-sections since γp and $\pi^{\pm} p$ have the same quantum numbers. Experimentally both sets of cross-sections exhibit spectacular resonances at low energies, flattening off at higher energies and eventually starting to rise slowly - in fact the following formula works remarkably well

$$\sigma_{tot}(\gamma p) = \frac{1}{220}\left\{\frac{\sigma_{tot}(\pi^{+}p) + \sigma_{tot}(\pi^{-}p)}{2}\right\} \qquad (2.4)$$

Secondly we expect $\gamma p \rightarrow \rho^{o} p$ to resemble elastic scattering and although there is no direct information on ρp scattering it should exhibit the diffractive features of high-energy hadron-hadron elastic scattering. These features are very nicely exhibited by ρ^{o} photo-production[43] and excellent fits to the data are predicted by

$$\left(\frac{d\sigma}{dt}\right)_{\gamma p \rightarrow \rho^{o} p} = \frac{1}{335}\left\{\frac{1}{2}\sqrt{\frac{d\sigma}{dt}(\pi^{+}p)} + \frac{1}{2}\sqrt{\frac{d\sigma}{dt}(\pi^{-}p)}\right\}^{2} \qquad (2.5)$$

Photon and hadron induced inclusive cross-sections also exhibit similar features and the phenomenon of shadowing in photon-nucleus interactions is extremely convincing evidence for the hadronic nature of the photon (see Chapter Three).

2.2 Radial Excitations and q^2-Dependence of f_V

The discovery of radially excited vector-mesons which couple non-negligibly to e^+e^- demands that the vector dominance model be extended to include their effects. Orbitally excited $^3D_1$ states also have the required quantum numbers for a photon coupling however as their leptonic (e^+e^-) widths are typically an order of magnitude down[44] on those of their $^3S_1$ partners the effect will be small and we neglect them in what follows.

We include in the analysis[45] the possibility of a q^2-dependence of the photon-vector-meson coupling constant f_V. The proposal that f_V is q^2-dependent is certainly not new[46-51] and several attempts have been made to calculate the form of $f_V(q^2)$ for both old and new mesons[49,50]. However no form has emerged which is universally used in vector dominance model calculations, and q^2-dependence is usually ignored. As improved measurements have shown differences between values of f_V measured indirectly at $q^2 = 0$ and at $q^2 = -m_V^2$ in e^+e^- colliding beam experiments[52],

'non-ideal' mixing has been proposed[53] as a solution to the problem for the ω and ϕ mesons. While mixing is a reasonable mechanism for understanding the ω and ϕ it will not solve the same problem for the ψ and so we turn to q^2-dependence for a more general solution. As we are making a case for q^2-dependence but not for a particular model-dependent form of $f_V(q^2)$ we adopt a simple exponential parameterisation which conforms to the expectation[46] that the photon progressively decouples from hadrons in the region $q^2 > 0$ and consequently that $f_V(0)/f_V(-m_V^2) < 1$.

We are effectively rejecting the smoothness assumption for f_V and a photon interaction may be intuitively viewed as the emission by the photon of an on-shell vector meson with a strength proportional to $f_V(q^2)$, q^2 being the unvariant (mass)^2 of the photon. This particular hadronic component of the photon can only exist for a time-interval determined by the uncertainty principle (see Chapter Three) however its subsequent hadronic interaction may be regarded as being on-shell and vector-dominance becomes a more exact hypothesis.

To establish the calculational prescription we will make assumptions about couplings entering it which are either not directly measurable, or are as yet unmeasured. In making these assumptions we are guided by the quark model and reasonable extrapolation. However, these guides are of little help in explaining or

quantifying the apparent suppression of the low multiplicity pion decays of the radial excitations, consequently we discuss each case as it arises.

Other authors have included the $\rho'(1.57)$ and $\psi'(3.68)$ in calculations involving the radiative decay widths of $\omega \to \pi\gamma$[54] and $\psi \to \eta\gamma$, $\psi' \to \eta\gamma$[55-59] and in both cases, in the absence of a q^2-dependent f_V, the effect of the radial excitation has been required to cancel that of the ground state meson. In one case the cancellation results in a larger hadronic coupling $g_{\omega\pi^0\rho^0}$, which improves the consequent prediction of the $\omega \to 3\pi$ width depending on how strongly ρ' couples to 2π. In the other case the cancellation is necessary to reduce the effect of the hadronic coupling $g_{\psi'\psi\eta}$. While the cancellation is plausible in the ρ, ρ' case it leads in the other to the requirement that $|g_{\psi'\psi\eta}| > |g_{\psi\psi\eta}| > |g_{\psi\psi\eta}|$ while in the quark model[59,60] one might expect the ground state coupling $g_{\psi\psi\eta}$ to dominate.

The introduction of q^2-dependence in addition to the radial excitations allows the quark model expectations to be restored in the ψ, ψ' case while retaining the enhancement of $g_{\omega\pi^0\rho^0}$ in the $\omega \to \pi\gamma$ decay calculation. To do this we will find it necessary to <u>add</u> the effect of the now suppressed radial excitations to that of the ground state vector meson. While this requirement emerges naturally from a study of the ψ, ψ' radiative decays in the next section, it is also necessary for the total cross-section predictions which we discuss in Chapter Three.

We include the effects of the well-established radial excitations $\rho'(1570)$, $\psi'(3684)$ which fit well into harmonic-oscillator quark model spectra where the spacings are described by the eigenvalue equation

$$M^2_{hadron} = \Omega\,(2n + l + 3/2) \qquad (2.6)$$

with $\Omega_{u,d} \sim 1\,GeV^2$, $\Omega_c \sim 2\,GeV^2$ as we have seen in Chapter One. The recent observations[61] of an $\omega'(1.78)$ and possibly a $\phi'(1.82)$[62-64] give further motivation for systematically including radial excitations in vector dominance model calculations.

In the sections that follow we use the vector dominance model without using SU(3) or the quark-model to extend the results except where it is required to make the point of the necessity of including radial excitations of the vector-mesons and the q^2-dependence of the photon vector-meson coupling. The quark model does constitute a background to the analysis as the ρ', ω', ϕ' and ψ' are regarded as radial excitations of the ρ, ω, ϕ and ψ and this fact is used to estimate the relative size of vertex couplings. Also it is assumed that the ρ is made up of u,d quarks, the ω and ϕ are essentially u,d and s quarks respectively and the ψ is primarily made up of c quarks. While the quark content and the Zweig rule are used as a guide in comparing reaction mechanisms, the actual mechanisms do not influence our conclusions.

The couplings f_V are measured at $q^2 = m_V^2$ in e^+e^-

colliding beam experiments, the width formula being (in the one-photon-exchange approximation)

$$\Gamma(V \to e^+e^-) = f_V^2(-m_V^2) \propto m_V/3 \qquad (2.7)$$

where $\alpha = e^2/4\pi = 1/137$. The measured values from ref. (65) are given in Table (2.1) along with f_V^2 and because of the many conventions in this subject we also tabulate $f_V^2/4\pi = \alpha/f_V^2$, $\gamma_V^2 = \alpha/4f_V^2$.

Table (2.1):

Decay widths and couplings for $V \to e^+e^-$

Vector Meson	m_V GeV	$\Gamma(V \to e^+e^-)$ keV	$f_V^2/10^4$	$f_V/10^2$	$f_V^2/4\pi = \alpha/f_V^2$	$\gamma_V^2 = \alpha/4f_V^2$
ρ	0.773	6.54±0.76	3.6	5.90	2.10	0.53
ω	0.783	0.76±0.17	4.0	2.00	18.25	4.56
ϕ	1.020	1.31±0.08	5.3	2.30	13.77	3.44
ψ	3.098	4.7±0.7	6.2	2.29	11.77	2.94
ρ'	1.57 (a)	1.60±0.47 (a)	4.3	2.08	16.97	4.24
ω'	1.75 (b)	0.43 (d)	0.8	0.89	91.24	22.81
ϕ'	1.82 (c)	1.07 (d)	2.0	1.40	36.50	9.12
ψ'	3.684	2.1±0.4	2.3	1.53	31.74	7.93

All data is from ref. (65) except (a) Ref. (52), (b) ref. (61), (c) ref. (64) and (d) which are predicted.

The right hand side of equation (2.1) is now modified to be a sum over all relevant vector-mesons and f_V becomes $f_V(q^2)$. We apply the model at $q^2 = 0$ where we

can write equation (2.1) for radiative vertices as

$$A(\gamma ab) = \sum_{v} f_v(0)\, A(vab) \qquad (2.8)$$

and for photoproduction amplitudes

$$A(\gamma a \to bc) = \sum_{v} f_v(0)\, A(va \to bc) \qquad (2.9)$$

where we have absorbed a factor $e = \sqrt{4\pi\alpha}$ into the photo-reaction amplitudes.

Assuming that there is a q^2-dependence of f_v, Barger and Phillips[46] note that the progressive decoupling of photons from hadrons in the $q^2 > 0$ region suggests

$$\frac{f_v(0)}{f_v(-m_v^2)} < 1 \qquad (2.10)$$

In the following we require a parameterisation of the q^2-dependence of f_v which reproduces (2.9) and we take

$$f_v(q^2) = f_v(0) \exp(-cq^2) \qquad (2.11)$$

and choose c to be the same for all vector mesons. The parameterisation is simple in that it makes no statement about poles in $f_v(q^2)$, their position or whether they are single or multiple.

If we take a quark model point of view (2.7) and (2.8) contain both ground state and radially excited vector mesons. Clavelli and Nussinov[59] have noted that one might expect the magnitude of couplings involving ground state and radially excited mesons to be

suppressed relative to the magnitude of couplings involving mesons of the same excitation and this suppression is attributed to poor overlap between the wave-functions of the radial excitations and the ground state meson. In what follows we will expect that ground state couplings are larger than those involving one or two radial excitations.

2.3 Radiative Decays of ψ and ψ'

The radiative decays of the ψ and ψ', especially $\psi \to \eta\gamma$, and $\psi' \to \eta\gamma$ provide evidence in support of a q^2-dependent f_V.

If one accepts the charmonium model view that the $\psi'(3.68)$ is the first radial excitation of the $\psi(3.1)$, a state made essentially from charmed (c) quarks, the photon in radiative ψ, ψ' decays can only be decomposed in terms of essentially $c\bar{c}$ states, although a very small amount[58] of u, d and s quarks in the ψ's is not ruled out. With this view the $\psi \to \eta\gamma$, $\psi' \to \eta\gamma$ decays are suppressed by the Zweig rule unless the η, η' contains an admixture of $c\bar{c}$[56, 66-69]. The actual mechanism for allowing the decay need not strictly concern us, as it drops out of the calculations which follow.

The Lagrangian for the decay of a $J^P = 1^-$ particle (Va) of mass m_{Va} into particles with $J^P = 0^-(P)$, $1^-(V_b)$, where V_b can be a photon, is

$$\mathcal{L} = g_{V_a V_b P}\, \varepsilon^{\mu\nu\alpha\beta} (\partial_\alpha V_{a\mu})(\partial_\beta V_{b\nu}) + h.c. \qquad (2.12)$$

and the decay width is

$$\Gamma(V' \to VP) = \frac{g^2_{V_a V_b P}}{12\pi} k^3 \qquad (2.13)$$

where

$$k^2 = (m^2_{V_a} - (m_{V_b} + m_P)^2)(m^2_{V_a} - (m_{V_b} - m_P)^2)/4m^2_{V_a} \qquad (2.14)$$

There are two measurements[70, 71] of the $\psi \to \eta\gamma$ width and we take the most recent[71] to get the coupling

$$g_{\psi\eta\gamma} = (1.0 \pm 0.2) \times 10^{-3} \ \text{GeV}^{-1} \qquad (2.15)$$

For the $\psi' \to \eta\gamma$ width only an upper bound is measured[70] which gives

$$g_{\psi'\eta\gamma} < 7.7 \times 10^{-4} \ \text{GeV}^{-1} \qquad (2.16)$$

and the hadronic width $\psi' \to \psi\eta$[73] determines

$$g_{\psi'\psi\eta} = 0.23 \pm 0.04 \ \text{GeV}^{-1} \qquad (2.17)$$

The overall sign ambiguity has been ignored in all couplings.

It is interesting to note that if mixing of $c\bar{c}$ in the η and η' is the mechanism by which the decays $\psi \to \eta\gamma\,(\eta'\gamma)$, $\psi' \to \eta\gamma\,(\eta'\gamma)$ proceed, then

$$\frac{g_{\psi\eta\gamma}}{g_{\psi'\eta\gamma}} = \frac{g_{\psi\eta'\gamma}}{g_{\psi'\eta'\gamma}} = \frac{g_{\psi\eta_c\gamma}}{g_{\psi'\eta_c\gamma}} \qquad (2.18)$$

where $\eta_c(2.88)$ is the pseudoscalar meson which is essentially made up of $c\bar{c}$ quarks. The data[70-72] give

$$\frac{g_{\psi\eta\gamma}}{g_{\psi'\eta\gamma}} > 1.3 \ , \quad \frac{g_{\psi\eta'\gamma}}{g_{\psi'\eta'\gamma}} > 1.1 \qquad (2.19)$$

which do not contradict the mixing hypothesis. The ratio for the η_c decays is poorly determined.

Applying the vector-dominance model to the radiative couplings $g_{\psi\eta\gamma}$, $g_{\psi'\eta\gamma}$ gives

$$g_{\psi\eta\gamma} = f_\psi(0)\, g_{\psi\psi\eta} \pm f_{\psi'}(0)\, g_{\psi'\psi\eta}$$
$$g_{\psi'\eta\gamma} = f_{\psi'}(0)\, g_{\psi'\psi\eta} \pm f_\psi(0)\, g_{\psi'\psi\eta} \qquad (2.20)$$

where the sign ambiguity results from taking the square root of the decay widths. It is this ambiguity which allows one to solve (2.20) by cancelling the ψ part of the photon against the ψ' part.

Defining the ratios,

$$X_\pm = \frac{g_{\psi\psi\eta}}{g_{\psi'\psi\eta}} \qquad X'_\pm = \frac{g_{\psi'\psi'\eta}}{g_{\psi'\psi\eta}} \qquad (2.21)$$

gives

$$g_{\psi\eta\gamma} = f_\psi(0)\left[X_\pm \pm \frac{f_{\psi'}(0)}{f_\psi(0)}\right] g_{\psi'\psi\eta}$$

$$g_{\psi'\eta\gamma} = f_\psi(0)\left[X'_\pm \frac{f_{\psi'}(0)}{f_\psi(0)} \pm 1\right] g_{\psi'\psi\eta} \qquad (2.22)$$

where the subscript on the $X_\pm$ is associated with the $\pm$ sign in (2.22). The contribution to (2.22) from decomposing the photon into ω and ϕ is negligible as can be seen by calculating the couplings for the $\omega\eta$ and $\phi\eta$ decay modes of ψ and ψ' from the data in[74] and justifies the assumption that the admixture of u,d quarks in the ψ and ψ' is small.

(2.22) provides a test of both q^2-dependence of f_V and of the effect of radial excitations. If f_V is not

q^2-dependent, then (2.22) determines X and X' to be

$$X_+ = -0.48, \quad X'_+ < -1.3$$
$$X_- = +0.86 \quad X'_- < +1.7 \qquad (2.23)$$

This suggests that $|g_{\psi\psi\eta}| > |g_{\psi\psi\eta}| > |g_{\psi\psi\eta}|$ and that a cancellation between the radial and ground state contributions is required to satisfy (2.22), no matter which solution is chosen.

The q^2 independent calculation clearly requires higher order radial excitations to play a major rather than a minor role in the vector-dominance model[48] and suggests[56] that the vector dominance series (2.8) converges as a result of cancellation between terms. This view is tenable if the couplings change sign each time a particle is replaced by its next order radial excitation[55], but one still requires that the couplings decrease in size with increasing order of excitation if the series is to be saturated by a small number of terms. The fact that $|g_{\psi\psi\eta}|$ is required to be the smallest, rather than the largest coupling in the solution to (2.22) contradicts the quark model expectation[55,59]. This contradiction, the apparently fortuitous cancellation necessary to satisfy (2.22) and the dominant role of radially excited states suggests that we consider the q^2-dependence of f_V with a view to finding a more satisfactory solution.

If we consider q^2-dependence of f_V we require $f_V(0) < f_V(-m_V^2)$, and also, if the radial excitation is

not to dominate, the suppression of $f_{\psi'}$ must be greater than that for f_{ψ} . Both these requirements are met by the parameterisation (2.11) and to determine the single parameter, C, we plot in Fig. (2.2) the values of $X_{\pm}$, $X'_{\pm}$

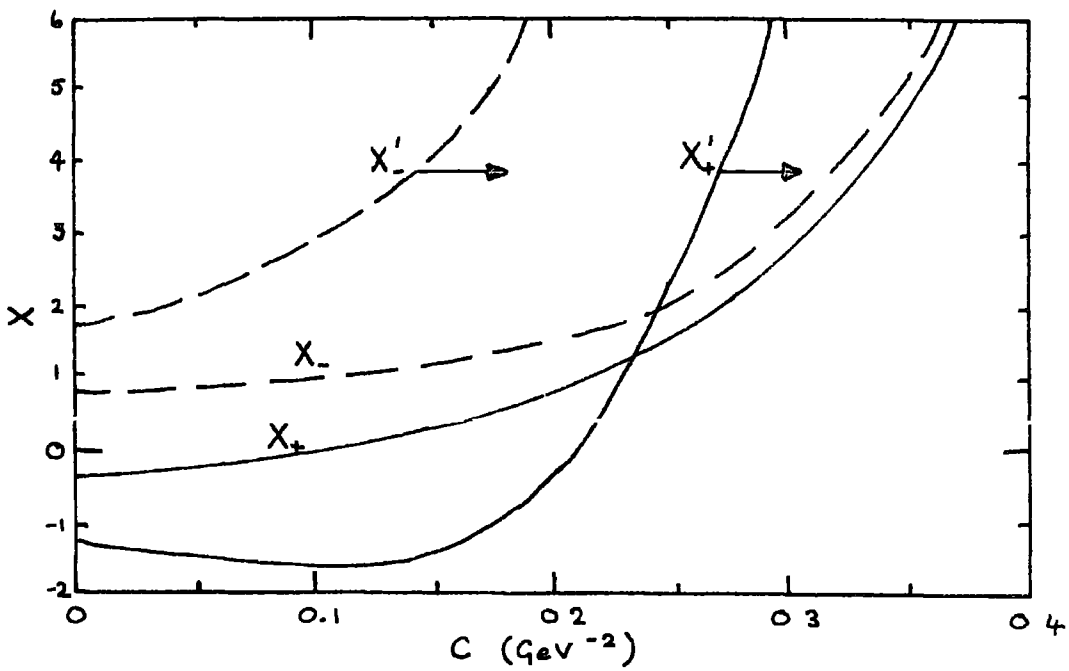

Fig. (2.2)

The value of the ratios $X_{\pm} = g_{\psi\psi\eta}/g_{\psi'\psi\eta}$ and $X'_{\pm} = g_{\psi'\psi\eta}/g_{\psi'\psi\eta}$ necessary to satisfy (2.22) plotted against the q^2-dependence parameter, C. The data used are given in Table (2.2)

which satisfy (2.22) against C. There are two solutions to consider, if we ignore the two where the sign of $g_{\psi\psi\eta}$ differs from that of $g_{\psi'\psi'\eta}$ on the grounds that this situation is unlikely to arise in a quark model.

The X_-, X'_- solution with no q^2-dependence (C = 0) is the one most commonly used to fit the data. However it requires one to accept that[56] $|g_{\psi'\psi\eta}| = |g_{\psi\psi\eta}|$, which means that the series (2.8) will contain a large

number of significant terms unless f_V decreases rapidly as V is replaced by its next order radial excitation. As the data for the ρ' and ψ' in Table (2.1) do not suggest such a rapid fall off we discard this solution for C = 0. As C increases beyond 0.2 GeV^{-2} we find $|g_{\psi\psi\eta}| > |g_{\psi'\psi\eta}|$, but from the X' curve we see that $|g_{\psi'\psi'\eta}| > |g_{\psi'\psi\eta}|$ and consequently that $|g_{\psi'\psi\eta}| >> |g_{\psi\psi\eta}|$ which does not restore the expected quark model results. Of course the X'_- curve represents only a bound on the $\psi' \to \eta\gamma$ width and it may well shift to the right, but even with a factor of 3 decrease the requirement imposed on the couplings is only slightly reduced. For these reasons we rule out the X_-, X'_- solution.

The X_+, X'_+ solution for $C \simeq 0.26$ GeV^{-2} gives $|g_{\psi'\psi\eta}| \simeq \frac{1}{2}|g_{\psi\psi\eta}|$ which is consistent with what we would expect from the quark model. For the same value of C, X'_+ is not well determined as the X'_+ curve corresponds to the measured upper bound of the $\psi' \to \eta\gamma$ width. The curve will shift to the right as the bound on the width decreases and the value of X'_+ at $C \simeq 0.26$ GeV^{-2} will fall from $X'_+ = 2.5$. How far the curve shifts and X'_+ falls at fixed C is an open question, however we will take $X'_+ = 1$, regarding it as an underbound, which is not incompatible with the data. $X_+ = 2$ and $X'_+ = 1$ then give $g_{\psi'\psi'\eta} = g_{\psi'\psi\eta} = \frac{1}{2} g_{\psi\psi\eta}$ at C = 0.26 GeV^{-2}. This choice is compatible with the quark model and it eliminates the need for a fortuitous cancellation between the ψ and ψ' parts of the photon. Also the first radial

excitation is no longer a dominant contribution to (2.22) and higher order radial excitations are even more suppressed. Having made the choice of parameters, we can use the hadronic width $\Gamma(\psi' \to \psi\eta)$ to predict the radiative decays and the results are given in Table (2.2)

Table (2.2):

Decay width predictions

Process	Experimental width	Ref	Prediction	Experimental input
$\psi \to \eta\gamma$	90±27 eV	(71)	90 eV	$\psi' \to \psi\eta$
$\psi' \to \eta\gamma$	<91 eV	(70)	45 eV	$\psi' \to \psi\eta$
$\psi' \to \eta'\gamma$	<250 eV	(72)	93 eV	$\psi' \to \psi\eta'$
$\psi' \to \gamma\chi$ (3 41)	17±9 keV	(76)	11±4 keV	$\rho' \to \rho\varepsilon$ and SU(4)
χ (3 41) $\to \psi\gamma$	-	-	0.15±0.05 MeV	$\rho' \to \rho\varepsilon$ and SU(4)
$\psi \to \pi^0\gamma$	5±3 eV	(70)	1 0±0 2 eV	$\psi \to \rho\pi$
$\psi' \to \pi^0\gamma$	<1.6 keV	(77)	0.5 eV	$\psi' \to \rho\pi$
$\psi' \to \tau\rho$	<230 eV	(71)	300±80 eV	$\psi \to \rho\pi$
$\rho' \to \pi\omega$	100→400 MeV	(65)	250 MeV	$\omega \to \pi\gamma$
$\rho' \to \pi\phi$	-	-	0.32 MeV	$\phi \to \pi\gamma$
$\rho \to \pi\gamma$	35±10 keV 190±60 keV	(86) (87)	108* keV	$\omega \to \pi\gamma$ $\phi \to \pi\gamma$
$\omega' \to \rho\pi$	-	-	1.4* GeV	$\omega \to \pi\gamma$
$\omega' \to \rho'\pi$	-	-	12 9 MeV	$\omega \to \pi\gamma$
$\phi' \to \rho\pi$	-	-	1.5* MeV	$\phi \to \pi\gamma$
$\phi' \to \rho'\pi$	-	-	0 03MeV	$\phi \to \pi\gamma$
$\phi \to \rho\pi$	0.57±0 03 MeV	(65)	0.3±0 1 MeV	$\phi \to \pi\gamma$

*These widths decrease if low multiplicity pion decays of radial excitations are suppressed

Equations of the form (2.22) can be used to determine the ratios of $g_{\psi\eta'\gamma}/g_{\psi'\eta'\gamma}$ and $g_{\psi\eta_c\gamma}/g_{\psi'\eta_c\gamma}$ but not the individual widths, as the necessary hadronic decays $\psi' \to \psi\eta'$, $\psi' \to \psi\eta_c$ are kinematically not allowed. Making the same choice for X_+, X'_+ and C as before we find that the ratios are equal, and equal to $g_{\psi\eta\gamma}/g_{\psi'\eta\gamma}$. This is consistent with the mixing argument discussed above.

Further evidence consistent with q^2-dependence of f_V is given by the decay $\psi' \to \gamma\chi(3.4)$ although additional assumptions are required. Proceeding as before we write

$$g_{\psi'\gamma\chi} = f_\psi(0)\left[X'_\pm \frac{f_{\psi'}(0)}{f_\psi(0)} \pm 1\right] g_{\psi'\psi\chi} \qquad (2.24)$$

with $X'_\pm = g_{\psi'\psi\chi}/g_{\psi'\psi\chi}$. To continue we require the SU(4) relation

$$\sqrt{2}\, g_{\rho'\rho\varepsilon} = g_{\psi'\psi\chi} \qquad (2.25)$$

and estimating the width to be $\Gamma(\rho' \to \rho\varepsilon) = 200\text{-}400$ MeV [48,75] gives $g_{\rho'\rho\varepsilon} = 33\text{-}47\ \text{GeV}^{-1}$. This assumes that $\chi(3.4)$ is a scalar resonance and the SU(4) partner of the ε, and the ε mass is about 750 MeV.

Guided by the η decays we select the additive solution to (2.24) and we have a choice of using the $\psi' \to \gamma\chi$ width to evaluate X'_+ or to take $X'_+ = 1$ as in the η decays and predict the width. Adopting the latter course we predict

$$\Gamma(\psi' \longrightarrow \gamma\, \chi(3\,4)) = 7\,4 - 14\,4 \quad keV \qquad (2.26)$$

compared with[76]

$$\Gamma(\psi' \longrightarrow \gamma\, \chi(3\,4)) = 17 \pm 9 \quad keV \qquad (2.27)$$

which is reasonable agreement. Using the same method we can calculate the $\chi(3.4) \longrightarrow \gamma\psi$ width and the result is in Table (2.2).

Turning to $\psi \longrightarrow \gamma\pi$, $\psi' \longrightarrow \gamma\pi$ decays which suggest a small admixture of u,d quarks[58] in the ψ and ψ' we find

$$g_{\psi\pi\gamma} = f_\rho(0)\left[1 \pm \frac{f_{\rho'}(0)}{f_\rho(0)}\,\frac{1}{X_\pm}\right] g_{\psi\pi\rho}$$

$$g_{\psi'\pi\gamma} = f_\rho(0)\left[\frac{f_{\rho'}(0)}{f_\rho(0)}\,X'_\pm \pm 1\right] g_{\psi'\pi\rho} \qquad (2.28)$$

with $X = \dfrac{g_{\psi\pi\rho}}{g_{\psi\pi\rho'}}$ and $X' = \dfrac{g_{\psi'\pi\rho'}}{g_{\psi'\pi\rho}}$. Taking the additive solution and the same parameters as before, the radiative widths can be deduced from the hadronic widths $\Gamma(\psi \longrightarrow \pi\rho) = 690 \pm 150$ eV, $\Gamma(\psi' \longrightarrow \pi\rho) < 230$ eV[71]. They are

$$\Gamma(\psi \longrightarrow \pi\gamma) = 1 \pm 0.2\,eV, \quad \Gamma(\psi' \longrightarrow \pi\gamma) < 0\,5eV \qquad (2.29)$$

compared with[70,77]

$$\Gamma(\psi \longrightarrow \pi\gamma) = 5 \pm 3\,eV, \quad \Gamma(\psi' \longrightarrow \pi\gamma) < 1.6\,keV \qquad (2.30)$$

We also note that if all couplings with one radially excited state are half the magnitude of the corresponding coupling with all the particles in the ground state, then

$$g_{\psi'\rho^0\pi^0} \simeq \tfrac{1}{2} g_{\psi\rho\pi^0} = 8.5\times10^{-4}\ \mathrm{GeV}^{-1} \qquad (2.31)$$

compared with the experimental value[71] of

$$g_{\psi'\rho^0\pi^0} < 7.5\times10^{-4}\ \mathrm{GeV}^{-1} \qquad (2.32)$$

in reasonable agreement, given the data. If, however, the low multiplicity decay of $\psi' \to 3\pi$ is suppressed, as it is in the case $\rho' \to 2\pi$ and $\omega' \to 3\pi$[60,61] we would expect $g_{\psi'\rho^0\pi^0} \ll g_{\psi\rho^0\pi^0}$, well within the experimental bound.

In summary, the radiative decays of ψ, ψ' to $\eta(\eta', \eta_c)$, $\chi(3.4)$ and π^0 are found to be in reasonable accord with the proposal that the vector meson-photon coupling is q^2-dependent and that the radial excitations of the vector mesons must be included in the decomposition of the photon in the vector dominance model. Choosing a simple parameterisation of the q^2-dependence of f_V we are able to fit the data on the radiative decay of ψ and ψ' to η in a way which does not require a cancellation of the ψ part of the photon with a large ψ' part. In fact the ψ and ψ' parts of the photon add, and the ratios $X = g_{\psi\psi\eta}/g_{\psi'\psi\eta}$, $X' = g_{\psi'\psi'\eta}/g_{\psi'\psi\eta}$ are determined or bounded by the data and quark model expectations. In what follows we take the same parameterisation and apply it to the data for , ω and ϕ. The same q^2 dependence (2.11) with $C = 0.26\ \mathrm{GeV}^{-2}$ is maintained throughout, however, in view of the apparent suppression of low multiplicity decays of ρ' and ω', X_+ is re-examined each time it is used.

2.4 Radiative Decays of 'Old' Vector Mesons

Vector dominance model calculations done on vertices involving ρ, ω and ϕ have been quite successful [54,78,79], although it has proved difficult to accommodate the data on $\rho^- \to \pi^- \gamma$ and on the SU(3) related process $K^{*0} \to K^0 \gamma$ [48,78].

This success has been achieved without requiring a q^2-dependence of f_V, although it has been proposed [47] as a mechanism for explaining the discrepancy between the vector-dominance model prediction and the new measurement of the $\phi \to \pi\rho$ width [80]. Mass dependence of hadronic vertices [78] has also been tried in an analysis of radiative decays, the motivation being that it is an SU(3) breaking mechanism.

Radial excitations, or heavy mesons have been included in radiative decay calculations in a variety of ways [54,78], but without q^2-dependence of f_V which would appear to be required by the ψ and ψ'. As the $\rho'(1.57)$ is established, and the $\omega'(1.78)$, $\phi'(1.82)$ have recently been seen [61-64] it is appropriate to demonstrate that a consistent calculational scheme can be established which includes both q^2-dependence, and the radial excitations of ρ, ω and ϕ.

Proceeding as before we can immediately write down the modified universality relation (2.3)

$$\frac{f_\rho(0)}{\sqrt{4\pi\alpha}}\, g_{\rho\pi\pi}\left[1 \pm \frac{f_{\rho'}(0)}{f_\rho(0)}\,\frac{1}{x_\pm}\right] = 1 \qquad (2.33)$$

Numerically we have (maintaining the X_+ solution)

$$\frac{f_\rho(0)}{\sqrt{4\pi\alpha}}\, g_{\rho\pi\pi}\left[1 + \frac{f_{\rho'}(0)}{f_\rho(0)}\,\frac{1}{2}\right] \simeq 1.1 \pm 0.1 \qquad (2.33a)$$

which is in better agreement than the value obtained without q^2-dependence and radial excitations (2.3a).

We now consider the $\omega \to \pi\gamma$ vertex. The width, $\Gamma(\omega \to \pi^0\gamma) = 880 \pm 50$ keV[65] gives a coupling $g_{\omega\pi^0\gamma} = (0.78 \pm 0.02)\text{GeV}^{-1}$ and continuing as before

$$g_{\omega\pi^0\gamma} = g_{\omega\pi^0\rho^0} f_\rho(0)\left[1 + \frac{f_{\rho'}(0)}{f_\rho(0)}\,\frac{1}{X_+}\right] \qquad (2.34)$$

where $X_+ = g_{\omega\pi^0\rho^0}/g_{\omega\pi^0\rho'^0}$. Again we take $X_+ = 2$ and deduce that $g_{\omega\pi^0\rho^0} = 13.95\text{GeV}^{-1}$ which can be compared with 13.22GeV^{-1} with no ρ' or q^2-dependence of f_ρ

An effect of increasing $g_{\omega\pi^0\rho^0}$ is to raise the prediction for the $\omega \to 3\pi$ width from the simple VDM value of 5.6 MeV[81] or 6.5 MeV[54] closer to the measured value of 9.0 ± 0.4 MeV[65]. The increase varies according to the method of calculation[54], and also on how strongly the ρ' couples to 2π. The point we would make is that q^2-dependence and the ρ' are consistent with an improved result for this width.

The calculation of $\omega \to 3\pi$ from $\omega \to \pi^0\gamma$ has been done without q^2-dependence[54]. The enhancement of $g_{\omega\pi^0\rho^0}$ necessary to fit the data has been achieved by letting the ρ' and ρ contributions have opposite signs and by not letting the ρ' couple to 2π. Such solution fits the data and requires $f_{\rho'}(m_{\rho'}^2)\, g_{\rho'^0\omega\pi^0}/f_\rho(m_\rho^2)\, g_{\omega\rho^0\pi^0} = -0.16 \pm 0.03$, or $|g_{\rho'^0\omega\pi^0}/g_{\omega\rho^0\pi^0}| \simeq 0.45$, a result

not inconsistent with the quark model. However, when the same solution is applied to the ψ radiative decays the ψ' makes a dominant contribution, and for this reason we discard the negative solution to (2.34).

Confirmation of the fact that $g_{\rho^0\omega\pi^0} \simeq \frac{1}{2} g_{\rho^0\omega\pi^0}$ comes from predicting $\Gamma(\rho'^0 \to \pi^0\omega) \simeq 250$ MeV. The experimental width can be estimated from $\Gamma(\rho') \simeq$ 200 - 800 MeV[65], and assuming that, at most, half of the 4π events go by an $\omega\pi$ intermediate state[82]. The result is $\Gamma(\rho' \to \pi\omega) \simeq 100 \to 400$ MeV if ρ' does not couple to 2π or $\Gamma(\rho' \to \pi\omega) \simeq 75 \to 300$ MeV if ρ' has a 25% branching ratio to 2π [83]. Thews[78] estimates $\Gamma(\rho' \to \pi\omega) \simeq 140$ MeV which would require $X_+ \simeq 3$ and consequently $g_{\omega\rho^0\pi^0} \simeq 14.4$ GeV^{-1} to yield $\Gamma(\rho' \to \pi\omega) \simeq 120$ MeV.

If we continue with $X_+ = 2$, then the effective photon coupling is

$$f_\rho(0)\left[1 + \frac{f_{\rho'}(0)}{f_\rho(0)} \frac{1}{X_+}\right] = 5.5 \times 10^{-2} \qquad (2.35)$$

compared with $f_\rho(m_\rho^2) = 5.9 \times 10^{-2}$. Using (2.35) and the hadronic width[80] $\Gamma(\phi \to \pi\rho) = 0.57 \pm 0.03$ MeV, we predict $\Gamma(\phi \to \pi\gamma) = 12.1$ keV compared with the experimental values of 5.9 ± 2.0 keV[84] and 10.6 ± 5.1 keV[85]. The discrepancy between the prediction and the recent measurement of 5.9 keV is difficult to resolve, as its removal requires $X_+ > -1$ if $C = 0$, or 0.26 GeV^{-2}, in conflict with the quark model and increasing C causes problems for the $\sigma(\rho N)$ calculation.

The $\rho^- \to \pi^- \gamma$ decay is analysed in a similar way to the above to give

$$g_{\rho^-\pi^-\gamma} \simeq g_{\omega\pi^0\rho^0} f_\omega(0) \left[1 + \frac{f_{\omega'}(0)}{f_\omega(0)} \frac{1}{X_+^\omega} \right]$$

$$+ g_{\phi\pi^0\rho^0} f_\phi(0) \left[1 + \frac{f_{\phi'}(0)}{f_\phi(0)} \frac{1}{X_+^\phi} \right] \qquad (2.36)$$

where the small ψ and ψ' contributions have been ignored. If we take $X_+^V = g_{V\pi\rho} / g_{V'\pi\rho} = 2$ there remain two unknowns, $f_{\omega'}(0)$ and $f_{\phi'}(0)$. From the following observation that

$$\frac{f_{\rho'}(0)}{f_\rho(0)} \simeq 0.21 \,, \qquad \frac{f_{\psi'}(0)}{f_\psi(0)} \simeq 0.24 \qquad (2.37)$$

we infer that

$$\frac{f_{\omega'}(0)}{f_\omega(0)} = \frac{f_{\phi'}(0)}{f_\phi(0)} \simeq 0.23 \qquad (2.38)$$

which allows us to estimate the values $f^2_{\omega'}(m^2_{\omega'})$ and $f^2_{\phi'}(m^2_{\phi'})$ given in Table (2.1). (2.36) becomes

$$g_{\rho^-\pi^-\gamma} \simeq \left[g_{\omega\pi^0\rho^0} f_\omega(0) + g_{\phi\pi^0\rho^0} f_\phi(0) \right] [1.1]$$

$$\simeq 0.28 \ \text{GeV}^{-1} \qquad (2.39)$$

The predicted width is $\Gamma(\rho^- \to \pi^- \gamma) = 108$ keV which is larger than the Primakof effect measurement[86] of $\Gamma(\rho^- \to \pi^- \gamma) = 35 \pm 10$ keV, but smaller than the measurement from $\gamma p \to \rho^+ n$ [87] of $\Gamma(\rho^- \to \pi^- \gamma) = 190 \pm 60$ keV. Using SU(3) we also predict $\Gamma(K^{*0} \to K^0 \gamma) = 140$ keV compared with the Primakof effect measurement[88] of $\Gamma(K^{*0} \to K^0 \gamma) = 75 \pm 35$ keV.

The discrepancy between theory and experiment for

$\rho^- \to \pi^- \gamma$ and $K^{*0} \to K^0 \gamma$ is a problem in simple vector dominance calculations and it is not going to be removed by q^2-dependence of f_v. As broken SU(3) models with considerable freedom are unable to fit satisfactorily these widths[78], the problem is either more fundamental than the one we are addressing, as it resides in the data.

The η (η') decays of the ρ, ω and ϕ vector mesons are analysed in the same way as above and we are able to predict the decays of the radially excited state $V' \to V\eta$, $V' \to \eta\gamma$ from an input of the $V \to \eta\gamma$ width.

The decomposition is as follows

$$g_{V\gamma\eta} = f_V(0)\left[X_+ + \frac{f_{V'}(0)}{f_V(0)}\right] g_{V'V\eta}$$

$$g_{V'\gamma\eta} = f_V(0)\left[1 + X'_+ \frac{f_{V'}(0)}{f_V(0)}\right] g_{V'V\eta} \qquad (2.40)$$

It is assumed as usual that $X_+ = 2$ and that we are not going to experience the additional suppression of low multiplicity decays found in the last section. We also take $X'_+ = 1$ and $f_V'(0)/f_V(0) \simeq 0.21$ to 0.23 to find

$$g_{V\eta\gamma} \simeq f_V(0)\,[2\ 21]\, g_{V'V\eta}$$

$$g_{V'\eta\gamma} \simeq f_V(0)\,[1\ 21]\, g_{V'V\eta} \qquad (2.41)$$

and the results are given in Table (2.3). The two values given for data from ref. (89) result from an experimental ambiguity.

Table (2.3):

Radiative $\eta(\eta')$ vertices for ρ, ω, ϕ.

Process	Experimental width keV	Ref	Prediction $\Gamma(V'\to V\eta)$ MeV	$\Gamma(V'\to\eta\gamma)$ MeV
$\rho\to\eta\gamma$	50±13 (76±15)	(89)	43±10 (55±12)	0.7±0.2 (1.05±0.2)
$\omega\to\eta\gamma$	12 (29±7)	(89)	51±40 (450±30)	07±05 (55±06)
$\phi\to\eta\gamma$	55±12	(89)	60±10	0.2±0.05
			$\Gamma(V'\to V\eta')$ MeV	$\Gamma(V'\to\eta'\gamma)$ MeV
$\eta'\to\rho\gamma$	≤300	(65)	-	≤0.76
$\eta'\to\omega\gamma$	≤50	(65)	≤18(η')	≤0.32

2.5 The Compton Sum Rule and Large Phase Space Decays

Because the q^2-dependence of f_V reduces the coupling at $q^2 = 0$, the Compton sum rule will be less well satisfied by ρ, ω, ϕ and ρ' contributions than if q^2-dependence was not considered. Evaluating it at $P_{lab} = 9.3$ GeV and taking the data from Table (3.1) (Chapter Three) gives

$$\left.\frac{d\sigma}{dt}(\gamma p \to \gamma p)\right|_{t=0} = 0.87 \pm 0.02 \ \mu b\ GeV^{-2}$$

$$\simeq \left[\sum_V \left(f_V^2(0)\left.\frac{d\sigma}{dt'}(\gamma p \to V p)\right|_{t'=0}\right)^{\frac{1}{2}}\right]^2$$

$$\simeq \big(0.506 \pm 0.02\,(\rho) + 0.057 \pm 0.005\,(\omega)$$

$$+ 0.028 \pm 0.001\,(\phi) + 0.042 \pm 0.007\,(\rho')\big)^2$$

$$= 0.40 \pm 0.04\ \mu b\ GeV^{-2} \qquad (2.42)$$

in contrast with 0.60 μbGeV^{-2} if there is no suppression. Using the methods of the previous sections we find that ω', ϕ', ψ and ψ' make a contribution to the sum rule of less than 1%.

In view of the various proposals reviewed by Silverman[52] to account for the discrepancy we do not regard its increase as a fundamental problem. It is a question of allocating the deficiency on the right hand side of the sum rule to non-resonating 2π contributions[53], higher mass and continuum contributions, or other mechanisms.

A more puzzling problem is the apparent experimental suppression of the low multiplicity pion decays of the light quark radially excited states. The coupling constant suppression factor of $X_+ = 2$ gives $\Gamma(\rho' \rightarrow \pi\omega) \simeq$ 250 MeV, $\Gamma(\rho' \rightarrow \pi\pi) \simeq 86$ MeV, $\Gamma(\phi' \rightarrow \rho\pi) \simeq 1.5$ MeV and $\Gamma(\omega' \rightarrow \rho\pi) \simeq 1.4$ GeV. The 2π branching ratio of the ρ' is consistent with one solution from phase-shift analyses[90], however, in view of the data[61] on the ω' which gives $\Gamma(\omega') = 150 \pm 30$ MeV and shows a preference for 5π rather than 3π decay the last result is absurd. This suppression of phase space favoured decays may indicate that for $\pi\gamma$ decay modes the assumption that $g_{V'\pi\alpha}/g_{V\pi\alpha} \simeq 0.5$ is too naive and that for ω' and ϕ' it should be much smaller. This would reduce the $\rho^- \rightarrow \pi^-\gamma$ and $K^{*0} \rightarrow K^0\gamma$ widths to 89 and 115 keV respectively. Because the suppression of the low multiplicity pion decays is not part of our

prescription here our predictions for such widths are expected to be much too large. Our predictions of the higher multiplicity decays $\omega' \longrightarrow \rho'\pi$, $\phi' \longrightarrow \rho'\pi$ are made assuming $g_{\omega'\rho'\pi} = \frac{1}{2} g_{\omega\rho\pi}$, $g_{\phi'\rho'\pi} = \frac{1}{2} g_{\phi\rho\pi}$ and the results are summarised in Table (2.2). In Chapters Four and Five we consider the puzzle of the low multiplicity decays within a specific quark model.

Summary

The simple vector-meson dominance model has been reviewed and an extended vector dominance model which includes both radial excitations and q^2-dependence of the photon-vector meson coupling applied to radiative decays of the vector mesons. The parameters estimated from ψ radiative decay define a phenomenological prescription in which the radial excitations play a minor role compared with the ground state vector mesons. Various predictions have been made for decay widths.

CHAPTER 3

VECTOR MESON PHOTOPRODUCTION AND TOTAL CROSS-SECTIONS ON NUCLEONS AND NUCLEI

3.1 The Space-Time Structure of Photon-Hadron Interactions

Before proceeding to apply the methods of Chapter Two to the prediction of vector-meson-nucleon total cross-sections we develop a more intuitive space-time description of the photons hadronic interactions. This description will facilitate an understanding of the nuclear shadowing phenomenon which is exploited in the experimental measurements of total cross-sections - measurements which are independent of any vector-meson-dominance assumptions and hence are important for testing our predictions.

The mean free path of photons in nuclear matter is given by

$$\left[\sigma_{tot}(\gamma N) \times (\text{density of nucleons})\right]^{-1} \sim 700\text{f} \tag{3.1}$$

and is large compared to typical nuclear dimensions. One expects, then, that every nucleon is illuminated by the full incident photon beam and will participate equally in the scattering process. Hence

$$\sigma_{tot}(\gamma A) = A(\sigma_{tot}(\gamma N)) \tag{3.2}$$

However it is always the case experimentally that $\sigma_{tot}(\gamma A) < A(\sigma_{tot}(\gamma N))$, an effect which is usually characterised by the expression

$$A_{eff} < A \tag{3.3}$$

where

$$A_{eff} = \frac{\sigma_{tot}(\gamma A)}{\sigma_{tot}(\gamma N)} \tag{3.4}$$

This phenomenon strongly bears out the underlying philosophy of verctor meson dominance where a photon incident on a large nucleus first converts itself into a linear combination of vector mesons. One certainly expects $\sigma_{tot}(\rho A)$ not to be proportional to A because of shadow effects: the mean free path of ρ's in nuclear matter

$$\left[\sigma_{tot}(\rho N) \times (\text{density of nucleons})\right]^{-1} \sim 3f \tag{3.5}$$

is comparable to nuclear sizes, so that nucleons deep inside the nucleus do not see the full incident ρ-flux. If hadronic mean free paths were negligible compared to nuclear sizes (i.e. if $\sigma_{tot}(\rho N)$ were infinite), interactions would be confined to the surface. The cross-section would then go as $A^{\frac{2}{3}}$ since the surface to volume behaves as the $\frac{2}{3}$ power. The fact that $\sigma_{tot}(\rho N) \sim 30mb$ means that shadowing is not that dramatic (typical hadronic cross-sections go like $A^{0.8}$ as A increases).

We have outlined in Chapter Two the similarities between photon and hadron interactions - these suggest

that the photon behaves like a hadron for a small fraction ($\sim\alpha$) of the time. We express this by expanding (to lowest order in e) a physical photon state $|\gamma\rangle$ of energy ν in terms of a "bare" photon state $|\gamma_B\rangle$ and eigenstates $|n\rangle$ of the Hamiltonian which includes the strong interactions but not the electromagnetic interaction H_{EM}[91]:

$$|\gamma\rangle = |\gamma_B\rangle + \sum_n |n\rangle \frac{\langle n|H_{EM}|\gamma_B\rangle}{E_n - \nu} \qquad (3.6)$$

The hadron states $|n\rangle$ which can contribute to the sum are those states that are produced in e^+e^- annihilation, in fact to lowest order in e there is an exact connection[92] which is given by perturbation theory. The states $|n\rangle$ are on-shell and massive so energy is not conserved at the γ_B–n vertex (Fig. (3.1)).

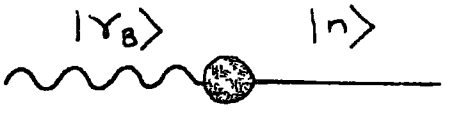

Fig. (3.1)
Photon-hadron vertex

The time during which the hadronic vacuum fluctuation lives is determined by the uncertainty principle

$$\Delta t = 1/\Delta E = 1/E_n - \nu \qquad (3.7)$$

and

$$\frac{1}{E_n - \nu} = \frac{1}{(\nu^2 + m^2)^{1/2} - \nu} = \frac{2\nu}{m^2} \quad (\nu^2 \gg m^2) \qquad (3.8)$$

We refer to Δt as the formation time of a particular hadronic component. When Δt is large (i.e. as ν increases)

we expect diffractive scattering features to emerge in nucleonic photoprocesses as the hadronic component of the photon becomes dominant - an expectation which is borne out experimentally as noted in the previous chapter.

The picture can easily be extended to electro-production processes where the photon acquires a mass squared

$$Q^2 = -q^2 = k^2 - \nu^2 \qquad (3.9)$$

The formation time (3.8) now becomes

$$\Delta t \approx \frac{2\nu}{Q^2+m^2} \qquad (3.10)$$

where the approximation is now $\nu^2 \gg Q^2+m^2$. Diffractive features are expected to show up in electroproduction for large Δt and hence[93] for large

$$\omega = \frac{2m\nu}{Q^2} \qquad (3.11)$$

which is the dimensionless Bjorken scaling variable[94]. This is indeed the case experimentally[95] (note that in this picture the parameter $\omega' = \frac{2m\nu}{Q^2+m^2}$ is a more natural candidate than ω for the scaling variable).

It is now natural to expect that the virtual photon exhibits a changing effective size as Q^2 is varied for large ω. This would be explicitly manifested as a shrinkage of the forward peak of the differential cross-section for ρ-electro-production on a nucleon target as

Q^2 decreases. The reason for this is that diffractive processes generally exhibit a forward differential cross-section of the form

$$\frac{d\sigma}{dt} = Ae^{bt} \qquad (3.12)$$

where the slope b and the interaction radius R are related by[96]

$$b = R^2/4 \qquad (3.13)$$

As Q^2 increases ω decreases reducing the photons effective "size" and b will decrease resulting in an anti-shrinkage of the forward peak.

An advantage of the picture of the photon we are painting is that the hadronic components of its structure are not restricted to vector meson poles as in simple VDM. Non-resonant components (e.g. $\pi\pi$, $D\bar{D}$, $N\bar{N}$, ...) will contribute to the interaction in the appropriate kinematical regions. Yennie[92] discusses the dipion component in detail assuming that it is ρ-meson dominated and finds that this component enhances the simple ρ-pole contribution to the photon total cross-section by 10→20% (an effect referred to in the discussion of the Compton sum rule in Chapter Two).

Further evidence for the importance of this component is to be seen in the mass distribution of pion pairs in diffractive $\pi^+\pi^-$ photoproduction. An example is shown in Fig. (3.2). The curve is the pure ρ^0 part of a best fit with an adjustable background[97]. It is

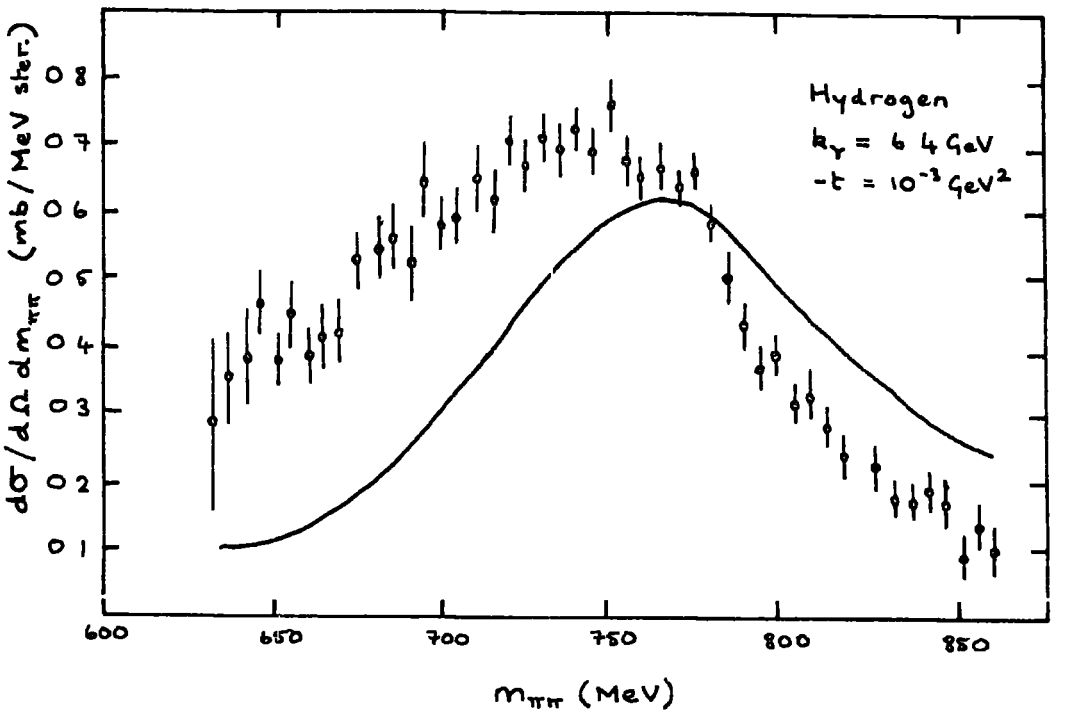

Fig. (3.2)
Mass distribution in 2pion photoproduction

obvious that the resonance peak is strongly skewed towards lower masses by an interfering background - this is qualitatively similar to the distribution we expect in the original photon structure as low mass non-resonant components should dominate due to their larger formation time. It is also worth noting that diffractive $\pi\pi$ photoproduction accounts for $\sim$15% of the photon total cross-section which agrees reasonably with the usual $\sigma_{el}/\sigma_{tot} \sim 0.2$ for hadronic processes.

Yennie proceeds to investigate the spatial structure of the non-resonant 2π contribution utilising the 2π scattering wave function. The "shrinking" of the 2π component with increasing Q^2 emerges naturally and he

regards this as suggestive of a shrinking of the whole hadronic structure. This expected behaviour is in accord with the analysis of Cheng and Wu[98] who investigated within the context of Q.E.D. the dissociation of a virtual photon into a lepton-anti-lepton pair which, after going through a Coulomb potential, recombines to form a virtual photon again. The calculation was conducted by first taking the $\omega \longrightarrow \infty$ limit and then investigating the spatial separation of the leptons as a function of Q^2. This separation was found to shrink to zero as Q^2 increases.

Nieh[91] offers a different viewpoint arguing that the calculation of Cheng and Wu is not physically relevant because of the absence of strong interactions in the model. As regards Yennies work although the non-resonant 2π tail will be drawn in as $Q^2 \uparrow$ the hadronic core will maintain its strong interaction size and the ρ-electroproduction slope parameter will be insensitive to Q^2 at large ω.

The experimental situation is shown in Fig. (3.3) where the data is taken from ref. (99). Due to notorious systematic difficulties in comparing results from different experiments it is difficult to firmly conclude shrinkage or no-shrinkage. The Cornell data is certainly consistent with no shrinkage and one may say that any substantial shrinkage will occur only at Q^2 of a few GeV^2.

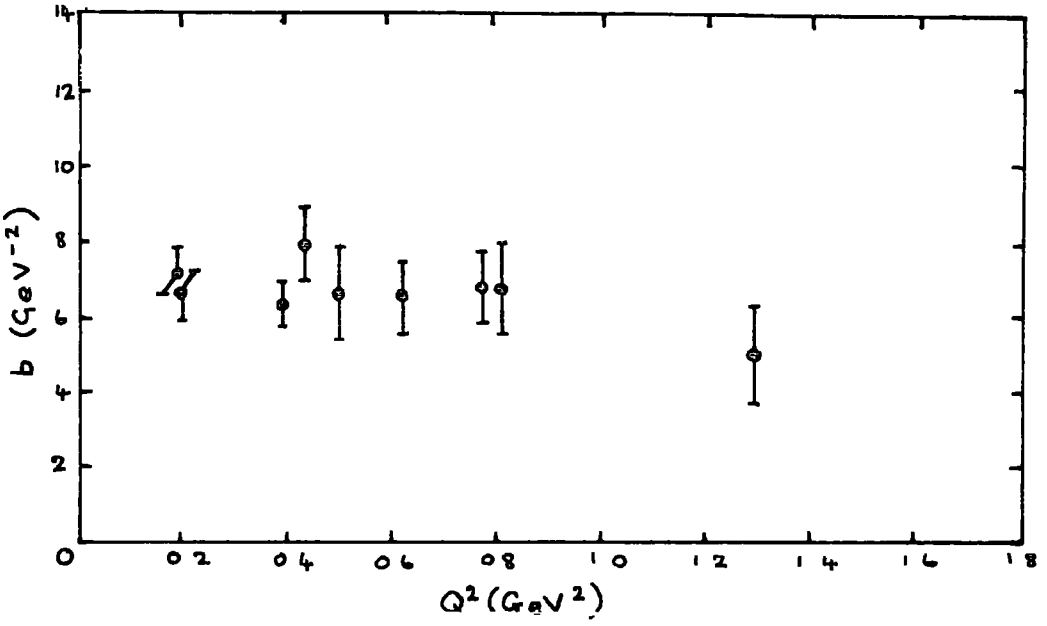

Fig. (3.3)
The slope parameter b of the electroproduction cross-section versus Q^2

We now apply the ideas developed so far to the nuclear shadowing phenomenon. In the shadow region of a single nucleon (Fig. 3.4) we expect the state to differ

Fig. (3.4)
Nuclear shadowing

from the initial state in 3 ways:

i) the original hadronic components will be strongly depleted;

ii) the bare photon component may be modified;

iii) new hadrons, different in nature from the initial components will be more or less

catastrophically present - the ultimate spreading out of these states represents diffractive photoproduction.

If we now reexpress (i) and (ii) in terms of physical states we will have a physical photon with a slightly reduced amplitude ($\sim\alpha$) together with a superposition of real hadronic states.

$$|\gamma_B\rangle = |\gamma\rangle - \sum_n |n\rangle\frac{\langle n|H_{EM}|\gamma_B\rangle}{E_n - \nu} \qquad (3.14)$$

Since it is the physical states which propagate with a definite wave number-energy relationship the superposition will ultimately spread out and become separated [100,101]. For example, a physical photon and a ρ^0 propogate with wave numbers k and $(k^2 + m_\rho^2)^{\frac{1}{2}}$ respectively, and to first order a comparison yields the coherence length (3.8). After a distance $\sim \frac{2k}{m_\rho^2}$ they will be sufficiently out of phase such that they no longer add up to the bare photon, hence if there is a second nucleon behind the first within a coherence length the bare photon state will pass straight through resulting, for a large nucleus, in $A_{eff} < A$.

An effect which is independent of any vector dominance assumptions but which is often classified as a shadowing phenomenon is the modification of a given photoproduction cross-section by absorption of the outgoing hadrons in nuclear matter [102]. The quantity

$$A_{eff} = \frac{\frac{d\sigma}{dt}(\gamma A \to VA)}{\frac{d\sigma}{dt}(\gamma N \to VN)} \qquad (3.15)$$

can be calculated using Glauber-type multi-scattering theory[102] or nuclear optical models[101, 103], the only unknown parameter being $\sigma_{tot}(\nu N)$. Measurements of A_{eff} or the ratio $\frac{A'_{eff}}{A^2_{eff}}$ for different nuclei can then be used to fix $\sigma_{tot}(\nu N)$, a method we discuss further in section (3.3).

Vector dominance is instrumental in the optical model calculations[101,103] of

$$A_{eff} = \frac{\sigma_{tot}(\gamma A)}{\sigma_{tot}(\gamma N)} \qquad (3.16)$$

the prediction being slightly too drastic in that[104] at ~ 16 GeV

$$A_{eff}^{VMD} \sim A^{0.89} \qquad (3.17)$$

with $\sigma_{tot}(\rho N) \simeq 26$mb and $Re/Im \sim 0.2$ for the $\gamma \to \rho$ amplitude. The experimental A_{eff} does not fall off this quickly, the reason for the overprediction being that the single hadron channel (the rho) accounts for only about 78% of $\sigma_{\gamma N}$ in the naive model. The modified formula

$$A_{eff} \sim 0.22A + 0.78A^{0.89} \qquad (3.18)$$

fits the data well.

The above discussion of the photons structure and the shadowing phenomena form an arena in which we can present the total cross-section predictions of the model developed in Chapter Two and critically analyse their determination from nuclear scattering experiments.

3.2 Extended V.M.D. Model Predictions of $\sigma_{tot}(VN)$

The total cross-section for transversely polarised vector mesons is related in the vector dominance model to $\frac{d\sigma}{dt}(\gamma N \rightarrow VN)$ as follows

$$\left.\frac{d\sigma}{dt}(\gamma N \rightarrow VN)\right|_{t=0} = \left(\frac{k_{VN}}{k_{\gamma N}}\right)^2 \frac{\sigma_{tot}^2(VN)}{16\pi} f_V^2 (1+\rho^2) \qquad (3.19)$$

where

$$k_{VN}^2 = (s - (m_V + m_N)^2)(s - (m_V - m_N)^2)/4s \qquad (3.20)$$

and the kinematic factor comes from applying the vector dominance model to the invariant amplitudes. The factor ρ is the ratio of the real to imaginary parts of the forward amplitude.

The assumptions contained in (3.19) are that s-channel helicity is conserved, that the process $\gamma N \rightarrow VN$ is diffractive and consequently that the amplitude is predominantly imaginary. Also it is assumed that contributions to (3.19) arising from expressing the photon in terms of vector mesons, other than the final state, V, are small.

The last assumption exposes the q^2 dependence of f_V as it eliminates compensating contributions from radial excitations of V, or other contributions of the same isospin. The consequences of this are illustrated by Table (3.1) where values of $\sigma_{tot}(VN)$ are presented which are calculated with and without a q^2 dependent f_V and assuming $\rho = 0$. It is clear that with q^2 dependence the $\sigma_{tot}(VN)$ are larger than when calculated with no q^2

TABLE (3.1)

Vector meson total cross section predictions

V	$\frac{d\sigma}{dt}(\gamma p \to Vp)\Big\|_{t=0}$ $\mu b/GeV^2$	S GeV^2	Ref	$\sigma_{tot}(VN)$ with q^2 dependence mb	$\sigma_{tot}(VN)$ with q^2 dependence mb	$\sigma_{tot}(VN)$ with q^2 dependence and VMD	$\sigma_{tot}(VN)$ experimental nuclear scattering	Ref	$\sigma_{tot}(VN)$ quark model prediction mb
ρ	100±10	18.3	(52)	27.1±1.4	31.6±1.7	28.5±1.5	28.6±1.4	(52)	27
ω	11.24±2	18.3	(52)	24.4±2	28.6±2.4	25.8±2.2	27.1±3.4	(52)	23
φ	2.49±0.15	18.3	(52)	10.3±0.4	13.5±0.5	12.2±0.4	12±3	(52)	13
J/ψ	$(17.4)\times10^{-2}$	35.7	(109)	1.04±0.12	12.6±1.5	11.2±1.4	3.5±0.8	(107)	-
ρ'	15±5	18.3	(52)	31±6	59.9±12	10.8±2	-	-	-
ω'	3.4±0.6	18.3	(a)	36±3	83±7	15.5±1.3	-	-	-
φ'	0.76±0.05	18.3	(a)	12.6±0.4	44±1	8.2±0.2	-	-	-
ψ'	~2.5$\times10^{-2}$	35.7	(109)	~0.8	~27.3	~4.9	-	-	-

Footnote

(a) Predicted value

dependence, and it is useful to know how large $\sigma_{tot}(VN)$ can be. Barger and Phillips[46] calculated that $\sigma_{tot}(VN) \leqslant 4\pi b GeV^{-2}$ where b is the logarithmic slope of the forward elastic differential cross-section. However their result is out by a factor of two[105]: Taking an exponential approximation for the forward peak

$$\frac{d\sigma}{dt}(VN \rightarrow VN) = \frac{\sigma_{tot}^2(VN)}{16\pi} e^{bt} \qquad (3.21)$$

we obtain

$$|A(s,t)| = s\sigma_{tot} e^{bt/2} \qquad (3.22)$$

Considering now the partial waves[106] (we are assuming diffraction, i.e. essentially imaginary and spin independent amplitudes)

$$A_l(s) = \frac{1}{32\pi}\int_{-1}^{1} dx \; P_l(x) \; A(s,t) \quad , \; x = \cos\theta \qquad (3.23)$$

we get, on substitution of (3.22)

$$A_l(s) \; \frac{is\sigma_{tot}}{32\pi}\int_{-1}^{1} dx \; P_l(x) \; e^{bt/2} \qquad (3.24)$$

where in the diffractive region

$$x = \frac{2t}{s} + 1 \qquad (3.25)$$

Unitarity now tells us that each partial wave is bounded by 1:

$$A_l(s) = \frac{e^{2i\delta_l(s)} - 1}{2i} \leqslant 1 \qquad (3.26)$$

and this implies bounds on $\frac{d\sigma}{dt}$ and σ_{tot}. The $l = 0$ partial wave reaches its limit first and sets the bound.

$$A_o(s) = \frac{i\sigma_{tot}}{16\pi}\int_{-s}^{o} dt \; e^{bt/2} \qquad (3.27$$

$$= \frac{i\sigma_{tot}}{8\pi b} \leqslant i \qquad (3.28)$$

and hence we have the corrected result

$$\sigma_{tot}(VN) \leqslant 8\pi b \qquad (3.29)$$

All of our predictions for the ground state mesons, including the Ψ, where $\sigma_{tot}(\Psi N) \leqslant 29.4$ mb, are within the unitary bound, however the Ψ prediction disagrees considerably with the data[107]. One cause of the discrepancy is the effect of the Ψ' on the calculation. Treating the problem generally, we find

$$A(\gamma N \to VN) = \left(\frac{k_{VN}}{k_{\gamma N}}\right) f_V(0)\; A(VN \to VN) + \left(\frac{k_{V'N}}{k_{\gamma N}}\right) f_{V'}(0)\; A(V'N \to VN) \qquad (3.30)$$

If we make the same assumptions as went into (3.19), with the exception that $A(V'N \to VN)$ is not zero, and assume in addition that the diffractive amplitudes are dominated by factorizable pomeron (P) exchange, we get

$$A(\gamma N \to VN) = f_V(0)A(VN \to VN)\left\{1 + \frac{k_{V'N}}{k_{VN}}\;\frac{f_{V'}(0)}{f_V(0)}\;\frac{1}{X_+}\right\} \qquad (3.31)$$

where $X_+ = g_{VVp}/g_{V'Vp}$. If we take $X_+ = 2$, as it was in Chapter Two, then the effect on the $\sigma_{tot}(VN)$ predictions in Table (3.1) calculated with q^2 dependence is to reduce them by factors of

$$\left\{1 + \frac{k_{V'N}}{k_{VN}} \frac{f_{V'}(0)}{f_V(0)} \frac{1}{X_+}\right\} \simeq 1.1 \quad (\rho,\omega,\phi)$$

$$\simeq 1.2 \quad (\psi) \qquad (3.32)$$

and these effects will not decrease with energy.

The proposal that the radial excitations affect the calculation of $\sigma_{tot}(VN)$ can be tested for consistency by predicting $\frac{d\sigma}{dt}(\gamma N \to V'N)$ at $t = 0$ and also $\sigma_{tot}(V'N)$. The result is

$$\left.\frac{d\sigma(\gamma N \to V'N)}{dt}\right|_{t=0} = \frac{d\sigma(\gamma N \to VN)}{dt} \frac{\left\{\frac{f_{V'}(0)}{f_V(0)} X'_+ + 1\right\}^2}{\left\{\frac{f_{V'}(0)}{f_V(0)} + X_+\right\}^2} \qquad (3.33)$$

where $X'_+ = g_{V'Vp}/g_{V'Vp}$. If, as in Chapter Two, $X'_+ = 1$, the suppression factor in (3.33) is 0.3 and at $t = 0$ we estimate

$$\frac{d\sigma}{dt}(\gamma N \to \rho' N) = 30 \pm 3\ \mu b/GeV^2$$

$$\frac{d\sigma}{dt}(\gamma N \to \psi' N) = 5.1 \pm 1.3\ nb/GeV^2 \qquad (3.34)$$

Given the errors on the measurements of these values we regard the results as encouraging. As they are weakly dependent on X'_+ they may be suggesting that X_+ is closer to 3 and this would give a reasonable ratio for

$\sigma(NN^*(1400)/\sigma(NN) \simeq 1/9$, if in fact $N^*(1400)$ is a radial excitation of the nucleon, and the suppression is the same for nucleons as for mesons. On the other hand studies of the decay $\psi' \longrightarrow \psi\pi\pi$ suggest[108] that $g_{\psi'\psi'\rho} \simeq g_{\psi\psi\rho}$, so we keep $X_+ = 2$.

The estimate of $\sigma(V'N)$ follows from

$$A(\gamma N \to V'N) = f_{V'}(0)A(V'N \to V'N)\left\{1 + \frac{f_V(0)}{f_{V'}(0)}\frac{1}{X'_+}\right\} \qquad (3.35)$$

is independent of X'_+, which, in the absence of any measurements of $\sigma_{tot}(\rho' N)$ or $\sigma_{tot}(\psi' N)$ is not well determined. We take $X'_+ = 1$ and predict the values of $\sigma_{tot}(V'N)$ given in Table (3.1), which are a considerable improvement on those calculated assuming only q^2 dependence, in that $\sigma(\rho' N)$ is now more safely below the unitary bound of 68 mb calculated from an assumed b of 7 GeV^{-2}. The improved estimate for $\sigma_{tot}(V'N)$ supports adding rather than subtracting the effect of the radial excitation and ground state meson, with or without q^2 dependence of f_V, if the same final results are to be achieved.

In summary, the $\sigma_{tot}(VN)$ predictions in the vector dominance model which includes both q^2 dependence of f_V and radial excitations of the vector mesons are in reasonable accord with the data for ρ, ω and ϕ. $\sigma_{tot}(\psi N)$ is predicted to be larger than the data at $s \simeq 36$ GeV^2 - we now go on to consider this data.

3.3 Analysis of Experimental Data on $\sigma_{tot}(\Psi N)$

The left hand side of (3.19) is given by measurements of $\frac{d\sigma}{dt}(\gamma N \rightarrow VN)$. The logarithmic slope, b, of the differential cross-section has to be well determined so that the extrapolation to t = 0 of $\frac{d\sigma}{dt}$ can be performed, and for ρ, ω and ϕ this presents little problem as there are many measurements and the extrapolation from $t' = t - t_{max} = 0$ to t = 0 is short. For the Ψ, the measurements are few, and for comparison with a $\sigma_{tot}(\Psi N)$ measurement made with a bremsstrahlung beam of E_0 = 20 GeV there is only one determination of b, in the right energy range[109]. It is a measurement on deuterium with a bremsstrahlung end point energy of E_0 = 20 GeV and a photon energy of k = 19 GeV which gives b = 2.9 GeV^{-2} from three data points, albeit with small error bars. As $t_{max} = -0.088$ GeV^{-2} for this b value, the extrapolation raises the differential cross-section of 15.0 ± 1.0 nb/GeV^2 at t' = 0 to 19.4 ± 1.3 nb/GeV^2 at t = 0[110]. The error on the measurement is statistical and the authors[109] report a 15% systematic error as well as a possible 20-30% inelastic contribution. In view of the error range, and the fact that three measurements[109] at k = 19 GeV give differential cross-sections at t = 0 ranging from 13.9 to 19.4 nb/GeV^2[110] we take 17 ± 4 nb/GeV^2 as the input to (3.19).

This yields the prediction, with q^2 dependence and the Ψ' correction, of 10.5 ± 1.5 mb which should be compared with the experimental determination[107] of 3.5 ± 0.8 mb.

The experiment is performed with a 20 GeV bremsstrahlung beam scattering off beryllium (A = 9) and tantalum (A = 181) nuclei. The scattering is incoherent as the A dependence data is taken with a spectrometer setting corresponding to a transverse momentum $P_\perp$ = 1.65 GeV. We can estimate the formation time of the hadronic component to be

$$\Delta t \approx \frac{2k}{m_V^2} \approx 4\ \text{GeV}^{-1} \qquad (3.36)$$

for a photon energy of 19 GeV. This is to be compared with the mean free path of Ψ's in nuclear matter

$$l_V = \left[\sigma_{tot}(\Psi N) \times (\text{dendity of nucleons})\right]^{-1}$$

$$\simeq 400 \rightarrow 40\ \text{GeV}^{-1} \text{ for } \sigma_{tot}(\Psi N) = 1 \rightarrow 10\ \text{mb} \qquad (3.37)$$

We see that even if $\sigma_{tot}(\Psi N)$ is 10 mb the formation time is small compared to the nuclear mean free path and a simple nuclear optics model[101] yields

$$A_{eff} = \frac{1}{\sigma_{tot}(\Psi N)} \int_0^\infty d^2b \left(1 - e^{-\sigma_{tot}(\Psi N) T(b)}\right) \qquad (3.38)$$

where

$$T(b) = \int_{-\infty}^{\infty} dz\ \rho(b,z) \qquad (3.39)$$

$\rho(b,z)$ is the nuclear density, the photon is incident along the z-axis and b is the impact parameter. In the notation of the nuclear optics models this expression for A_{eff} is valid if the process is incoherent and if

$$\xi_V = \frac{m_V^2 l_V}{k} >> 1 \qquad (3.40)$$

For the case we consider ξ_ν takes the value $200 \rightarrow 20$ for $\sigma_{tot}(\Psi N) = 1 \rightarrow 10$ mb.

Anderson et al[107] use a hard sphere model[111] for the nuclear density

$$T(b) = \frac{3A}{2\pi R^3}(R^2 - b^2)^{1/2}, \quad b < R$$
$$= 0, \quad b > R \qquad (3.41)$$

where the nuclear radius $R = r_0 A^{\frac{1}{3}}$ and the r_0's for Be and Ta are determined from the measurements of effective nuclear radii as determined from rho photoproduction data[112]. The substitution of (3.41) in (3.38) yields

$$A_{eff} = \frac{2\pi}{\sigma_{tot} k^2}\left\{\frac{k^2R^2}{2} - \gamma(2, kR)\right\} \qquad (3.42)$$

where

$$kR = \frac{3A^{1/3}\sigma_{tot}}{2\pi r_0^2} \qquad (3.43)$$

and

$$\gamma(a,x) = \Gamma(a) - \Gamma(a,x) \qquad (3.44)$$

is the incplete gamma function. This function can be reexpressed to yield

$$A_{eff} = \frac{2\pi}{\sigma_{tot} k^2}\left\{\frac{k^2R^2}{2} - 1 + e^{-kR}(1 + kR)\right\} \qquad (3.45)$$

Then <u>if σ_{tot} is small</u> the extreme right hand term can be expanded and the whole expression approximated by the first two terms yielding

$$A_{eff} = A\left(1 - \tfrac{3}{8}kR\right) \qquad (3.46)$$

$$= A\left(1 - \frac{9A^{1/3}\sigma_{tot}}{16\pi r_0^2}\right) \qquad (3.47)$$

and this is the expression used in ref. (107).

If $\sigma_{tot}(\psi N) \sim 0.8$ mb as predicted by naive vector dominance then the approximations made above are reasonable, however if $\sigma_{tot}(\psi N) \sim 10$ mb as predicted in the previous section then even for beryllium, $kR \simeq 1$ and the analysis must be modified.

Maintaining the exact expression for A_{eff} (3.45) we solved numerically for $\sigma_{tot}(\psi N)$ (the experimentally measured quantity is in fact

$$\mu = A_{eff}^{Be} / A_{eff}^{Ta} \qquad (3.48)$$

and the equation to be solved becomes more cumbersome) with the result

$$\sigma_{tot}(\psi N) = 4.4 \pm 1.2 \text{ mb} \qquad (3.49)$$

One more refinement was included in the analysis as the hard sphere model is a reliable model only for heavier ($A \gtrsim 27$) nuclei. The harmonic oscillator model

$$T(b) = \rho_o A \int_{-\infty}^{\infty} \left(1 + \frac{6}{(A-4)a_o^2}(b^2+z^2)\right) e^{-(b^2+z^2)/a_o^2} dz \qquad (3.50)$$

(where ρ_o is the normalisation constant determined by $A_{eff} = A$ as $\sigma \to 0$) is known to be more appropriate for light nuclei and its inclusion in the analysis yields the final result

$$\sigma_{tot}(\psi N) = 4.6 \pm 1.8 \text{ mb} \qquad (3.51)$$

Although this value is larger than the published cross-section (and is now considerably larger than the naive vector dominance estimate) there is still a factor of ~ 2

discrepancy between prediction and experiment.

The cross-section $\sigma_{tot}(\psi N)$ deduced from $\frac{d\sigma}{dt}(\gamma N \rightarrow \psi N)$ at $t = 0$ is very energy dependent in the photon energy range up to 20 GeV and this would appear to suggest the opening of an inelastic channel at $S = 23.5 \pm 2.0$ GeV^2 consistent with charmed particle production. Thorndike[113] using dispersion relation arguments, has observed that the real part of the elastic ψN scattering amplitude cannot be zero given the energy dependence of $\sigma_{tot}(\psi N)$. The effect of a non-zero ratio of real to imaginary parts of the elastic scattering amplitude is to reduce the predicted value of $\sigma_{tot}(\psi N)$ by a factor $(1+\rho^2)^{\frac{1}{2}}$. As ρ decreases in magnitude as energy increases in other diffractive processes, the measurement of $\sigma_{tot}(\psi N)$ at energies above 55 GeV, along with more accurate data for $\frac{d\sigma}{dt}(\gamma N \rightarrow \psi N)$ in that energy range would help to remove ρ as a cause of discrepancy between prediction and measurement. A point in favour of our prediction which will persist at higher energies is that $\sigma_{el}/\sigma_{tot} \simeq 0.2$ in accord with other diffractive processes.

3.4 Summary of the q^2-Dependence Prescription

We have demonstrated that radiative decays and photoporduction of the ρ, ω, ϕ and ψ mesons can all be treated in the same way in vector dominance model calculations with good results. To achieve this it is necessary to include the effect of the radially excited

states ρ', ω', ϕ' and ψ' and also the q^2 dependence of the photon-vector meson coupling f_V.

We write the vector dominance series as

$$|\gamma, q^2 = 0\rangle = \sum_V f_V(0) |V\rangle \qquad (3.52)$$

where the summation includes all possible ground state vector mesons and their radial excitations (the contributions of $^3D_1$ states are negligible). The q^2 dependence is parameterised simply as $f_V(q^2) = \exp(cq^2) f_V(0)$ with the same c for all vector mesons. (3.52) is used to fit the available data on ψ, ψ' decay to $\gamma\eta$ with the photon decomposed only into ψ and ψ'. This leads to several possible solutions and to select one we use the quark model criterion that the magnitude of vertex couplings involving no radially excited states should be larger than that for couplings involving one or two such states. The acceptable solution is given by $c = 0.26\ \text{GeV}^{-2}$, $g_{\psi'\omega'\eta} = g_{\psi'\omega\eta} = \frac{1}{2} g_{\psi\omega\eta}$, and that effectively defines a calculational prescription for vector dominance calculations as we require that $g_{V'a'b} = g_{V'ab} = \frac{1}{2} g_{Vab}$ and $c = 0.26\ \text{GeV}^{-2}$ throughout.

All of the terms in the series (3.52) add in the chosen solution, and a distinct advantage of this and the q^2-dependence is that the series converges rapidly as $f_{V'}(0)/f_V(0) \approx 0.2$, and consequently higher order radial excitations make negligible contribution. This is to be contrasted with the commonly used solution in which there is no q^2-dependence, and the terms in the

series alternate in sign with each increase in radial excitation, and the series appears to converge slowly.

Having integrated V and V' into a single prescription we are able to relate the radiative decays of V' and V to the appropriate hadronic vertices. We achieve reasonable success with the various ψ, ψ' decays, and with $\omega \longrightarrow \pi\gamma$, in that the predicted width for $\rho' \longrightarrow \pi\omega$ is about what is expected and the prescription predicts a larger $g_{\omega\pi\rho}$ than that of simple vector dominance.

Consequently a larger width for $\omega \longrightarrow 3\pi$ decay is predicted which is an improvement over the simple model. If a factorisable pomeron is assumed to dominate vector meson photoproduction, cross sections for V and V' are related, and predictions for $\sigma_{tot}(VN)$ are in good agreement with the data for ρ, ω and ϕ.

The prescription also experiences difficulties. The recent measurement of the $\phi \longrightarrow \pi\gamma$ decay [84] cannot be reconciled with the hadronic width[80] for $\phi \longrightarrow \pi\rho$. To achieve the necessary suppression, with $C = 0.26\ GeV^{-2}$ or with $C = 0$ requires $g_{\phi'\pi\rho} / g_{\phi\pi\rho} < -1$ in contradiction with the quark model, and to account for it through increasing the q^2-dependence leads to a very large $g_{\omega\pi\rho}$ coupling and also to a $\rho'\rho$ pomeron coupling much larger than for $\rho\rho$ pomeron. The conflicting measurements for the $\rho^- \longrightarrow \pi^-\gamma$ width [86,87] are not fitted either, although we incline more to the Primakoff effect measurement[86].

Because $f_V(0)/f_V(m_V^2) < 1$ in this scheme the Compton sum rule is less well satisfied than in a scheme with no q^2-dependence. But with the inclusion of the ρ'. This is not regarded as a failure of the prescription as the same mechanisms can be invoked to fill the gap in both cases.

The most striking prediction of the prescription is that $\sigma_{tot}(\Psi N)$ at $S \simeq 36$ GeV^2 is larger than the experimental measurement[107]. As this may just be reflecting the presence of a relatively large real part in the elastic scattering amplitude, the difference could be resolved by repeating the measurement at higher energies where the effect of the real part is expected to decrease.

An interesting effect arises in the discussion of the hadronic decays of the 'old meson' radial excitations, especially the decay $\omega'(1780) \longrightarrow \rho\pi$. The prediction is an order of magnitude larger than the measured total width - furthermore the state prefers experimentally a 5π decay relative to the 3π mode. While there are general arguments[114] for expecting a suppression of low multiplicity pion decays we have not added the suppression as we wish to concentrate solely on q^2-dependence and the role of the V'. In the following chapters we investigate the suppression phenomenon and the status of radial excitation spectroscopy in the light of more recent experimental developments in these areas.

Summary

We have described an intuitive approach to the photons hadronic interactions based on the space-time development of its hadronic components. This promotes an understanding of the nuclear shadowing phenomenon which is experimentally employed to determine vector meson-nucleon total cross-sections. The predictions of the extended vector dominance model for these quantities were presented and compared with experiment.

CHAPTER 4

SPECTRA OF RADIAL EXCITATIONS

4.1 Experimental Situation

We have seen in Chapter Two that the case for structure in the process

$$e^+e^- \longrightarrow \pi^+\pi^-\pi^+\pi^-$$

at about 1570 MeV is reasonably strong[115] and the case for it being resonant structure is supported by the observation[116] of a small signal in the 2 invariant mass distribution in the process

$$\gamma\, Be \longrightarrow \pi^+\pi^-\, Be$$

We also saw that evidence was forming for an ω-like excitation with a mass of 1780 MeV and possible a ϕ-excitation at approximately 1820 MeV.

More recent observations of structure in this low energy region have intensified interest in light-quark spectroscopy and so we now review the experimental situation in more detail.

We regard the ρ-like state at 1570 MeV as well-established although its width is not accurately determined. A similar state which would not fit so naively into a harmonic oscillator spectrum has been controversial for some years now. First indications[117] of

a ρ-like state with a mass of 1250 MeV and total width $\sim$150 MeV came from analyses of angular distributions in the reaction

$$p\bar{p} \longrightarrow \omega \pi^+\pi^-$$

where both $J^P = 1^-$ and 1^+ structures were required (the 1^+ structure being the B-resonance). An enhancement at 1.24 GeV was also observed[118] in

$$\gamma p \longrightarrow p \pi^+\pi^- \text{ (+ neutrals)}$$

although neither the B- meson nor a Deck-type background could be ruled out as alternative explanations.

Analyses of pion form-factor data in the time-like region indicate an enhancement over the Gournais-Sakurai fit[119] at about 1250 MeV and fits to this region which include a ρ' state at 1250 MeV suggest a possible 7% branching ratio for $\rho'(1250) \longrightarrow 2\pi$. Alternative explanations for this enhancement have been offered[120,121] and this type of evidence can be regarded as indirect. A signal has also been seen[122] in

$$e^+e^- \longrightarrow \pi^+\pi^-\pi^0\pi^0$$

however a more recent combined analysis[123] of data on $e^+e^- \longrightarrow \pi^+\pi^-$, $e^+e^- \longrightarrow 4\pi$ and $\pi\pi$ phase shift favours a model with ρ-like states at 1250 and 1600 MeV, both coupled weakly to $\pi\pi$. This picture is also supported by the direct observation[124] of the $\rho'(1250)$ as a 5 standard-deviation effect in the Compton process (Fig. (4.1))

$$\gamma p \longrightarrow p e^+e^-$$

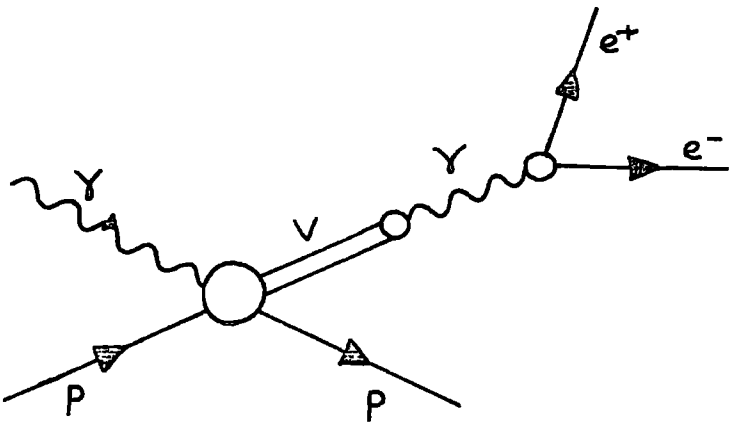

Fig. (4.1)
The Compton Scattering Process $\gamma p \rightarrow p e^+ e^-$

Because of dominant Bethe-Heitler amplitudes interference plots are studied rather than invariant mass distributions and the Compton amplitudes are parameterised with vector meson poles. Further rich structure is seen up to 1800 MeV although individual resonances cannot be reliably isolated.

The observation of ρ-recurrencies and the establishment of the charmonium radial spectrum made the case for ω and ϕ excitations compelling. The search began to prove fruitful in early 1977 when an Orsay group observed[61] structure at 1780 MeV in e^+e^- collisions (Fig. 4.2)). They were registering final states of 3

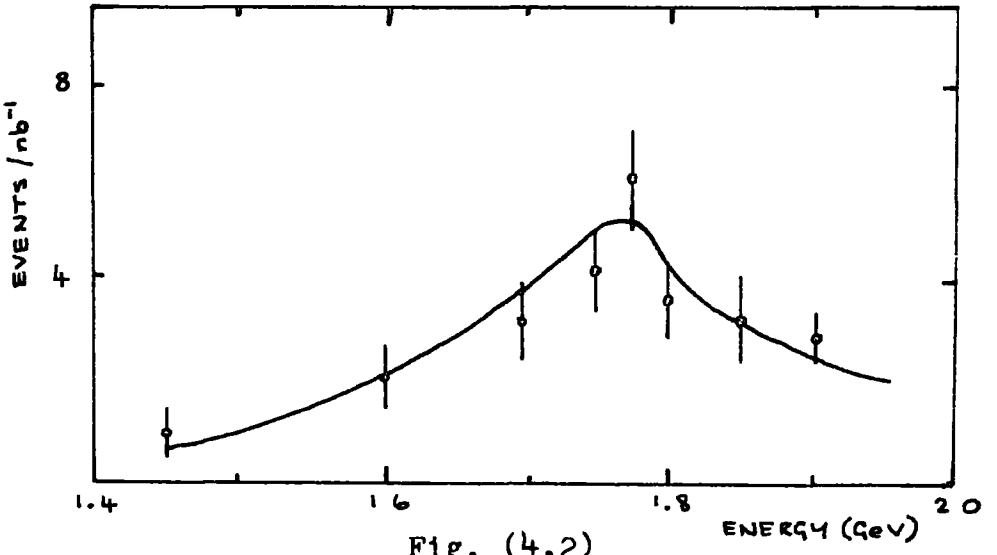

Fig. (4.2)
Orsay evidence (61) for the $\omega'(1780)$

or 4 charged particles and 1 or 2 photons and were able to establish that most (>85%) of the tracks were pions. The resonance decays mainly to 5π's with a total width of 150 ± 70 MeV which is narrower than might have been expected for an ω-excitation - an identification made because of the dominant decay to an odd number of pions.

Better statistics in the same energy region at Adone permitted three groups[62-64] to analyse and publish more comprehensive data. All three groups saw a second and narrower resonance at about 1820 MeV. The one group that saw the $\omega(1780)$ in association with this new state produced the data of Fig. (4.3). Final states

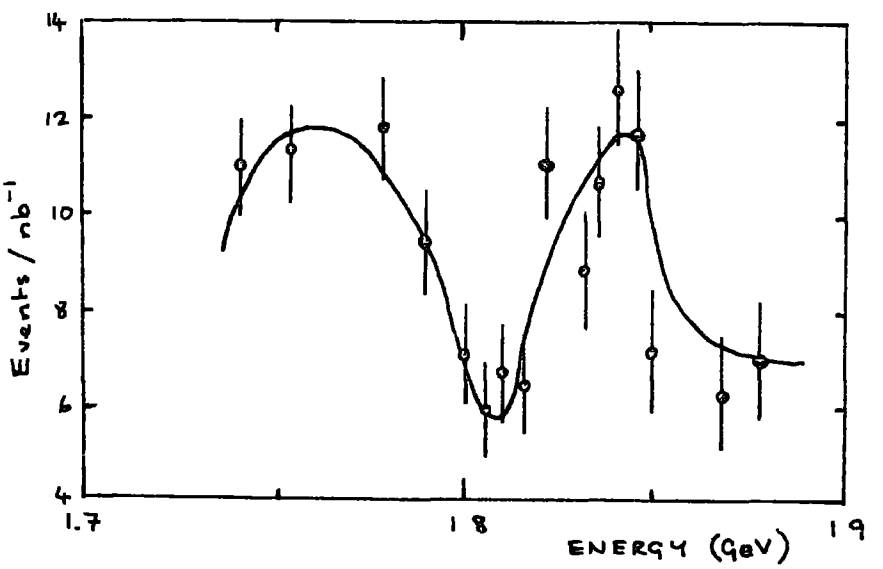

Fig. (4.3)
Adone data in the $\phi(1820)$,$\omega(1780)$ region

of at least 3 charged tracks were being observed and resonance parameters depend on whether an interference term is included in the fit. Average values for the new state are

$$M = 1820 \text{ MeV}, \quad \Gamma = 35 \pm 20 \text{ MeV}$$

The relatively extreme narrowness prompts the identification of this state as an excitation of the Ø-meson - an identification which is supported by indications of similar states at 2.1 GeV[125] and possibly 1.5 GeV[126].

In conclusion we summarise briefly in Table (4.1) the experimental evidence for light quark (u,d,s) radially excited states.

Table (4.1)

STATE	EXPERIMENT	REF.	STATE	EXPERIMENT	REF.
$\rho(1250)$ **	$pp \to \omega\pi^+\pi^-$ angular distributions. Poss. seen in $\gamma p \to p\pi^+\pi^-$ $\gamma p \to pe^+e^-$ $e^+e^- \to \pi^+\pi^-\pi^0\pi^0$	(117) (118) (124) (122)	$\phi(1500)$ *	Seen in e^+e^- but extreme narrowness suggests alternative explanations	(126)
$\rho(1570)$ ****	$ee \to 2\pi^+ 2\pi^-$ $\gamma Be \to \pi^+\pi^- Be$ Phase-shift analyses of $\pi^+\pi^- \to \pi^+\pi^-$	(115) (116) (131)	$\phi(1820)$ ***	$e^+e^- \to \geq 3cn$	(62-64)
$\omega(1780)$ ***	$e^+e^- \to$ 3cn + 1,2γs 4cn + 1,2γs $e^+e^- \to \geq 3cn$	(61) (62-64)	$\phi(2130)$ ***	Resonant K* prod^n observed at 2.13 GeV.	(125)

(*)- personal rating.

Table (4.2)

Expressions for α and β in equation (4.20)

	$V_V = ar + b$	$V_S = ar + b$	$V_S = ar$ $V_V = b$
α	$\frac{(E-b)^2}{4} - m_q^2$	$\frac{E^2}{4} - (m_q+b)^2$	$\frac{(E-b)^2}{4} - m_q^2$
β	$(E-b)a/2$	$2a(m_q+b)$	$2am_q$

4.2 Problems with Observed States

Whether the present experimental evidence for the Veneziano-type odd daughters (e.g. $\rho'(1250)$) should be considered compelling or not it has been a general trend to associate the $\omega(1780)$ with the $\rho(1570)$; i.e. they are generally regarded as equally excited radial partners, the $\phi(1820)$ being the second isoscalar partner of the $\rho(1570)$. This type of identification scheme poses many problems as have been discussed in the literature[114,127].

In the non-relativistic quark model (together with a zero width approximation) SU(3) breaking within the 1^- (ρ, ω, ϕ, K^*) nonet is postulated to be due to a strange-nonstrange quark mass difference Δ_{su} i.e.

$$\Delta_{su} = m_s - m_{ud} \simeq m_{K^*} - m_\rho \simeq m_\phi - m_{K^*} \simeq 0.125\,\text{GeV} \quad (4.1)$$

(This simple model also works surprisingly well for heavier quarks:

$$\Delta_{cu} = m_c - m_{ud} \simeq m_{D^*} - m_\rho \simeq m_\psi - m_{D^0} \simeq 1.16\,\text{GeV} \quad (4.2)$$

$$\Delta_{cs} = m_c - m_s \simeq m_{F^0} - m_\phi \simeq m_\psi - m_{F^*} \simeq 1.04\,\text{GeV} \quad (4.3)$$

Analagous simple predictions for b-quark states follow immediately from a knowledge of the upsilon mass

$$m_\Upsilon - m_\rho \Rightarrow \Delta_{bu} = 4.26\,\text{GeV} \Rightarrow m(b\bar{u}, J^P = 1^-) = 5.03\,\text{GeV}$$

$$m_\Upsilon - m_\phi \Rightarrow \Delta_{bs} = 4.19\,\text{GeV} \Rightarrow m(b\bar{s}, J^P = 1^-) = 5.21\,\text{GeV}$$

$$m_\Upsilon - m_\psi \Rightarrow \Delta_{bc} = 3.15\,\text{GeV} \Rightarrow m(b\bar{c}, J^P = 1^-) = 6.25\,\text{GeV}) \quad (4.4,5,6)$$

A naive repetition of the ground state nonet would predict

$$m_{\omega'} = m_{\rho'} \simeq 1.57 \text{ GeV} \qquad (4.7)$$

$$m_{K^{*\prime}} = m_{\rho'} + \Delta_{su} = 1.7 \text{ GeV} \qquad (4.8)$$

$$m_{\phi'} = m_{K^{*\prime}} + \Delta_{su} = 1.82 \text{ GeV} \qquad (4.9)$$

The inclusion of the $\omega'(1780)$ in this nonet can be achieved only at the expense of the ideal symmetry which works so well for the ground state mesons. The mass matrix is diagonalised without the ideal condition $m_1 = m_8$ and the physical ϕ' mass is predicted on substitution of the octet mass $m_8 = m_{\rho'} = 1.57$ and the physical ω mass $m_\omega = 1.78$. This solution requires

$$m_{\phi'} \gtrsim 2.2 \text{ GeV}$$

and the symmetry is far from ideal. An abundance of strange quarks in both the ϕ' and the ω' then makes the dominant pionic decay of the ω' difficult to understand. There is also of course the problem of the origin of the departure from the ideal nonet symmetry.

Layssac and Renard[114] went on to consider the effect of finite widths and coupled decay channels $(V \longrightarrow f \longrightarrow V')$ on the mass matrix. Using SU(3) relations between the V-f couplings they showed that the ideal symmetry could be recovered if the ϕ' mass is slightly heavier than 2 GeV. If the $\phi'(1.82)$ is the $s\bar{s}$ state relevant to this nonet then we again have confusion.

The discovery of the $\omega(1780)$ also highlighted another apparent puzzle associated with radial excitations and that is the experimentally observed suppression

of their large-phase-space decays. This state was observed to decay mainly to 5π's[61] (no 3π branching ratio has yet been published however it is known to be suppressed) - also the 2π decay mode of the $\rho(1.57)$ was conspicuous by its absence for some years. A small signal was eventually seen in photo-production experiments[116] - up until this time non-resonant explanations of the 1.57 bump had been afforded.

More recent and extensive work by phase-shifters[128,129] looking at $\pi\pi$ elastic scattering, has led to the same conclusions. Extracting their information from data on the process $\pi^- p \longrightarrow \pi^+\pi^- n$ (Fig. (4.4)).they conclude that two solutions (α,β) are

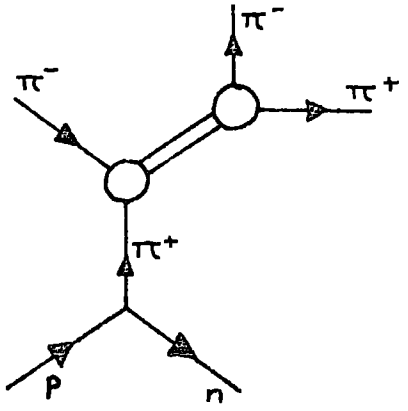

Fig. (4.4)
$\pi\pi$ scattering from $\pi p \rightarrow \pi\pi n$

compatible with analyticity and unitarity of the scattering amplitudes. Solution α has a structureless P-wave showing no evidence for a ρ' coupling to $\pi\pi$ either 1.25 or 1.57 GeV at the 2% level. Solution β on the other hand, has a P-wave clearly resonating at 1.57 GeV showing a 15 $\longrightarrow$ 30% elasticity. This solution

may be preferred[128] although both solutions tell us that the phase-space-favoured 2π decay mode of the $\rho(1.57)$ is suppressed.

As we mentioned in section (4.1) indirect indications from π form-factor analyses suggest a similar suppression for the decay $\rho(1250) \longrightarrow 2\pi$, the fitted branching ratio being $\sim 7\%$.

A more spectacular large-phase-space suppression is to be seen in the decays of the $\psi''(4.03\ \text{GeV})$. The measured cross-sections[130] for the final states $D^0\bar{D}^0$, $D^0\overline{D^{0*}} + D^{0*}\bar{D}^0$, $D^{0*}\overline{D^{0*}}$ seen in e^+e^- experiments are in the ratio

$$1 : 22 : 20$$

If the available phase-spaces are taken into account the enhancement factors become

$$1 : 40 : 1400$$

which should be compared with the quark-model spin-counting predictions[131] of

$$1 : 4 : 7$$

This suppression phenomenon is evidently a general feature of the decays of radially excited states and this has been noted and investigated by many people. Notably Tornqvist[132] offered an explanation which requires there to be nearly degenerate states at each of the sites 1.25 GeV, 1.57 GeV, 1.78 GeV and 4.03 GeV. Then consistency with unitarity requires the states at each site to mix in such a way that the large-phase-space modes of one of the states become suppressed.

The remaining states at that site are predicted to be so wide as to be unobservable.

A more spectacular postulate was proffered by De. Rújula et al[133] in order to explain the enhanced $D^{o*}\overline{D^{o*}}$ decays of the (4.028). They argued that the identification of this resonance as a $D^{o*}\overline{D^{o*}}$ molecular bound state would explain its preferred decay modes. Indeed it would however critics argue that this is just a tautology (see ref. (134)) - to say there is a $D^*\bar{D}^*$ resonance is equivalent to saying that the $D^*\bar{D}^*$ are produced more often than expected!

A more recent treatment of this problem due to Le Yaouanc et al[135,136] demonstrating that the $\psi''(4.03)$ decays can be understood without the inclusion of such drastic assumptions. The suppressions can be seen to be due to the spatial structure of the radially excited wave function describing the ψ''. They calculate within a quark-pair-creation model employing non-relativistic, harmonic oscillator wave-functions. Coupling constants are compared under the approximation of equal radii for all hadrons and they reproduce well the suppression of the large-phase-space decays and also the observed narrowness of the $\psi'''(4.41)$.

It is this philosophy that we shall go on to investigate in Chapter Five, particularly as applied to light quark radially excited states.

4.3 Qualitative Solution

We have seen that the status of the light quark meson radial excitation spectra is one of confusion and untidiness with the states exhibiting unexpected properties in their hadronic decay modes.

We look first for guidance at the form of the best established spectrum of radial states - the charmonium particle $\psi(3.1)$ and its excitations (Fig. (4.5)).

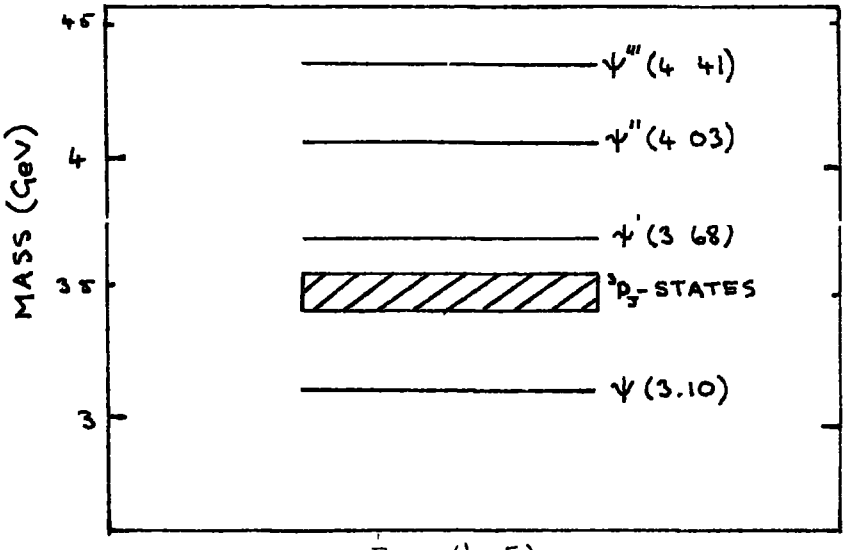

Fig. (4.5)
Charmonium spectrum of radially excited states

A harmonic oscillator potential would feel at home amongst the levels below 4 GeV. The first orbitally excited states lie mid-way in mass-squared between the $n = 0$ and $n = 1$ states and, as we saw in Chapter One, a spring constant $\Omega = 2\ \text{GeV}^2$ in the eigenvalue equation

$$M^2 = \Omega (2n + l + 3/2) \qquad (4.10)$$

fits the levels nicely. However the relatively rapid convergence of the higher states tells us that this is not the spectrum of an harmonic oscillator - it is more

characteristic of a linear $q\bar{q}$ binding potential and this notion has been discussed extensively in the literature (137-145). We will carry over this clue of rapid convergence to the spectra of light quark states.

We saw in Chapter Two that radial excitations can be combined with traditional vector dominance ideas to yield a consistent prescription for all vector-meson radiative decays. However it was not possible to explain the observed suppression of the large-phase-space decays. The particle identifications made in that work were harmonic-oscillator like, the (1570), $\omega(1780)$ and $\phi(1820)$ particles all being n = 1 states. However it is apparent from the structure of radially excited wave-functions that if these states are in fact higher n-excitations, then their (large-phase-space) couplings to n = 0 states will be reduced because of the reduced overlap of the spatial wave-functions.

This reasoning, combined with the expected convergence of states and the problems associated with deviations from ideal nonet symmetry suggest that we expect light-quark spectra of the type shown in Fig. (4.6).

The new assignment of the $\omega(1780)$ as the (n = 3) third radial excitation of the ω and the postulation of the existence of its isovextor partner (ρ''') will remove all the problems of associating the $\omega(1780)$ with the ρ(1570). (We will review later the experimental evidence for the predicted new states.) We will discuss in

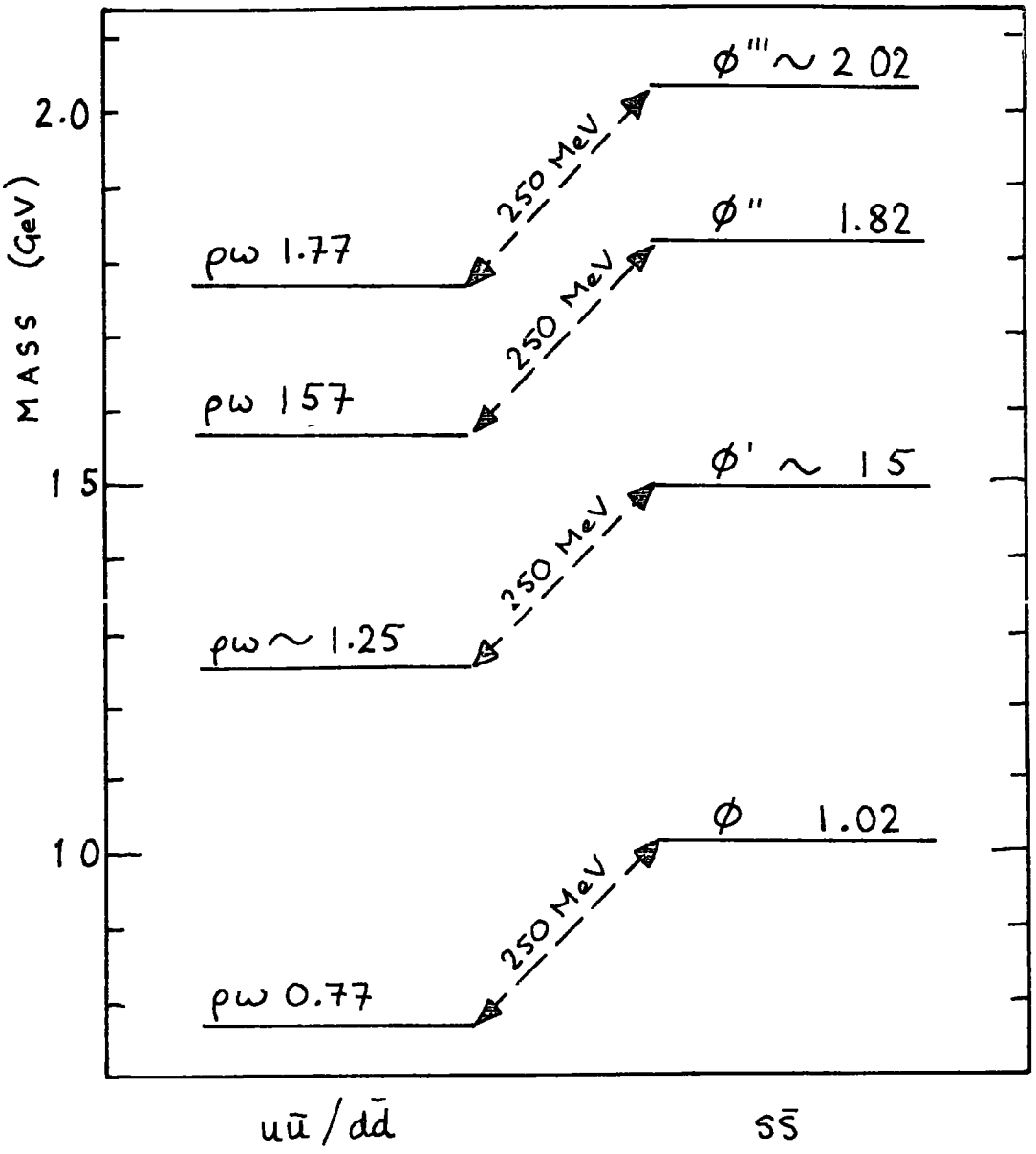

Fig. (4.6)
Re-identified states in the light quark radial spectra

Chapter Five how qualitatively and quantitatively this scheme leads to an understanding of the suppressed decays of the excited states. We will calculate various branching ratios within a specific quark model for which we require wave-functions describing the vector mesons

and their excitations. Consequently we go on now to discuss the application of linear potential models to both light and heavy quark-antiquark bound systems. We want both to describe the observed spectra and to obtain simple wave-functions with which we can calculate.

4.4 Potential Models

We first review briefly various potential model approaches to the problem in order that we might find the most economical way to describe the spectra and obtain simple wave-functions.

As mentioned in Chapter One the constituents of hadrons are generally believed to be light. The experimental non-observation of such constituents outside hadrons leads naturally to the proposition of a confining mechanism and this is the basis for the potential model approach which was originally motivated by indications from colour gauge theories that the forces binding quarks are independent of the inter-quark separation.

The first treatments of meson spectra were non-relativistic and applied to the charmonium spectrum in the hope that it may be non-relativistic. Harrington[138] solved the Schroedinger equation

$$\left\{ p^2/m + V \right\} \psi = E \psi \qquad (4.11)$$

with $V = ar$. The lowest two 1^- states of the spectrum

fix the two parameters a, m_c and the higher levels are predicted. The higher radial levels are rather too spaced out although a notable prediction was that the D states should be at ~ 3.77 GeV which is where the $^3D_1$ state has been recently seen[146].

Kang and Schnitzer[140] solved a Klein-Gordon equation (in the centre of momentum system)

$$E - V = (p^2 + m_1^2)^{1/2} + (p^2 + m_2^2)^{1/2} \qquad (4.12)$$

with a potential $V = ar + b$ transforming as the fourth component of a four-vector. They noted an inconsistency in their approach in that the equivalent potential

$$\left[-\frac{\nabla^2}{2\mu} + \underbrace{\frac{1}{2\mu}\left\{\frac{aEr}{2} - \frac{a^2r^2}{4}\right\}}_{U(r)} \right]\psi(r) = \frac{E^2/4 - m^2}{2\mu}\psi(r) \qquad (4.13)$$

$U(r)$ grows to a maximum and subsequently tends to $-\infty$. However they neglect any possible tunnelling through the barrier (the tunnelling coefficient being reasonably small) and apply the equation to old and new mesons. They find that, in common with many similar approaches they must regard the $\rho(1600)$ as a first radial excitation. In fitting the spectra they argue that, again because of indications from gauge theories, they must regard the confinement constant a as universal - however b, which must account for short range spin-independent and spin-dependent corrections - both of which depend on the quark mass, must vary with the quark mass.

Gunion and Li[137] noted that if the confinement potential transforms as a Larantz scalar then the

difficulty with the effective potential is removed. They considered both Klein-Gardon and Dirac equations

$$\left[\nabla^2 + \tfrac{E^2}{4} - (m + V_s)^2\right]\psi(r) = 0 \qquad (4.14)$$

and

$$\left[\tfrac{M}{2}\gamma_0 + i\,\underline{\gamma}.\underline{\nabla} - (m + V_s)\right]_{\alpha\delta}\psi_{\delta\beta}(r) = 0 \qquad (4.15)$$

and solved numerically with $V_s = a|r|$. They found the term quadratic in the quark separation to be unimportant for the first few levels and also the Dirac and Klein-Gordon equations yield identical spectra with identical parameters.

It appears then that spin-dependent corrections are relatively unimportant for a description of the radial spectra. This observation is supported by the work of Barbieri et al[145] who solved the Schroedinger equation with a "linear + Coulomb" potential and then calculated Fermi-Breit and "relativistic corrections" (the third term in the expansion of $(m^2 + p^2)^{\frac{1}{2}}$). They found that the Fermi-Breit corrections were relatively small in all cases.

These indications influence our philosophy which is that: within the context of potential models with simple choices of potentials the effects of a relativistic treatment of the quark motion are much more significant than any relativistic treatment of the quark spin. A Klein-Gordon equation is adequate here and the term quadratic in r is unimportant for the first few radial

levels. We will employ a linear quark confinement potential of the form V = ar + b - both because of its possible theoretical adequacy, and because the light quark states we have identified together with the charmonium states constitute spectra that are more rapidly converging than the eigenvalues of a harmonic oscillator wave equation.

We will expect the constant a to be universal whilst b, which subsumes all effects other than the confinement mechanism, will be constant within any system of excitations. We will not initially choose the Lorentz transformation properties of the potential, rather we will consider three cases

(i) V = ar + b is a Lorentz scalar

(ii) V = ar + b is Coulomb-like

(iii) The confining potential is scalar and the short range term vector.

Also we will treat all flavour sectors with the same wave-equation, and so will not assume the charmonium states to be non-relativistic. Our criterion for relying upon the wave-functions generated is that the eigenvalues of the wave-equation describe the observed spectra.

For equal mass constituents interacting via vector and scalar potentials the Klein-Gordon equation reads

$$(E - V_v)^2\psi(\underline{r}) = 4(p^2 + (m+V_s)^2)\psi(\underline{r}) \qquad (4.16)$$

which with the usual quantum-mechanical substitutions

reads

$$\left\{\nabla^2 + \tfrac{1}{4}(E - V_v)^2 - (m + V_s)^2\right\}\psi(\underline{r}) = 0 \qquad (4.17)$$

We neglect the term quadratic in r and consider the three cases

$$\left.\begin{array}{lllll} \text{(i)} & V_s = ar + b & , & V_v = 0 \\ \text{(ii)} & V_s = 0 & , & V_v = ar + b \\ \text{(iii)} & V_s = ar & , & V_v = b \end{array}\right\} \qquad (4.18)$$

Separating angular variables in the usual way and considering $l = 0$ systems only we obtain the radial equation

$$\frac{d^2R(r)}{dr^2} + (\alpha - \beta r)R(r) = 0 \qquad (4.19)$$

where

$$\psi(r) = Y_0^0(\theta, \phi)\, R(r)/r \qquad (4.20)$$

The expressions for α and β for the three potentials considered are given in Table(42(p86)). Substituting now $x = \beta^{1/3} r$, equation (4.19) becomes

$$\frac{d^2R(x)}{dx^2} + (\lambda - x)R(x) = 0 \qquad (4.21)$$

with

$$\lambda = \alpha/\beta^{2/3} \qquad (4.22)$$

The solution which approaches zero as $x \to \infty$ is an Airy function[147],

$$R(x) = Ai(x - \lambda) \qquad (4.23)$$

$$= \frac{(x-\lambda)^{1/2}}{\pi\sqrt{3}} K_{1/3}\left(\tfrac{2}{3}(x-\lambda)^{3/2}\right) \qquad (4.24)$$

where $K_{\frac{1}{3}}$ is the usual modified Bessel function. The requirement that $R \rightarrow 0$ as $r \rightarrow 0$ determines the eigenvalue equation

$$A_1(-\lambda) = 0 \qquad (4.25)$$

$$\text{i.e.} \qquad \lambda = a_n \qquad (4.26)$$

where a_n are the zeros of the Airy function along the negative real axis (only positive energy solutions are allowed). Hence the eigenvalue equation reads

$$\alpha = \beta^{2/3} a_n \qquad (4.27)$$

where α and β are given in Table (4.2). For example for case three we have

$$E - b = 2\left\{m^2 + (2am)^{\frac{2}{3}} a_n\right\}^{\frac{1}{2}} \qquad (4.28)$$

The full solutions to equation (4.17) then read

$$\psi(r) = K\, Y_0^0(\theta,\phi)\, \frac{A_i(\beta^{1/3} r - \alpha/\beta^{2/3})}{r} \qquad (4.29)$$

where K is the normalisation constant given by

$$K = \frac{-\beta^{1/6}}{\sqrt{4\pi}\, A_i'(-\alpha/\beta^{2/3})} \qquad (4.30)$$

where

$$A_i'(z) = \frac{d}{dz} A_i(z) \qquad (4.31)$$

4.5 Spectra of the Model

In order to determine the parameters entering into the wave-functions (namely a, b and the quark masses) we attempt to describe the particle assignments made earlier and the more established resonances using the eigenvalue

equations (4.27). This procedure singles out a unique potential from the three considered capable of accommodating our new particle assignments.

(i) The purely scalar potential does not allow any fit as the constant b merely renormalises the quark masses.

(ii) The purely vector potential cannot accommodate all flavour sectors with a universal confinement constant a.

The charmonium system puts a lower bound on a and this in turn puts a lower bound on the spacing in the non-charmed sectors. This lower bound is too large to accommodate the $\rho(1250)$ however consistency can be achieved by identifying the $\rho(1570)$ as the <u>first</u> radial recurrence of the $\rho(770)$, the second excitation appearing at approximately 2.2 GeV (these were the particle identifications made by Kang and Schnitzer[140] as they were considering precisely this potential). However as this is in contradiction to our philosophy and possibly to experiment[117-119, 122-124] we reject this form of potential.

The third potential type considered, scalar confining term and short-range-vector potential with the parameters

$$a = 0.19\ \text{GeV}^2 \qquad m_{ud} = 0.3\ \text{GeV} \qquad b_u = -0.827\ \text{GeV}$$
$$m_s = 0.37\ \text{GeV} \qquad b_s = -0.734\ \text{GeV}$$
$$m_c = 1.055\ \text{GeV} \qquad b_c = 0$$

yields the spectrum shown in Fig. (4.7). The short range

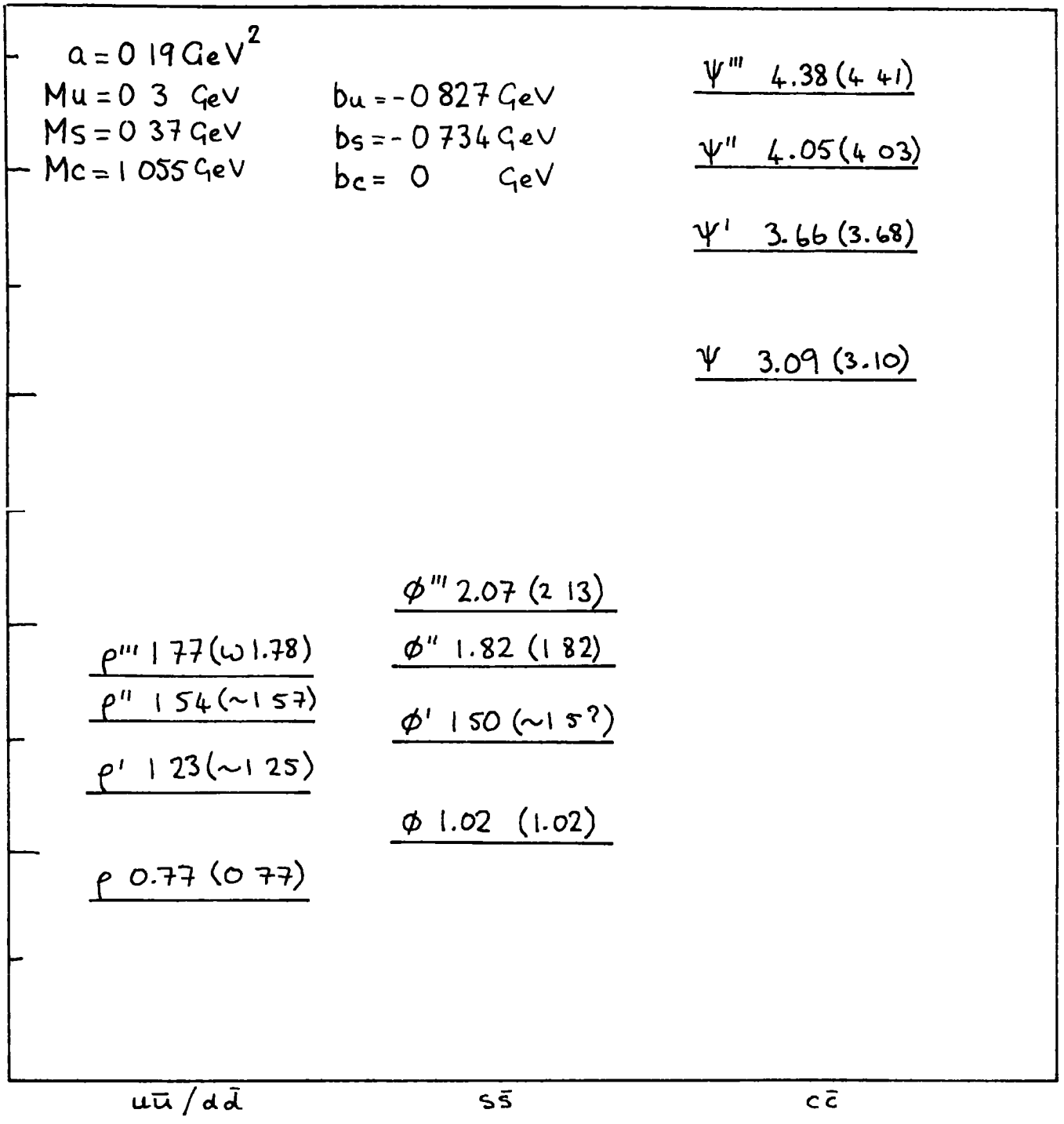

Fig. (4.7)
The mass spectra predicted by the eigenvalue equation (4.28)(experimental masses given in brackets) together with the potential parameters and quark masses.

potential is attractive and its effect decreases with increasing mass as asymptotic freedom arguments suggest. The quark masses are reasonable in that they are in accord with simple quark model prejudices. The mass of the charmed quark is smaller than that obtained in some treatments[139-142, 145]. However for similar and smaller values see[137, 138, 143, 144]. It is not clear from detailed considerations of the fine structure of the charmonium spectrum (for a brief review see (148)) that this system is essentially a non-relativistic one - however we examined the sensitivity of the spectra to each of the parameters in order to determine the uniqueness within this model of the quark masses.

The charmonium spectrum is sensitive to the confinement parameter and essentially fixes $a = 0.19$ GeV^2 however m_c can reasonably vary between 1 and 1.35 GeV, 1.055 GeV giving the best statistical fit. With (a) fixed m_q and b_q for the light quarks are determined by the $n = 0,1$ states and the higher levels predicted.

Structure has recently been observed[25] in $\mu^+\mu^-$ mass distributions emerging from proton-nucleus collisions and it has been suggested by many authors (see for example (149)) that this may correspond to bound states of at least one new heavy quark. The resonance mass values are given as

$$M_{\Upsilon_1} = 9.40 \pm 0.014 \text{ GeV}$$
$$M_{\Upsilon_2} = 10.00 \pm 0.05 \text{ GeV}$$
$$M_{\Upsilon_3} = 10.4 \pm 0.15 \text{ GeV}$$

We are in a position to give predictions supporting the identification of these states as a ground state of a heavy (b) quark and its first two radial excitations.

For such massive systems we expect b, the short range constant, to be approximately zero, so with (a) fixed we have one free parameter, the new quark mass. $M_{\Upsilon_1} = 9.4$ GeV fixes $m_b \simeq 4.35$ GeV and the predicted masses are

$$M_{\Upsilon} = 9.4 \text{ GeV}$$
$$M_{\Upsilon'} = 9.95 \text{ GeV}$$
$$M_{\Upsilon''} = 10.35 \text{ GeV}$$

in reasonable agreement with the published parameters.

It would be over-optimistic to attach any basic significance to the parameters we obtain as our model is simple.

However the fact that the radial excitation spectra are so well-described in all the mass ranges considered adds weight to the light particle identifications made earlier.

As a check on the consistency of our parameters we calculate the energies of the first orbitally excited states. We use the W.K.B. approximation which works well in this type of calculation[138], even for low n states, because the effective potential is a slowly varying function of $\underline{r}$ between the classical turning points.

The W.K.B. quantisation condition is given by

$$\int_{r_o}^{r_1} q_r dr = (n + \tfrac{1}{2})\pi \qquad (4.32)$$

with

$$q_r = \left\{ \left(\frac{E_{nl} - b}{4} \right)^2 - m^2 - 2amr - \frac{(l + \frac{1}{2})^2}{r^2} \right\}^{\frac{1}{2}} \tag{4.33}$$

where $r_o < r_1$, the classical turning points, are the two positive roots of

$$q_r = 0 \tag{4.34}$$

Solving (4.32) for u,d quarks yields

$$E_{01} = 1.06 \text{ GeV}$$

and for c quarks

$$E_{01} = 3.44 \text{ GeV}$$

to be compared with the ^3P_J triplets

	$A_2(1.31)$
ud quarks	$A_1(1.10)$
	$\delta(0.97)$
	$\chi(3.55)$
c quarks	$\chi(3.51)$
	$\chi(3.41)$

in reasonable agreement.

We will use the wave-functions (4.29) in Chapter Five to calculate the decay properties of the excited states where we also discuss the predicted new states of this model ($\omega'(1260)$, $\omega''(1580)$, $\rho'''(1770)$) as their eventual detection is obviously crucial to our arguments.

Summary

We discussed the experimental status of radial excitation spectroscopy and various potential model attempts to describe these spectra. By re-identifying some of the vector meson states more recently observed coupling to e^+e^- we showed that in all flavour sectors the spectra of radial excitations can be well described by a Klein-Gordon type wave-equation employing a simple, linear $q\bar{q}$ potential.

CHAPTER 5

DECAY PROPERTIES OF RADIALLY EXCITED STATES

5.1 Properties of the Wave-Functions

The charmonium system is frequently regarded as a non-relativistic one and this is an assumption we can immediately test within the context of the model outlined in the previous chapter. The non-relativistic limit of the wave-equation (4.16) is derived by expanding the square-root operator

$$(p^2 + m(m + 2V_s))^{\frac{1}{2}} \qquad (5.1)$$

to first order in powers of $1/m^2$ to obtain

$$(E - V_v)\psi(\underline{r}) = 2m(1 + \frac{2mV_s + p^2}{2m^2})\psi(\underline{r}) \qquad (5.2)$$

i.e.

$$E\psi(\underline{r}) = \left\{ 2m + \frac{p^2}{m} + (2V_s + V_v) \right\}\psi(\underline{r}) \qquad (5.3)$$

the desired Schrödinger equation. The expectation value of the quark velocity within any meson will determine whether this equation represents an adequate description of the system.

We calculate the root-mean-square quark velocities using the following identity

$$\langle v_q^2 \rangle = \frac{1}{E_q^2} \langle p_q^2 \rangle = \frac{4}{(M-b)^2} \langle p_q^2 \rangle \qquad (5.4)$$

in the notation of Chapter Four. From the wave-equation (4.16) we have

$$\langle p^2 \rangle = \tfrac{1}{4}(M-b)^2 - m^2 - 2m \langle V_s \rangle \qquad (5.5)$$

and substituting in (5.4) we obtain

$$\langle v^2 \rangle^{1/2} = \left\{ 1 - \frac{4m^2}{(M-b)^2} - \frac{8am}{(M-b)^2} \int \psi^* \psi \, r^3 \, dr \, d\Omega \right\}^{1/2} \qquad (5.6)$$

Using the normalised wave functions (4.29) and evaluating the radial integral numerically we find the results listed in Table (5.1). It is clear that only the upsilon

Table (5.1):

Root mean square quark velocities in radially excited states

STATE	$\langle v^2 \rangle^{1/2}$	STATE	$\langle v^2 \rangle^{1/2}$
ρ (0.77)	0.540	ψ (3.098)	0.430
ρ'(1.25)	0.570	ψ'(3.684)	0.485
ρ''(1.57)	0.580	ψ''(4.028)	0.491
ϕ (1.02)	0.520	Υ (9.400)	0.21
ϕ'(1.50)	0.547	Υ'(10.00)	0.30
ϕ''(1.82)	0.554	Υ''(10.35)	0.32

($b\bar{b}$) system can reasonably be regarded as a non-relativistic one, the r.m.s. velocity for c quarks in the Ψ being almost half the velocity of light.

The rates for the decays of vector mesons into e^+e^- pairs are easily accessible experimentally and consequently form a good testing ground for models of the type that we have developed. Classically the widths are sensitive to the bound state wave-function at the origin - this is a non-relativistic result originally written down in the context of the quark model by Van Royen and Weisskopf[14]. They obtained the width formula by the expansion of the matrix element about $\underline{p} = 0$ (the quark momentum) keeping only the leading term, the specific expression for the width being

$$\Gamma(V \to e^+e^-) = 3C_V^2 \alpha^2 \frac{16\pi}{3m_V^2} |\psi(0)|^2 \qquad (5.7)$$

where

$$C_V = \sum_{\text{quarks}} a_i e_i/e \ . \qquad (5.8)$$

a_i is the Clebsch-Gordon coefficient of quark i in meson V and e_i its electric charge. (The extra factor of 3 over the original expression is due to colour).

The employment of our wave-functions in this expression would be unrealistic for ρ, ω, ϕ, Ψ mesons and their excitations because of the relativistic nature of the quark velocities. We do expect

$$\frac{\Gamma(\rho \to e^+e^-)}{9} = \Gamma(\omega \to e^+e^-) \qquad (5.9)$$

since $|\psi_\rho(0)| = |\psi_\omega(0)|$ and $m_\rho \simeq m_\omega$. This relationship holds well experimentally and we would also predict it to hold for every degree of radial excitation. However due to the relativistic corrections which must be involved the remarkable experimental fact that[150]

$$\frac{\Gamma(\rho \to e^+e^-)}{9} \approx \frac{\Gamma(\phi \to e^+e^-)}{2} \approx \frac{\Gamma(\psi \to e^+e^-)}{8} \qquad (5.10)$$

(remarkable because the c_v's are in this ratio) must be regarded as fortuitous. Because of its non-relativistic nature we can predict with some confidence the leptonic width of the upsilon mesons.

In any potential model with a linear confinement potential $|\psi(0)|$ is independent of the degree of radial excitation. From (4.29)

$$|\psi(0)| = \left| \frac{\beta^{1/6}}{\sqrt{4\pi}\, A_i'(-\alpha/\beta^{2/3})} \lim_{r\to 0} \frac{A_i(\beta^{1/3} r - \alpha/\beta^{2/3})}{r} \right| \qquad (5.11)$$

and since $A_i(-\alpha/\beta^{2/3}) = 0$ we use de l'Hopital's rule to obtain

$$|\psi(0)| = \left| \frac{\beta^{1/3}}{\sqrt{4\pi}} \right| \qquad (5.12)$$

i.e.

$$|\psi(0)|^2 = \frac{a m_q}{2\pi} \qquad \forall n \qquad (5.13)$$

Assuming a preferred charge of $-\frac{1}{3}$ for the new quark[151] we find

$$\Gamma(\Upsilon \to e^+e^-) \simeq 0.44 \text{ KeV}$$
$$\Gamma(\Upsilon' \to e^+e^-) \simeq 0.39 \text{ KeV}$$

Another measurable quantity which is a powerful tool for discrimination among competing theoretical models is the pion charge radius. The r.m.s. charge radius is related to the pions electromagnetic form factor by

$$\langle r_\pi^2 \rangle^{1/2} = \left[-6 \frac{d}{dq^2} F_\pi(q^2) \Big|_{q^2=0} \right]^{1/2} \qquad (5.14)$$

and the simple vector-dominance model wherein F_π is well described by the $\rho(770)$ pole.

$$F_\pi(q^2) = (1 + q^2/m_\rho^2)^{-1} \qquad (5.15)$$

yields a prediction for $\langle r_\pi^2 \rangle^{1/2}$ of 0.63 fm. A knowledge of the pion spatial wave function allows the direct calculation of this quantity, i.e.

$$2 \langle r_\pi^2 \rangle^{1/2} = \left[\int \psi^* \psi \, r^4 \, dr \, d\Omega \right]^{1/2} \qquad (5.16)$$

In our model the ρ and π spatial wave-functions are identical, hyperfine splittings being absorbed into the constant b. Substituting in (5.16) the ρ/π wave-function and integrating numerically we find

$$\langle r_\pi^2 \rangle^{1/2} = \langle r_\rho^2 \rangle^{1/2} = 0.35 \text{ fm}$$

Many measurements have been made of this quantity. The most recent determination[152] is a <u>direct</u> measurement from pion-electron scattering experiments and yields

$$\langle r_\pi^2 \rangle^{1/2} = 0.56 \pm 0.04 \text{ fm} \quad (152)$$

The prediction is reasonable and gives us further confidence in the relevance of our wave-functions.

It is the structure of the radially excited wave-functions that allows us to understand, firstly in a qualitative way, the suppression of the large-phase-space decays of the excited states. The situation can be paraphrased as the dominance of cascade decays. The 'overlap' of an excited wave-function with ground-state wave-functions at a 3-meson vertex will be poor compared to vertex where one of the final state particles is excited also. Hence, because states like $\rho(1570)$, (1780) have been identified as higher excitations than was originally thought to be the case, their couplings

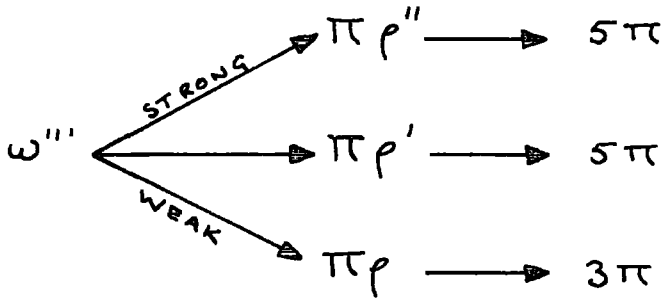

to final states which include excited mesons will be strong and the small phase-space barrier will be overcome. In this way we might expect the higher multiplicity pion decays of these states to dominate over the phase-space favoured low multiplicity decays.

We now go on to treat this problem quantitatively and calculate the three-meson vertices within a simple quark model.

5.2 Quark Pair Creation Model

The model we use has its origins in the graphical forms for 3-point vertices originally suggested by Zweig[153] and extended to 4-part amplitudes by Harari[10] and Rosner[11] - by forbidding exotic resonances and $q\bar{q}$ annihilation within external hadrons their diagrams exhibit the duality principle in a simple and striking way. A three-meson vertex is diagrammatically represented as in Fig. (5.1). The decay proceeds via the creation

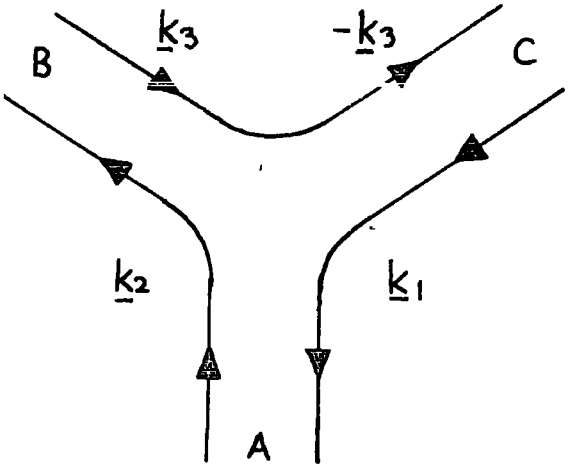

Fig. (5.1)
Three meson vertex in the quark pair creation model

(within the hadronic matter of particle A) of a $q\bar{q}$ pair with vacuum quantum numbers. The quarks of meson A are regarded only as spectators. Conservation of parity $P = (-1)^{L+1}$ (for a $q\bar{q}$ pair) requires the created pair to be in an odd L state and conservation of angular momentum then implies the pair must form a spin triplet and the pair is in an overall $^3P_0$ state (we will refer to this

vertex symmetry model as the $^3P_0$ model)

$$J = 0 , \quad L = S = 1 \qquad (5.17)$$

The first advocates of this picture[154,156] imposed the further constraint that $L = S = 0$ neglecting transverse motions of the created quarks (we are working in the Lorentz frame in which the final state particle momenta are collinear along the z-axis) and this yields the structure of the collinear spin symmetry $SU(2)_W$[155]. This 'relativistic' symmetry, although allowing SU(6) forbidden decays such as $\rho \longrightarrow \pi\pi$, $\Delta \longrightarrow N\pi$, was known to be an unsatisfactory description of strong interaction vertices. For example since the B-meson is in a state $W = 1$, $W_z = 0$ under $SU(6)_W$ its $B \longrightarrow \pi\omega$ decay to the helicity ± 1 states of the ω does not conserve W_z. Only the decay to the helicity zero state should occur whereas the experimental results are inverse to these predictions, the helicity ± 1 modes being almost exclusively preferred. (A similar reversal occurs for the decay $A_1 \longrightarrow \rho\pi$, whereas $SU(2)_W$ predicts a decay from the $J = \pm 1$ states, the $J = 0$ state seems to predominate).

These restrictive predictions of the $^3P_0$ model were removed by Colglazier and Rosner[157] by relaxing the condition $L = S = 0$, the freedom of an extra parameter so introduced then allowed the A_1 and B decays to be understood.

A second way to explain the failure of $SU(6)_W$ for

vertices is to postulate a second $SU(6)_w$ which is appropriate for vertices and non-trivially related to the $SU(6)_w$ describing states at rest (equivalent to postulating "current quarks" when the new $SU(6)_w$ is identified as the algebra of currents introduced by Dashen and Gell-Mann[158]). It was Melosh[159] who went some way to relating the generators of the two groups by solving the free quark case only. Assuming then that the physical axial charge transforms in the same way as the free quark axial charge PCAC can be used to calculate pionic vertices with good results[162]. This treatment can be shown to be equivalent to the $^3P_0$ model of Colglazier and Rosner which was later generalised by Petersen and Rosner[163].

A more dynamical approach to the same problem was that of Mitra and Ross[160]. In a naive quark model the process $A \to B\pi$ is treated by pion emission from a single quark, the interaction being proportional to $\underline{\sigma}_i \cdot \underline{k}_\pi$. This coupling is known to fail for many processes close to threshold and especially for ρ, ω polarisations in the A_1 and B decays described above. Mitra and Ross, on the basis of Galilean invariance, introduced a recoil term into the interaction obtaining

$$\underline{\sigma}_i \cdot \left(\underline{k}_\pi - \frac{E_\pi}{m_q} \underline{k}_i \right) \qquad (5.18)$$

and this improves the bad predictions of the naive interaction.

The quark-pair-creation model of Le Yaouanc et al[161]

leads to a more unified understanding of the approaches set out above. $SU(6)_W$ is broken without invoking the notion of current quarks and the phenomenological recoil term of Mitra and Ross appears naturally in matrix elements which specifically involve the hadron spatial wave functions.

Defining the S-matrix

$$S = 1 - 2\pi i\, \delta(E_f - E_i)\, T \qquad (5.19)$$

we can write the T-matrix element between hadronic states for the process $A \rightarrow BC$ as

$$\langle BC|T|A\rangle = \gamma \sum_m \langle 1,1,m,-m|00\rangle \langle \Phi_B \Phi_C | \Phi_A \Phi_{vac}^{-m}\rangle I_m(A,BC) \qquad (5.20)$$

where the Φ_i are the meson SU(6) wave-functions and

$$\Phi_{vac}^{-m} = \chi_1^{-m}\, \phi_0 \qquad (5.21)$$

is the SU(6) wave-function of the created pair ($\phi_0 = \frac{1}{\sqrt{3}}(u\bar{u} + d\bar{d} + s\bar{s})$ is the Su(3) singlet wave function and χ_1^{-m} the spin triplet wave-function.

γ is the dimensionless pair-creation constant and the Clebsch-Gordon coefficient is that relevant to the L=S=1 combination to give J=0. $I_m(A,BC)$ is the spatial overlap intergral written as simply as possible as

$$I_m(A,BC) = \int d\underline{k}_1\, d\underline{k}_2\, d\underline{k}_3\, \delta(\underline{k}_1 + \underline{k}_2 - \underline{k}_A)\, \delta(\underline{k}_2 + \underline{k}_3 - \underline{k}_B)\, \delta(\underline{k}_1 - \underline{k}_3 - \underline{k}_C)$$

$$\times\, \mathcal{Y}_1^m(2\underline{k}_3)\, \psi_A(\underline{k}_1 - \underline{k}_2)\, \psi_B^*(\underline{k}_3 - \underline{k}_2)\, \psi_C^*(-\underline{k}_3 - \underline{k}_1) \qquad (5.22)$$

where the delta-functions just reflect the conservation

of momentum within each meson and $\mathcal{Y}_1^m(2\underline{k}_3)$ is a solid harmonic representing the relative L=1 state of the created pair. Eliminating the δ-functions we obtain

$$I_m(ABC) = \delta(\underline{k}_c+\underline{k}_B)\int d\underline{k}_1\, \mathcal{Y}_1^m(-2(\underline{k}_c-\underline{k}_1))\,\psi_A(2\underline{k}_1)\,\psi_B^*(2\underline{k}_1-\underline{k}_c)\,\psi_c^*(\underline{k}_c-2\underline{k}_1) \qquad (5.23)$$

We can see now how the phenominological recoil term of Mitra and Ross arises naturally in this model. Considering C= π we can write

$$\begin{aligned}\langle \Phi_B \Phi_c \,|\, \Phi_{vac}^{-m}\Phi_A\rangle &= \langle \Phi_B \chi_0^0 \phi_\pi \,|\, \phi_0 \chi_1^{-m}\Phi_A\rangle \\ &= \langle \Phi_B | \sigma_{-m}\underline{\tau}\cdot\underline{\phi}\,|\,\Phi_A\rangle \end{aligned} \qquad (5.24)$$

where σ and τ are spin and isospin Pauli matrices and $\underline{\phi}$ is the pion isovector. ($\sigma_{\pm 1} = \frac{\pm\sigma_x + i\sigma_y}{\sqrt{2}}$, $\sigma_0 = \sigma_z$). Combining (5.24) with $I_m(A,BC)$ and noting that

$$\mathcal{Y}_1^m(-2(\underline{k}_\pi-\underline{k}_1)) \propto \underline{\varepsilon}_m\cdot(\underline{k}_\pi-\underline{k}_1) \qquad (5.25)$$

we see that the operator to be taken between Φ_A and Φ_B takes the form

$$\delta(\underline{k}_B+\underline{k}_\pi)\,\gamma\int d\underline{k}_1\,\psi_A(2\underline{k}_1)\left\{\underline{\sigma}\cdot(\underline{k}_\pi-\underline{k}_1)\,[\underline{\tau}\cdot\underline{\phi}_\pi]\,\psi_\pi^*(\underline{k}_\pi-2\underline{k}_1)\right\}\psi_B^*(2\underline{k}_1-\underline{k}_\pi) \qquad (5.26)$$

where all trivial numerical factors have been absorbed into γ. The central operator is similar to that of Mitra and Ross however there is an extra factor $\psi_\pi^*(\underline{k}_\pi - 2\underline{k}_1)$ expressing the composite nature of the pion. In the limit of a small pion radius $\psi_\pi(\underline{k}) \longrightarrow \psi_\pi(0)$ the elementary pion emission of Mitra and Ross is fully recovered (with $E_\pi \approx m_q$) .

Transforming the wave-functions in (5.23) to configuration space we obtain

$$I_m(A,BC) = \delta(\underline{k}_B + \underline{k}_C) \int d\underline{q}\, d\underline{x}_A\, d\underline{x}_B\, d\underline{x}_C\, \mathcal{Y}_1^m(\underline{q})\, \psi_A(\underline{x}_A)\, \psi_B^*(\underline{x}_B) \times \psi_C^*(\underline{x}_C)\, e^{i\underline{q}\cdot(\underline{x}_B - \underline{x}_A - \underline{x}_C)}\, e^{i\underline{k}_B\cdot(2\underline{x}_A - \underline{x}_B + \underline{x}_C)} \quad (5.27)$$

and this is an expression in which we can employ the spatial wave-functions obtained in Chapter Four.

Transverse polarisations of the created pair are allowed but are coupled here with a spatial overlap integral and summed over. The polarisation phenomena of the A_1 and B decays are calculated by employing non-relativistic harmonic-oscillator spatial wave-functions under the approximation of equal radii for all hadrons. This leads to an adequate explanation of the data without the introduction of an extra free parameter[157]. The model also removes all ambiguities of the choice of which emitted field is elementary - an ambiguity which leads to well-known inconsistencies in standard quark models[22].

5.3 Previous Applications of the Model and Our Approach

The significance of the model of Le Yaouanc et al has been noted and exploited by many authors. Kaufmann and Jacob[164], working strictly within the spirit of the original model, were able to go some way towards explaining the suppression of the 2π decay mode of the $\rho(1570)$. They identified this particle as a first radially excited state within a non-relativistic harmonic-oscillator framework and calculated its 2π branching ratio - again within the approximation of equal radii for all hadrons.

Barbieri et al[165] trivially extended the group structure to SU(4) in an early attempt to describe quantitatively the behaviour of $\sigma(e^+e^- \rightarrow \text{hadrons})$ in the region just above charm threshold. Again harmonic oscillator wave-functions were employed however in a later work[145] they adopted a philosophy similar to our own[60]. Motivated by hopes from colour gauge theories they solved a wave-equation involving a long-range, spin-independent confining potential and a short-range one gluon Coulomb potential. In contrast to our approach they assumed that hadrons can be described mainly by non-relativistic dynamics and solved the Schrödinger wave-equation. They went on to use their numerical wave-functions in the quark-pair-creation model to calculate coupling constants for the vertices $\psi \rightarrow DD$, $\psi' \rightarrow DD$, $\psi \rightarrow FF$ etc. assuming that the form-factors for these charmed mesons are dominated by the (off-mass-shell) vector meson poles. The aim was to fit the cross-section $\sigma(e^+e^- \rightarrow \text{hadrons})$ with the pair creation constant γ being the only inknown parameter nowever this was not possible because of the poor data.

The wave-functions obtained in this work were re-used subsequently by Chaichian and Kögerler[166] to treat radiative transitions amongst the charmonium states in a vector-dominance spirit. Even with a weak q^2-suppression factor

$$f_{\psi_i}(q^2 = 0) \sim \frac{1}{2.5} f_{\psi_i}(q^2 = m^2_{\psi_i}) \qquad (5.28)$$

(which is applied rather unrealistically to all the radial excitations as well as the gound state) and a $\frac{-3}{\sqrt{12}}$ $c\bar{c}$ content of the η_c they predict large branching ratios for decays such as $\psi \longrightarrow \eta_c \gamma$, $\psi' \longrightarrow \eta_c \gamma$. These details are more relevant to Chapter Two however the spirit of the approach of this series of papers is similar to ours - the non-relativistic harmonic oscillator wave functions are abandoned in favour of solutions to a wave equation which employs a theoretically motivated $q\bar{q}$ potential.

Our interest lies in the comparison of the small phase-space decays of radially excited states to their large-phase-space counter parts. The difference in the structure of the matrix elements is expected to be due to the different spatial overlap integrals which are determined by the structure of radially excited wave-functions. Hence the group theoretical properties of the vertices are not our main concern. We will consider only the processes $V \longrightarrow PP$, $V' \longrightarrow VP$ (V = vector, P = pseudoscalar) in which only one polarisation state of the created pair is allowed - hence the virtues of the model discussed earlier in relation to broken SU(6) treatments will not affect our calculations.

Our wave-functions were not derived under the assumption of non-relativistic quark dynamics, and this generality allows us to calculate coupling constants for the hadronic decays of the old (light quark) mesons. We will not be able to treat the decays of ϕ^n and ψ^n

mesons because their decay products (K and D mesons) are composed of unequal mass constituents (we solved the wave equation only in the equal mass case). In this context we mention again the recent work of Le Yaouanc et al[135,136] who were able to understand the suppressed decays of the $\psi''(4.03)$ and $\psi'''(4.41)$ within the context of the quark-pair-creation model and harmonic oscillator wave functions.

We calculate vertices involving light quarks by substitution of the wave-functions (4.29) into the spatial overlap integral (5.27). Transformation to spherical co-ordinates allows the angular integrals to be performed analytically using integral relations for Bessel functions (see Appendix 3). The remaining convolution of four, one dimensional integrals is calculated numerically on a computer yielding $I_m(ABC)$. For each particular vertex the value of this integral is combined with the spin-SU(3) matrix element and the L-S Clebsch-Gordon coefficient. For illustration we calculate the T-matrix element for the decay $\rho^+(J_z = 0) \longrightarrow \pi^+\pi^0$.

The SU(6) wave-functions involved are (Appendix 2)

$$|\rho^+\rangle = \frac{1}{\sqrt{2}}\left(|u_+\bar{d}_-\rangle + |u_-\bar{d}_+\rangle\right)$$

$$|\pi^+\rangle = \frac{1}{\sqrt{2}}\left(|u_+\bar{d}_-\rangle - |u_-\bar{d}_+\rangle\right)$$

$$|\pi^0\rangle = \frac{1}{2}\left(|u_+\bar{u}_-\rangle - |u_-\bar{u}_+\rangle - |d_+\bar{d}_-\rangle + |d_-\bar{d}_+\rangle\right)$$

$$|\Phi^0_{inc}\rangle = \frac{1}{\sqrt{3}}\left(|u_+\bar{u}_-\rangle + |u_-\bar{u}_+\rangle + |d_+\bar{d}_-\rangle + |d_-\bar{d}_+\rangle\right)$$

and these are combined into the matrix element under the general rule for any vertex of the form (Fig. (5.1)).

$$\langle q_B \bar{q}_B | \langle q_C \bar{q}_C | q_A \bar{q}_A \rangle | q_{anc} \bar{q}_{anc} \rangle = \delta_{q_A q_B} \delta_{\bar{q}_A \bar{q}_C} \delta_{q_{anc} q_C} \delta_{\bar{q}_{anc} \bar{q}_B} \quad (5.29)$$

where

$$\delta_{ij} = 1 \quad , \quad i = j$$
$$= 0 \quad , \quad i \neq j \quad (5.30)$$

Note that in the case we are considering we pick up an extra minus sign between the two diagrams Figs. 5.2a/b because of the relative sign of the pion momenta

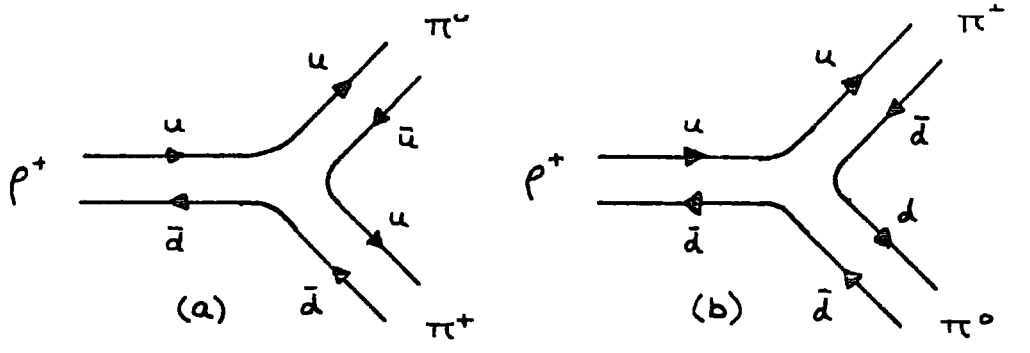

Fig. (5.2)
The two quark diagrams contributing to the process $\rho^+ \longrightarrow \pi^+ \pi^0$

appearing in $I_m(A,BC)$ - the matrix element would be zero if this were omitted. The result for the SU(6) matrix element here is $\frac{1}{\sqrt{6}}$ and thus is combined with the Clebsch-Gordon coefficient

$$\langle 1,1;0,0 | 0,0 \rangle = -1/\sqrt{3} \quad (5.31)$$

to yield the T-matrix element

$$T_{fi} = -\frac{\gamma}{3\sqrt{2}} I_m(A,BC) \quad (5.32)$$

This is then compared with the T-matrix element obtained from the usual phenomenological interaction Hamiltonian (167).

$$T_{fi}^{phenom} = \frac{2i\delta^3(\underline{k}_{\pi^0} + \underline{k}_{\pi^+}) g_{\rho\pi\pi}\, \underline{\varepsilon} \cdot \underline{k}_\pi}{(2\pi)^{3/2}\, m_\rho\, (2m_\rho)^{1/2}} \qquad (5.33)$$

(where we have set $E_\pi = \frac{m_\rho}{2}$) to obtain the coupling constant $g_{\rho\pi\pi}$. The width is then calculated via the width formula.

$$\Gamma(V \to PP) = \frac{k_P^3\, g_{VPP}^2}{6\pi m_V^2} \qquad (5.34)$$

As in ref. (136) we regard the simplifying quark-pair-creation scheme as being only an approximation; however in comparing decay rates of large and small phase-space processes it should be the structure of our wave-functions which is the controlling factor.

5.4 Results and Relation to Experiment

We calculate the kinematically allowed decays of ρ and ω-meson excitations. The well-established decay width of the ρ-meson into 2π's is used as input to determine the only unknown parameter γ. All the results listed in Table (5.2) then uniquely follow. We summarise here the predicted properties of each resonance.

(1) The $\rho'(1250)$ has a width of $500 \to 600$ MeV and decays mainly to 4π's , the 2π branching ratio being $\sim 5\%$.

Table (5.2):

Decay width predictions

PROCESS A → BC	PREDICTED WIDTH (MeV)	EXPT. (MeV)
$\rho \to \pi\pi$	152	152
$\rho'_{1250} \to \pi\pi$	26	B R. $\rho' \to \pi\pi$ small
$\to \pi\omega$	528	
$\omega'_{1260} \to \pi\rho$	1 6 GeV	-
$\rho''_{1570} \to \pi\pi$	59	$\Gamma_{tot} \sim 200-800$
$\to \pi\omega$	228	B.R. $\rho'' \to \pi\pi$ = 10→30% or <2%
$\to \pi\omega'$	224	
$\omega''_{1580} \to \pi\rho$	732	-
$\to \pi\rho'$	864	
$\rho'''_{1770} \to \pi\pi$	68	-
$\to \pi\omega$	164	
$\to \pi\omega'$	112	
$\to \pi\omega''$	100	
$\omega'''_{1780} \to \pi\rho$	468	Γ_{tot}=150±70 Decays mainly to 5π's
$\to \pi\rho'$	348	
$\to \pi\rho''$	372	

(ii) The $\omega'(1260)$ decays into 3π's and is wide ($\sim$1.6 GeV).

(iii) The $\rho''(1570)$ decays mainly to 4π's and has a width of 500 MeV or greater depending on the magnitude of its non-resonant 4π decays or '$\rho\varepsilon$' decays. However the 2π channel is suppressed with a branching ratio of $\sim$12%.

(iv) The unobserved $\omega''(1580)$ decays mainly to 5π's with a large width ~ 1.6 MeV and the unobserved $\rho'''(1770)$ decays mainly to 4π's with a total width of ~ 450 MeV, its 6π branching ratio being small ($\sim 10\%$).

(v) The $\omega'''(1780)$ is also predicted to be wide, however, it decays mainly to 5π's, the 3π branching ratio being $\sim 30\%$.

The total width of the $\omega'''(1780)$ is in bad disagreement with experiment and this is the case to a lesser degree for the ρ excitations. However these are predictions of the particular vertex model we are using. We have succeeded in describing the suppression of the large-phase-space decays relative to the small-phase-space channels for every radial excitation, the predicted branching ratios being

PREDICTION	EXPT.	COMMENT
B.R. ($\rho' \rightarrow 3\pi$) $\sim 5\%$	7 ± 1 %	Form-factor analyses
B.R. ($\rho'' \rightarrow \pi\pi$) $\sim 12\%$	$10 \rightarrow 30\%$ or $< 2\%$	Both solutions equally favoured
B.R. ($\rho''' \rightarrow \pi\pi$) $\sim 15\%$	-	-
B.R. ($\omega'' \rightarrow 3\pi$) $\sim 50\%$	-	-
B.R. ($\omega''' \rightarrow 3\pi$) $\sim 30\%$	-	5π decay favoured over 3π decay

These suppressions which dramatically overpower the considerable phase-space enhancements are due to the structure of the radially excited wave-functions and the particle identifications made. We have also learned that a simple quark-pair-creation model employing a universal pair-creation strength cannot describe the narrowness of the excited states.

This narrowness of radially excited states is also becoming apparent in the $s\bar{s}$ spectrum. The $\phi(1.02)$ is much narrower than the $\rho(770)$ mainly because of the unfavourable phase-space factors ($m_K >> m_\pi$) - in fact on removing these factors the coupling constants $g_{\rho\pi\pi}$ and $g_{\phi KK}$ emerge as being comparable. Hence for the excited states there is no compelling reason to expect the ϕ excitations to be exceedingly narrow. However, the $\phi(1820)$ and $\phi(\sim 2.1)$ both have 40 MeV widths and the reported[126] $\phi(1.5)$ is considerably longer lived ($\Gamma \lesssim 5$ MeV, although this state may possibly be identified as a $^3D_1$ orbital excitation[127]).

These long lifetimes will place strong restrictions on dynamical quark models which attempt to describe 3-meson vertices - models which must incorporate a more complete understanding of pair-creation and shielding of the long-range gluon exchange forces.

Finally we examine possible indications of a vector meson at 1770 MeV, the mass of the predicted ρ'''. Bartalucci et al[124] have measured the yield of e^+e^- pairs in the Compton process $\gamma p \rightarrow p e^+ e^-$ (Fig. (5.3a)).

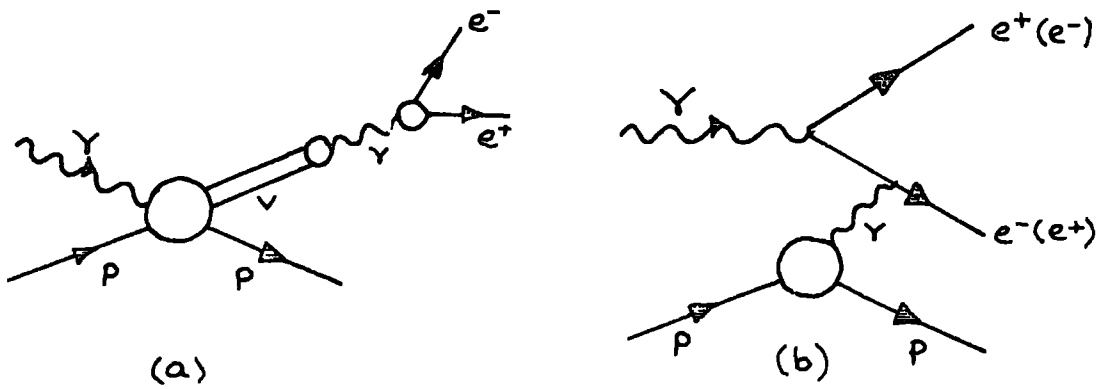

Fig. (5.3)
Compton (a) and Bethe-Heitler (b) diagrams

They parameterise the scattering amplitudes with vector dominance poles and fit the data. Because of strong Bethe-Heitler amplitudes (Fig. (5.3b)) they find it preferable to study interference plots rather than invariant mass distributions. Between 1200 and 1800 MeV they see a rich structure which they fit with 2,3 and 4 resonances.

In both the 3 and 4 resonance fits they see the $\rho(1570)$ with the expected width and also an X(1770) with a slightly narrower width. No firm conclusions can be drawn because of the excessive amount of structure in this region however we find this suggestive as the isovector $\rho'''(1770)$ would be expected to couple more strongly to e^+e^- than an ω or ϕ excitation.

We have seen that there is now experimental evidence for the following light quark radial states:

$\rho(1250)$,	$\rho(1570)$,	$\rho(1770)$ ...
-	-	$\omega(1780)$ ...
$\phi(1500)$,	$\phi(1820)$	$\phi(2100)$ ...

all of which fit well into the model we have proposed. We feel that this area of meson spectroscopy and decays will become a rigorous testing ground for phenomenological models describing the internal structure of hadrons.

Summary

We have investigated the properties of the meson wave-functions generated in Chapter Four and coupled them with a quark-pair-creation hypothesis in order to formulate a modified version of the vertex model originally proposed by Le Yaouanc et al[101]. We applied this scheme to the hadronic decays of the light-quark radially excited states and found good agreement with the observed suppression of the phase-space favoured decays.

CHAPTER 6

CONCLUSIONS

A summary of Chapters 1-3, together with the relevant conclusions, was set out in Section 3.4. We recall here only brief conclusions from the first three Chapters and then present the conclusions from Chapters Four and Five.

We have shown that the consideration of radially excited states and a q^2-dependence of f_V allows a consistent vector dominance description of new particle (ψ, ψ') radiative decays whilst the good predictions of simple vector dominance are maintained (and in some cases slightly improved). An outstanding prediction of the extended model is that the psi-nucleon total cross-section is predicted to be larger (at a centre of momentum energy of 36 GeV^2) than a recent measurement of 3.5 mb. The experimental situation was discussed in detail.

More surprisingly some of the large phase space decay rates of the excited states (e.g. $\omega'(1780) \longrightarrow 3\pi$) were predicted to be larger than the experimental values. It was this feature of radially excited states that we went on to investigate in Chapter Four and Five.

By re-identifying some of the states recently observed in e^+e^- experiments (motivated by the properties of the well established charmonium spectrum) we showed that in all flavour sectors the spectra of radial excitations can be well described by a Klein-Gordon wave equation employing a simple linear quark-antiquark potential. We went on to couple the analytical wave-functions obtained by solving the wave equation with a quark-pair-creation hypothesis to predict a number of partial decay widths of the light quark radially excited states. The suppression of the large-phase-space decays were predicted to be in good agreement with the experimental values.

We calculated the eigenvalues of the radial spectra within the context of a potential model. Motivated by indications from gauge theories that a linear potential may be responsible for the confinement of quarks within colourless hadrons, many authors had calculated the spectra of both heavy and light quark-antiquark bound systems. Our aim was to generate wave-functions describing vector-mesons and their radial excitations in order to estimate decay widths of the excited states. The criterion for relying on the wave-functions was that they be solutions to a wave equation, the eigenvalues of which describe the observed spectra of excitations.

The rapid convergence of the charmonium radial spectrum and the strong evidence for the $\rho(1250)$

suggested a light quark spectrum in which the $\omega(1780)$ is identified as a third radial excitation and an isovector partner is postulated to have a mass of about 1770 MeV (there is now evidence for this state). The $\rho(1570)$ is a second excited state and the $\rho(1250)$ the first excitation. The $s\bar{s}$ spectrum takes the form $\phi(1020)$, $\phi'(1500)$, $\phi''(1820)$, $\phi'''(2100)$, ... and it is these spectra which appeared quantitatively from the solution to a Klein-Gordon equation employing a linear quark confinement potential. The confinement potential was assumed to be linearly rising both because of hopeful indications from gauge theories and because the Ψ and its radial excitations together with the states identified above constitute spectra which are more rapidly converging than the eigenvalues of a harmonic oscillator potential.

Analysis of previous potential model treatments of the meson spectrum indicated that relativistic spin effects were unimportant compared to a relativistic treatment of the spatial quark motion and hence that a Klein-Gordon type wave equation was adequate. The Lorentz transformation properties of the $q\bar{q}$ potential were not chosen a priori. The effective potential consisted of a linear confinement potential and a constant term describing all short range effects. Scalar and vector transformation properties were considered for each term in the potential and only one combination was found to be capable of describing the spectra - the

confining potential transforming as a Lorentz scalar (multi-gluon effect) and the short range term as the fourth component of a four-vector (one-gluon exchange). The wave equation was solved analytically and the eigenvalue equation was found to describe the spectra excellently.

The quark mass parameters that emerged were reasonable and the asymptotic freedom expectations that short-range effects become less important as the bound state mass increases were borne out. The energies of the first orbitally excited states of the $u\bar{u}$ and $c\bar{c}$ systems were calculated and found to agree with experimental mass values. The recently observed spectrum of upsilon ($b\bar{b}$) stateswas well described by the eigenvalue equation with a b-quark mass of 4.35 GeV. in contrast to the poor results of previous models in this flavour sector.

Having obtained normalised, analytical wave-functions with the parameters determined by the spectral masses we used them in the quark-pair-creation model of Le Yaouanc et al.to calculate the hadronic decays of the light quark excited states. This quark model has its origins in duality diagrams and the graphical forms for vertices suggested originally by Zweig. It embodies a group-theoretical structure for vertices similar to the l-broken $SU(6)_W$ scheme but more importantly this is coupled with a quark wave-function overlap integral which should be the controlling factor in comparing hadronic decays of radially-excited states.

The T-matrix elements for the various decays of the excited states were calculated within the model using the previously obtained relativistic wave-functions and compared with the usual phenomenological T-matrix elements in order to extract the coupling constant magnitudes. The decay rates for the main hadronic modes of the excited states are then predicted using the rate for the decay $\rho \rightarrow 2\pi$ as input to fix the one unknown model parameter. The results are in good agreement with experiment - the suppression of the 3π decay mode of the $\omega(1780)$ being qualitatively predicted. The suppression of the 2π decay modes of the $\phi'(1250)$ and the $\rho''(1570)$ are also explained. The existence of as yet unobserved states is predicted and the experimental search for these states is encouraged.

APPENDIX 1

Basic Conventions

a) Units

Natural units are employed throughout in which $c = \hbar = 1$. Energies, momenta and masses expressed in eV (electron volts), keV ($= 10^3$eV), MeV ($= 10^6$eV) or GeV ($= 10^9$eV), GeV being the natural unit. Hence one natural unit of length $= \frac{\hbar c}{1\ \text{GeV}} = 1.973 \times 10^{-16}$m. A convenient alternative unit of length is the fermi

$$1f \equiv 10^{-15}\text{m} \simeq 5\ \text{GeV}^{-1} \qquad (A1,1)$$

Cross-sections are usually measured in millibarns which may be converted to GeV units using

$$\text{GeV}^{-2} = 0.3893\ \text{mb} \qquad (A1,2)$$

b) 4-vectors

Contravariant 4-vector $A^\mu = (A^0, A^1, A^2, A^3) = (A^0, \underline{A})$.

Metric $g_{\mu\nu} = (1,-1,-1,-1)$ with $A_\mu = g_{\mu\nu} A^\nu$ where repeated indices are summed

4-position $x^\mu = (x^0, \underline{x})$ where x^0 is the time and $\underline{x}$ is the spatial position.

4-momentum operator $p^\mu = i\partial^\mu = i\frac{\partial}{\partial x^\mu} = (i\frac{\partial}{\partial x^0}, -i\nabla)$

c) Dirac Matrices

We adhere to the conventions of ref. (168).

d) Decay width Formulae

The following centre of momentum phenomenological decay width expressions are used throughout (V ≡ vector, P ≡ pseudoscalar)

i) $V \rightarrow e^+e^-$

$$\Gamma(V \rightarrow e^+e^-) = f_V^2 \propto \frac{m_V}{3} \qquad (A1,3)$$

ii) $V' \rightarrow VP$

$$\Gamma(V' \rightarrow VP) = \frac{k^3 g^2_{V'VP}}{12\pi} \qquad (A1,4)$$

iii) $V \rightarrow PP$

$$\Gamma(V \rightarrow PP) = \frac{k^3 g^2_{VPP}}{6\pi} \qquad (A1,5)$$

where k is the momentum of a final state particle.

APPENDIX 2

Meson SU(6) wave-functions

The meson superscript refers to the particle's charge, while the subscript represents the z-component of its spin.

0^- mesons

Ptcle.	Combination
$\eta_o^{o\prime}$	$\frac{1}{\sqrt{6}}(u_+\bar{u}_- - u_-\bar{u}_+ + d_+\bar{d}_- - d_-\bar{d}_+ + s_+\bar{s}_- - s_-\bar{s}_+)$
η_o^o	$\frac{1}{\sqrt{12}}(u_+\bar{u}_- - u_-\bar{u}_+ + d_+\bar{d}_- - d_-\bar{d}_+ - s_+\bar{s}_- + s_-\bar{s}_+)$
π_o^+	$\frac{1}{\sqrt{2}}(u_+\bar{d}_- - u_-\bar{d}_+)$
π_o^o	$\frac{1}{2}(u_+\bar{u}_- - u_-\bar{u}_+ - d_+\bar{d}_- + d_-\bar{d}_+)$
π_o^-	$\frac{1}{\sqrt{2}}(d_+\bar{u}_- - d_-\bar{u}_+)$
K_o^+	$\frac{1}{\sqrt{2}}(u_+\bar{s}_- - u_-\bar{s}_+)$
K_o^o	$\frac{1}{\sqrt{2}}(d_+\bar{s}_- - d_-\bar{s}_+)$
$\bar{K}_o^o$	$\frac{1}{\sqrt{2}}(s_+\bar{d}_- - s_-\bar{d}_+)$
K_o^-	$\frac{1}{\sqrt{2}}(s_+\bar{u}_- - s_-\bar{u}_+)$

1^- mesons

Ptcle.	Combination
$\phi^0_{\pm 1}$	$s_{+,-}\ \bar{s}_{+,-}$
ϕ^0_0	$\frac{1}{\sqrt{2}}(s_+\bar{s}_- + s_-\bar{s}_+)$
$\omega^0_{\pm 1}$	$\frac{1}{\sqrt{2}}(u_{+,-}\ \bar{u}_{+,-} + d_{+,-}\ \bar{d}_{+,-})$
ω^0_0	$\frac{1}{2}(u_+\bar{u}_- + u_-\bar{u}_+ + d_+\bar{d}_- + d_-\bar{d}_+)$
$\rho^+_{\pm 1}$	$u_{+,-}\ \bar{d}_{+,-}$
ρ^+_0	$\frac{1}{\sqrt{2}}(u_+\bar{d}_- + u_-\bar{d}_+)$
$\rho^0_{\pm 1}$	$\frac{1}{2}(u_{+,-}\ \bar{u}_{+,-} - d_{+,-}\ \bar{d}_{+,-})$
ρ^0_0	$\frac{1}{2}(u_+\bar{u}_- + u_-\bar{u}_+ - d_+\bar{d}_- - d_-\bar{d}_+)$
$\rho^-_{\pm 1}$	$d_{+,-}\ \bar{u}_{+,-}$
ρ^-_0	$\frac{1}{\sqrt{2}}(d_+\bar{u}_- + d_-\bar{u}_+)$
$K^{*+}_{\pm 1}$	$u_{+,-}\ \bar{s}_{+,-}$
K^{*+}_0	$\frac{1}{\sqrt{2}}(u_+\bar{s}_- + u_-\bar{s}_+)$
$K^{*0}_{\pm 1}$	$d_{+,-}\ s_{+,-}$
K^{*0}_0	$\frac{1}{\sqrt{2}}(d_+\bar{s}_- + d_-\bar{s}_+)$
$\overline{K^{*0}_{\pm 1}}$	$s_{+,-}\ \bar{d}_{+,-}$
$\overline{K^{*0}_0}$	$\frac{1}{\sqrt{2}}(s_+\bar{d}_- + s_-\bar{d}_+)$
$K^{*-}_{\pm 1}$	$s_{+,-}\ \bar{u}_{+,-}$
K^{*-}_0	$\frac{1}{\sqrt{2}}(s_+\bar{u}_- + s_-\bar{u}_+)$

APPENDIX 3

Spatial Overlap Integral

Equation (5.27) is the expression to be simplified and reads:

$$I_m(A,BC) = \delta^3(\underline{k}_C + \underline{k}_B)\int_{-\infty}^{\infty} d\underline{q}\, d\underline{x}_A\, d\underline{x}_B\, d\underline{x}_C\, \mathcal{Y}_l^m(\underline{q})\, \psi_A(\underline{x}_A)\, \psi_B^*(\underline{x}_B) \times \psi_C^*(\underline{x}_C)\, e^{i\underline{q}\cdot(\underline{x}_B - \underline{x}_A - \underline{x}_C)}\, e^{i\underline{k}_B\cdot\underline{x}_A} \qquad (A3,1)$$

where

$$\mathcal{Y}_l^m(\underline{q}) = q\, K_m\, P_l^m(\cos\theta_q)\, e^{im\phi_q} \qquad (A3,2)$$

and

$$K_m = (-1)^m \left[\frac{3}{4\pi}\,\frac{(l-m)!}{(l+m)!}\right]^{1/2} \qquad (A3,3)$$

The angular integrals can be performed by making use of the following relationships involving Bessel functions[1]

$$\int_0^{2\pi} e^{-ipx\sin\theta_x \sin\theta_p \cos(\phi_x - \phi_p)}\, e^{im\phi_x}\, d\phi_x = 2\pi\, i^m\, e^{im\phi_p}\, J_m(px\sin\theta_x \sin\theta_p) \qquad (A3,4)$$

and

$$\int_0^{\pi} e^{-ipx\cos\theta_x\cos\theta_p}\, J_m(px\sin\theta_x\sin\theta_p)\, P_l^m(\cos\theta_x)\sin\theta_x\, d\theta_x = -(-i)^{l+m}\sqrt{\frac{2\pi}{px}}\, P_l^m(\cos\theta_p)\, J_{l+\frac{1}{2}}(px) \qquad (A3,5)$$

(i) $\underline{x}_C$ integral

The $\underline{x}_C$ integral from (A3,1) is

$$\int_{-\infty}^{\infty} d\underline{x}_C\, \psi_C^*(\underline{x}_C)\, e^{-i\underline{q}\cdot\underline{x}_C} \qquad (A3,6)$$

We are dealing with L = 0 mesons only and ψ_c^* is a function of $|\underline{x}_c|$ only. Writing

$$\underline{q}\cdot\underline{x}_c = q x_c(\sin\theta_q \sin\theta_{x_c}\cos(\phi_{x_c}-\phi_q) + \cos\theta_{x_c}\cos\theta_q) \qquad (A3,7)$$

and using (A3,4), (A3,5) with L = m = 0 we obtain

$$\int_{-\infty}^{\infty} d\underline{x}_c\, \psi_c^*(\underline{x}_c)\, e^{-i\underline{q}\cdot\underline{x}_c} = -\frac{(2\pi)^{3/2}}{\sqrt{q}}\int_0^{\infty} J_{1/2}(qx_c)\psi_c^*(x_c)x_c^{3/2}dx_c \qquad (A3,8)$$

(ii) <u>$\underline{x}_B$ integral</u>

Similarly we obtain

$$\int_{-\infty}^{\infty} d\underline{x}_B\, \psi_B^*(\underline{x}_B)\, e^{-i\underline{q}\cdot\underline{x}_B} = -\frac{(2\pi)^{1/2}}{\sqrt{q}}\int_0^{\infty} J_{1/2}(qx_B)\psi_B^*(x_B)x_B^{3/2}dx_B \qquad (A3,9)$$

(iii) <u>$\underline{q}$ integral</u>

From (A3,1) we must evaluate

$$\int d\underline{q}\; Y_1^m(\underline{q})\, e^{-i\underline{x}_A\cdot\underline{q}}$$

$$= \int q^3 dq \sin\theta_q\, d\theta_q\, K_m P_1^m(\cos\theta_q)\, e^{im\phi_q} \times e^{-ix_A q(\sin\theta_q\sin\theta_{x_A}\cos(\phi_{x_A}-\phi_q)+\cos\theta_{x_A}\cos\theta_q)} \qquad (A3,10)$$

and using (A3,4), (A3,5) we obtain

$$\int d\underline{q}\; Y_1^m(\underline{q})\, e^{-i\underline{x}_A\cdot\underline{q}} = (2\pi)^{3/2} i\, \frac{Y_1^m(\underline{x}_A)}{x_A^{3/2}}\int_0^{\infty} q^{3/2}\, dq\, J_{3/2}(qx_A) \qquad (A3,11)$$

(iv) <u>$\underline{x}_A$ integral</u>

From (A3,1) and (A3,11) we have

$$\int d\underline{x}_A\, \psi_A(x_A)\, e^{i\underline{k}_B\cdot\underline{x}_A} K_m e^{im\phi_{x_A}} P_1^m(\cos\theta_{x_A}) \qquad (A3,12)$$

and using again (A3,4) and (A3,5) we get

$$(A3,12) = (2\pi)^{3/2} \iota \int_0^\infty \frac{x_A}{\sqrt{k_B}} dx_A \psi_A(x_A) J_{\frac{3}{2}}(k_B x_A) K_m e^{\iota m \phi_{-k_B}} P_l^m(\cos\theta_{-k_B}) \quad (A3,13)$$

Finally combining (A3,1), (A3,8), (A3,9), (A3,11) and (A3,13)

$$I_m(A,Bc) = \delta^3(\underline{k}_B + \underline{k}_c)(\underline{k}_B \cdot \underline{\varepsilon}(m)) \frac{2\pi}{8} \sqrt{\frac{3}{2}} \frac{1}{k_B^{3/2}} \left(\begin{matrix} \text{spatial} \\ \text{integral} \end{matrix} \right) \quad (A3,14)$$

where the dimensionless spatial integral takes the form

$$\int_0^\infty dx_A\, x_A\, \psi_A(x_A)\, J_{\frac{3}{2}}(k_B x_A) \int_0^\infty q^{3/2} dq\, J_{\frac{3}{2}}(q x_A) \int_0^\infty x_c^{3/2} dx_c\, \psi_c^*(x_c)$$

$$\times J_{\frac{1}{2}}(q x_c) \int_0^\infty x_B^{3/2} dx_B\, \psi_B^*(x_B)\, J_{\frac{1}{2}}(q x_B) \quad (A3,15)$$

and it is this expression which is calculated numerically on a computer for each particular vertex considered.

REFERENCES

1. see for example "Methods of Theoretical Physics", P. M. Morse and H. Feshbach, McGraw-Hill (1953)
2. U. S. Kim and M. E. Noz, Phys. Rev. D12 (1975) 129
3. M. Krasemann and M. Krammer, Phys. Lett. 70B (1977) 457
4. M. Gell-Mann, Phys. Lett. 8 (1964) 214
5. G. Zweig, Cern Reports TH401 and 402 (1964)
6. F. Gursey and L. A. Radicati, Phys. Rev. Lett. 13 (1964) 173
7. see for example R. H. Dalitz and M. Horgan, Nucl. Phys. B66 (1973) 135
8. see for example P. D. B. Collins, An Introduction to Regge theory and high energy physics. Cambridge Univ. Press (1977)
9. R. Dolen et al., Phys. Rev. 166 (1968) 1768
10. H. Harari, Phys. Rev. Lett. 22 (1969) 562
11. J. L. Rosner, Phys. Rev. Lett. 22 (1969) 689
12. R. L. Jaffe, Phys. Rev. D15 (1977) 267, 281
13. H. Harari, Phys. Rev. Lett. 20 (1968) 1385
14. R. Van Royen and V. F. Weisskopf, Nuovo Cim. 50A (1967) 617
15. M. Beg, B. W. Lee and A. Pais, Phys. Rev. Lett. 13 (1964) 514
16. E. Allen, Phys. Lett. 57B (1975) 263
17. E. E. Salpeter and H. A. Bethe, Phys. Rev. 82 (1951) 1232
18. M. Bohm et al., Nucl. Phys. B51 (1973) 397

19. P. J. Walters et al., J. Phys. A7 (1974) 1681

20. M. Bohm et al., Cern Preprint 1715 (1973)

21. O. W. Greenberg, Phys. Rev. Lett. 13 (1964) 598

22. R. P. Feynman et al., Phys. Rev. D3 (1971) 2706

23. B. J. Bjorken and S. L. Glashow, Phys. Lett. 11 (1964) 225

24. S. L. Glashow et al., Phys. Rev. D2 (1970) 1285

25. W. R. Innes et al., Phys. Rev. Lett. 39 (1977) 1240

26. M. Gell-Mann, in Elementary Particle Physics, Springer-Verlag, Vienna (1972), p.733

27. S. D. Jackson in Proceedings of Summer Institute on Particle Physics, SIAC (1976)

28. H. D. Politzer, Phys. Rev. Lett. 30 (1973) 1346

29. D. Gross and F. Wilczek, Phys. Rev. Lett. 30 (1973) 1343

30. E. Eichten et al., Phys. Rev. Lett. 34 (1976) 369

31. J. Kogut and L. Susskind, Phys. Rev. D11 (1975) 395

32. F. E. Close, Partons and Quarks - Daresbury Lecture Note Series No. 12 DNPL/R31 (1973)

33. F. J. Gilman, Phys. Rep. 4C (1972)

34. J. D. Bjorken, Phys. Rev. 179 (1969) 1547

35. F. E. Close in Proceedings of the Scottish Universities Summer School in Physics, St. Andrews (1976)

36. M. L. Perl in Proceedings of the International Symposium on Lepton and Photon Interactions at High Energies, Hamburg (1977)

37. F. E. Close, Invited Talk at International Symposium on Storage Ring Physics,

38. M. Greco, Nucl. Phys. B 63 (1973) 398

39. M. Gell-Mann and F. Zachariasen, Phys. Rev. 124 (1961) 953

40. J. J. Sakurai, Ann. Phys. 11 (1960) 1

41. P. Kroll and S. Meyer, Lett. Al Nuovo Cim. 5 (1972) 889

42. C. F. Cho and J. J. Sakurai, Phys. Rev. D2 (1970) 517

43. R. Anderson et al., Phys. Rev. D1 (1970) 27

44. K. Gottfried in Proceedings of the International Symposium on Lepton and Photon Interactions at High Energies, Hamburg, 1977

45. A. Bradley and F. D. Gault, Nucl. Phys. B128 (1977) 313

46. V. Barger and R. J. N. Phillips, Phys. Lett. 58B (1975) 433

47. R. L. Thews, Phys. Lett. 65B (1976) 343

48. D. P. Roy, Phys. Lett. 63B (1976) 324

49. J. Pumplin and W. Repko, Phys. Rev. D12 (1975) 1376

50. D. Sivers et al., Phys. Rev. D13 (1975) 1234

51. T. Bauer and D. R. Yennie, Phys. Lett. 60B (1976) 165

52. A. Silverman in Proceedings of the International Symposium on Lepton and Photon Interactions at High Energies, Stanford, 1975

53. T. Bauer and D. R. Yennie, Phys. Lett. 60B (1976) 169

54. A. Bramon and M. Greco, Nuovo Cim. 14A (1973) 323

55. M. Chaichian and R. Kogerler, Phys. Lett. 63B (1976) 75

56. J. F. Bolzan et al, Phys. Rev. D14 (1976) 1920

57. H. F. Jones and B. Mathur, J. Phys. G. 3(1977) 287

58. R. L. Heinemann, Nuovo Cim. 39A (1977) 461

59. L. Clavelli and S. Nussinov, Phys. Rev. D13 (1976) 125

60. A. Bradley, Durham University Preprint 80084 (1977)

61. G. Cosme et al, Phys. Lett. 67B (1977) 231

62. B. Esposito et al., Phys. Lett. 68B (1977) 389

63. C. Bacci et al., Phys. Lett. 68B (1977) 393

64. G. Barbiellini et al., Phys. Lett. 68B (1977) 397

65. Particle Data Group, Rev. Mod. Phys. 48 (1975) 51

66. V. S. Mathur et al., Phys. Rev. D11 (1975) 2572

67. H. Harari, Phys. Lett. 60B (1975) 172

68. H. Fritzsh and J. D. Jackson, Phys. Lett. 66B (1977) 365

69. J. Randa and A. Donnachie, Nucl. Phys. B125 (1977) 303

70. W. Braunschweig et al., DESY report (1976)

71. W. Bartel et al., Phys. Lett. 66B (1977) 489

72. W. Bartel et al., Phys. Lett. 64B (1976) 483

73. W. Tannenbaum et al., Phys. Rev. Lett. 36 (1976) 402

74. B. H. Wiik and G. Wolf, DESY report (1977)

75. R. Aviv et al., Phys. Rev. D12 (1975) 2862

76. J. S. Whitaker et al., Phys. Rev. Lett. 37 (1976) 1596

77. E. B. Hughes et al., Phys. Rev. Lett. 36 (1976) 76

78. R. L. Thews, Phys. Rev. D14 (1976) 3021

79. G. L. Gounaris, Phys. Lett. 63B (1976) 307

80. G. Parrour et al., Phys. Lett. 63B (1976) 362

81. P. J. O'Donnell, Phys. Rev. Lett. 36 (1976) 177

82. M. Davier, Proceedings of the XVI International Conference on High Energy Physics (NAL, Batavia, Ill., 1973) Vol. I, p.104

83. R. C. Johnson et al., Phys. Lett. 63B (1976) 95

84. G. Cosme et al., Phys. Lett. 63B (1976) 352

85. D. Benaksas et al., Phys. Lett. 42B (1972) 511

86. G. Gobbi et al., Phys. Rev. Lett. 33 (1974) 1450

87. G. Alexander et al., Phys. Lett. 57B (1975) 487

88. W. C. Carithers et al., Phys. Rev. Lett. 35 (1975) 349

89. D. E. Andrews et al., Phys. Rev. Lett. 38(1977) 198

90. A. D. Martin and M. R. Pennington, Cern preprint to be published in Am. Phys.

91. H. T. Nieh, Phys. Lett. 38B (1971) 100

92. D. R. Yennie, Rev. Mod. Phys. 47 (1975) 311

93. H. T. Nieh, Phys. Rev. D1 (1970) 3161

94. J. D. Bjorken, Phys. Rev. 179 (1969) 1547

95. H. Kendall in Proceedings of the International Symposium on electron and photon interactions at high energies, Cornell (1971)

96. H. Harari in Proceedings of the International Symposium on electron and photon interactions at high energies, Cornell (1971)

97. R. Spital and D. R. Yennie, Phys. Rev. D9(1974) 126

98. H. Cheng and T. T. Wu, Phys. Rev. 183 (1969) 1324

99. R. Talman in Proceedings of the International Symposium on electron and photon interactions at high energies, Bonn (1973)

100. L. Stodolsky, Phys. Rev. Lett. 18 (1967) 135

101. K. Gottfried and D. R. Yennie, Phys. Rev. 182 (1969) 1595

102. K. S. Kölbig and B. Margolis, Nucl. Phys. B6 (1968) 85

103. S. J. Brodsky and J. Pumplin, Phys. Rev. 182 (1969) 1794

104. S. J. Brodsky et al., Phys. Rev. D6 (1972) 177

105. X. Y. Pham, LPTPE Paris preprint (1976)

106. See for example: P. D. B. Collins, An Introduction to Regge Theory and High Energy Physics, Cambridge University Press (1972) p.49

107. R. L. Anderson et al., Phys. Rev. Lett. 38 (1977) 263

108. L. Clavelli and S. Nussinov, Phys. Rev. D13 (1976) 125

109. M. Camerini et al., Phys. Rev. Lett. 35 (1975) 483

110. T. Nash et al., Phys. Rev. Lett. 36 (1976) 1233

111. see for example D. W. G. S. Leith in Hadronic Interactions of Electrons and Photons, Academic Press (1971) p.200

112. H. Alvensleben et al., Phys. Rev. Lett. 24 (1970) 792

113. E. H. Thorndike, Phys. Rev. D14 (1976) 3059

114. J. Layssac and F. M. Renard, Phys. Lett. 67B (1977) 446

115. G. Barbarino et al., NCL 3 (1972) 689

116. W. Lee, in Proceedings of the International Symposium on electron and photon interactions at high energies, Stanford (1975)

117. P. Frenkiel et al., NP B47 (1972) 61

118. J. Ballam et al., NP B76 (1974) 375

119. G. J. Gournais & J. J. Sakurai PRL 21 (1968) 244

120. T. N. Pham and Tran. N. Truong, PR D14 (1976) 185

121. B. Costa de Beauregard et al., PL 67B (1977) 213

122. M. Conversi et al., PL 52B (1974) 493

123. N. M. Budnev et al., PL 70B (1977) 365

124. S. Bartalucci et al., DESY/Frascati Preprint (1977)

125. R. Bernabei et al., Frascati Report LNF-76/64(P) (1976)

126. G. Capon, Invited Talk to Budapest Conf. on Particle Physics, Budapest (1977)

127. M. Greco, Phys. Lett. 70B (1977) 441

128. C. D. Froggatt & J. L. Petersen, Nucl. Phys. B129 (1977) 89

129. A. D. Martin and M. R. Pennington, Cern Preprint TH.2353 (1977)

130. V. Luth at the Frühjahrstagung der Deutschen Physikalischen Gesellschaft, Aachen (1977)

131. A. de Rújula et al., Phys. Rev. Lett. 37 (1976) 398

132. Nils A. Tornqvist, Phys. Lett. 69B 193

133. A. De Rújula et al., Phys. Rev. Lett. 38 (1977) 317

134. F. E. Close, Nature 266 (1977) 301

135. A. Le Yaouanc et al., Phys. Lett. 71B (1977) 397

136. A. Le Yaouanc et al., Phys. Lett. 72B (1977) 57

137. J. F. Gunion and L. F. Li, Phys. Rev. D12 (1975) 3583

138. B. J. Harrington et al., Phys. Rev. Lett. 34 (1975) 168 and Phys. Rev. Lett. 34 (1975) 706

139. L. Eichten et al., Phys. Rev. Lett. 34 (1975) 369

140. J. S. Kang and H. J. Schnitzer, Phys. Rev. D12 (1975) 841

141. E. P. Tyron, Phys. Rev. Lett. 36 (1976) 455

142. A. B. Henriques et al., Phys. Lett. 64B (1976) 85

143. K. S. Jhung et al., Phys. Rev. D12 (1975) 1999

144. H. W. Crater, Phys. Rev. D16 (1977) 1580

145. R. Barbieri et al., Nucl. Phys. B105 (1976) 125

146. P. A. Rapidis et al., Phys. Rev. Lett. 39 (1977) 526, 974(E)

147. see for example, Y. L. Luke, Mathematical Functions and their approximations (Academic Press 1975) p.312

148. X. Y. Pham and J. M. Richard, Phys. Lett. 70B (1977) 370

149. E. Eichten and K. Gottfried, Phys. Lett. 66B (1977) 286

150. D. R. Yennie, Phys. Rev. Lett. 34 (1975) 239

151. See references contained in Ref. (25)

152. E. B. Dally et al., Phys. Rev. Lett. 39 (1977) 1176

153. G. Zweig, Cern Report No. TH-402 (1964) (unpublished)

154. L. Micu, Nucl. Phys. B10 (1969) 521

155. H. J. Lipkin and S. Meshkov, Phys. Rev. Lett. 14 (1965) 670

156. R. Carlitz and M. Kislinger, Phys. Rev. D2 (1970) 336

157. E. W. Colglazier and J. L. Rosner, Nucl. Phys. B27 (1971) 349

158. R. Dashen and M. Gell-Mann, Phys. Lett. 17 (1965) 142, 145

159. H. J. Melosh, Ph.D. Thesis, Cal. Tech. (1973) (unpublished)

160. A. N. Mitra and M. Ross, Phys. Rev. 158 (1967) 1630

161. A. Le Yaouanc et al., Phys. Rev. D8 (1973) 2223

162. A. J. G. Hey et al., Nucl. Phys. B61 (1973) 205

163. J. Rosner and W. Petersen, Phys. Rev. D6 (1972) 820

164. W. B. Kaufmann and R. J. Jacob, Phys. Rev. D10 (1974) 1051

165. R. Barbieri et al., Phys. Lett. 56B (1975) 477

166. M. Chaichian and R. Kögerler, Phys. Lett. 63B (1976) 75

167. see for example K. Nishijimi, Fundamental Particles (W. A. Benjamin 1964) p.133

168. J. D. Bjorken and S. D. Drell, "Relativistic Quantum Mechanics", McGraw Hill, New York (1964)

AN EXPERIMENTAL AND ANALYTICAL STUDY

OF

HYPERBOLIC PARABOLOID SANDWICH PANELS

by

D. L. Collins

Thesis submitted for the degree of Doctor of Philosophy in the Faculty of Science, University of Durham.

Department of Engineering Science,
University of Durham.

November 1977.

Dedicated to my parents.

CONTENTS Page

Acknowledgements

I would like to thank my supervisor, Dr. G. M. Parton for his guidance and assistance in both the practical and theoretical work.

Thanks must be given also to Dr. P. Bettess, Lecturer at the Department of Civil Engineering, University College of Swansea, for his help and suggestions about the numerical analysis, and to the British Ship Research Association, Wallsend, for providing the original finite element programme.

For their contribution to the experimental work I thank the Technicians of the Engineering Science Department, especially Mr. F. Emery, who assisted greatly in the fabrication of the panels.

SUMMARY

The finite element method was used to analyse several hyperbolic paraboloid sandwich shells, and a sandwich plate. The elements are developments of the isoparametric finite element allowing for transverse shear, and for the differing material and structural properties associated with the layers of a sandwich panel.

The results of the numerical analysis were compared with other flat sandwich panel results with close agreement for the stress resultants, and excellent agreement for the displacements.

Experimental data for the displacements of the hypar sandwich shells was compared with the numerical analysis with good agreement, provided that the boundary conditions and loading are well defined. Poor agreement results when the panels exhibit non linear effects caused by the visco-elastic behaviour of the materials.

The introduction of curvature into the sandwich panel produces marked reductions in the deflections and moments, and an increase of the membrane effects. The results indicate the necessity of including bending effects, and the importance of the edge conditions in determining the stress distribution within these shells.

1. INTRODUCTION

The sandwich construction used for the panels presented in this work follows the definition of Plantema (54) of a "three layer type of construction, consisting of two thin sheets of high-strength material between which a thick layer of low average strength and density is sandwiched. The two thin sheets are called the faces, and the intermediate layer is the core of the sandwich."

This thesis presents the experimental and numerical analysis of such panels when they are formed into doubly curved shells, hyperbolic paraboloids (hypars).

Previous workers (8, 43, 51) have considered the approximation to a doubly curved surface by a series of interconnected flat plates, and analysed these sandwich structures using flat finite elements.

The choice of a doubly curved shell was made because the curvature causes the loading to be distributed to the edges of the shell, and reduces the displacements, which with the materials used are more pronounced than with conventional materials.

A hyperbolic paraboloid was chosen because its geometric definition is the most simple second order polynomial is x and y, and by choosing its form as that of a warped rectangle its generators are all straight lines, simplifying the construction of such shells.

The advantages of sandwich construction are that there is a high degree of rigidity for a given dead weight, compared to conventional constructional materials; construction is usually easy; the materials have good thermal and acoustic properties; structurally sandwich panels can be efficient, as demonstrated by their applications which have been mainly in the aircraft industry.

One of the objectives of the research carried out by members of the Engineering Department is to demonstrate the applicability of sandwich panels to structural forms other than those used by the specialised aircraft industry.

The inherent strength of a sandwich panel is due to the thin faces acting as the outer layers of a beam or plate. In this application the additional twist given to the plate producing the shells gives added strength because of the new geometry.

The disadvantages associated with sandwich panels are due to the materials and the bonding between the layers. It is important if the sandwich is to work efficiently, that the bonding between the faces and the core is such that the faces do act as outer layers of the shell.

In addition, the panels exhibit visco-elastic behaviour. Thus the displacements can be considered as those due to an initial elastic response, followed by a time dependent response which increases, depending upon the magnitude of the load.

The work presented in this thesis is concerned with the elastic response of the structures.

The materials used to construct the hypars were glass reinforced polyester for the faces, and polyurethane for the core.

The face material was found to have a large variation in Young's modulus, which imposes a limitation on the numerical analysis in that the properties associated with an element were assumed to be constant throughout the shell.

The polyurethane core was not examined, as Elliott and previous workers (20, 5, 8, 43, 51) have tested this material. Following their work, an orthotropic definition of material properties is used.

The analysis of hypar shells has been treated differently by a number of authors (10, 11, 12, 14, 22, 26, 27, 37, 38, 46). All the references indicate the weakness of a membrane solution expressed by Tottenham (60).

The classical solution depends upon defining a stress function. The stress function substituted into the equations of equilibrium and compatability leads to a linear partial differential equation of the second order. On substituting the surface definition of the hypar the resulting characteristic equation of the equilibrium of the hypar relates the stress function to the loads applied to the structure.

The solution for the membrane stress resultants is such that the normal stress resultants Nx and Ny can be chosen such that any arbitrary load, a function of y for Nx and x for Ny can be chosen such that they satisfy equilibrium.

These additional loads $Nx = f(y)$, $Ny = f(x)$ applying equally to both boundaries cannot, in general, reduce the normal stresses to zero at the edges.

This result led researchers to a more comprehensive solution from a non-linear analysis or bending theory (10, 14, 26, 27, 37). The conclusions of the work of Hadid (26, 27) and the other researchers was that the bending stresses in shallow hypars were significant, and that the membrane analysis is only adequate away from the boundaries.

The different analytical methods which incorporate a bending analysis have been Finite Difference (6), Integral methods (26, 27), Finite Element (11, 60, 61), and lumped parameter (47). The integral method used by Hadid and Tottenham (26, 27) did not include the transverse shear which would be necessary in the analysis of a sandwich hypar.

Mohraz' lumped parameter method (47) which idealizes the shell structure into a series of rigid bars and a deformable node, again does not include the transverse shear strain. The finite difference method of Beg (6) did include the transverse shear, but as it is possible to separate membrane and flexure for a sandwich shell, it was felt the isoparametric finite element of Ahmad (2) could be developed to provide a general sandwich shell analysis capability.

The choice of the Ahmad (2) isoparametric element was a logical extension to the finite elements developed by Parton and Bettess (51, 8). These displacement elements use a kinematic hypothesis similar to the Ahmad shell element. In the Ahmad element the shell is considered as a series of membranes (29), and the strain energy is the summation of the strain energy as each membrane slides relative to its neighbours.

The fact that Ahmad's formulation depends upon the shear strains caused Irons and Razzaque (34) to develop the thin shell "semi-loof" element. This element imposes zero transverse shear at the integration points, and so would be inapplicable for a sandwich shell where the transverse shear effects are large.

Its superior performance in the analysis of thin shells could, perhaps, be adopted in the formulation of the face contributions for a sandwich element, although problems would exist due to the rotations along the edges of the element.

The methods used to analyse sandwich structures have been displacement finite elements (8, 51, 43, 47, 44 41, 1), mixed models (43) and hybrid models (4, 43, 16).

Mawenya and Davies use an isoparametric, displacement finite element to analyse sandwich plates, incorporating differing material properties for a layer, and allowing for local deformations within a layer. They assume that the normal rotations are independent of lateral displacement,

but can vary from layer to layer. The isoparametric element developed in this thesis does not allow for local deformations within a layer, but it is shown in Chapter 3 that this facility could easily be incorporated. Also, as the element is a shell element, the normal rotations are assumed to be dependent upon the lateral displacement as well as normal displacements, and the geometric form of the reference surface of element takes the more general form, including the variation with respect to the thickness co-ordinate.

The papers of Zienkiewicz (64), Pawsey (53) and others (15, 34, 29, 17, 49, 52, 57) indicate the improvement for an isoparametric thin shell element if reduced Gaussian integration is used to evaluate the strain energy contributions for the differing displacement nodes.

This is explained by the displacement function imposing an unrealistic form upon the shear deformations. In view of the arguments put forward by Pawsey, Chapter 4 includes a survey of the effect the different orders of integration have upon the sandwich shell element developed for this application.

The final choice for the quadrilateral element was a 2 x 2 Gauss rule in each layer of the sandwich.

An alternative approach to reduced integration is made by Takemoto and Cook (57). They add an extra node in the centre of an element which has the effect of allowing the displacement function the freedom to accommodate zero energy deformation modes, and overcome some of the difficulty when curved elements are used.

Summarising, this thesis presents experimental results for vertical displacements in several sandwich hyperbolic paraboloids. An account is given of the difficulties in the fabrication of these panels. The numerical analysis of these shells is performed using isoparametric displacement shell elements developed to account for the differing material properties between

the layers of the sandwich, and from the assumption that flexure and membrane effects can be separated.

A survey of differing orders of integration within the sandwich finite elements is presented, although no theoretical justification is given for the order used.

2. THEORY

The mathematical basis of the displacement finite element method resembles the Ritz method. In the Ritz method one set of functions describes the displacement field in the entire continuum. The finite element method assumes individual displacement fields for each element and the internal displacements are uniquely defined by the nodal point displacements. Thus the entire displacement field is assumed to consist of large numbers of piecewise continuous fields, each one being over an element.

2.1 Element Characteristics

Consider a typical element and define the displacement at any point within the element as

$$\{f\} = [N]\{\delta_e\} \qquad 2.1.1$$

$[N]$ are shape functions taking a value of unity at a preferred node and zero at other nodal points.

$\{\delta_e\}$ is the displacement vector for the displacement at the nodal points of an element. The strains are defined as

$$\{\epsilon\} = [B]\{\delta\}_e \qquad 2.1.2$$

Where $[B]$ is derived from equation 2.1.1 and the stresses, assuming elastic behaviour, are defined as

$$\{\sigma\} = [D](\{\epsilon\} - \{\epsilon_0\}) + \{\sigma_0\}$$

Where $\{\epsilon_0\}$ are any initial strains and $\{\sigma_0\}$ are any initial stresses, $[D]$ is the elasticity matrix containing the material properties.

The equivalent nodal forces are $\{F\}_e$ which are statically equivalent to the boundary stresses and distributed loads on an element. $\{p\}$ are the distributed loads acting on a unit volume in an element.

To make the nodal forces statically equivalent to the boundary stress resultants and loads an arbitrary nodal displacement is imposed and the internal and external work done are equated. The work done by the nodal forces for a displacement of $d\{\delta\}_e$ at the nodes is

$$(d\{\delta\}_e)^T . \{F\}_e \qquad 2.1.4$$

The internal work per unit volume done by the stresses and distributed loads is

$$d\{\epsilon\}^T\{\sigma\} - d\{f\}^T\{p\} \qquad 2.1.5$$

Equating the external and internal work:-

$$(d\{\delta\}_e)^T\{F\}_e = (d\{\delta\}_e)^T\int[B]^T\{\sigma\}dVol - \int[N]^T\{p\}dVol \qquad 2.1.6$$

Substituting equations 2.1.3 and 2.1.2:-

$$\{F\}_e = \left(\int[B]^T[D][B]dVol\right)\{\delta\}_e - \int[B]^T[D]\{\epsilon_o\}dVol + \int[B]^T\{\sigma_o\}dVol - \int[N]^T\{p\}dVol \qquad 2.1.7$$

The first term of equation 2.1.7 contains the stiffness matrix:-

$$[k]_e = \int[B]^T[D][B]dVol \qquad 2.1.8$$

The nodal forces due to distributed loads are:-

$$\{F\}_{ep} = -\int[N]^T\{p\}dVol \qquad 2.1.9$$

Those due to any initial strains:-

$$\{F\}_{e\epsilon_o} = -\int[B]^T[D]\{\epsilon_o\}dVol \qquad 2.1.10$$

and due to any initial stress:-

$$\{F\}_{e\sigma_o} = \int[B]^T\{\sigma_o\}dVol \qquad 2.1.11$$

In addition to the above terms there are terms to describe the concentrated forces at a node:

$$\{R\} = \begin{Bmatrix} R_1 \\ R_2 \\ R_3 \\ \vdots \\ R_N \end{Bmatrix}$$

2.1.12

and if the element is at a boundary and the boundary is subject to a distributed load of $\{q\}$ per unit area, then the term describing the loading on the nodes of this boundary element $\{\bar{F}\}_{eb}$ need to be added.

$$\{F\}_{eb} = -\int [N]^T \{q\}\, dAREA$$

This results in the equation

$$\{F\}_e = [k_e]\{\delta\}_e + \{F\}_{ee_0} + \{F\}_{e\sigma_0} + \{F\}_{eb} \qquad 2.1.14$$

where $\{F\}_e$ are the equivalent nodal forces.

2.2 Characteristics of the whole structure

The inter element forces must be in equilibrium with each other and need not be included in a virtual work expression. The sum of the contributions of internal work for all elements may be equated to the external virtual work done by the Applied loads to the structure. Considering a displacement of $d\{\delta\}$ acting on all the nodes of the structure the virtual work done is:-

$$\int \delta\{\epsilon\}^T\{\sigma\}\, dVol - \left[d\{\delta\}^T R + \int d\{f\}^T\{p\}\, dVol + \int d\{f\}^T\{q\}\, dAREA \right] = 0.$$

2.2.1

Equation 2.2.1 includes the effects of initial strains and stresses by the constitutive relation of equation 2.1.3.

Simplifying the terms the equation becomes

$$[k]\{\delta\} + \{F\}_p + \{F\}_b + \{F\}_{\epsilon_0} + \{F\}_{\sigma_0} - R = 0. \qquad 2.2.2$$

where each of the terms of equation 2.2.2 are now integrals over the whole region and not just one element.

The First term in equation 2.2.1 is the strain energy, U , of the structure and the second the potential Energy of the external loads W , and the equation 2.2.1 is re-stated as

$$d(U+W) = d(\chi) = 0. \qquad 2.2.3$$

where χ is the total potential energy of the structure.

The finite element method is, therefore, a minimisation of the total potential Energy χ with respect to a finite number of unknowns. As the potential Energy χ is only an approximation to the true potential Energy it is necessary to develop convergence criteria to ensure the assumed displacement function represents as closely as possible the true displacement of the structure, and hence the true potential energy. These criteria as stated by Zienkiewicz (65) are that of conformability and continuity. Conformability depends upon the displacement function prescribing a continuous variation within an element with no discontinuities across element boundaries, and continuity depends not only upon the displacements being continuous but the first derivatives being continuous. These points are explained in Chapter 3 with the derivation of the elements.

The criteria stated above are due to the element being a displacement model. Other derivations depending upon complementary energy, or formulations involving both

potential and complementary energy produce different bounds to the solution (65, 63, 11, 18, 25, 43, 56). The analysis developed here is a lower bound to the true potential energy and the stiffness relation of equation 2.2.2 will result in displacements which are too large. By refining the mesh of elements, and therefore increasing the number of unknowns the solution by the finite elements will converge to the true solution.

3. NUMERICAL ANALYSIS

3.1 Introduction

As stated in the Introduction (Chapter 1), it was decided to develop the Ahmad (2) isoparametric shell element to analyse sandwich shells. This element allows for arbitrary geometry within the constraints imposed by Shape functions (Appendix A), and by assuming that normals to the mid-surface of the shell remain straight, but are permitted to rotate relative to the deformed mid-surface, allows for shear deformation to occur.

The choice of shape functions was made such that they defined both the geometry and displacement function, using the same order (quadratic) for both. Also by choosing the order of the shape functions from the standard families (18, 65, 25) the element is made to satisfy both the continuity requirements, and the constant derivative requirement.

The formulation of such an isoparametric element requires a unique relationship to be defined between the cartesian co-ordinates, and an undistorted local set of co-ordinates. Once this relationship has been defined suitable transformations can be performed to enable the element properties to be calculated with respect to the simplified local co-ordinate set, most importantly the element stiffness matrix.

3.2 Definition of the Geometry

Figure 3.1 shows an element of the shell

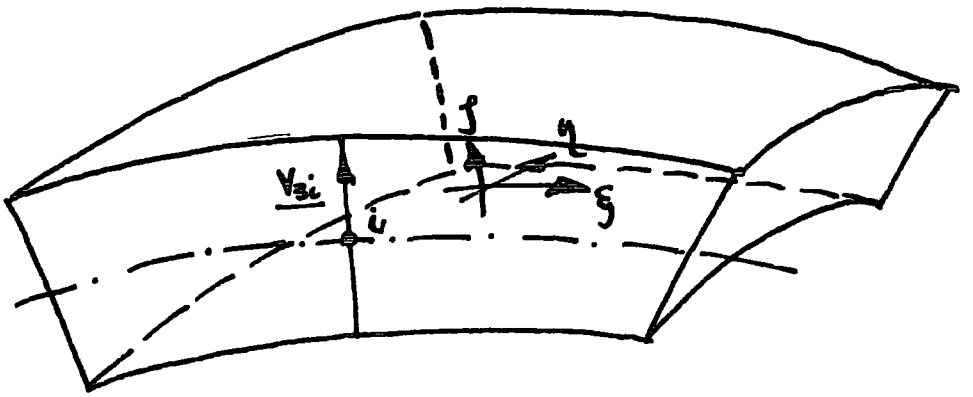

Figure 3.1

In Ahmad's formulation the geometry is defined as:-

$$\begin{Bmatrix} x \\ y \\ z \end{Bmatrix} = \sum [N_i] \begin{Bmatrix} x_i \\ y_i \\ z_i \end{Bmatrix} + \sum [N_i] \frac{\zeta}{2} V_{3i} \qquad 3.2.1$$

i represents a node on the mid-surface and V_{3i} is the Thickness vector for the ith node. $[N_i]$ are the shape functions. For both the quadrilateral and the triangular elements these were quadratic functions of the "Serendipity" family. A description of the shape functions is given in Appendix A. The advantage of using shape functions is that they remove the necessity of defining the displacement function explicitly as a polynomial.

For the sandwich shell element the mid-surface of the shell is retained, but the displacement function is modified to account for the layered construction. To ensure the element is isoparametric an additional transformation is made so that the matrices apply to a specific layer. This requires the thickness vector V_{3i} and the thickness function ζ to be specific to the layer being considered.

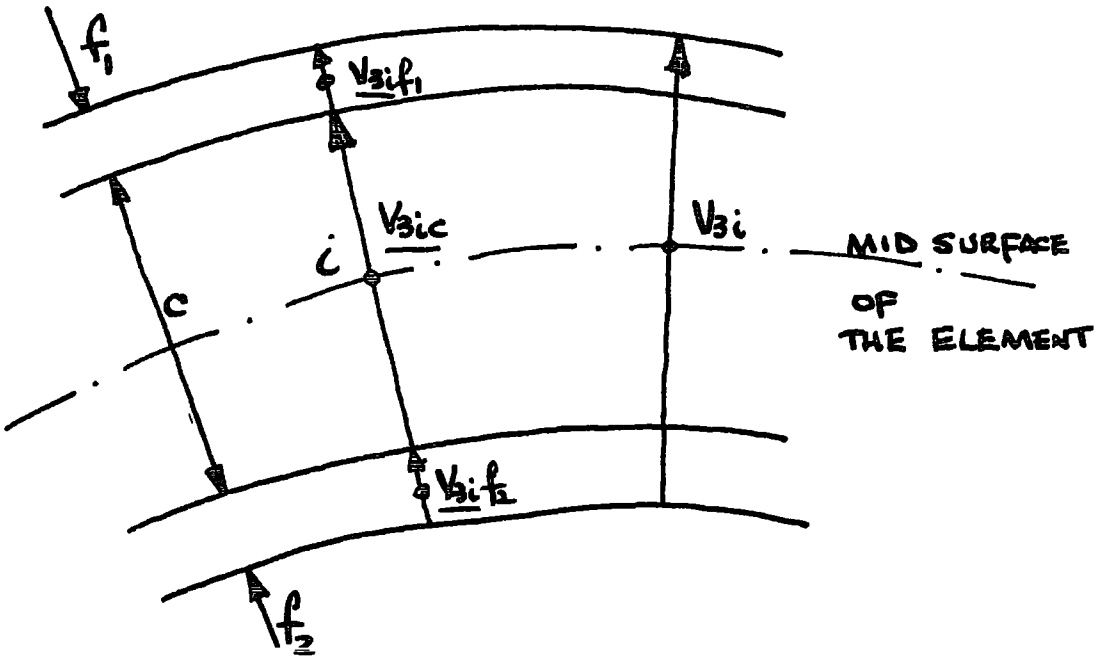

Figure 3.2

Figure 3.2 shows the modification to preserve the isoparametric form of the element.

The sketch also shows the mid-surface of the core layer as being the mid-surface of the element, but the formulation does not have this restriction.

As the variation of the in plane co-ordinates is identical for each layer the additional transformation relating the curvilinear co-ordinates (ξ, η, ζ) to the local layer curvilinear co-ordinates (ξ, η, ζ_2) is of the form

$$\begin{Bmatrix} \xi \\ \eta \\ \zeta_2 \end{Bmatrix} = \begin{bmatrix} 1 & 0 & 0 \\ 0 & 1 & 0 \\ 0 & 0 & T_j \end{bmatrix} \begin{Bmatrix} \xi \\ \eta \\ \zeta \end{Bmatrix} + \begin{bmatrix} 0 & 0 & 0 \\ 0 & 0 & 0 \\ 0 & 0 & K_j \end{bmatrix} \qquad 3.2.2$$

j refers to the jth layer $j = 1$ defines the top face

$$T_1 = f_1 / f_1+f_2+c \qquad K_1 = f_2+c / f_1+f_2+c$$
$$T_2 = c / f_1+f_2+c \qquad K_2 = -f_1+f_2 / f_1+f_2+c$$
$$T_3 = f_2 / f_1+f_2+c \qquad K_3 = -f_1-c / f_1+f_2+c \qquad 3.2.3$$

This definition preserves the numerical integration limits of plus one and minus one. The global co-ordinates of the mid-surface of any layer , are determined from putting $\zeta_2 = 0.0$ into the geometric definition of ζ .

Thus a separate definition of the geometry is obtained for each layer in terms of the mid-surface of the parent shell element, and its thickness vector $\underline{V_{3i}}$

These definitions are:

$$\begin{Bmatrix} x \\ y \\ z \end{Bmatrix}_{\text{TOP FACE}} = \sum [N_i] \begin{Bmatrix} x_i \\ y_i \\ z_i \end{Bmatrix} + \sum [N_i] \frac{(\zeta f_1 + f_2 + c)}{2(f_1 + f_2 + c)} \underline{V_{3i}} \qquad \text{(a)}$$

$$\begin{Bmatrix} x \\ y \\ z \end{Bmatrix}_{\text{CORE}} = \sum [N_i] \begin{Bmatrix} x_i \\ y_i \\ z_i \end{Bmatrix} + \sum [N_i] \frac{(-f_1 + f_2 + \zeta c)}{2(f_1 + f_2 + c)} \underline{V_{3i}} \qquad \text{(b)}$$

$$\begin{Bmatrix} x \\ y \\ z \end{Bmatrix}_{\text{BOTTOM FACE}} = \sum [N_i] \begin{Bmatrix} x_i \\ y_i \\ z_i \end{Bmatrix} + \sum [N_i] \frac{(-f_1 - c + \zeta f_2)}{2(f_1 + f_2 + c)} \underline{V_{3i}} \qquad \text{(c)} \qquad 3.2.4$$

In the limit as f_1 and f_2 tend to zero equations 3.2.4a and 3.2.4c define the top and bottom surfaces respectively and 3.2.4b is identical to equation 3.2.1.

3.3 The Definition of the displacement function

To satisfy convergence the choice of displacement function must meet the constant derivative requirement, and continuity requirements. In the isoparametric formulation these requirements are met, for the first condition if the sum of the shape functions is unity, and for the second if the variation of the unknown function ϕ is continuous in the parent set of co-ordinates, Zienkiewicz (63). The unknown function ϕ is in this shell element the function describing the variation of displacement within an element.

The choice of shape functions described in Appendix A satisfies the first condition, and by defining the displacement function for each layer in the form:

$$\begin{Bmatrix} U \\ V \\ W \end{Bmatrix} = \sum [N_i] \begin{Bmatrix} U_i \\ V_i \\ W_i \end{Bmatrix} + \sum [N_i] \frac{t_i}{2} [\underline{V}_{1i} \quad \underline{V}_{2i}] \begin{Bmatrix} \alpha_i \\ \beta_i \end{Bmatrix} \qquad 3.3.1$$

this satisfies the second condition in that the uniqueness of the displacement function is identical to the uniqueness of the geometric definition. As adjacent elements are given the same sets of co-ordinates at nodes, continuity is implied in the displacement function because of the continuity implicit in the geometric definition.

The terms defined in equation 3.3.1 are

$\begin{Bmatrix} U \\ V \\ W \end{Bmatrix}$ The mid-surface displacements.

t_i The magnitude of the thickness Vector.

$[\underline{V}_{1i} \quad \underline{V}_{2i}]$ Unit Vectors defining two orthogonal directions normal to the thickness vector.

$\begin{Bmatrix} \alpha_i \\ \beta_i \end{Bmatrix}$ The two scalar rotations of the $\underline{V}_{2i}$ vector.

The definition of the displacement function in equation 3.3.1 does not account for the layered construction, in that the transverse shear can be assumed to be entirely in the core and the in plane and bending resistance determined by the faces.

Expressing equation 3.3.1 in terms of the mid-surface of the shell and the rotations within each layer the displacement functions are:

$$\begin{Bmatrix} U \\ V \\ W \end{Bmatrix}_{\substack{\text{TOP} \\ \text{FACE}}} = \sum [N_i] \begin{Bmatrix} U_i \\ V_i \\ W_i \end{Bmatrix} + \sum [N_i] \frac{-f_1+f_2+c}{f_1+f_2+c} \frac{t_{ie}}{2} [\underline{V}_{1i}\ \underline{V}_{2i}] \begin{Bmatrix} \alpha_i \\ \beta_i \end{Bmatrix}_c$$

$$+ \sum [N_i] \frac{(f+1) f_1}{f_1+f_2+c} \frac{t_{ie}}{2} [\underline{V}_{1i}\ \underline{V}_{2i}] \begin{Bmatrix} \alpha_i \\ \beta_i \end{Bmatrix}_{f_1}$$

(a)

$$\begin{Bmatrix} U \\ V \\ W \end{Bmatrix}_{\text{CORE}} = \sum [N_i] \begin{Bmatrix} U_i \\ V_i \\ W_i \end{Bmatrix} + \sum [N_i] \frac{f c}{f_1+f_2+c} \frac{t_{ie}}{2} [\underline{V}_{1i}\ \underline{V}_{2i}] \begin{Bmatrix} \alpha_i \\ \beta_i \end{Bmatrix}_c$$

(b)

$$\begin{Bmatrix} U \\ V \\ W \end{Bmatrix}_{\substack{\text{BOTTOM} \\ \text{FACE}}} = \sum [N_i] \begin{Bmatrix} U_i \\ V_i \\ W_i \end{Bmatrix} + \sum [N_i] \frac{-f_1+f_2-c}{f_1+f_2+c} \frac{t_{ie}}{2} [\underline{V}_{1i}\ \underline{V}_{2i}] \begin{Bmatrix} \alpha_i \\ \beta_i \end{Bmatrix}_c$$

$$+ \sum [N_i] \frac{(f+1) f_2}{f_1+f_2+c} \frac{t_{ie}}{2} [\underline{V}_{1i}\ \underline{V}_{2i}] \begin{Bmatrix} \alpha_i \\ \beta_i \end{Bmatrix}_{f_2}$$

(c)

Equations 3.3.2

These equations are of the same form as equation 3.3.1, the additional terms of 3.3.2(a) and 3.3.2(c) correct the mid-surface displacements of the element to that of the mid-surface of the layer, and by considering the extra rotations of the faces allow for shearing within the face layers.

This general definition does not allow for the properties associated with sandwich materials, and would also pay the penalty in computational effort associated with nearly doubling the degrees of freedom (72 against 40 for the quadrilateral and 54 against 30 for the triangle. Both elements with an assumed quadratic variation in ξ and η).

The assumptions made reduce the number of degrees of freedom at a node to five instead of the nine associated with equations 3.3.2.

(i) The face to core thickness ratio is small ($f \ll c$). The rotations of the $\underline{V_{3i}}$ vector are therefore, assumed to act throughout the thickness of the element.

(ii) The stiffness of the faces is two orders of magnitude greater than the core, and so the transverse rotations within the faces are neglected.

These assumptions result in the displacement functions:

$$\begin{Bmatrix} U \\ V \\ W \end{Bmatrix}_{\text{TOP FACE}} = \sum [N_i] \begin{Bmatrix} U_i \\ V_i \\ W_i \end{Bmatrix} + \sum [N_i] \frac{(f_1 f_1 + f_2 + c)}{2(f_1 + f_2 + c)} t_i [\underline{V_{1i}} \;\; \underline{V_{2i}}] \begin{Bmatrix} \alpha_i \\ \beta_i \end{Bmatrix} \quad \text{(a)}$$

$$\begin{Bmatrix} U \\ V \\ W \end{Bmatrix}_{\text{CORE}} = \sum [N_i] \begin{Bmatrix} U_i \\ V_i \\ W_i \end{Bmatrix} + \sum [N_i] \frac{(f_1 - f_2 + f_c)}{2(f_1 + f_2 + c)} t_i [\underline{V_{1i}} \;\; \underline{V_{2i}}] \begin{Bmatrix} \alpha_i \\ \beta_i \end{Bmatrix} \quad \text{(b)}$$

$$\begin{Bmatrix} U \\ V \\ W \end{Bmatrix}_{\text{BOTTOM FACE}} = \sum [N_i] \begin{Bmatrix} U_i \\ V_i \\ W_i \end{Bmatrix} + \sum [N_i] \frac{(-f_1 - c + \beta f_2)}{2(f_1 + f_2 + c)} t_i [\underline{V}_{1i} \; \underline{V}_{2i}] \begin{Bmatrix} \alpha_i \\ \beta_i \end{Bmatrix}$$

(c)

Equations 3.3.3

These displacement functions state that the displacement at a point within a layer is given by the mid-surface translations, and an amount dependent upon the rotations α and β within the core.

There is also continuity between layers, in that $\beta = \mp 1.$ for the top or bottom faces respectively, the displacement is identical to that of $\beta = +1.$ or $-1.$ in the core layer. The shape functions describing the variation of displacement are identical to the functions describing the variation of the geometry and so the isoparametric form is preserved, again with the limits of integration between plus and minus one.

3.4 Definition of Strains and Stresses

The displacement functions described in the previous section (Equations 3.3.3) the five degrees of freedom associated with a node are two in plane displacements, a transverse displacement, and two rotations.

As a result of the assumptions made about the thickness and relative stiffnesses of the sandwich materials the contributions to the stiffness matrix of an element can be separated into those from a face and those from the core.

As the faces are stiffer than the core, and much thinner, the transverse shear contributions are neglected, and for the core the in plane contributions are neglected.

The vector of strains at a point (ξ, η, β) within the element is defined:

$$\{\epsilon'\} = \begin{Bmatrix} \epsilon_{x'} \\ \epsilon_{y'} \\ \gamma_{x'y'} \\ \gamma_{x'z'} \\ \gamma_{yz'} \end{Bmatrix} = \begin{Bmatrix} \frac{\partial u'}{\partial x'} \\ \frac{\partial v'}{\partial y'} \\ \frac{\partial u'}{\partial y'} + \frac{\partial v'}{\partial x'} \\ \frac{\partial w'}{\partial x'} + \frac{\partial u'}{\partial z'} \\ \frac{\partial w}{\partial y'} + \frac{\partial v'}{\partial z'} \end{Bmatrix} \qquad 3.4.1$$

The dash refers to a local orthogonal set of cartesian co-ordinates calculated at the point within the element. This is to enable the curvature of the shell to be accounted for. In the flat plate the transformation to these local cartesian co-ordinates is unnecessary, a global definition of the strains and stresses being possible, but in the computer programme written to analyse the shells this was not done, as this gave a check on the validity of the programme.

The evaluation of the direction cosines relating the local cartesian set of co-ordinates (x', y', z') to the global co-ordinates is given in Appendix B. This enables the orientation of the local stresses necessary to calculate the Stress Resultants, and also the stiffness matrix to be assembled.

For the sandwich shell the strains at a point within the layers are separated into membrane and transverse components. For the faces the strains at a point within the face layer were defined as:

$$\{\epsilon'\}_{FACE} = \begin{Bmatrix} \epsilon_{x'} \\ \epsilon_{y'} \\ \gamma_{x'y'} \end{Bmatrix} = \begin{Bmatrix} \frac{\partial u'}{\partial x'} \\ \frac{\partial v'}{\partial y'} \\ \frac{\partial u'}{\partial y'} + \frac{\partial v'}{\partial x'} \end{Bmatrix} \qquad 3.4.2$$

and for the core:

$$\{\epsilon'\}_{CORE} = \begin{Bmatrix} \gamma_{x'y'} \\ \gamma_{x'z'} \\ \gamma_{y'z'} \end{Bmatrix} = \begin{Bmatrix} \frac{\partial u'}{\partial y'} + \frac{\partial v'}{\partial x'} \\ \frac{\partial w'}{\partial x'} + \frac{\partial u'}{\partial z'} \\ \frac{\partial w'}{\partial y'} + \frac{\partial v'}{\partial z'} \end{Bmatrix} \qquad 3.4.3$$

Similarly, as the shells had no initial strains or stresses imposed upon them, the stresses at a point within the shell were defined as:

$$\{\sigma'\}_{FACES} = \begin{Bmatrix} \sigma_{x'} \\ \sigma_{y'} \\ \tau_{x'y'} \end{Bmatrix} \qquad 3.4.4$$

and

$$\{\sigma'\}_{CORE} = \begin{Bmatrix} \tau_{x'y'} \\ \tau_{x'z'} \\ \tau_{y'z'} \end{Bmatrix} \qquad 3.4.5$$

The constitutive relationships were:-

$$\{\sigma'\}_{FACE} = [D_f]\{\epsilon'\}_{FACE} \qquad 3.4.6$$

with

$$[D]_{FACE} = \frac{E_{FACE}}{1-\nu_f^2}\begin{bmatrix} 1 & \nu_f & 0 \\ \nu_f & 1 & 0 \\ 0 & 0 & \frac{1-\nu_f}{2} \end{bmatrix} \qquad 3.4.7$$

and

$$\{\sigma'\}_{CORE} = [D_c]\{\epsilon'\}_{CORE} \qquad 3.4.8$$

with

$$[D] = \frac{E_{CORE}}{1-\nu_c^2}\begin{bmatrix} \frac{1-\nu_c}{2} & 0 & 0 \\ 0 & \frac{1-\nu_c}{2} & 0 \\ 0 & 0 & \frac{1-\nu_c}{2} \end{bmatrix} \qquad 3.4.9$$

The evaluation of the strains, and hence the stresses, requires two transformations; one the transformation from curvilinear co-ordinates, and the second to the local cartesian co-ordinates. The first transformation is performed using the geometric definitions (equations 3.2.3) and forming the inverse Jacobean, and the second by forming the direction cosines of the local cartesian set, mentioned previously.

The description of how these matrices are derived and used is given in Appendix B.

The partitioning of the local strain components, and the orthogonality between the direction cosine matrix and inverse Jacobean, allowed a more direct formulation of the element stiffnesses. The orthogonality results from the vectors normal to a surface (ξ, η at ζ = constant) being in the same sense for both matrices.

A full description of the formation of the local strains and hence the stiffness matrices is given in Appendix C.

3.5 The Stress Resultants

Figure 3.5 shows an elemental section of sandwich shell. The strains and the stresses are evaluated at points within the face and core layers, and the direction cosines of these local strains and stresses output by the programme. The assumptions used to devlop the shell elements allow a simple derivation of the stress resultants.

The Stress resultants are defined as:

$$N_{ij} = \int_{-c/2-f_2}^{-c/2} \sigma_{ij}\, dz + \int_{c/2}^{c/2+f_1} \sigma_{ij}\, dz \qquad 3.5.1$$

$$M_{ij} = \int_{-c/2-f_2}^{-c/2} \sigma_{ij} z \, dz + \int_{c/2}^{c/2+f_1} \sigma_{ij} z \, dz \qquad 3.5.2$$

$$Q_{ij} = \int_{-c/2}^{c/2} \tau_{ij} \, dz \qquad 3.5.3$$

The assumptions that the faces act as membranes, and the core contributes to the transverse shear are implicit in the limits of integration of equations 3.5.1 to 3.5.3.

Assuming that the variation of direct stress within a face is zero the membrane stress resultants are:

$$N_x = \sigma_{x1} f_1 + \sigma_{x2} f_2$$

$$N_y = \sigma_{y1} f_1 + \sigma_{y2} f_2$$

$$N_{xy} = \tau_{xy} f_1 + \tau_{xy} f_2$$

and the Bending stress resultants:-

$$M_x = (\sigma_{x1} f_1 - \sigma_{x2} f_2) \times (c+f)/2$$

$$M_y = (\sigma_{y1} f_1 - \sigma_{y2} f_2) \times (c+f)/2$$

$$M_{xy} = (\tau_{xy} f_1 - \tau_{xy} f_2) \times (c+f)/2$$

Assuming constant transverse shear within the core the transverse shear stress resultants are:

$$Q_x = \tau_{xz} \times c$$

$$Q_y = \tau_{yz} \times c$$

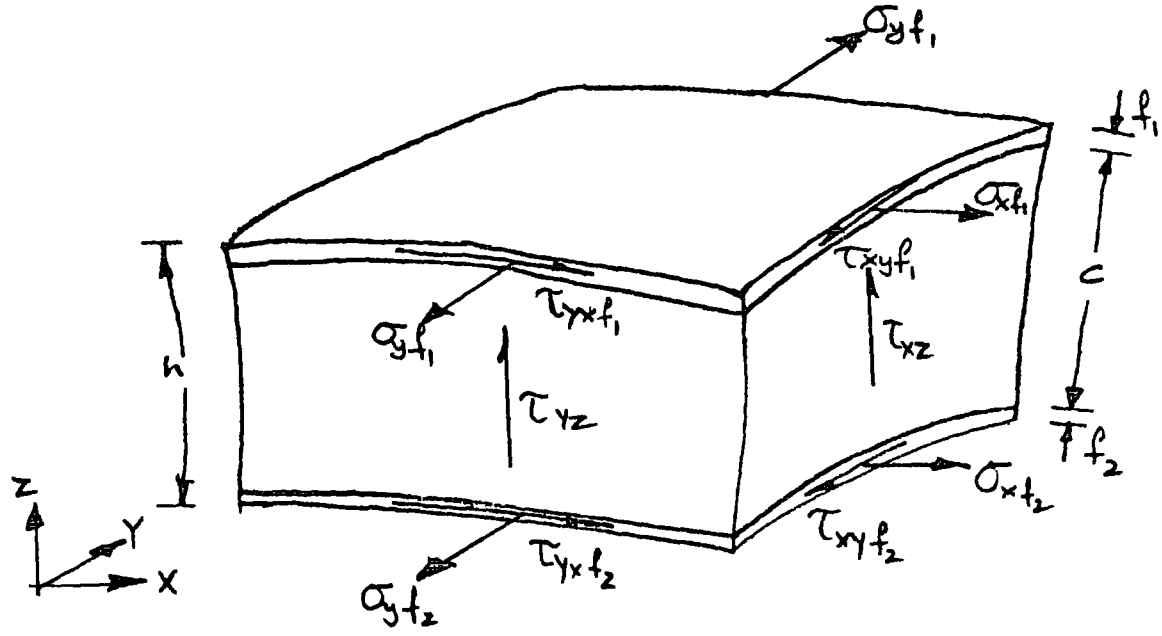

3.5.1 STRESSES

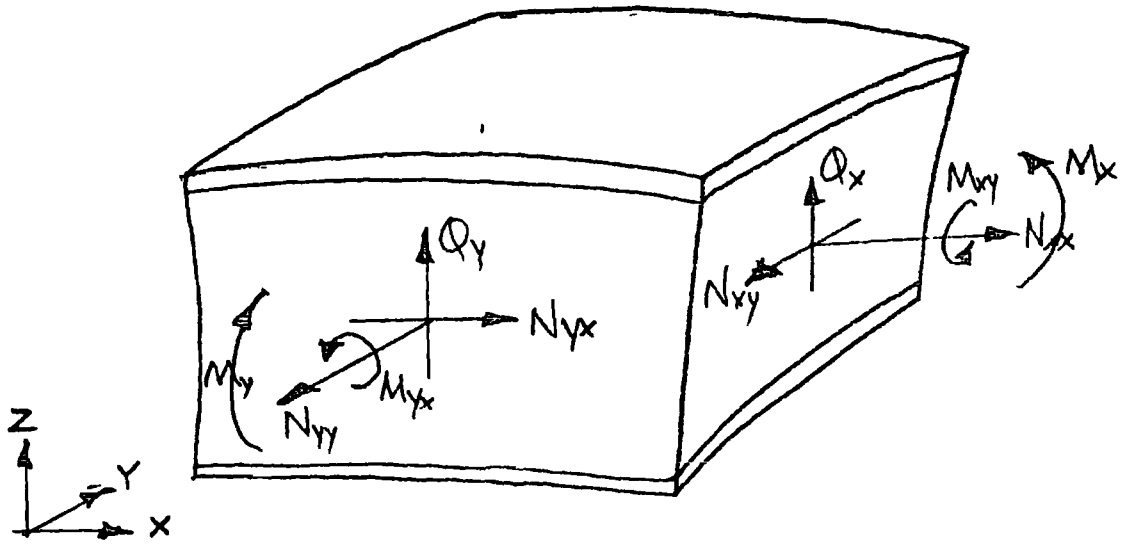

3.5.2 STRESS RESULTANTS

FIGURE 3.5 STRESSES AND STRESS RESULTANTS ON AN ELEMENTAL SECTION OF SANDWICH SHELL

3.6 The Solution of the Equations

The simultaneous equations formed in equation 2.2.2, with the assumption of no initial strains or stresses, reduce to:

$$[k]\{\delta\} - \{R\} = 0. \qquad 3.6.1$$

The solution for the unknown displacements depends upon the stiffness matrix of the structure and the applied loading. The technique used is based upon the frontal solution programme developed by Irons (35, 33).

In this programme a degree of freedom or unknown is complete when there are no more contributions to be added into the system stiffness matrix for that freedom. Once complete, and even though other degrees of freedom are incomplete, then that freedom is eliminated. Eventually there remains one freedom which can be determined explicitly. The programme then back-substitutes into the relationships for the eliminated freedoms until all the equations are solved.

This method depends upon the element numbering and not the nodal numbering. Elimination of a degree of freedom depends upon its completeness which, in turn, depends upon the order in which the adjoining elements are added into the system stiffness matrix.

The hypars in this work were sub-divided into a symmetric mesh of quadrilaterals and the element numbering would not affect the solution procedure.

4. NUMERICAL ANALYSIS COMPARISONS AND NUMERICAL INTEGRATION

The references of Pawsey and Clough(53) and Zienkiewicz, Taylor and Too (64) indicate that the choice of integration order used in a shell finite element can make a significant difference to its performance. A survey is carried out to compare the differing orders of integration of the sandwich shell element, to determine the best order to be used in the analysis of the sandwich hypars.

4.1 Numerical Integration

To obtain the stiffness matrix of an element numerical integration of the form:

$$[k] = \int_{VOL} [B]^T [D] [B] \, dVol \qquad 4.1.1$$

is required. This integration is performed numerically by choosing a mesh of Gauss points within the element. The order used depends upon the variation within the element of the various straining modes. Both Pawsey (53) and Zienkiewicz (64) indicate that high integration orders choose points within an element such that the transverse shear contributions to the strain energy can be too large, especially in thin shell situations. This results from the displacement

function imposing unrealistic restrictions upon the modes of deformation of the element.

The example given by Pawsey is of the quadrilateral membrane element of Doherty (19), where the 'bending' deformations, if integrated at a single central node, would produce contributions of zero, whereas the constant strain modes, using a higher order for the normal strains, and the central node for the shear strain, would result in the correct contributions to the stiffness matrix.

Using a higher order (2 x 2)integration formula would result in the 'bending' deformations contributing to the strain energy, and the shear strain contributing too great a value to the strain energy. This would result in an element which would be too stiff.

In addition, Pawsey demonstrated that curvature in an element is important in determining where the strain energy contributions should be evaluated.

The example given for this situation is of a one dimensional quadratically curved element subjected to a constant moment. To produce the result of the normal strain at the mid-surface being zero, then the normal strain energy needs to be evaluated at the Gauss points.

The arguments put forward by Pawsey are to selectively integrate the stiffness contributions depending upon the straining mode being considered. The rules he defined being extrapolations of the examples he gave, to allow for the higher order displacement function and general curvature associated with the isoparametric elements.

Zienkiewicz et al. (64) performed a similar analysis using the Ahmad element in thin shell situations but proposed reduced integration being applied to all the straining modes. This resulted in the element performing well for both thin and thick shell situations with the added benefit that the computational effort in forming the stiffness matrix is reduced due to the smaller number of integration points used.

In thin shells where the lateral shears account for a small proportion of the strain energy a further development was made by Irons and Razzaque (34). They chose to make these shear contributions exactly zero at the Gauss points. This "semi-loof" element is inapplicable for the current problem where the transverse shears cannot be assumed to be zero.

Following the arguments put forward by both sets of researchers the sandwich shell element would require a two by two mesh of points within a face which would allow for the normal straining modes and the membrane shear strain, the transverse shear strain contributions being zero for the faces.

For the core a two by two rule should be sufficient within its thickness to allow for the transverse shear contributions and the zero membrane contributions. This was found not to be the case, and is described in the following section.

The reasons for this are due to the definition of the displacement functions. For the faces the choice of a mid-surface mesh of Gauss points would produce the membrane effects associated with the face being centred on the mid-surface of the element, and not at the outer edge of the shell, and for the core a set of points on its mid-surface would result in no contribution from the transverse shear rotations.

The results using the differing orders (Table 4.1) are shown for both the triangular element, and the quadrilateral element in comparison with Abel and Popov's beam results (1).

4.2 Comparison with Abel and Popov

Abel and Popov (1) analyse a cantilever sandwich beam using a finite element with a cubic variation of transverse displacement and a linear variation of shear rotation.

As this element allows for shear within the faces of the sandwich, it gives a more accurate representation of the warping and shear at the built-in end of the beam, than the elements developed by the author.

The dimensions and material properties of the cantilever are given below:

Thickness of the faces	f = 0.04 in.
Thickness of the core	c = 0.5 in.
Span	L = 10 ins.
Breadth	B = 1.0 in.
Young's modulus for the faces	Ef = 10 p.s.i.
Young's modulus for the core	Ec = 2 x 10 p.s.i.
Shear modulus for the faces	Gf = 4 x 10 p.s.i.
Shear modulus for the core	Gc = 10 p.s.i.
The Applied load	P = 1.0 lb.

As this sandwich beam has a weak core ($Ec \ll Ef$) and the face thicknesses are much less than the core thickness ($f \ll c$) it can be assumed (Plantema, Allen 54, 3) that the core is too weak to contribute to the flexural stiffness of the sandwich and the shear stress is constant over its depth. Also the faces are assumed to have a linear distribution of normal stress which for very thin faces is constant.

In view of the arguments put forward by Pawsey and Zienkiewicz a single node in each of the layers would be sufficient to enable the strain energy contributions to be evaluated with respect to the thickness co-ordinate and two nodes in each element along the length of the beam to accommodate the linear variation in the normal stress.

The differing integration orders are shown in Table 4.1. The Triangular element showed even with an aspect ratio of ten to one, that the choice of integration order produced little variation in displacement.

The Quadrilateral element produced a more marked variation. The worst results for the displacement of the beam was produced by the high order mesh in plane on the reference surface of the element.

This is due to the displacement function for the core contributing to the strain energy the effects of the reference surface translations and not the rotations.

The results obtained when either the core or the faces has the single mesh were a slight improvement upon the previous results.

The best results were produced by the 2 x 2 mesh of nodal points and it was decided to use this formulation for the sandwich plates, and finally in the analysis of the hypars.

4.3 Chapman and Williams

As the two by two Gaussian rule used to integrate the element stiffnesses produced good agreement with the cantilever beam of Abel and Popov (1) it was decided to compare its performance with Chapman and Williams' work on shear deformation effects of uniformly loaded orthotropic plates.

The solutions Chapman and Williams used were based upon series solutions for plates simply supported, and a finite difference solution for the clamped boundary conditions. For the comparison between the clamped plates with the two loading conditions of a uniform distributed load, and a linearly varying load the finite element mesh was four by four, and a quarter of the plate was analysed because of symmetry in loading and boundary conditions.

To provide a comparison of the shear effects a shear parameter γ_x is varied between 25 and 500. This shear parameter is defined as

$$\gamma_x = \frac{a^2 S_x}{D_x}$$

where

$$S_x = \frac{A_x E}{2(1+\nu)}$$

$$D_x = \frac{E h^3}{12(1-\nu^2)}$$

A_x is the unit effective web area

h the thickness

a the length of a side of the plate

E, ν Young s modulus and Poisson's ratio.

Figure 4.3.1 shows the finite element results for moment, shear and displacement for the points defined in the diagram. The displacement of the centre of the panel shows close agreement for all values of shear parameter, the moment and shear however show good agreement for values of shear parameter greater than 50.

The lower value is for a plate with greater shear effects. The effect of the shear is to cause a more even distribution of load, demonstrated in 4.3.2 by the edge shear Qy, and the bending moment distribution M_x across the centre line.

Agreement between the Chapman and Williams results and the finite element solution were good for all displacements and the bending moment at the centre line, fair for the edge shear and good for twisting moment for γ_x greater than 50.

A similar comparison was made for the clamped square plate with a linearly varying load (Figure 4.3.3). Again agreement with the results was good, except for the shear force along the edge of the plate.

The comparisons were made with rectangular elements only, but with the same two by two Gauss rule in each case. For γ_x =156 two analyses were performed; the first with the sixteen elements, and the second with only four elements. The results shown in Figure 4.3.1 show that for both displacement and moment the coarse mesh is insufficient.

As the comparisons of both the sandwich beam and 'sandwich' plate showed good agreement, the order of integration was kept at a two by two Gauss mesh to evaluate the stiffness of the elements for the hypars. Its performance is described in Chapter 6.

8 NODED QUADRILATERAL :

OPTION NO	FACE	CORE
3	3 x 3 x 2	2 x 2 x 2
4	3 x 3 x 1	3 x 3 x 1
5	2 x 2 x 2	2 x 2 x 2
6	2 x 2 x 1	2 x 2 x 1
7	3 x 3 x 2	2 x 2 x 2
8	3 x 3 x 1	2 x 2 x 2
9	3 x 3 x 2	2 x 2 x 1
10	3 x 3 x 1	2 x 2 x 1
11	2 x 2 x 2	3 x 3 x 2
12	2 x 2 x 2	3 x 3 x 1
13	2 x 2 x 1	3 x 3 x 2
14	2 x 2 x 1	3 x 3 x 1
15	3 x 3 x 1	3 x 3 x 2

6 NODED TRIANGLE

OPTION NO	FACE	CORE
1	7x2	7x2
2	3x2	3x2
3	3x2	7x2
4	3x1	7x2
5	3x2	7x1
6	7x2	3x2
7	7x1	3x2
8	7x2	3x1
9	3x1	3x1
10	7x1	7x1

TABLE 4.1

NUMERICAL INTEGRATION ORDERS USED BY THE QUADRILATERAL AND TRIANGULAR ELEMENTS

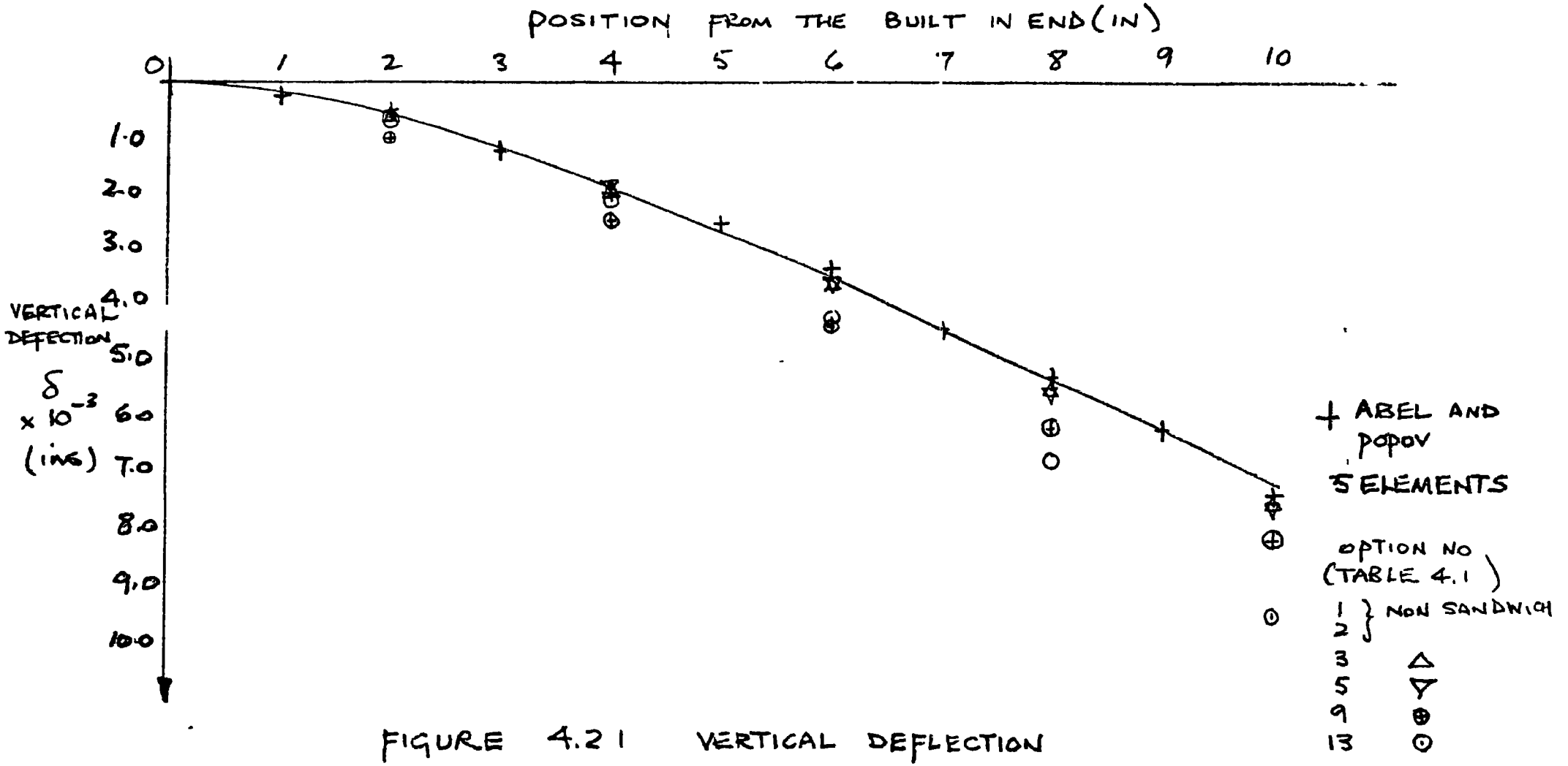

FIGURE 4.21 VERTICAL DEFLECTION

CANTILEVER BEAM

COMPARISON BETWEEN ABEL AND POPOV

AND THE QUADRILATERAL ELEMENTS

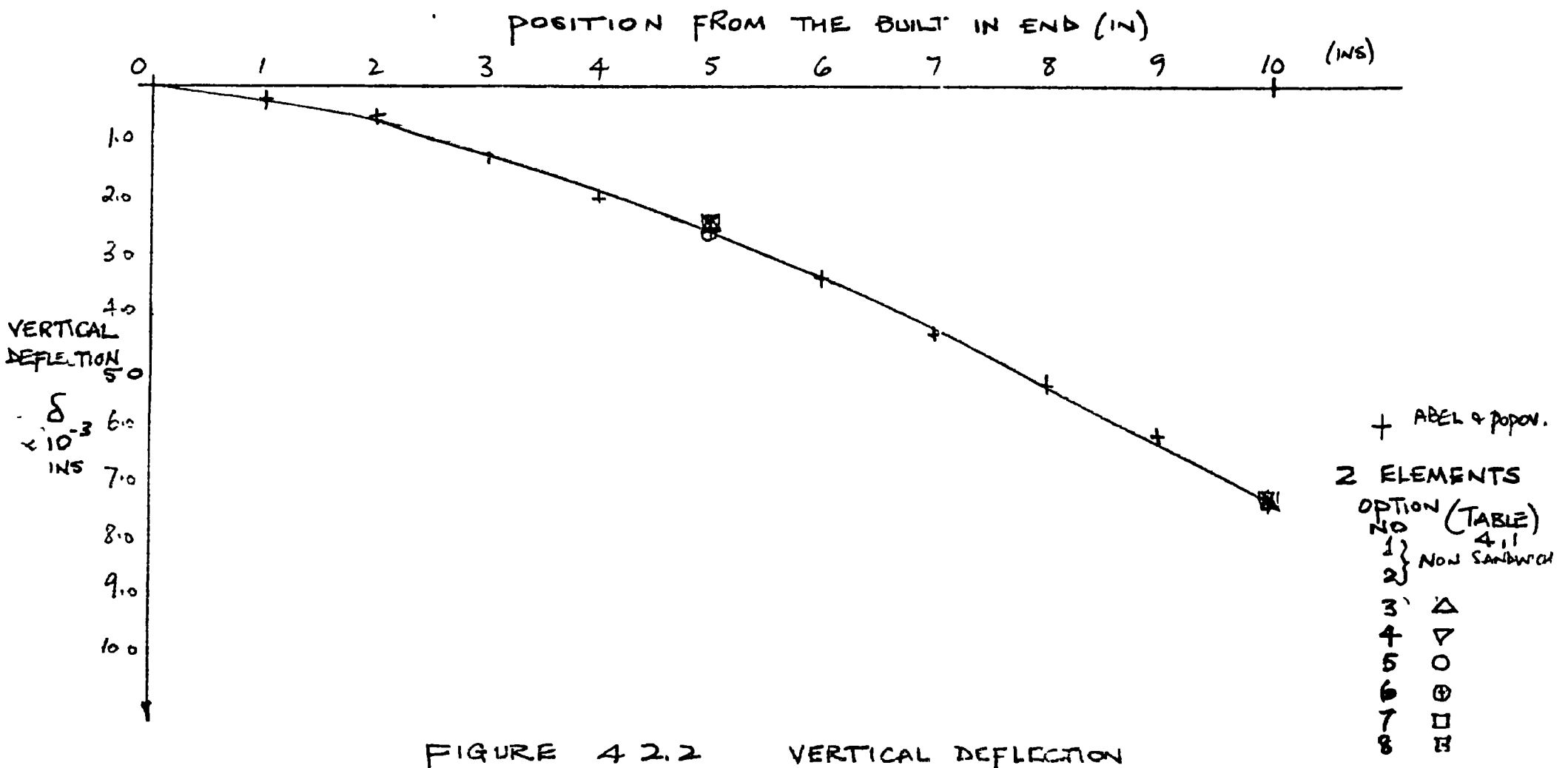

FIGURE 4 2.2 VERTICAL DEFLECTION

CANTILEVER BEAM

COMPARISON BETWEEN ABEL AND POPOV

AND THE TRIANGULAR ELEMENTS

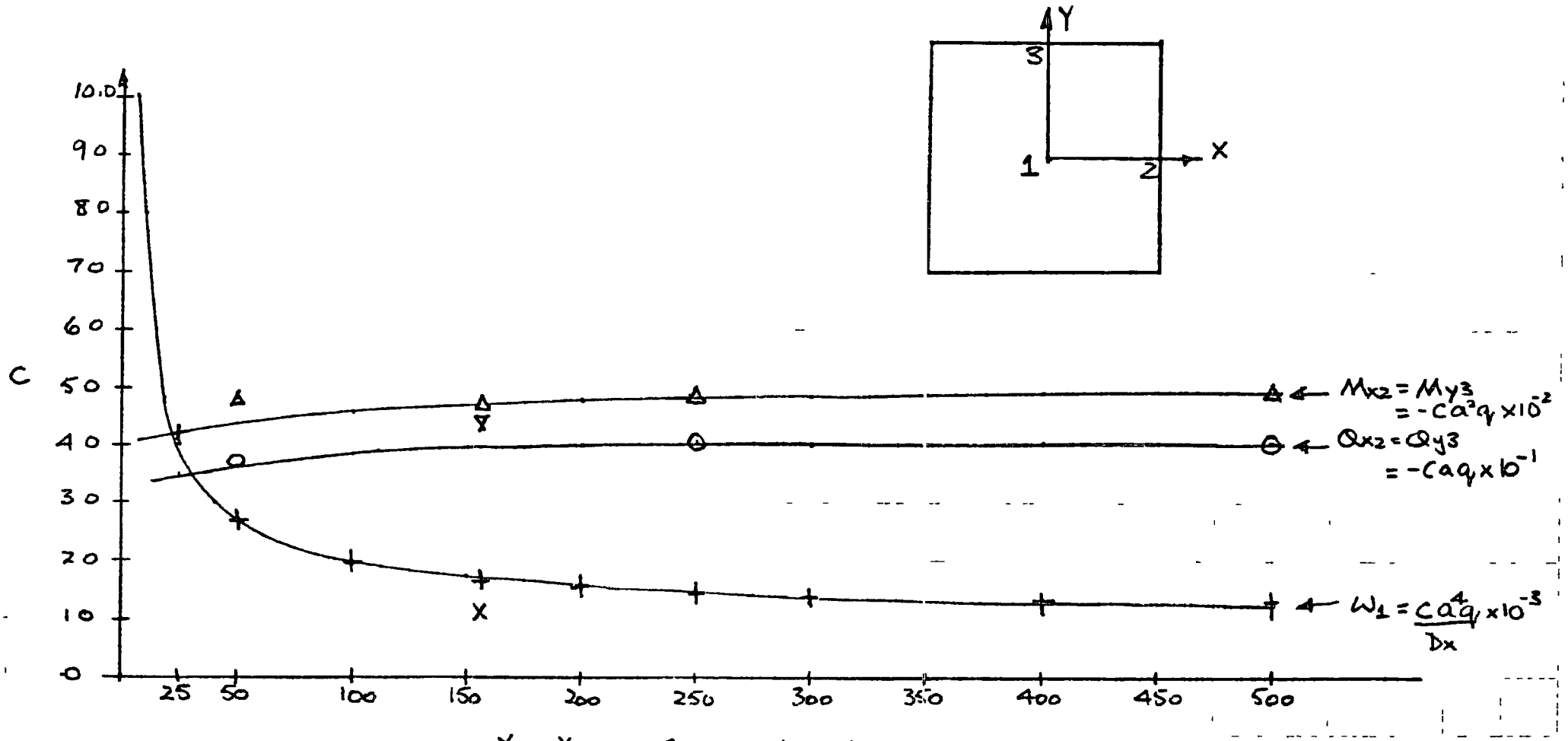

FIGURE 4 3.1 CLAMPED PLATE UNDER A UNIFORM TRANSVERSE LOAD : EFFECT OF SHEAR STIFFNESS ($\zeta_x = a^2 S_x / D_x$)

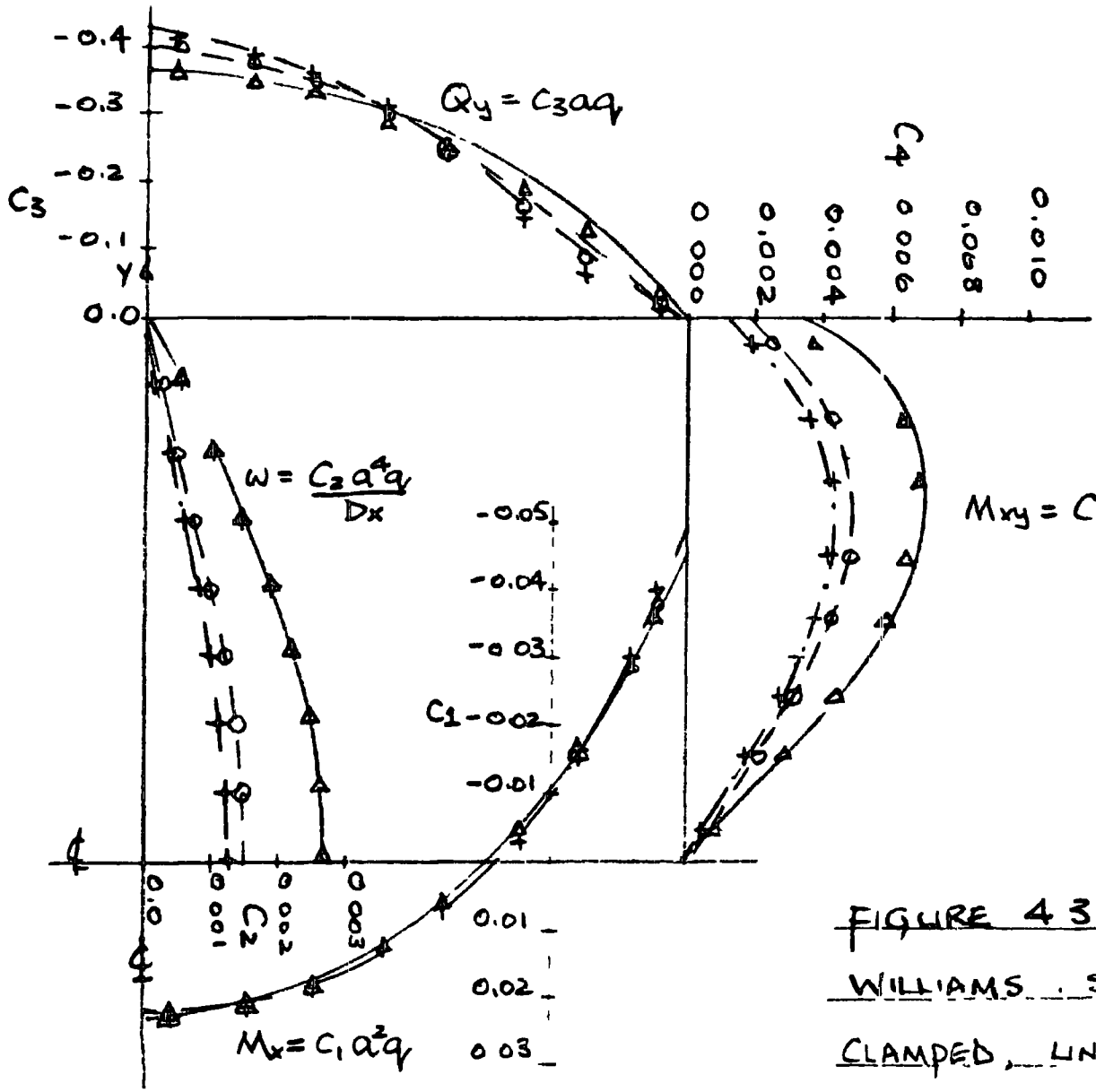

SOLID AND DOTTED LINES
CHAPMAN AND WILLIAMS RESULTS
— Δ $\gamma_x = 50$ 4×4 FE
- - - ⊙ $\gamma_x = 250$ 4×4 FE
—·— + $\gamma_x = 500$ 4×4 FE

$a = 50$ $q = 0.1$
$\alpha = 1$ $\beta = 0.769$
$\epsilon = a/b = 1$
$\nu_x = \nu_y = 0.3$
$\gamma_x = a^2 S_x / D_x$

FIGURE 432 : CHAPMAN AND WILLIAMS . SQUARE PLATE, CLAMPED, UNIFORM TRANSVERSE LOAD

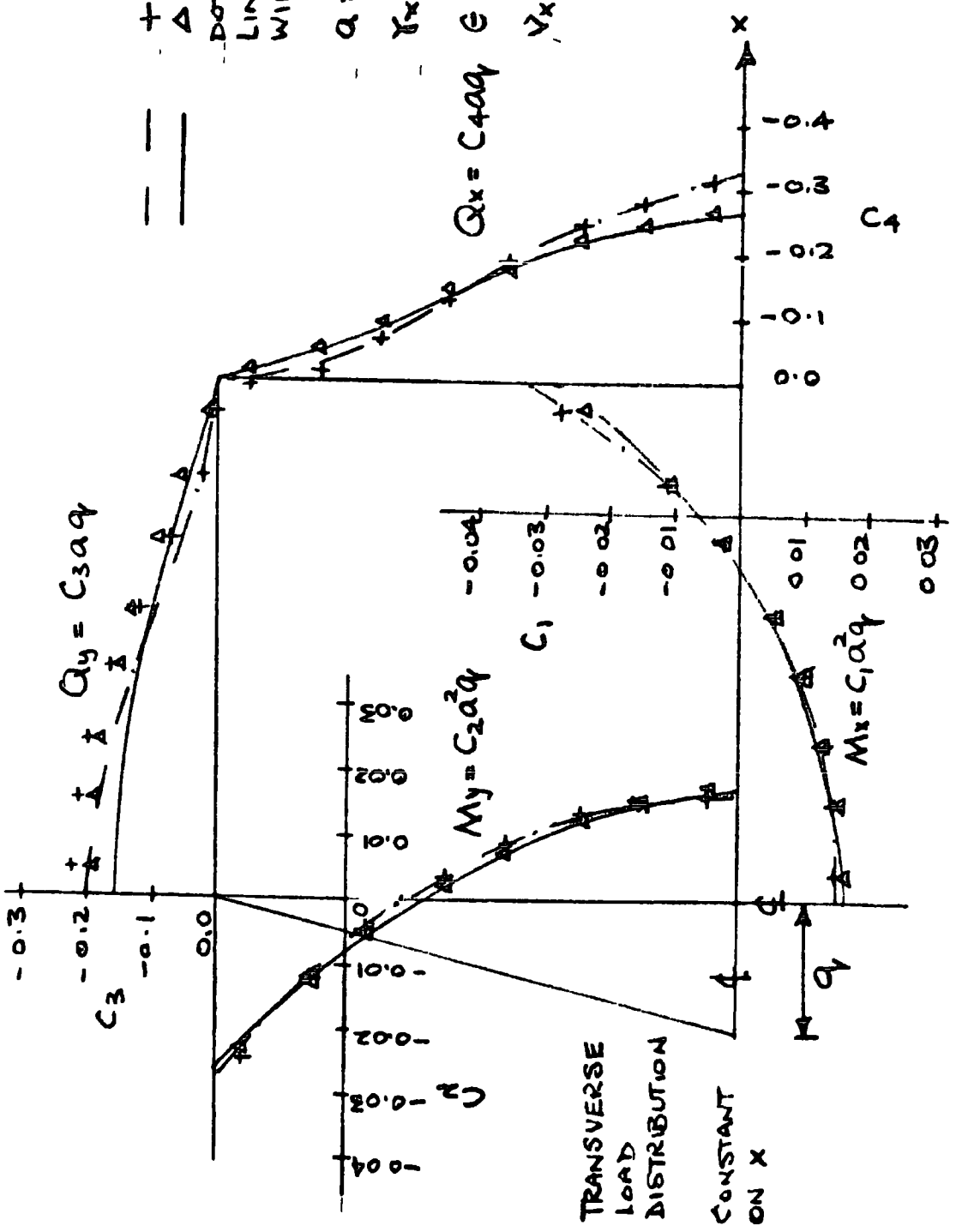

FIGURE 4.3.3 SQUARE PLATE - THE EFFECT OF NON-UNIFORM TRANSVERSE LOAD

5. EXPERIMENTAL WORK

5.1 Introduction

The experimental work consisted of the construction and testing of four hyperbolic paraboloid sandwich shells and a flat sandwich plate of the same materials as the shells.

The dimensions of the plate and shells were limited to the size of the polyurethane sheets available from the manufacturers, which are rectangles nominally eight feet by four feet (2.44m x 1.22m) and one inch (25mm) thick.

The hypars were square in plan with sides of four feet (1.22m). After the faces of the panels had been formed this was reduced to a metre square, and the metre square used to measure the displacements.

The face materials of the shells were manufactured in fibreglass, due to the construction difficulties encountered with plywood and hardboard.

Loading of the shells was done by loading 'crabs' (Fig. 5.1) with the loads perpendicular to the x, y plane and not normal to the surface of the shell.

The resulting displacements were measured using dial gauges, and the results used as the comparison with the finite element programme.

5.2 Geometry

The Geometry of a hyperbolic paraboloid can be defined in two ways, either that of a surface of translation (Fig. 5.2a) or as a warped parallelogram (Fig.5.2b).

In the first case the surface can be defined by translating a parabola in the vertical plane having upward curvature (ABC in Figure 5.2a) over another in a plane normal to the first having downward curvature (BOF). The surface is formed by moving ABC along BOF keeping the point B on the parabola BOF.

In the second case the surface is generated by moving a straight line parallel to the XZ plans, but rotating uniformly such that $\frac{\partial \theta_y}{\partial x} = k$ where k is a constant (Fig. 5.2b).

The surface is, therefore, generated by moving EDC along the y axis as shown in the Figure.

Referring to the quadrant OHGF the geometric properties required to define the surface are the rise, which is C, and the lengths of the quadrant along the x and y axes, which are a and b respectively. The equation defining the surface becomes:

$$z = k x y \qquad 5.2.1$$

where

$$k = \frac{c}{ab} \qquad 5.2.2$$

Relating this Geometric definition to the parabolic definition given first, the curved lines parallel to EOA in figure 5.2b are equivalent to lines parallel to BOF in figure 5.2a and similarly for the lines GOC and DOH. The hyperbola in the definition, for both forms of the shell, is produced by taking a section through the shell parallel to the xy plane.

The advantage of the second definition is that the doubly curved surface can be generated by a mesh of two intersecting systems of straight lines.

5.3 Construction

Initially it was decided that the materials to be used to form the hypars would be similar to those previously tested by other workers in the Department (20, 43, 51, 8); that is, a core of polyurethane and face materials of either plywood or hardboard.

It was found, when using square sheets of either plywood (3 ply, 1.5mm thick) or hardboard (¼ in. thick), that these materials would not take up the shape of the surface. They could be formed in one direction, say, parallel to the tension parabola, but produced large distortions when made to take up the curvature parallel to the compression parabola. The resulting sandwich always produced air pockets between the core and the faces such that there was no realistic bond between the layers.

The methods used in those attempts differed depending upon which material was used. The difficulties encountered were always with the face materials, and not with the flexible polyurethane core.

5.3.1 The Hardboard and Polyurethane sandwich hypar

The initial hypar was to be formed from a square of side four feet and having a rise of 6 ins. These dimensions were chosen so that the hypar would be significantly different from a flat plate.

The glue used to bond the layers was a Urea-Formaldyhyde resin (Aerolite 336) with the hardener W.148 which extended the pot life to 30 minutes. The long pot life was to allow time to place the sandwich into the forming frame and generate the hypar.

The first attempt was with the hardboard faces dry. One side of the panel was glued to the polyurethane core with no attempt to twist the panel. Once this was set the half-sandwich was placed in the frame, the glue applied and the second face placed to form the sandwich.

This flat sandwich was then clamped to a rigid bar along two parallel edges of panel and the rigid bars were rotated until the degree of twist was achieved. The clamps used are shown in Figure 5.3, and were spaced at two inch (50mm) intervals along each of the edges.

The panel was allowed to set and checks were made upon the resulting geometry.

The edges of the panel did not remain straight, and where the clamps were attached the edges had quite severe corrugations. Also, within the unsupported part of the hypar, bonding between the layers of as much as six inches square had not taken place.

The reasons for this failure were due to the significant stiffness of the preformed core and single face and the inability of the faces to form the doubly curved shape with relatively little support.

The second attempt tried to overcome the difficulty of forming the doubly curved faces by preforming them.

The hardboard sheets were placed in a tank of water and left for forty-eight hours to soak. When saturated they were placed upon the Dexion framework supported by the runners shown in Figure 5.4. Sandbags and other weights were applied to the faces to force them into the required shape. They were then left to dry.

The procedure described for the 'dry' hypar was repeated.

The resulting hypar was again checked and found to be similarly inaccurate. The bonding within the unsupported part of the hypar was not as poor, but areas of about two inches square had not formed the sandwich, and the non-linearity had similarly improved, but not with the desired degree of accuracy.

The next attempt was with a reduced rise of hypar (3 ins. instead of 6 ins.). The areas within the hypar, where the bonding had not taken place in the previous attempts, were loaded with the sandbags and weights.

The faces were again preformed and the procedure for the second hypar repeated, but with four feet lengths of Dexion attached under the panel to give extra support.

Again there was an improvement upon the previous attempts, but the straight line generators deviated from the calculated straight lines by ± 1.25 cms. along a four feet length. These lines were not parallel to the XZ plane nor the YZ plane as they should have been, and in the areas where bonding had not taken place previously, the panel had formed flat areas. The failure of the hypars was due to a number of reasons.

(i) The face material could not be forced into the doubly curved shape. When dry the stiffness induced by bending the hardboard in one direction made the bending of it in the orthogonal direction too difficult.

(ii) When the hardboard was preformed into the desired shape it was possible to get nearer to the form of the hypar but as the faces dried out they attempted to return to their original flat shape.

(iii) The loads required to ensure bonding between layers were so large (20 kgs. per 200 mm. square) they distorted the shape of the panel.

(iv) For even the shallowest hypar there were audible noises caused by the bonding between layers breaking down.

(v) The clamps used along two of the edges were insufficient to provide a distribution of the loading required to twist the panel.

(vi) The area of the panel unsupported was too great to guarantee the form of the surface.

To enable a hypar to be formed using hardboard and polyurethane which is originally in the form of flat sheets, and if autoclave pressing is not to be used, the preforming of the faces is essential. In addition, support should be given all over the hypar, perhaps using a plaster (or other similar) cast of the desired shape.

5.3.2 The Plywood and Polyurethane sandwich hypar

As a result of the failures with the hardboard it was decided to try plywood as a face material.

Rather than glue the panel together, it was decided to see if the plywood would more easily form the shape by loading it by itself upon the supporting frame.

The thickness of the face (1.5 mm) was much less than the hardboard (6.4 mm) but it would twist only in one direction, and not in the orthogonal direction.

It seemed apparent that similar difficulties to those in forming the hardboard faces would be met, therefore attempts to form the faces using a sheet of material were given up in favour of fibreglass.

5.3.3 The Fibreglass and Polyurethane sandwich hypar

To form the hypars a frame was needed which was adjustable to allow for the variation of rise required for the models.

This was in the range $c/a = 0$. for the flat plate to $c/a = 1/6$ for the steepest hypar.

The frame was to be used for testing the hypars as well as forming them, and had to be substantial enough to take the loading required for both purposes.

This was accomplished using "Dexion".

5.3.3.1 The Dexion frame.

The frame was built five feet square to allow for the runners and box structure used to construct the hypars. It was reinforced with Dexion along each edge, and across its area both at ground level and two feet above ground level.

Figures 5.5a and 5.5b show, not to scale, a schematic drawing of two sides of the frame.

5.3.3.2 The supporting runners

The runners, shown in Figure 5.4a, were made from 20 mm. plywood (5 ply) and were in two parts, male and female.

The male part of the runner had two tongues at the ends to fit the female part. These tongues were rounded to allow the runner to rotate. This enabled its width to act as a support rather than an edge. Twenty such runners were used as support for the core.

In the Figure 5.4, a small gap is shown separating the male and female parts. To ensure the runners remained rigid while forming the shell, pieces of wood were used as wedges and forced into the gaps.

The wedges had the added advantage that they forced the female parts hard against the support beam.

The dimensions of the timber used to form the runners was sufficient to ensure that the loads, used to hold the core on to these runners, did not cause them to deflect.

5.3.3.3 The support beam

The support beam was made of solid mild steel. This was circular in section and was a neat fit in the female parts of the runner. The beam was clamped to the Dexion by "U" bolts shown as crosses in Figure 5.5a.

5.3.3.4 The Box Former

The Box former was used for two purposes, the first for the forming process, and the second in supporting the hypars under load.

In the forming process the box was used to generate the shape of the hypar and as support for the edges. This ensured that all four edges were used to induce the required twist.

The box was manufactured from four pieces of block board four feet in length mitred together, with a reinforcing block of wood in each corner.

The edges of the box adjacent to the panel were filed to accommodate the curvature over the thickness of the box (25.4 mm). The box was placed on to the runners with no core in between, and the runners brought into contact with the edges.

This was done by rotating the support beams. Once the runners and support beam were firmly clamped in to the desired shape the box was removed and the core placed on to the runners.

The box was then returned to the frame. Extra pieces of Dexion were used to ensure that the unsupported edges of the core, perpendicular to the support beams, were clamped to the box.

5.3.3.5 The Core

The core shown lying along the runners in Figure 5.5 had the paper facing on one side removed. The paper on the other side is used in the forming process of the "Purlboard" and cannot easily be removed.

As the Purlboard is initially a flat plate, loads were applied to it, two on the compression parabola and two on the tension parabola to force it on to the runners.

The greatest load applied to these points was 4 kg. These loads, together with the box former, were sufficient to hold the core on to the runners. The loads applied at the four points were attached to the core by pieces of wire extending through the core and wrapped around a flat piece of scrap metal, usually about 50 mm x 25 mm x 1.5 mm thick.

This distributed the point loads more evenly on the surface of the core, but did cause small local deformities. Once satisfied that the core had taken the required shape the fibreglass was applied to the face.

The core used for all the hypars was polyurethane.

5.3.3.6 The Fibreglass

The fibreglass used for all the hypars was applied to each face in turn.

A layer of the fabric was placed on the core and the polyester resin applied. When the layer was drying, but still tacky, a second layer of the fabric was placed on the first, but at right angles to the first. The resin was re-applied and the surface formed.

At the same time, a flat piece of sandwich was formed to determine the elastic properties using the same mix of resin.

The procedure outlined above was used for each hypar in turn.

The box former was rebuilt for each hypar.

The ratio of rise to quadrant length $(c/a, a=b)$ for the hypars was $0, 1/24, 1/12, 1/8, 1/6$

5.4 Checking the Geometry

After the panel had cured, the edges of the resulting hypar were trimmed and a grid one metre square drawn on to a face.

This grid was formed by 100 - 10 cm x 10 cm squares, giving 121 points on the surface of the shell.

Taking one corner of the grid as a datum, a cathetometer was used to measure the vertical height of a point above this arbitrary datum.

Graphs of these points were plotted along the lengths of the generators to determine the deviation from the calculated straight line and the measured line. An estimate of the error in the geometry was determined.

This was repeated for each hypar in turn.

The limitations of this method are that checks are made only upon the grid points, and no account is taken of drawing the grid on to the hypars.

From the checks the following errors were found in the Z co-ordinate:

c/a a=b	MAXIMUM ERROR %
0	± 0.45cms
1/24	8.0%
1/12	9.8%
1/8	6.8%
1/6	7.1%

% ERROR $\frac{Z_c - Z_M}{Z_c} \times 100$

Z_c CALCULATED VALUE

Z_M MEASURED VALUE

TABLE 5.4

As the errors in the Z co-ordinate did not exceed 10% comparing the measured and calculated values (Table 5.4) and the visual checks on the generators (using a steel rule) indicated they were approximately parallel, it was decided the co-ordinates used in the numerical analysis would be calculated values.

In addition, no check could be made upon the thicknesses of the layers of the hypar until the testing was completed.

Thus the thickness of the faces was assumed to be the same as that of the test specimens used to determine the elastic properties of the panels.

5.5 Material properties

5.5.1 The faces

A polyester resin was used with the glass fibre matting to form the faces. The resin had a number of desirable properties:

(i) Air bubbles trapped within the glass mat could be removed easily.

(ii) The resin wet the glass quickly.

(iii) The resin could be applied with a 2½ inch paint brush.

(iv) The rate of curing allowed sufficient time to apply a second layer when the first layer had not set completely.

The resin is commonly used in the construction of light weight boats. Other properties such as the electrical resistance, heat resistance, and translucency were unimportant in this application.

The glass matting used differed between the hypars in its weight per unit area.

For the hypars with c/a ratios of 1/6 ; 1/8 ; 0 the fabric was:

> QZ, loomstate, nominally 0.010 ins. thick, weighing 322.39 gm per square metre.

For the hypars with c/a ratios 1/12, 1/24 the fabric was:

> "Strand" Glass open weave fabric weighing 330 gm per square metre.

The resin for all the hypars was "Siesta" polyester resin.

The curing times for all the hypars was twenty-four hours for the first face, and forty-eight hours for the second face.

The longer time allowed after the formation of the second face was to ensure that the completed hypar had fully cured.

To determine the Young's modulus of the face material a number of tests using a standard shaped specimen shown in Figure 5.6 were performed.

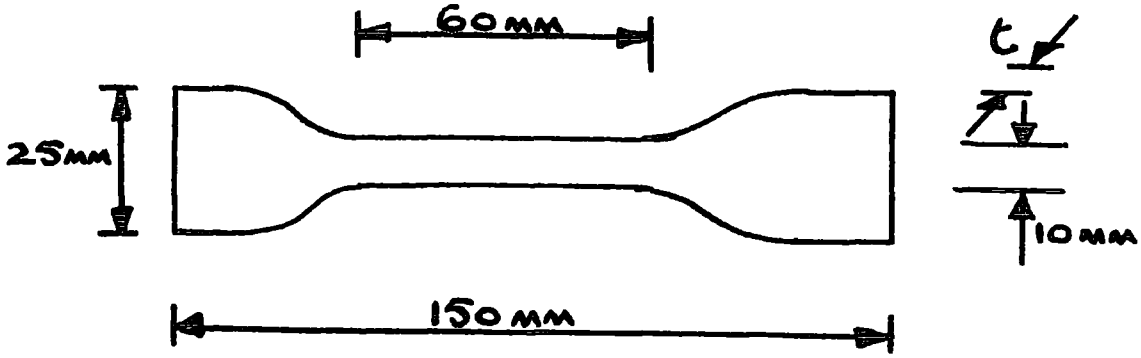

Figure 5.6

These specimens were formed using the same materials and mix of resin as the hypars.

The specimens were taken at varying angles to the direction of the weave in the fabric, including where there was an overlap of the fabric.

The dimensions of the test pieces were constant in plan, but the thickness varied, resulting from the method of application of the resin.

This variation was ±10% on the average thickness of 2.09 mm.

Young's modulus from the test specimens varied similarly, the median value was $6.56 \times 10^9 N/m^2$ with a variation ±30%.

Unfortunately this variation could not be attributed to a given test specimen at a given orientation with respect to the direction of the weave, nor to a particular set of specimens for a given mix of resin, so the choice of Young's modulus and thickness of layer was set for all panels at the median values.

There was a similar variation of both thickness and Young s modulus for both fabrics.

Poisson's ratio was set at 0.3 following the values in Finney (40) for a 'rigid' plastic.

5.5.2 The core

The polyurethane core has been used extensively by other researchers (20, 43, 51) and no testing of its properties was done.

The value of shear modulus used for the numerical analysis was taken to be $2 \times 10^6 N/m^2$

5.6 The loading and displacement measurements

5.6.1 The loading

The loading was applied at points on the hypar using the loading crabls of Figure 5.1.

A hole 3/16 in. in diameter (4.5 mm) was drilled through the panel, sufficient to allow the 1/8 in. (3 mm) rod to pass through the panel unhindered.

The loading platform was set over the hole and adjusted by means of the legs until it was level. The legs were then locked with the nuts, and fixed by plasticine on to the panel. The rod was placed on the platform using the steel collets (Figure 5.1) and the dial gauge mounted over the top collet cover.

At the lower end of the rod a jacking arrangement was used to ensure the loads were uniformly applied and removed.

5.6.2 The Displacements

The displacements were measured at grid points using dial gauges. The position of these gauges was determined by the load, taking into account any symmetry.

The gauges were mounted on a Dexion framework attached to the outer frame. Extra gauges were placed upon this dial gauge frame to check for movement which would affect the accuracy of the results.

The details of the load points and the position of the dial gauges is given in Chapter 6 where a comparison is made between the practical and numerical results.

5.7 Edge conditions for the test hypars

The hypars formed using the method described in Section 5.3 were four feet square in plan, but because of the construction of the faces they were unsuitable for testing.

A new box was built (Figure 5.5) with its dimensions as a metre square in plan, and with the calculated rise for each hypar.

This support box was screwed on to the Dexion framework with the sloping sides uppermost (the reverse of that shown in Figure 5.5).

The hypars reduced to a metre square were placed on to the box, and the "simple supports" of Figure 5.4(c) were attached loosely by screws through the support and panel, into the box. This meant that rigid body movement of the test panels was not permitted, but any rotation of the edges was permitted.

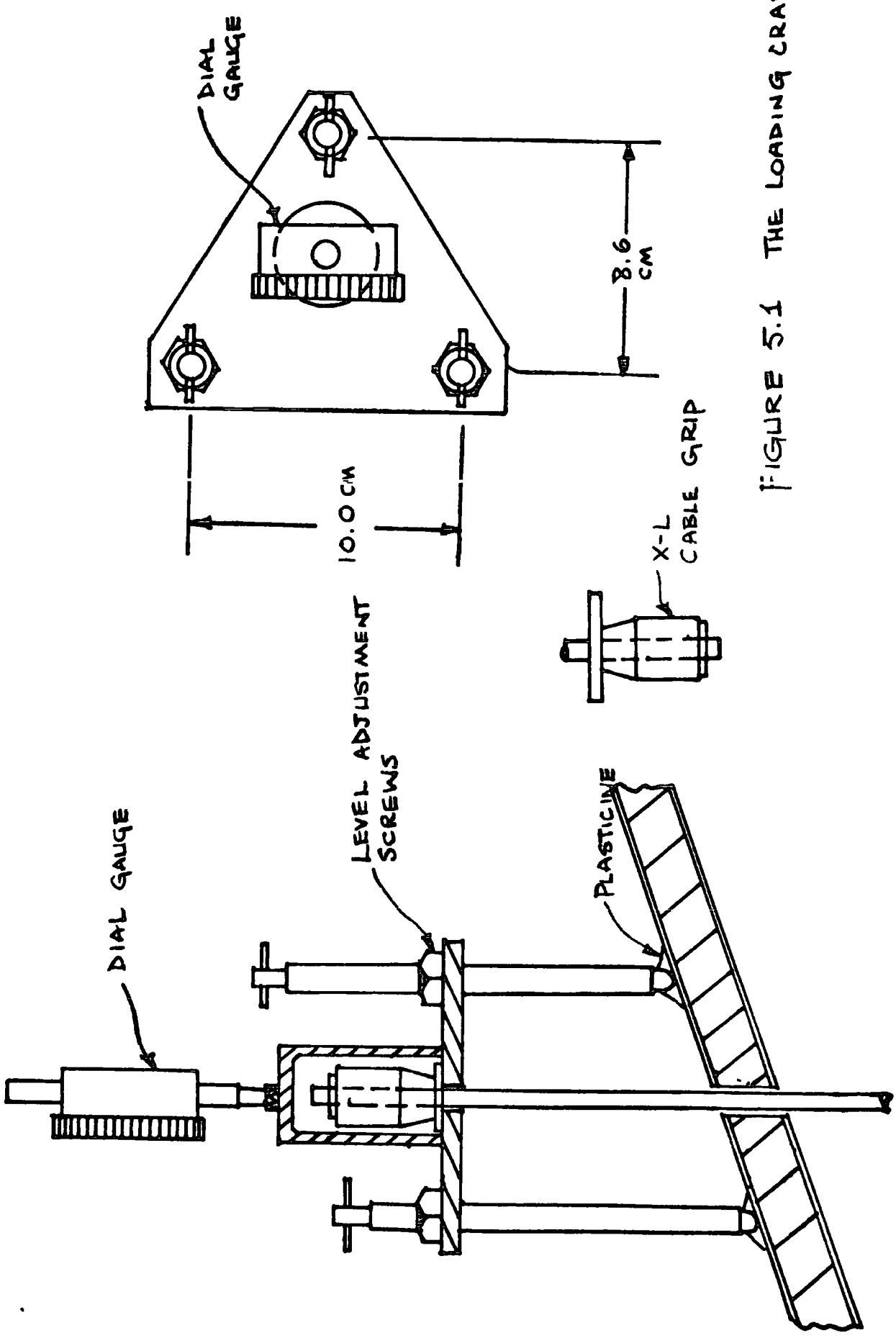

FIGURE 5.1 THE LOADING CRAB

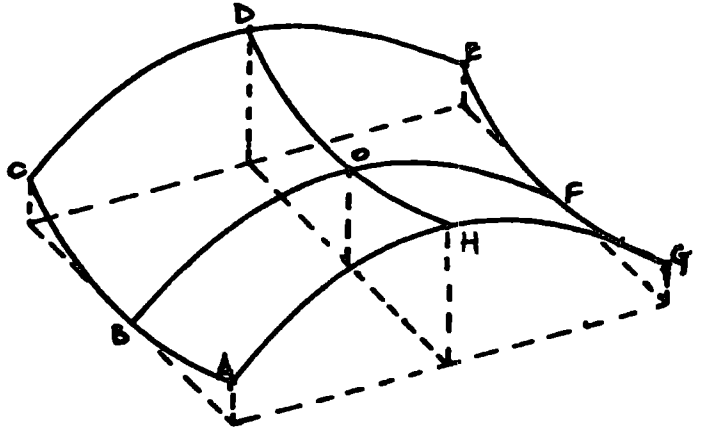

FIGURE 5.2(a)
HYPAR AS A SURFACE OF TRANSLATION

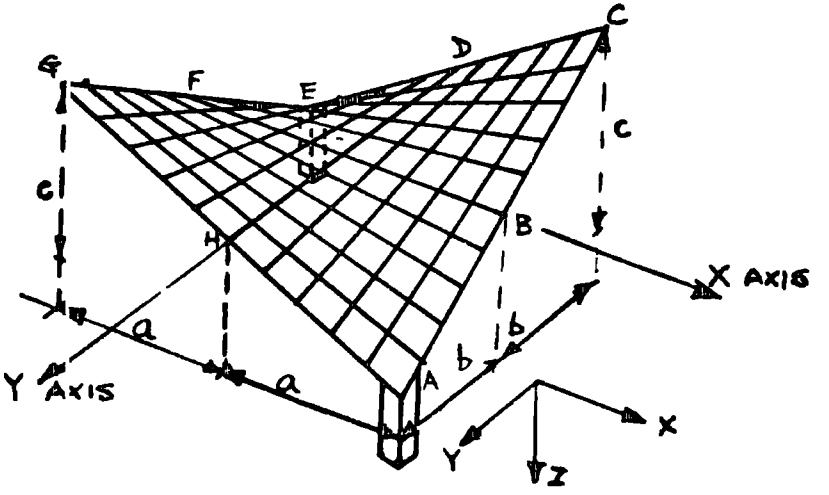

FIGURE 5.2(b)
HYPAR AS A WARPED PARALLELOGRAM

FIGURE 5.2 · THE TWO GEOMETRIC FORMS OF THE HYPERBOLIC PARABOLOID

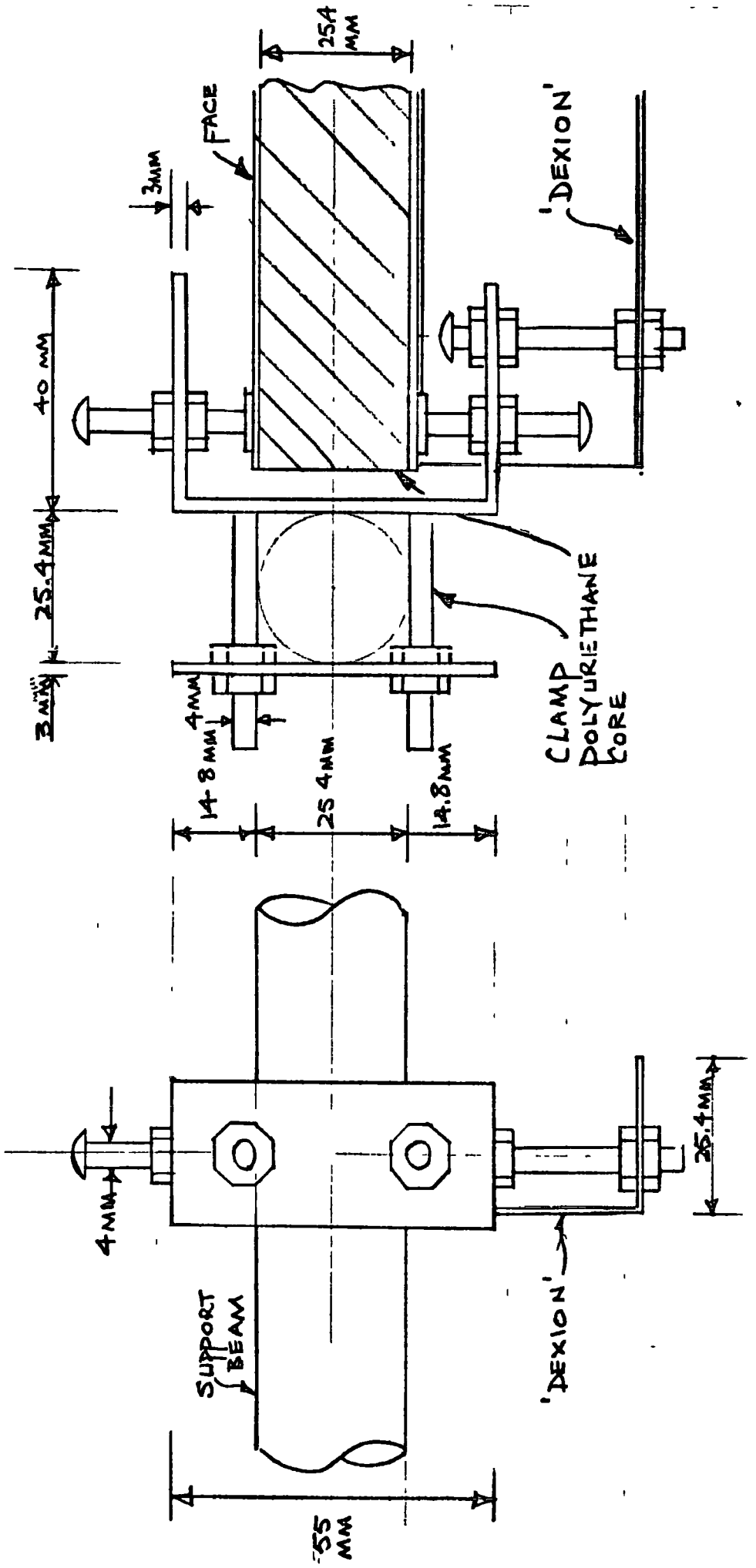

FIGURE 5.3 : CLAMPING CONFIGURATION HARDBOARD AND POLYURETHANE SANDWICH

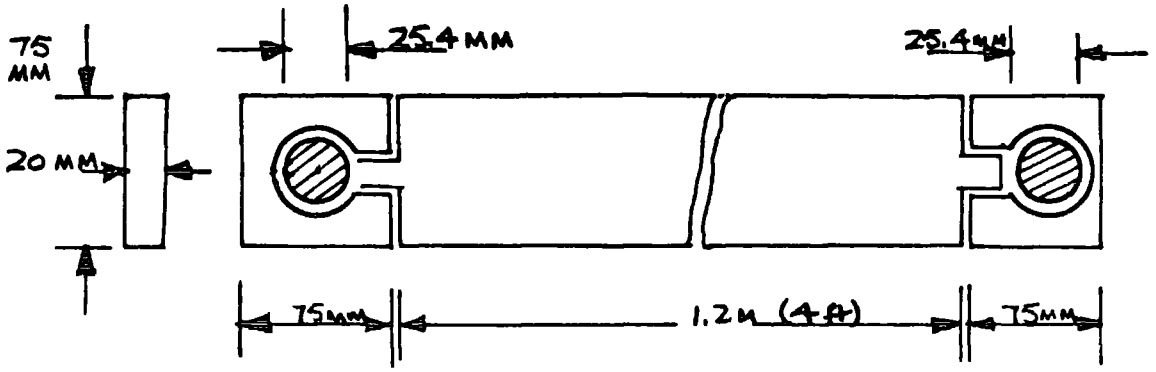

5.4(a) SUPPORT BEAM AND RUNNER

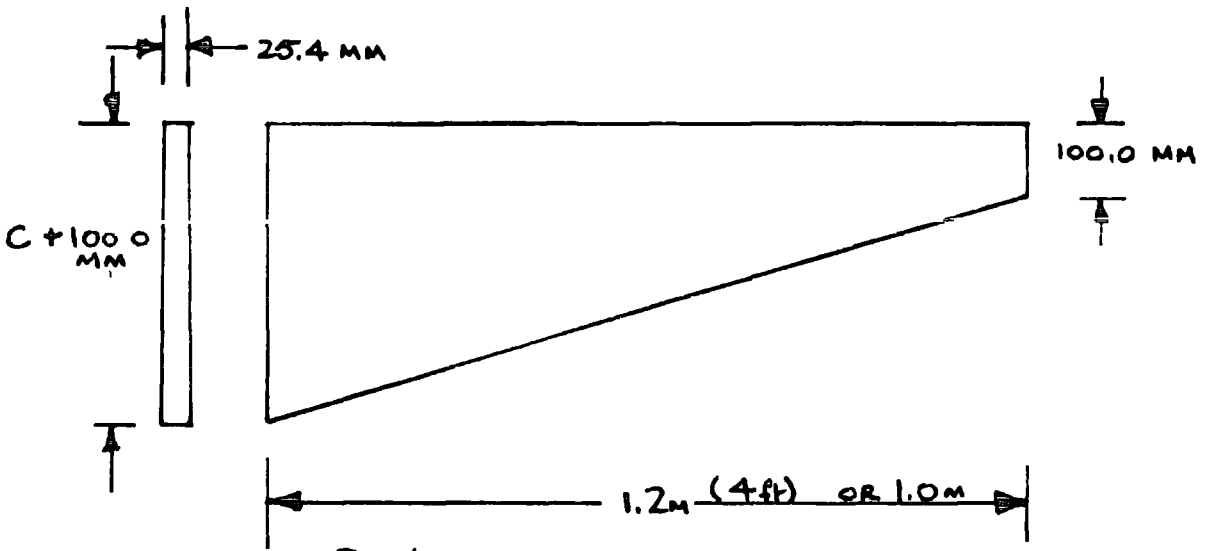

5.4(b) BOX FORMER OR SUPPORT

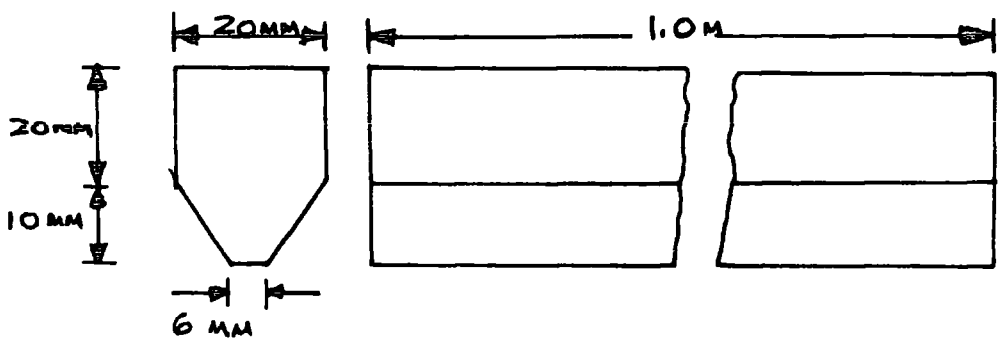

5.4(c) THE SIMPLE SUPPORT

FIGURE 5.4 DETAILS OF THE SUPPORT BEAM, BOX FORMER, SIMPLE SUPPORT (NOT TO SCALE)

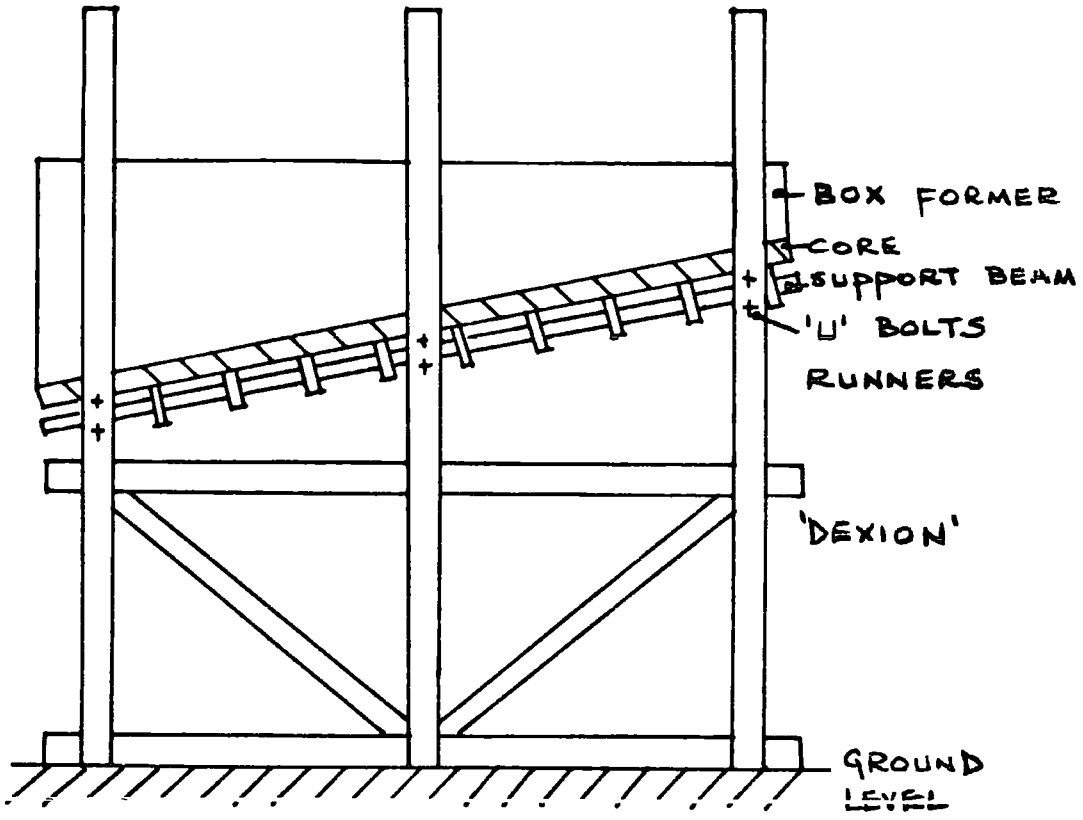

FIGURE 5.5 (a)

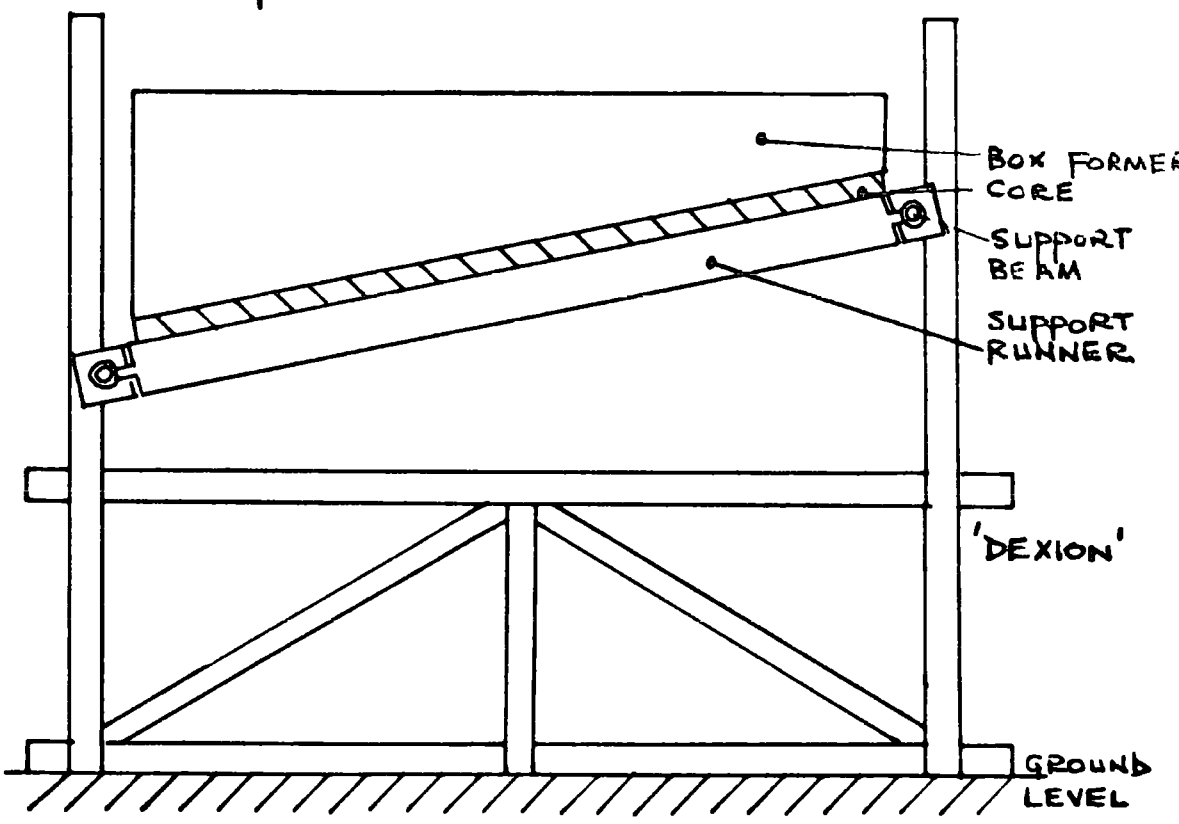

FIGURE 5.5 (b)

FIGURE 5.5 · SCHEMATIC SECTIONS OF THE 'DEXION' CONSTRUCTION FRAME

6. COMPARISON BETWEEN FINITE ELEMENT RESULTS AND EXPERIMENTAL RESULTS FOR THE SANDWICH HYPARS.

6.1 The Finite Element Analysis

All the meshes of elements used were rectangular, being square in plan. Figures 6.1.1 and 6.1.2 show the eight by eight mesh used for most of the results. Other meshes were 5 x 5, 6 x 6 and 10 x 10. The numbers on all the figures refer to the ten by ten mesh used for the experimental results. Figure 6.1.2 shows the element numbering, and the position of the load points.

As the panels tested experimentally were simply supported, the boundary conditions for each of the edges were:

$W , \theta_y = 0.0$ along edges parallel to the x axis

$W , \theta_x = 0.0$ along edges parallel to the y axis

These boundary conditions were sufficient to represent the constraints along the edges of the panel, but to remove rigid body movement both u and v were constrained at the two low corners, and u constrained at node 111. As will be seen later, the lack of symmetry of these constraints produces a corresponding lack of symmetry for the in plane displacements and stresses. Also the two low corners are effectively clamped, which is not truly representative of the experimental hypars.

As the mesh used most frequently was eight by eight, the point loads applied when loading the tension and compression paraboloae needed an extra calculation to produce nodal equivalent forces. This was accomplished using the virtual work principle applied from Chapter 2. The work done by a virtual displacement and the equivalent nodal forces was equated to the work done by the applied load on the element and its virtual displacement. The relationship between the virtual displacements was determined from the displacement function.

The output from the finite element programme consisted of the three translations of the mid-surface u, v, w and the two rotations of the thickness vector, α and β . These rotations for the flat plate sandwich element represent the rotations θ_x and θ_y where: (Figure 6.1.3)

$$\theta_x = \frac{\partial w}{\partial x} - \gamma_x$$

$$\theta_y = \frac{\partial w}{\partial y} - \gamma_y$$

The stresses output from the programme were σ_x, σ_y , τ_{xy} , τ_{xz} , τ_{yz} all evaluated at the integration points and calculated with the relevant Elasticity matrix. The Global co-ordinates of the integration points and the direction cosines of the local orthogonal axes are also output. A programme was written to output the Moments and shear forces assuming plate behaviour, and the relationships of 3.3.9.

6.2 Convergence

The convergence of the element was checked by comparing the vertical displacements predicted by the numerical model with the experimental results. Both sets of values obtained for the hypar with c/a equal to one eighth.

It was obvious for even the coarse mesh (5 x 5) that the displacements away from the point of application of the load showed good agreement, but under the load very poor agreement. Figures 6.2.1 and 6.2.2 show results for the vertical displacements on x axis and the compression parabola using the different meshes. As the mesh is refined the discrepancy in displacements under the load point (node 61) gets worse, but improves for points away from the load. Both the 8 x 8 mesh and the 10 x 10 mesh produce agreement for points away from the load, within the accuracy expected from the experimental results.

It was decided to use the eight by eight mesh of elements to model the hypars, neglecting the results produced at the load point.

In all the other load cases the model required a set of equivalent nodal forces due to the point of application of load being within the element boundary. Agreement between experiment and numerical analysis was acceptable for the loads applied to the compression and tension parabolae separately, but not so for the four point load case. The mesh was refined further (10 x 10) for this final load case.

6.3 The Experimental Results

The results obtained from the hypars were restricted to vertical displacements. The in plane displacements were an order of magnitude smaller than the vertical displacements. The magnitude of the loads applied to the hypars was increased in steps of 5 kg. to 20 kg. for the shallower hypars (c/a = 1/24, 1/12) with a maximum load of 25 kg. for the steeper hypars (c/a = 1/8, 1/6).

At the four load points of the final case the loads were identical, with an increment of 2 or 3 kg. up to a maximum of 20 kg. for each point.

The measured displacements proved to be non-linear. For a single load on the panel the values of vertical displacement under the load were linear up to 10 kg.

At the higher loads (20 kg. and 25 kg.) the measured displacement was up to 10% greater than that predicted by the initial elastic response. The four point load produced similar results. The initial linearity stopped at 5 kg. per point, and the measured displacement was up to 20% greater than the extrapolated value assuming the initial elastic behaviour.

This non-linearity is attributed to the local pinching which occurs under the load, and the time dependent behavour of the panels.

The first cause is a local effect which the loading crab is intended to reduce. The second is the result of the materials used in the construction of the hypars.

The displacement can be considered as having an elastic component and a visco-elastic component. Figure 6.3.4 shows the central deflection against time for the hypar (c/a = 1/12) with a constant load of 20 kg. applied to the centre of the hypar. The figure gives an indication of the error which can be introduced due to the time at which the displacements are taken.

A standard procedure was adopted:

(i) The panel was loaded;

(ii) Two minutes allowed for the distribution of the load;

(iii) Readings from the dial gauges taken;

(iv) The panel was unloaded;

(v) Fifteen minutes was allowed for the panel to recover its initial geometry;

(vi) The procedure is repeated for the next increment of load.

The length of time allowed after unloading was sufficient to enable the hypars to return to their original geometry. For the larger loads (20 kg., 25 kg.) and the four point load case this recovery time was increased to half an hour.

Parton (51) shows that the visco-elastic displacement occurs within the first few minutes of application of the load, for the pyramid structures he tested. The single test performed on the hypar indicates that this may well not be the case for these structures, the visco-elastic component of displacement occurring over several minutes after the application of load.

To minimise these effects it was decided to reduce the magnitudes of the applied loading. The reduction in applied load results in smaller displacements, with a corresponding reduction in the strains. The smaller strains, and variability of material properties meant that strain gauges were not used.

Figure 6.3.2 shows the positions of the dial gauges and load points for the experimental results. The positions of the dial gauges varied depending upon the load. Generally they are concentrated near to the load point with checks also being made upon the symmetry.

The displacements of points symmetrically placed with respect to the geometry and loading were found to be within 5% of each other for the single load cases, and 10% for the four point load.

For the larger loads (20 kg. and 25 kg.) applied to the hypars the measuring procedure would result in the displacements being 10% greater than the initial instantaneous displacement. A reduction of 10% for the vertical displacements would produce results which would more closely follow the initial elastic response.

6.4 Comparisons for the Central Point load

Figures 6.4.3 to 6.4.7 show isometric drawings of the vertical displacements for both the experimental and numerical analyses. Profiles common to the two meshes are drawn separately (Figures 6.4.8 to 6.4.15). A comparison showing the effect of rise of hypar for the vertical displacement along the x axis is shown in Figure 6.4.1, and for the x displacement along an edge in Figure 6.4.2.

As the rise of the hypars increases the vertical displacements reduce, and the in plane displacements increase with good agreement between numerical and experimental results. Figures 6.4.3 to 6.4.7 show that the area over which most of the vertical displacement takes place is reduced, with the tendency to concentrate closer to the point of loading. The experimental results show an overall reduction of 30% in the vertical displacements comparing the flat plate (c/a = 0) and the steepest hypar (c/a = 1/6) (Figure 6.4.1).

Due to the lack of symmetry in the in plane constraints the in plane displacements were greater when approaching the corner which had only the vertical displacement and rotations constrained (node 11 Figure 6.1.2). This did not produce a lack of symmetry in the vertical displacements.

Figures 6.4.8 to 6.4.15 demonstrate that the finite element results tended to be too stiff, but as the experimental results are produced from all the loading applied to the panels they include the non-linear effects described in Section 6.3.

A reduction of 10% in the experimental results would give closer agreement with the finite element results.

6.5 Comparisons for the tension and compression parabola load cases.

Isometric drawings of the vertical displacements for the tension parabola load case are shown in Figures 6.5.1 to 6.5.5. Individual profiles are shown in Figures 6.5.6 to 6.5.12. For the compression parabola load case the individual profiles are shown in Figures 6.5.13 to 6.5.19.

The results for both these load cases were similar in form, the vertical displacements being slightly greater in the compression parabola load case. The peak displacements reducing by 26% comparing the flat plate displacement

(c/a = 0) with the steepest hypar (c/a = 1/6) in the tension parabola load case, and 30% in the compression parabola load case. For both these load cases the eight by eight finite element mesh produces good results for the vertical displacements, following the reduction in displacement as the rise of hypar increases. As with the central point load case there is a tendency for the vertical displacement to concentrate closer to the point of loading as the rise increases, and for the in plane displacements to increase.

6.6 Comparison for the four point load case

Isometric drawings are shown in Figures 6.6.1 to 6.6.5. This load case shows large discrepancies between experiment and finite element results, even with the refined mesh of elements (10 x 10).

The main reason is the non-linear behaviour of the panels which is accentuated in this case. The time taken to apply the loads is greater than for the single load case, increasing the non-linear displacement, and the magnitude of the applied loads was four times that of the single load case.

The results for the hypar c/a = 1/24 (Figures 6.6.7 to 6.6.9) show good agreement. This is due to the much smaller loads applied to this panel. The loads used to calculate these results did not exceed 10 kg./pt. but for the other hypars up to 20 kg./pt. were used.

As a check against non-linear effects the experimental results for the single point load cases, on the tension and compression parabolas, were superposed and these are plotted for the hypar c/a = 1/12 (Figures 6.6.10 to 6.6.12) with closer agreement to the finite element results. The discrepancy in displacement between the finite element results and the experimental results is of the order of 30% and sometimes closer to the load as much as 50%.

The combination of the larger displacements and a steeper stress gradient near the load points suggest that the element mesh round these points should be refined further.

The larger displacements may result in geometric changes which, being of the order of a face thickness, would make a large displacement analysis more applicable. Although the current programme is not able to perform a large displacement analysis the isoparametric form of the element would enable variations in geometry to be accounted for relatively easily.

6.7 The Stresses

As no strain gauges were used on the hypars there is no check upon the stresses predicted by the finite element programme. The Moment (M_x) and Shear force (Q_y) are shown for each load case in Figures 6.7.1 to 6.7.4. The results clearly show the marked reduction in the stresses as the rise is increased.

In Chapter 4 the shear stiffness parameter γ_x was varied between 25 and 500 and the stress resultants show close agreement for $\gamma_x \geq 50$. This parameter for the sandwich hypars tested was between the limits of 40 and 100. Following the analysis performed on the Chapman and Williams plates the predicted values of Shear and Moment may be low.

All stresses are evaluated at the integration points, and the values plotted refer to the integration points closest to the centre line, or edge.

To ensure symmetry for both displacements and stresses the corners of the hypars were all clamped.

Under most practical circumstances a hypar would have edge beams which would resist translation along their length, and provide the means by which membrane loads can be transmitted to the high and low corners of the shell. It was shown by Kerentsky (37, 38) that for the timber hypars he investigated, the edge beams determined the moment distribution within the shell.

As the stiffness of the edge beam increased there was corresponding increase in the area which could be assumed to be momentless, and a membrane analysis would be sufficient for design purposes.

The simple support conditions used in the author's analysis have no stiffness in the direction normal to an edge, and rotations about the edge are not suppressed. The effect of the support is clearly shown in the moment distribution shown in Figures 6.7.1 to 6.7.10. There is a reduction in the bending moments but they are still significant even for the steepest hypar. The form of the moment distribution corresponding more to the flat plate tested than a shell.

Figure 6.7.6 shows that the bending moment Mx (x axis) at the edges of the panel follow the flat plate solution, and only at the centre of the shell is the moment reduction more significant (50% reduction).

The bending moment My (x axis Figure 6.7.8) shows a similar reduction to Mx in the centre of the shell but as the edges are approached there is significant decrease in the bending moments, even for the shallowest hypar (c/a = 1/24).

At the edge the hypar has a bending moment one tenth of the flat plate moment. The redistribution of the load is in the membrane force Nxy (Figures 6.7.11 and 6.7.12).

The transverse shear forces (Figures 6.7.1 to 6.7.4) show a reduction at the edges of about 25% comparing the steepest hypar to the flat plate.

At the centre of the shell where the geometry more closely resembles the flat plate the loading is distributed by the moments, and membrane shear. As the edges are approached there is a reduction in the moment, with a rapid build-up of membrane actions. The normal membrane loads, because of the boundary conditions, are then forced to die away, with a redistribution to the membrane shear, especially at the clamped corners.

The solution for the stress resultants shows that the distribution of the applied loads to both the membrane loads and bending moments, instead of just the bending moments of the flat plate, results in a more efficient structure caused by the geometric form of the shell. Its shape results in the increase of strain energy caused by the membrane displacements being less than the reduction caused by the change in transverse displacements.

As the rise of hypar increases this comparison with the flat plate improves further. It is also clear that the simple support causes a complex distribution of the moments, and membrane forces.

It is suggested for future work that clamped boundary conditions be used, followed by edge beams with varying degrees of stiffness. In addition, it is suggested that a uniformly distributed load be applied as well as point loads.

7. CONCLUSIONS

The areas of work presented in this thesis cover the development of a sandwich shell analysis capability, and the correlation between the experimental and numerical modelling of hyperbolic paraboloid sandwich shells.

The finite elements developed to form the analysis capability can be critisized for a number of reasons, but have the merit of being easy to develop. The disadvantages associated with the elements are due to modelling each layer of the sandwich independently, the geometry and displacement functions being different for each layer. This results in the numerical integration requirements, even using a reduced integration order, being large.

Immediate improvements could be made by a closer investigation of the numerical procedure, explicitly performing the integrations with respect to the thickness co-ordinate. The description of the sandwich elements in Appendix C partly achieves this as the assemblage of the matrix relating the strains to the unknown displacements can be partitioned, and the number of operations to form the stiffness matrix reduced.

The current elements allow a sandwich shell to have differing layer thickness and material properties. The penalty is paid in the quantity of additional data required.

An additional limitation is that the faces are assumed to have no transverse shear stiffness which imposes limitations in the general applicability of these elements.

In the development of these elements immediate gains could be made by reducing the integration further, and including transverse shear displacements within the faces. If transverse shear is unimportant within the faces then an approach similar to the "semi-loof" shell elements may produce an even more refined analysis.

As a longer term development it would be possible to develop a large displacement capability. The isoparametric form of the elements allows modifications to be made to the geometry of the structure relatively easily. The initial solution for the displacements could be made to modify the co-ordinates of the nodal points and a further analysis executed.

This does have other implications in that the performance of isoparametric elements is reduced if the area modelled by the element becomes too distorted. A check would be necessary to accommodate this, perhaps even using routines which would automatically refine the mesh if the distortion was too great.

Given the facility to refine the mesh in an iterative procedure it could also be used if the stress distribution from the initial solution became excessive across an element. The criteria for refining the mesh would become functions of both the geometric distortion and stress variation, both of which are related to the materials used.

The performance of the finite elements can be considered in two areas; firstly, of the analysis of sandwich problems, and secondly the analysis of shell problems.

The plate problems were shown to give good agreement for both displacements, and stresses. The comparisons with Abel and Popov, and Chapman and Williams were however, problems in which the boundary conditions and loading were well defined.

Abel and Popov's results included the effects of transverse shear within the faces which with the inclusion

of the extra rotations indicated in Chapter 3, the current element could accommodate. The effects of varying the integration orders within the layers showed no clear pattern, except that because of the displacement functions used it became necessary to specify two points within the thickness of a layer.

The plates analysed by Chapman and Williams using a finite difference solution showed the effects of increasing transverse shear. The comparison between the finite difference solution and the author's finite element produced close agreement for displacements and stresses.

The stresses diverged from Chapman and Williams' results when the transverse shear effect was extremely large.

The analysis of the sandwich hypars showed that the inclusion of bending effects is necessary, supporting the work of previous authors (10, 14, 26, 27, 60). This was reinforced especially as a result of the boundary conditions. Thus, the situation where a simplified analysis in which the central area of a hypar is considered momentless, was shown to be inapplicable.

The 'simple' support edge conditions imposed for all the hypars and the flat plate, were such that no direct force could be carried perpendicular to them, and at elements other than at the corners no direct force could be carried along them.

This restriction is unimportant for the flat plates as none of the applied load is distributed by membrane forces. For the hypars, however, this results in constraints upon the distribution which in a practical situation would not exist. The bending moments and twisting moment are reduced but remain significant within the central area of shell. The direct membrane forces are forced to rise to peak values within the quadrants of the hypar, and to die away quickly to zero at the edges.

The remaining loading is by membrane and transverse shears. In both cases the effect at the clamped corners is marked, the membrane shear increasing steeply as it approaches the corners and in the twisting moment which, when approaching the corners, changes sign.

This results from the corners restraining the in plane displacements, the variation of which is greatest as the corners are approached. The transverse shear force is also reduced, again following that of the flat sandwich plate. This reduction is due to the increase in membrane loading, and is an indication of the improved performance of the hypar shells compared to the flat plate, the change in sign apparent in the steepest hypar is caused by the panels wishing to lift off the edge supports.

The effect upon the distribution of loading within the hypars due to the edge conditions is great. Future work should, therefore, include a detailed analysis of these effects, a more refined mesh of elements being used, especially at the corners.

An additional topic could be the analysis of the hypars using different edge beams. Defining the effects of the beams upon the hypars could be achieved either by developing a beam element compatible to the finite elements used, or using Lagrange multipliers to define the associated boundary conditions.

The divergence between the experimental results and numerical analysis has been suggested to be the result of the non-linear behaviour of the panels. This non-linearity is caused by the materials used. To enable the elements to perform a creep analysis would require a large reduction in the computational effort involved in forming them, and in their present form would appear to be unsuitable.

The modelling of the material properties of the hypars could be significantly improved. This results

from the ability of the element to have differing properties for each layer. The large variation found for Young's modulus could be represented accurately, and if material testing showed that different values were obtained for compression compared to tension this could also be modelled. Also, no account is taken of the different values obtained as a result of different fibre densities, or orientation. The choice of materials with well defined properties would enable a more accurate comparison between the numerical analysis and the experimental results to be made, but the constructional difficulties indicated in this work need to be overcome.

Finally, the analysis of the hypar sandwich shells shows the effect of the double curvature is to improve both the load carrying capacity and the displacements.

The combination of this fact with a shape which is aesthetically pleasing produces a structural form which should be given more serious consideration, especially if the application requires the use of light weight materials.

REFERENCES

(1) Abel, J. F., and Popov, E. P., "Static and Dynamic finite element analysis of sandwich structures". Proceedings of the Second Conference on Matrix Methods in Structural Mechanics, Wright Patterson Air Force Base, Dayton, Ohio, 1968. AFFDL-TR-68-150.

(2) Ahmad, A., Irons, B. M., and Zienkiewicz, O. C., "Analysis of thick and thin shell structures by curved finite elements", International Journal of Numerical Methods in Engineering, Vo.2 pp.419-451, 1970.

(3) Allen, H. G., "Analysis and design of structural sandwich panels", Pergamon 1969.

(4) Barnard, A. J., "A sandwich plate finite element", Loughborough University of Technology.

(5) Basu, A. K., and Dawson, J. M. "Orthotropic sandwich plates", Proceedings of the I.C.E. 1970.

(6) Beg, M. I., "Finite Difference Approach to Hyperbolic Paraboloids", Proceedings American Society of Civil Engineers, pp.429-445, 1972.

(7) Beisinger, Z. E., and Key, S. W., "The analysis of thin shells with transverse shear strains by the finite element method", Proceedings of the Second Conference on Matrix Methods in Structural Mechanics, Wright Patterson Air Force Base Dayton, Ohio, 1968. AFFDL-TR-68-150.

(8) Bettess, P., "Analysis of polyhedral dome structures composed of flat plates of sandwich materials", Ph.D. thesis, University of Durham 1971.

(9) Bond, Swannell, Henshall and Warburton, "Comparison of some curved two-dimensional finite elements", Jnl. of Strain Analysis, Vo.8, No.3, 1973.

(10) Bouma, A. L., "Some Applications of the bending theory regarding Doubly Curved Shells.", Proc. Symposium on the theory of thin elastic shells, pp.202-234, North Holland Publishing Delft 1959.

(11) Brebbia, C., "On Hyperbolic Paraboloid shells", Ph.D. thesis, University of Southampton 1968.

(12) Candela, F., "General Formulas for membrane stresses in Hyperbolic Paraboloid Shells", Jnl. Am. Conc. Inst. Vol. 4, pp.353-371, 1960.

(13) Chapman, J. C., and Williams, D. G., "Effect of shear deformation on uniformly loaded rectangular orthotropic plates", Proc. I.C.E. 1969.

(14) Chetty, S. M. K., and Tottenham, H., "An Investigation into the bending analysis of hyperbolic paraboloid shells", Indian Concrete Journal, July 1964, pp.248-258.

(15) Cook, R. D., "More on reduced integration and isoparametric elements" Int.Jnl. for Num. Methods in Engineering, Vol.5 pp.141-142 1972.

(16) Cook, R. D., "Two hybrid elements for analysis of thick thin and sandwich plates. Int.Jnl. for Num Methods in Engineering, Vo.5, pp.277-288, 1972.

(17) Cowper, G. R., "Gaussian Quadrature formula for Triangles" Int.Jnl. Num. Methods in Engineering pp.405-408, 1973.

(18) Desai C. S., and Abel, J. F. "Introduction to the finite element method", Van Nostrand 1972.

(19) Doherty, W. P., Wilson, Ed., Taylor, R. L., "Stress Analysis of Axi-symmetric solids using higher order Quadrilateral Finite Elements." Structural Engineering Laboratory Report SESM 69-3, University of California, Berkely 1969.

(20) Elliott D. J., "Structural properties of flat sandwich panels." M.Sc. thesis, University of Durham 1969.

(21) Ergatoudis, J., Irons, B. M. Zienkiewicz O. C., "Curved, Isoparametric, Quadrilateral elements for finite element analysis." Int.Jnl. Solids and Structures, Vol. 7, 1968.

(22) Flugge, W., "Stresses in Shells", Springer-Verlay, 1962.

(23) Fried, I., "Some aspects of the Natural Co-ordinate System in the Finite Element Method.", AIAA Journal Vol. 7 No.7 pp.1366-1368.

(24) Gergely, P., and Winter, G., "Experimental Investigation of thin steel Hyperbolic Paraboloid Structures", Jnl. of Struct.Division. Am.Soc. of Civil Engineers 2165-2179, 1972.

(25) Holand, I., and Bell, K., "Finite Element Methods in Stress Analysis.", TAPIR, The Technical University of Norway, 1970.

(26) Hadid, H. A., and Tottenham, H., "Variational and Integral Methods for the Analysis of Hypar Shell."

(27) Hadid, H. A., "Bending Analysis of hyperbolic paraboloid shells." Int.Coll. on progress of shell structures in the last ten years and its Future Development. Madrid 1969.

(28) Irons, B. M., "Engineering Applications of Numerical Integration in Stiffness Methods." A.I.A.A.Jnl. Vol.4 1965.

(29) Irons, B. M., "The Semi-Loof Shell Element." Finite Elements of thin shells and curved members.

(30) Irons, B. M. "Round-off criteria in the direct stiffness method." A.I.A.A.Jnl. Vol.6, No.7 1969.

(31) Irons, B. M. "Computer program report No.7; Mark VI frontal assembly and solution for finite element scheme", Department of Civil Engineering, University of Swansea.

(32) Irons, B. M., "Numerical Integration applied to Finite Element Methods." Conf. on the Use of Digital Computers in Structural Engineering, University of Newcastle upon Tyne 1966.

(33) Irons, B. M., "A Frontal Solution program for finite element analysis." Int.Jnl. for Num.Methods in Engineering, Vol. 2, pp.5-32, 1970.

(34) Irons, B. M. and Razzaque, A., "A Further modification to Ahmad's shell element.". Int. Jnl. Num.Methods in Engineering pp.588-589, 1972.

(35) Irons, B. M. "Structural Eigenvalve Problems: Elimination of Unwanted Variables.". A.I.A.A.Jnl. Vol.3, pp.191-192, 1965.

(36) Kavanagh, K. T. and Key, S. W., "A note on selective and Reduced Integration Techniques in the Finite Element Method." Int. Jnl. Num. Methods in Engineering 4, pp.148-150, 1972.

(37) Kerentsky, L. O., "An Experimental Investigation into the Stress and displacement distribution in Hyperbolic Paraboloid Timber Shell Roofs." Timber Research and Development Association, Study E/S/2.

(38) Kerentsky, L. O., "The Edge disturbance and the free corner displacement of laminated timber Hypar shells bounded by straight generators." Timber Research and Development Association, Study E/S/1. 1965.

(39) Khatua, T. P., and Cheung, Y. K., "Bending and Vibration of Multilayer Sandwich Beams and Plates." Int.Jnl. for Num.Methods in Engineering Vol.6, pp.11-24, 1973.

(40) Kinney, G. F., "Engineering properties and applications of Plastics." Wiley and Sons 1964.

(41) Kolar, V., and Nemec, I., "The Efficient Finite Analysis of rectangular and skew laminated plates." Int. Jnl. for Numerical Methods in Engineering Vol.7, pp.309-323, 1973.

(42) Kreyszig, E., "Advanced Engineering Mathematics." Wiley 1967.

(43) Manos, G. C., "Analysis of Polyhedral Domed Sandwich Structures.", Ph.D. thesis, University of Durham 1975.

(44) Mawenya, A. S., and Davies, J. D., "Finite Element Bending Analysis of Multilayer Plates." Int.Jnl. for Num. Methods in Engineering, Vol.8, pp.215-225 1974.

(45) Melosh, R. J., "Basis for Derivation of Matrices for the Direct Stiffness Method.", A.I.A.A.Jnl. Vol.1, No.7, July 1963.

(46) Meyers, V. J., Ramani, D. T., Greenwood, M. E., "Plastic Sandwich Buckle-Shell Structures." Jnl. of Struct. Div. Am.Soc. of Civil Engineers 2381-2397, 1972.

(47) Mohraz, B., "A lumped parameter element for the analysis of hyperbolic paraboloid shells." Int.Jnl. for Num. Methods in Engineering, Vol.4, pp.235-249, 1972.

(48) Monforton, G. R., and Schmidt, L. A., "Finite Element Analysis of sandwich plates and cylindrical shells with laminated faces." Proc. Second Conference on Matrix Methods, Wright Patterson Air Force Base, Dayton, Ohio, 1968, pp.573-614.

(49) Newton, R. E., "Degeneration of Brick-Type Isoparametric Elements." Int.Jnl. Num. Methods in Engineering, pp.579-581, 1973.

(50) Novozhilov, V. V., "Thin Shell Theory" Wolters-Noordhoff Publishing pp.94-104.

(51) Parton, G. M., "The Structural Behaviour of Polyhedral Sandwich Shells." Ph.D. thesis, University of Durham 1974.

(52) Pawsey, S. F., "A discussion of references 62 and 51" Int.Jnl. of Num. Methods in Engineering Vol.4, pp.449-450 1972.

(53) Pawsey, S. F., and Clough, R. W., "Improved Numerical Integration of thick shell Finite Elements." Int. Jnl. for Num. Methods in Engineering. Vol.3, pp.575-586, 1971.

(54) Plantema, F. J., "Sandwich Construction", Wiley, 1967.

(55) Pryor, C. W., and Barker, R. M., "A Finite Element Analysis including transverse shear effects for Applications to Laminated Plates", A.I.A.A.Jnl. Vol.9, No.5, pp. 912-917, 1971.

(56) Przemieniecki, J. S., "Theory of Matrix Structural Analysis", McGraw-Hill 1968.

(57) Takemoto, H., and Cook, R. D., "Some modifications of an Isoparametric Shell Element." Int.Jnl. Num Methods in Engineering pp.401-405, 1973.

(58) Timoshenko, S., and Woinowsky-Krieger, S., "Theory of plates and shells.", McGraw-Hill.

(59) Tong, P., and Pian, T. H. H., "The Convergence of Finite Element Method in solving linear elastic problems.", Int. Jnl. Solids Struct. 3, pp.865-879, 1967.

(60) Tottenham, H., "The Analysis of Hyperbolic Paraboloid Shells - Membrane (Momentless) Condition." Timber Research and Development Association, Research Report E/RR/5 1958.

(61) Tottenham, H., and Brebbia, C. A. "Finite Element Techniques in Structural Mechanics." Southampton University Press, 1970.

(62) Yang, T. Y., "High Order Rectangular Shallow Shell Finite Element.", Eng.Mech.Division, Proceedings of Am.Soc. of Civil Engineers, pp.157-181, 1973.

(63) Zienkiewicz, O. C., and Hollister, G. S. "Stress Analysis", Wiley 1965.

(64) Zienkiewicz, O. C., Taylor, R. L., and Too, J. M., "Reduced Integration Technique in General Analysis of Plates and Shells." Int.Jnl. for Num Methods in Engineering Vol.3, pp.275-290, 1971.

(65) Zienkiewicz, O. C., "The Finite Element Method in Engineering Science.", McGraw-Hill 1971.

(66) Anon. "Elementary Analysis of Hyperbolic Paraboloid Shells." Concrete Information, Portland Cement Association 1960.

APPENDIX A

Serendipity shape functions used in the isoparametric sandwich shell element

In Chapter 3 the definition of the displacement functions (equation 3.3.3) and the assumed variation of the geometry (equation 3.2.4) depend upon the definition of the shape functions. Shape functions are defined in terms of the local co-ordinates within an element, having the property that at a specific node they take the value of unity and at all other nodes the value of zero.

For an isoparametric formulation the assumed variation of the unknown displacement function is identical to the geometric variation. As the hypars are quadratic in x and y, this implies the shape functions must be at least quadratic. Also in defining the displacement function the choice of an assumed quadratic variation for the unknown displacements allows for a linear variation in strain components, and hence the stresses, over an element.

By going to even higher orders of shape function the element can be made to allow for higher orders of variation in the displacements and strain components, but the penalty paid is in numerically integrating the stiffness matrix, a higher number of Gauss points being required to account for the more complex variation.

Both the quadrilateral and triangular elements used in this work have an assumed quadratic variation of shape function.

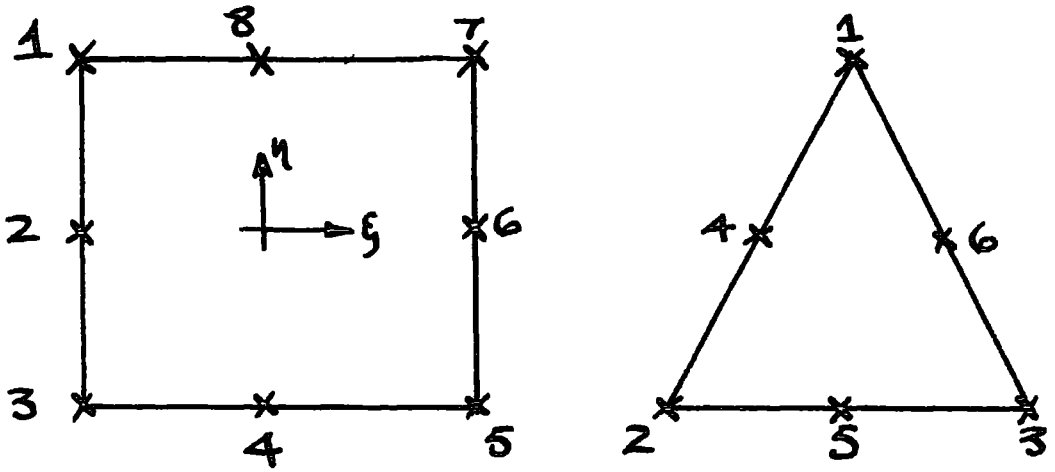

(a) (b)

Figure A.1

The quadrilateral element Figure A.1(a) has shape functions:-

Corner nodes: $$N_i = \frac{1}{4}(1+\xi_0)(1+\eta_0)(\xi_0+\eta_0-1)$$

Mid-side nodes:

$$\xi_i = 0.0 \quad N_i = \frac{1}{2}(1-\xi^2)(1+\eta_0)$$

$$\eta_i = 0.0 \quad N_i = \frac{1}{2}(1-\eta^2)(1+\xi_0)$$

where $$\xi_0 = \xi\xi_i \qquad \eta_0 = \eta\eta_i$$

The triangular elements used Areal co-ordinates (Figure A.1(b) and the shape functions are:

Corner nodes: $$N_i = (2L_i - 1).L_i \quad i=1,3$$

Mid-side nodes:

$$N_4 = 4L_1L_2$$

$$N_5 = 4L_2L_3$$

$$N_6 = 4L_1L_3$$

These shape functions are chosen to preserve both continuity of displacement, and the condition that any arbitrary value of first derivative (constant strain criterion) should exist.

As the shape functions are quadratic in ξ and η the first condition is satisfied by the three nodes along an edge being identical to the three defined in an adjacent element.

This is due to the three nodal points determining a unique quadratic function.

The second requirement of constant first derivative is met so long as the shape functions retain all the linear terms. In the case of the quadrilateral and triangle the unknown displacement function ϕ is expressed as

$$\phi = [N_i] \begin{Bmatrix} u_i \\ v_i \\ w_i \end{Bmatrix}$$

where the N_i are functions of ξ, η or L_1, L_2, L_3 and u_i, v_i, w_i are the nodal values. The constant strain requirement states that

$$\frac{\partial \phi}{\partial \delta} = \text{constant.}$$

The derivative of the displacement with respect to the unknown δ must be a constant. In the finite elements used in this work ϕ is the function u, v, w, the displacement function and δ is a global direction (x, y or z).

As the isoparametric form defines a unique relationship between x, y and z and ξ, η, ζ the condition of constant strain is met so long as linear terms of ξ in N_i are preserved, which they are for both the quadrilateral and triangular shape functions.

Thus, for both the quadrilateral and the triangle the choice of shape functions preserve both continuity and the constant strain requirement. They also have the added advantage that the co-ordinates used are generalised and can be applied to each element identically, removing the necessity of defining the displacement function explicitly as a polynomial for each element in turn.

APPENDIX B.

Formulation of the transformation matrices

The transformation matrices mentioned in Chapter 3 are those required to form the strains with respect of the local orthogonal axes x', y', z'.

These are the Inverse Jacobean Matrix and the direction cosine matrix relating orthogonal co-ordinates to the global co-ordinates.

Both matrices are evaluated at a point ξ, η, ζ within an element of the shell.

The geometric definitions are of the form

$$\begin{Bmatrix} x \\ y \\ z \end{Bmatrix} = \sum f(\xi,\eta,\zeta) \begin{Bmatrix} x_i \\ y_i \\ z_i \end{Bmatrix} \qquad \text{B.1}$$

where i is a node of the element and x_i, y_i, z_i a vector of the co-ordinates of the ith node.

The Jacobean defines the variation of the global co-ordinates to the curvilinear co-ordinates

$$[J] = \begin{bmatrix} x_\xi & y_\xi & z_\xi \\ x_\eta & y_\eta & z_\eta \\ x_\zeta & y_\zeta & z_\zeta \end{bmatrix} = \begin{Bmatrix} \underline{S_1} \\ \underline{S_2} \\ \underline{N} \end{Bmatrix} \qquad \text{B.2}$$

where $x_\xi = \dfrac{\partial x}{\partial \xi}$ etc.

The Jacobean becomes layer dependent for the sandwich shell elements in that the vector normal to the reference surface ($\underline{N}$) is a function of the thickness co-ordinate within a layer.

Similarly, the two vectors $\underline{S_1}$, and $\underline{S_2}$ tangential to the reference surface (ξ, η) are modified in that $\frac{\partial z}{\partial \xi}$ and $\frac{\partial z}{\partial \eta}$ are the variation of z co-ordinate within the layer.

The Ahmad Element would define the vector normal to the reference surface as:

$$\{\underline{N}\} = \begin{Bmatrix} \frac{\partial x}{\partial \xi} \\ \frac{\partial y}{\partial \xi} \\ \frac{\partial z}{\partial \xi} \end{Bmatrix} = \sum [N_i] \frac{(c + f_1 + f_2)}{2(c + \hat{f}_1 + \hat{f}_2)} \begin{Bmatrix} \underline{V_{3ix}} \\ \underline{V_{3iy}} \\ \underline{V_{3iz}} \end{Bmatrix} \qquad \text{B.3}$$

The sandwich shell element defines the normal vectors as:

$$\{\underline{N_f}\} = \sum [N_i] \frac{f_1}{2(f_1 + f_2 + c)} \begin{Bmatrix} \underline{V_{3ix}} \\ \underline{V_{3iy}} \\ \underline{V_{3iz}} \end{Bmatrix} \text{ for the faces} \qquad \text{B.4}$$

$$\{\underline{N_c}\} = \sum [N_i] \frac{c}{2(f_1 + f_2 + c)} \begin{Bmatrix} \underline{V_{3ix}} \\ \underline{V_{3iy}} \\ \underline{V_{3iz}} \end{Bmatrix} \text{ for the core}$$

The tangential vectors in the original Ahmad element would have contributions which include:

$$\frac{\partial z}{\partial \xi} = \sum \frac{\partial N_i}{\partial \xi} \begin{Bmatrix} x_i \\ y_i \\ z_i \end{Bmatrix} + \sum \frac{\partial N_i}{\partial \xi} \times f \times \frac{\underline{V_{3i}}}{2}$$

which, for the sandwich shell element, become:

$$\frac{\partial z}{\partial \xi} = \sum \frac{\partial N_i}{\partial \xi} \begin{Bmatrix} X_i \\ Y_i \\ Z_i \end{Bmatrix} + \sum \frac{\partial N_i}{\partial \xi} \times (T_i \zeta + k_i) \times \frac{\underline{V_{3i}}}{2} \qquad \text{B.5}$$

The resulting Jacobean matrix becomes a description of the variation of the geometry within a layer of the element, and not the total element.

The direction cosine matrix again is evaluated at the point (ξ, η, ζ) within the element, with ζ being the co-ordinate which is across the thickness of the layer being considered. By forming the vector product of two vectors lying in the surface (ξ, η) at ζ constant the vector normal to the surface can be calculated.

Thus $\underline{V_3}$ for the direction cosine matrix is defined as:

$$\underline{V_3} = \{\underline{S_1} \times \underline{S_2}\} = \begin{Bmatrix} \frac{\partial x}{\partial \xi} \\ \frac{\partial y}{\partial \xi} \\ \frac{\partial z}{\partial \xi} \end{Bmatrix} \times \begin{Bmatrix} \frac{\partial x}{\partial \eta} \\ \frac{\partial y}{\partial \eta} \\ \frac{\partial z}{\partial \eta} \end{Bmatrix} = \begin{Bmatrix} \frac{\partial y}{\partial \xi}\frac{\partial z}{\partial \eta} - \frac{\partial y}{\partial \eta}\frac{\partial z}{\partial \xi} \\ \frac{\partial x}{\partial \eta}\frac{\partial z}{\partial \xi} - \frac{\partial x}{\partial \xi}\frac{\partial z}{\partial \eta} \\ \frac{\partial x}{\partial \xi}\frac{\partial y}{\partial \eta} - \frac{\partial x}{\partial \eta}\frac{\partial y}{\partial \xi} \end{Bmatrix} \qquad \text{B.6}$$

To define a unique set of local orthogonal directions the cross product between the $\underline{V_3}$ axis and the X axis is used to define $\underline{V_1}$, care being taken if $\underline{V_3}$ lies parallel to the X axis.

Forming the cross product between the vectors $\underline{V}_1$ and $\underline{V}_3$ the final vector $\underline{V}_2$ can be defined. After normalising these three vectors ($\underline{V}_1, \underline{V}_2, \underline{V}_3$) are the direction cosine matrix $[\theta]$ relating the local orthogonal directions to the global directions.

Using the Jacobean matrix and the direction cosine matrix the local strains can be evaluated, and hence the stiffness matrix formed. This is described in Appendix C.

APPENDIX C

Formulation of the sandwich shell element stiffness matrices

The derivation of the element stiffness matrix requires the strains to be evaluated with respect to the unknown displacements. Equation 2.1 of Chapter 2 defines the strains as

$$\{\epsilon\} = [B]\{\delta\} \qquad \text{C.1}$$

$\{\epsilon\}$ is the vector of strains.

$\{\delta\}$ is the vector of unknown displacements.

$[B]$ is the matrix defined by the assumed variation of displacement.

The Element Stiffness matrix is formed by calculating the contributions of the faces, and of the core over the volume of the element

$$[K] = \int_{\substack{\text{VOL} \\ \text{TOP FACE}}} [B_t]^T [D_t][B_t] d\text{Vol} + \int_{\substack{\text{VOL} \\ \text{CORE}}} [B_c]^T [D_c][B_c] d\text{Vol} + \int_{\substack{\text{VOL} \\ \text{BOTTOM FACE}}} [B_t]^T [D_t][B_t] d\text{Vol} \qquad \text{C.2}$$

$[\ ]^T$ defines the transpose of a matrix.

$[\ ]^{-1}$ defines the inverse of a matrix.

To form the $[B]$ matrices use is made of the decoupling of strain components into membrane and transverse strains associated with a particular layer.

In addition, use is made of the work of Zienkiewicz et al. (64) in that the strain components can be evaluated more directly by accounting for the orthogonality of the Jacobean and Direction cosine matrix explained in Appendix B.

The strains are evaluated in the local co-ordinate set of co-ordinates so the stiffness matrix requires the numerical integration of expressions of the form

$$[k] = \int_{-1}^{1}\int_{-1}^{1}\int_{-1}^{1} [B_i]^T [D_i][B_i] \det J \, d\xi \, d\eta \, d\zeta \qquad i=1,3$$

C.4

In the following derivation a dash refers to the local orthogonal set of co-ordinates. A subscript within a matrix defines the derivative with respect to the subscript ($U_x = \frac{\partial u}{\partial x}$).

The Global strains are given by

$$\begin{bmatrix} U_x & V_x & W_x \\ U_y & V_y & W_y \\ U_z & V_z & W_z \end{bmatrix} = [J]^{-1} \begin{bmatrix} U_\xi & V_\xi & W_\xi \\ U_\eta & V_\eta & W_\eta \\ U_\zeta & V_\zeta & W_\zeta \end{bmatrix}$$

C.5

with $[J]$ the Jacobean $\begin{Bmatrix} S_1 \\ S_2 \\ N \end{Bmatrix}$ and

the inverse Jacobean $[J]^{-1}$ given by $\begin{Bmatrix} S_2 \times N \\ N \times S_1 \\ S_1 \times S_2 \end{Bmatrix} \div \det J$

C.6

The vectors S_1 and S_2 are two tangents to the surface at the point ξ, η, ζ and the normal to the surface N .

As these global strains need to be expressed as local strains the direction cosine matrix is used:

$$[\theta] = [\underline{V}_1 \quad \underline{V}_2 \quad \underline{V}_3] \qquad \text{C.7}$$

Also $\underline{V}_3$ of the direction cosine matrix is in the same sense as normal $[\underline{S}_1 \times \underline{S}_2]$ of the inverse Jacobean matrix.

To evaluate the local strains the transformation from curvilinear to local orthogonal co-ordinates is:

$$\begin{bmatrix} U'_{x'} & V'_{x'} & W'_{x'} \\ U'_{y'} & V'_{y'} & W'_{y'} \\ U'_{z'} & V'_{z'} & W'_{z'} \end{bmatrix} = [\theta]^T [J]^{-1} \begin{bmatrix} U_\xi & V_\xi & W_\xi \\ U_\eta & V_\eta & W_\eta \\ U_\zeta & V_\zeta & W_\zeta \end{bmatrix} [\theta] \qquad \text{C.8}$$

As $\underline{V}_3$ and $\underline{S}_1 \times \underline{S}_2$ are normal to the surface at the point ξ, η, ζ, the matrix resulting from $[\theta]^T \times [J]^{-1}$ is of the form

$$[A] = [\theta]^T [J]^{-1} = \begin{bmatrix} A_{11} & A_{12} & 0 \\ A_{21} & A_{22} & 0 \\ 0 & 0 & A_{33} \end{bmatrix} \qquad \text{C.9}$$

and the local strains can be expressed as

$$\{\epsilon_1\}' = \begin{bmatrix} A_{11} & A_{12} \\ A_{21} & A_{22} \end{bmatrix} \begin{Bmatrix} u_\xi & v_\xi & w_\xi \\ u_\eta & v_\eta & w_\eta \end{Bmatrix} [\theta] \qquad \text{C.10}$$

$$\{\epsilon_2\}' = [A_{33}] \{u_\zeta \quad v_\zeta \quad w_\zeta\} [\theta] \qquad \text{C.11}$$

These partitioned strains are expressed directly as derivatives of the displacement functions with respect to the curvilinear co-ordinates.

By defining two further matrices $[C]$ and $[D]$ such that $[C]$ contains all terms of the local strains which are derivatives of x' and y', and $[D]$ as the derivatives

with respect to z' then further reductions can be made for the sandwich elements

$$[C] = \begin{bmatrix} C_1 & 0 & 0 \\ 0 & C_2 & 0 \\ C_2 & C_1 & 0 \\ 0 & 0 & C_1 \\ 0 & 0 & C_2 \end{bmatrix} \qquad [D] = \begin{bmatrix} 0 & 0 & 0 \\ 0 & 0 & 0 \\ 0 & 0 & 0 \\ D_1 & 0 & 0 \\ 0 & D_1 & 0 \end{bmatrix} \qquad \text{C.12}$$

where

$$\begin{aligned} C_1 &= A_{11} N_{i,\xi} + A_{12} N_{i,\eta} \\ C_2 &= A_{21} N_{i,\xi} + A_{22} N_{i,\eta} \\ D_1 &= A_{33} N_i \end{aligned} \qquad \text{C.13}$$

As the $[C]$ and $[D]$ matrices defined in C.12 and C.13 define the full strain vector containing both membrane and transverse shear terms, these are simplified in evaluating the sandwich strains.

For the faces there is no need to consider the transverse shears and combining the displacement functions of equation 3.3.3 the strains become:

for the top face

$$\{\epsilon'\}_{\substack{\text{Top} \\ \text{FACE}}} = \begin{Bmatrix} \epsilon'_{x'} \\ \epsilon'_{y'} \\ \gamma'_{x'y'} \end{Bmatrix} = \begin{bmatrix} C_1 & 0 & 0 \\ 0 & C_2 & 0 \\ C_2 & C_1 & 0 \end{bmatrix} [\Theta]^T \begin{Bmatrix} U_i \\ V_i \\ W_i \end{Bmatrix} +$$

$$\frac{t_i}{2} \frac{f(1+f)+c}{(2f+c)} \begin{bmatrix} C_1 & 0 & 0 \\ 0 & C_2 & 0 \\ C_2 & C_1 & 0 \end{bmatrix} [\Theta]^T [\underline{V_{ii}} \;\; \underline{V_{bi}}] \begin{Bmatrix} \alpha_i \\ \beta_i \end{Bmatrix} \qquad \text{C.14}$$

for the bottom face:

$$\{\epsilon'\}_{\substack{\text{BOTTOM}\\\text{FACE}}} = \begin{Bmatrix}\epsilon'_{x'}\\ \epsilon'_{y'}\\ \gamma'_{x'y'}\end{Bmatrix} = \begin{bmatrix}C_1 & 0 & 0\\ 0 & C_2 & 0\\ C_2 & C_1 & 0\end{bmatrix}[\Theta]^T\begin{Bmatrix}U_i\\ V_i\\ W_i\end{Bmatrix} +$$

$$\frac{t_i}{2}\frac{f(\beta-1)-c}{2f+c}\begin{bmatrix}C_1 & 0 & 0\\ 0 & C_2 & 0\\ C_2 & C_1 & 0\end{bmatrix}[\Theta]^T\begin{bmatrix}\underline{V_{1i}} & \underline{V_{2i}}\end{bmatrix}\begin{Bmatrix}\alpha_i\\ \beta_i\end{Bmatrix}$$

C.15

and as the core has included its membrane shear contribution:

$$\{\epsilon'\}_{\text{CORE}} = \begin{Bmatrix}\gamma'_{x'y'}\\ \gamma'_{x'z'}\\ \gamma'_{y'z'}\end{Bmatrix} = \begin{bmatrix}C_2 & C_1 & 0\\ 0 & 0 & C_1\\ 0 & 0 & C_2\end{bmatrix}[\Theta]^T\begin{Bmatrix}U_i\\ V_i\\ W_i\end{Bmatrix} +$$

$$\frac{t_i}{2}\left[\frac{fc}{2f+c}\begin{bmatrix}C_2 & C_1 & 0\\ 0 & 0 & C_1\\ 0 & 0 & C_2\end{bmatrix} + \begin{bmatrix}0 & 0 & 0\\ D_1 & 0 & 0\\ 0 & D_1 & 0\end{bmatrix}\right][\Theta]^T\begin{bmatrix}\underline{V_{1i}} & \underline{V_{2i}}\end{bmatrix}\begin{Bmatrix}\alpha_i\\ \beta_i\end{Bmatrix}$$

C.16

Equations C.14 to C.16 define the local strains within a layer explicitly in terms of the derivatives of the shape functions combined with the direction cosine matrix and Jacobean.

Thus, equation C.1 is defined, $[B]$ being defined for the assumed displacement function in each layer.

Using the relevant elasticity matrix for either the faces or the core then all terms of the stiffness matrix are calculable, and by Gaussian integration of equation C.4 the element stiffness matrix formed.

By replacing the quadrilateral shape functions $N_i(\xi, \eta, J)$ and their derivatives by the Areal

co-ordinate definition $N_i(L_1, L_2, L_3, L_4)$ with their derivatives a similar formulation was used to determine the stiffness matrix for the triangular elements.

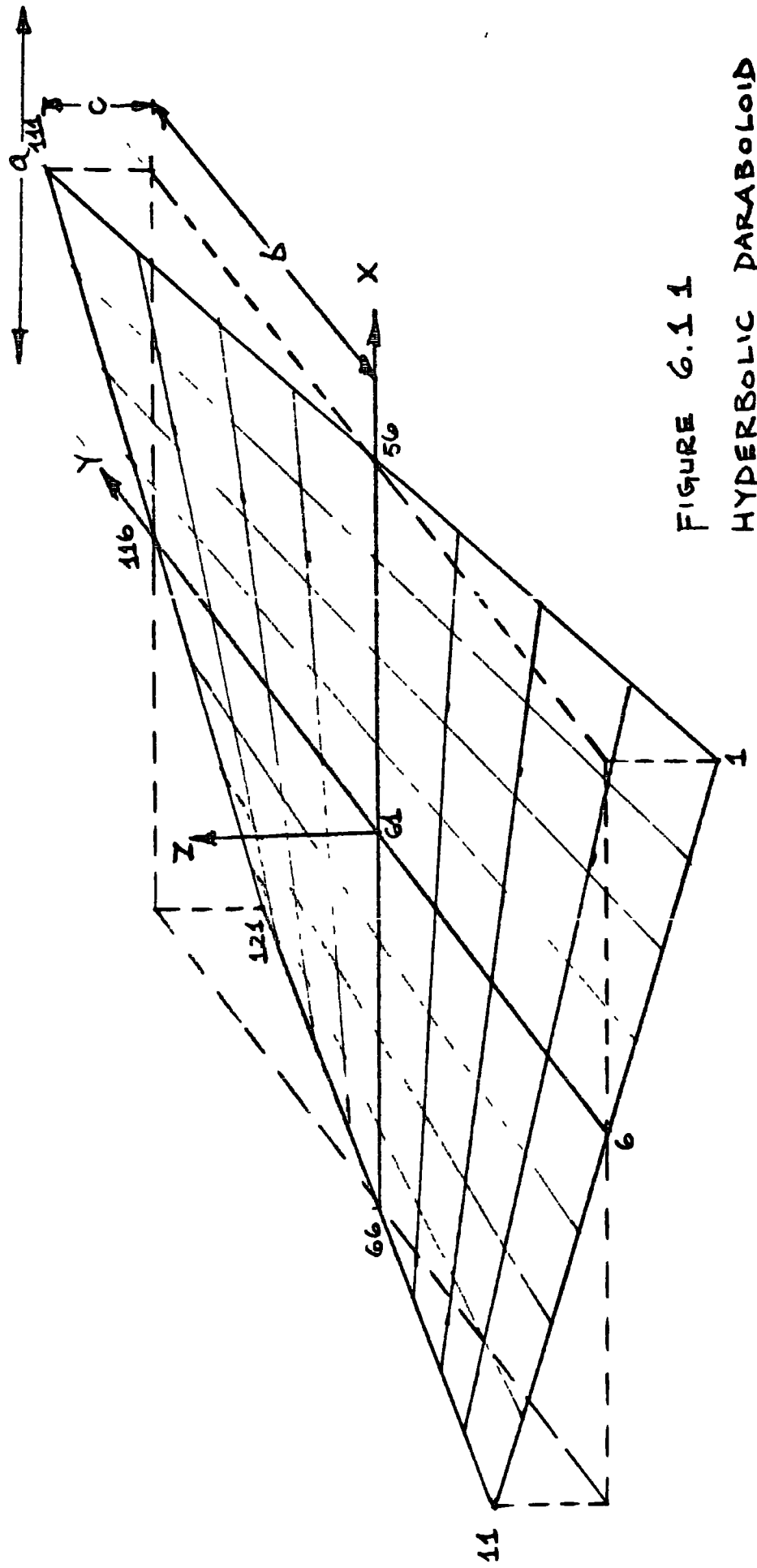

FIGURE 6.11
HYPERBOLIC PARABOLOID
SHELL, 8 x 8 FINITE ELEMENT
GRID.

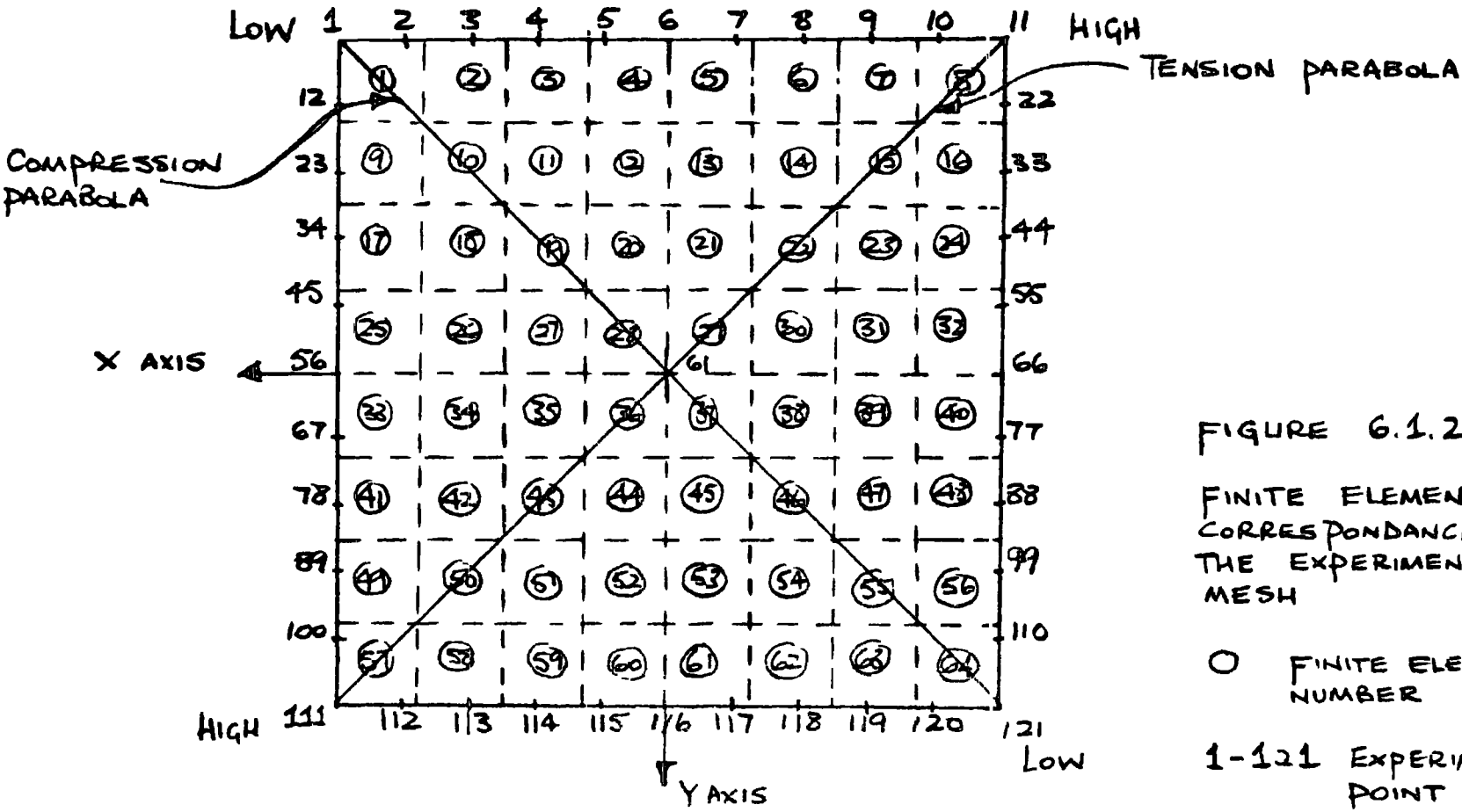

FIGURE 6.1.2 .

FINITE ELEMENT CORRESPONDANCE WITH THE EXPERIMENTAL MESH

O FINITE ELEMENT NUMBER

1-121 EXPERIMENTAL POINT

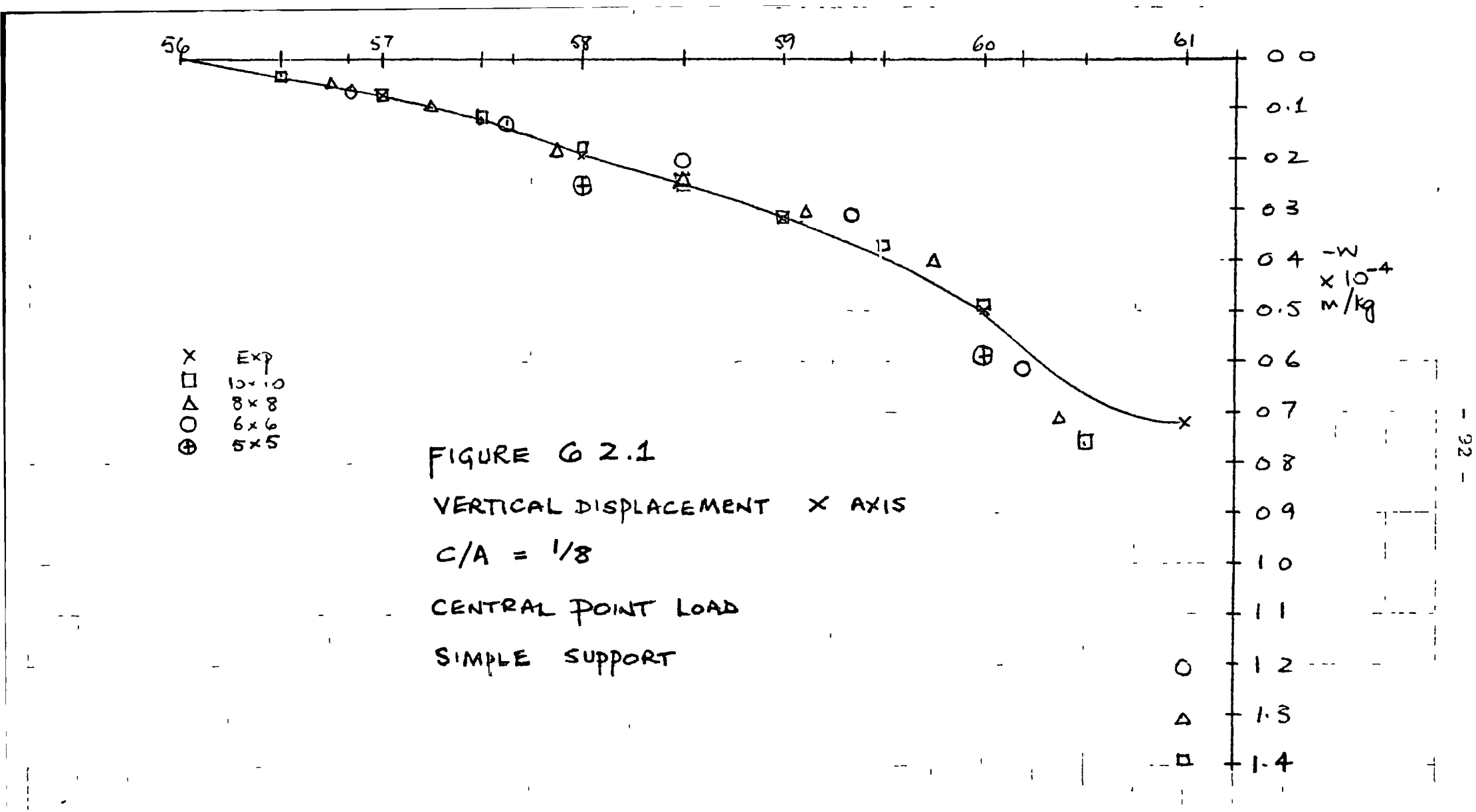

FIGURE G 2.1

VERTICAL DISPLACEMENT X AXIS

C/A = 1/8

CENTRAL POINT LOAD

SIMPLE SUPPORT

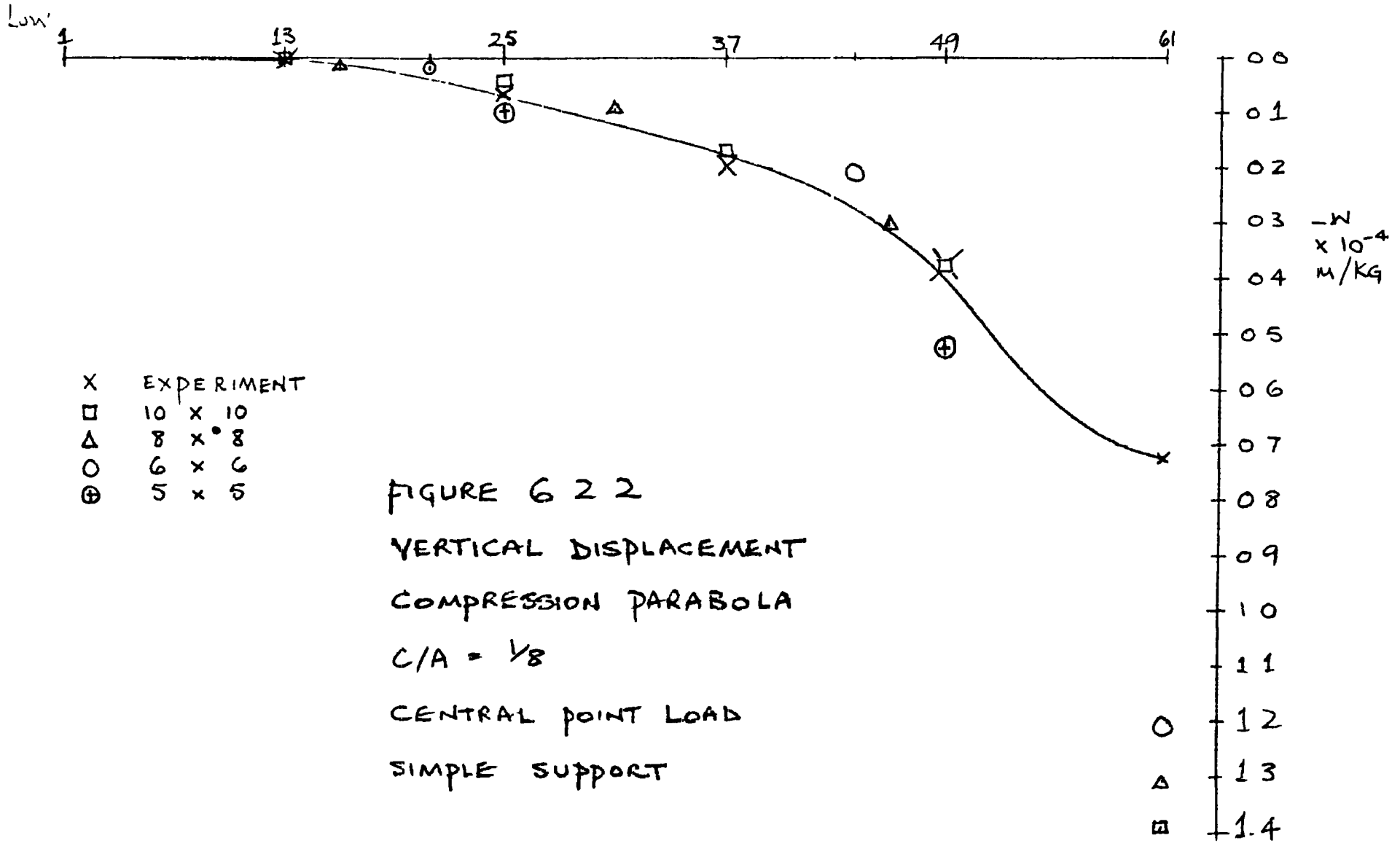

FIGURE 6 2 2

VERTICAL DISPLACEMENT

COMPRESSION PARABOLA

C/A = 1/8

CENTRAL POINT LOAD

SIMPLE SUPPORT

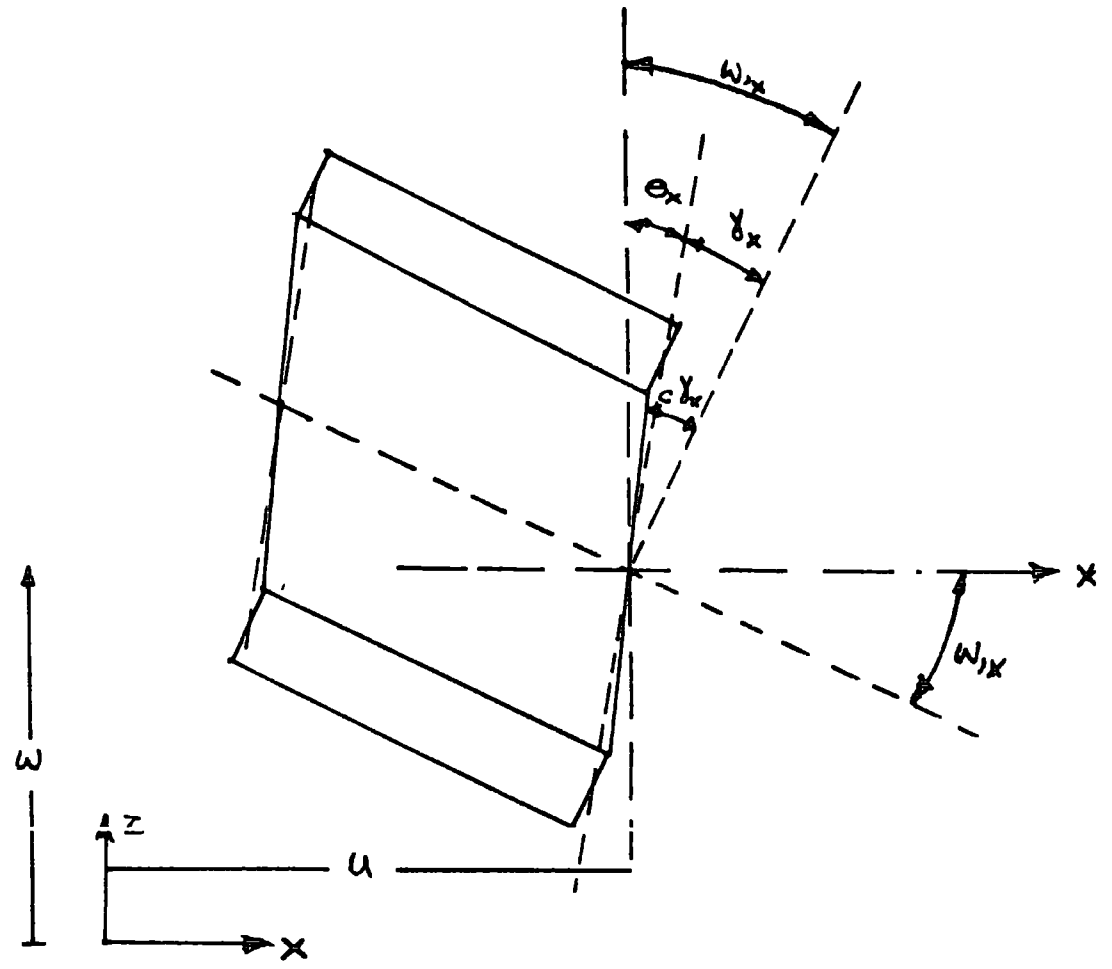

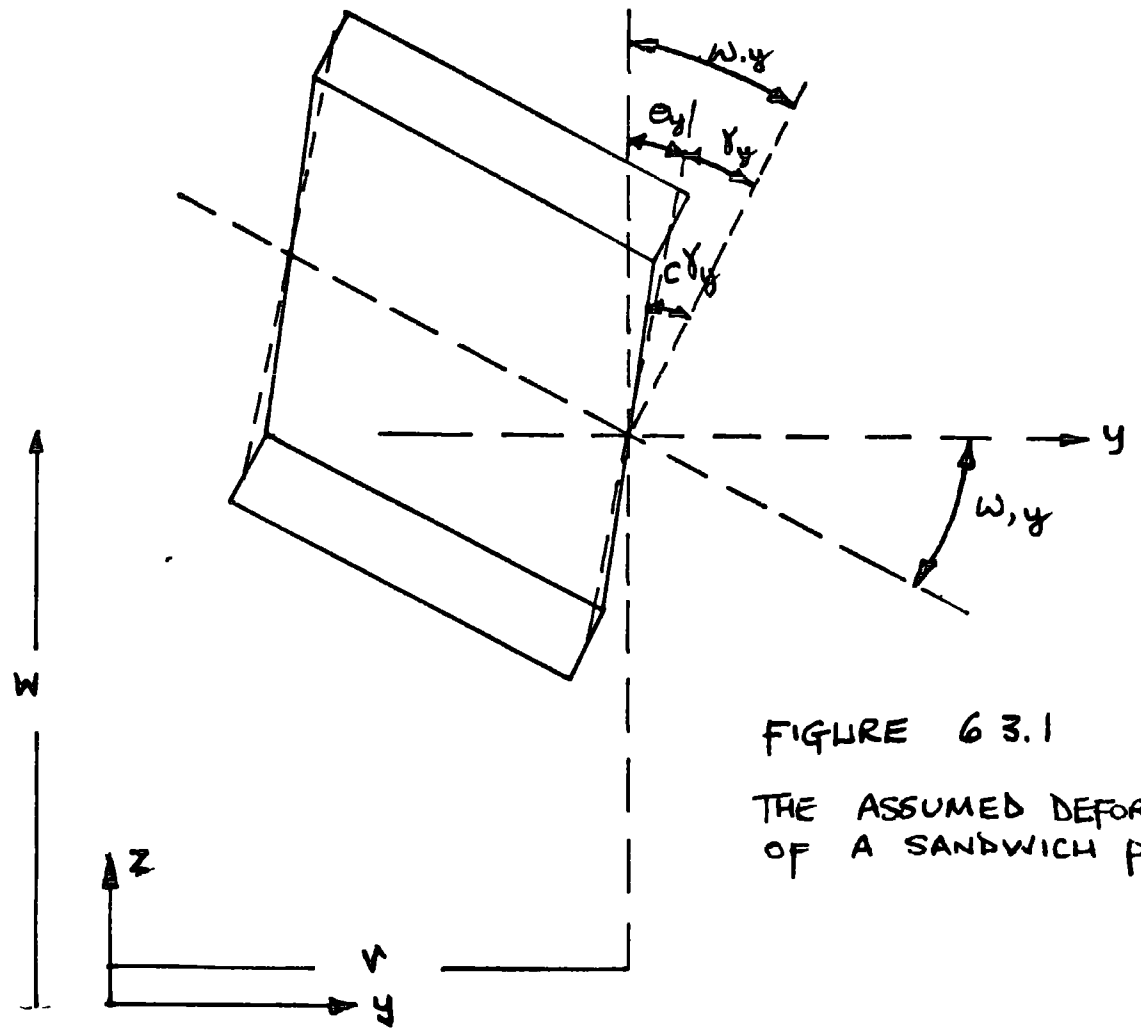

FIGURE 6 3.1

THE ASSUMED DEFORMATION OF A SANDWICH PLATE

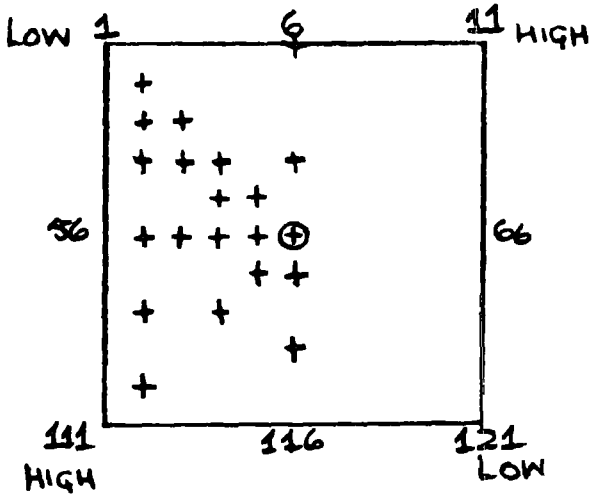

CENTRAL POINT LOAD

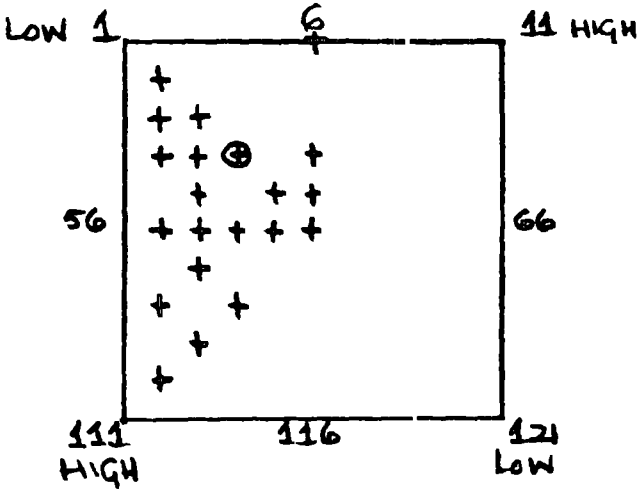

LOAD ON COMPRESSION PARABOLA

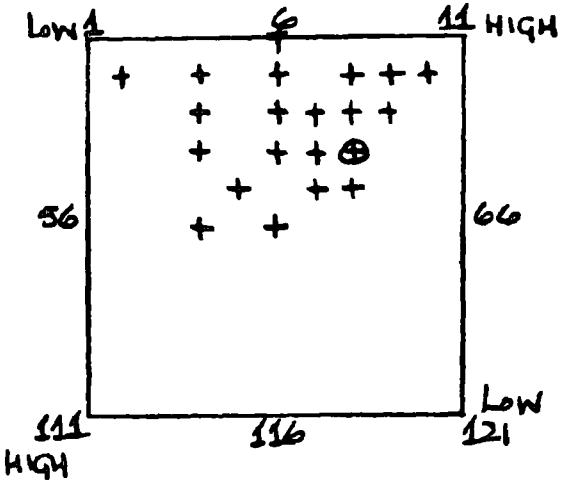

LOAD ON TENSION PARABOLA

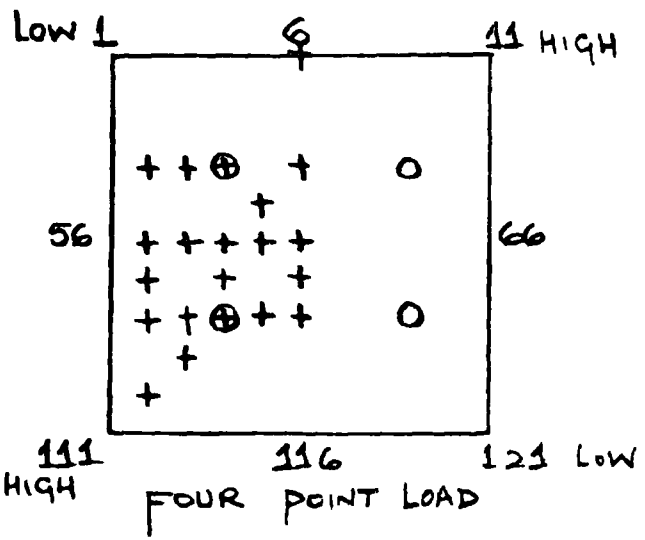

FOUR POINT LOAD

+ DIAL GAUGE
O LOAD POINT

FIGURE 6.3.2

POSITIONING OF THE DIAL GAUGES AND LOAD POINTS

FIGURE 6.34

VERTICAL DISPLACENT OF CENTRAL POINT AGAINST TIME
C/a = 1/12
CENTRAL POINT LOAD

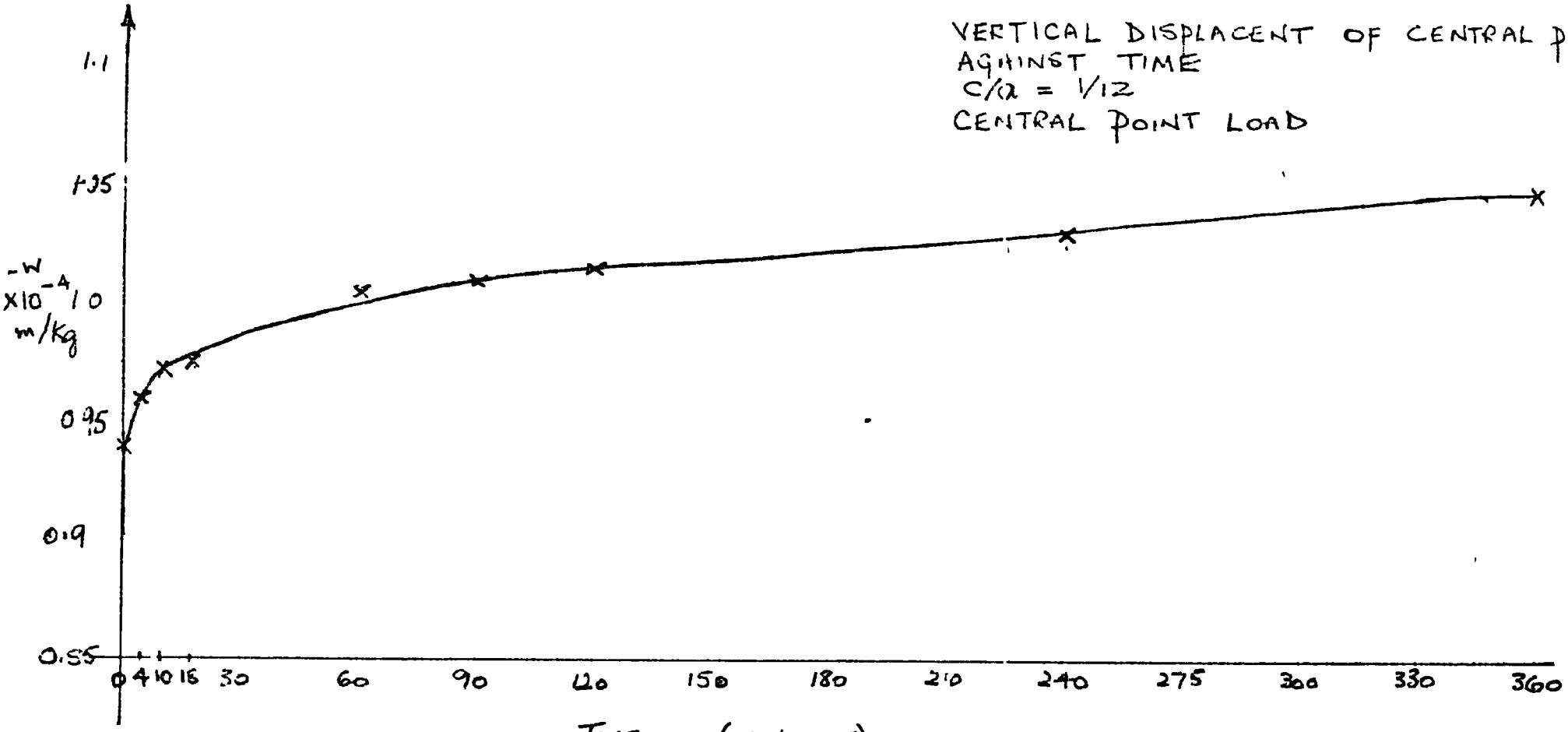

FIGURE 6.3.4

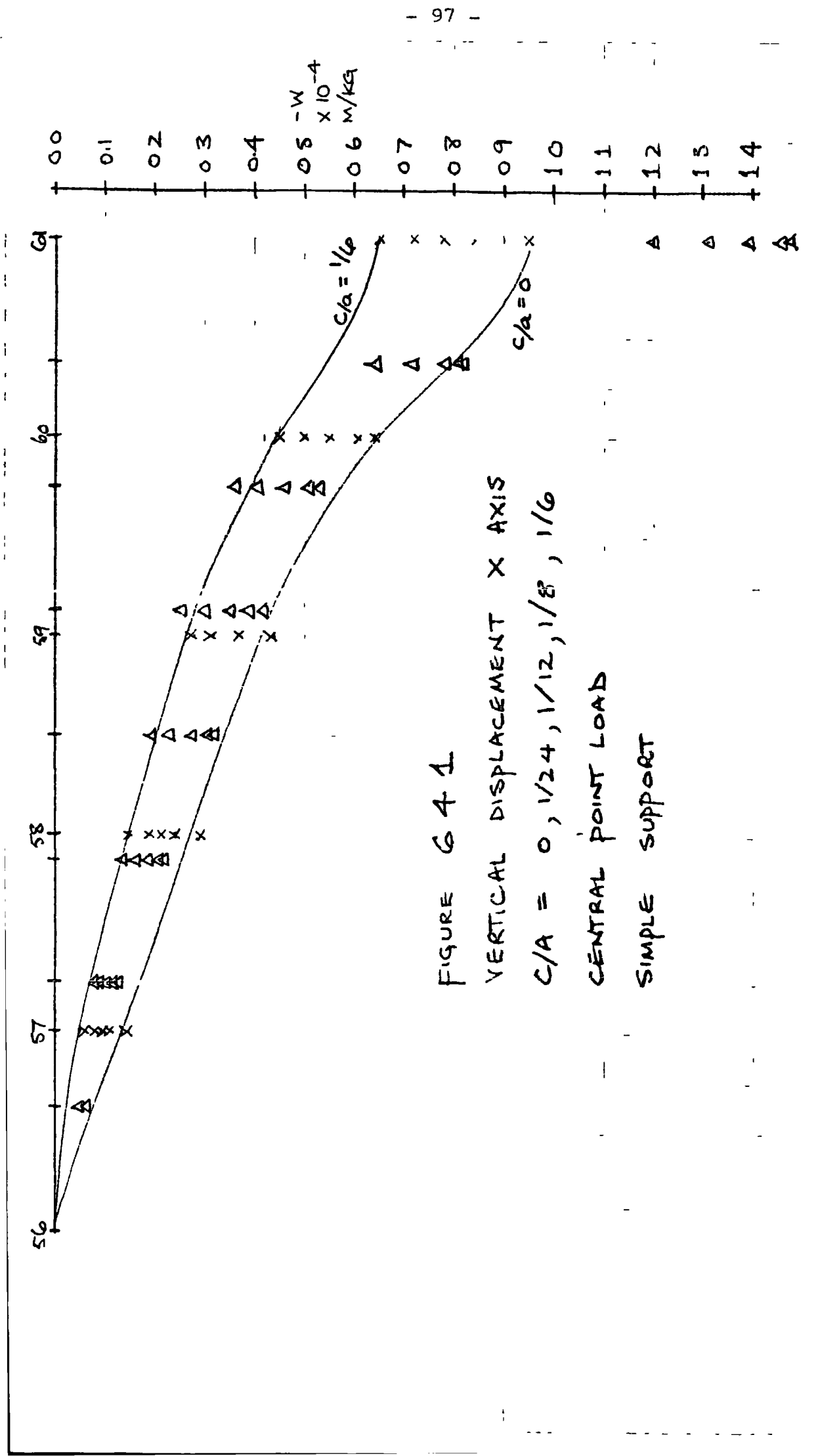

FIGURE 6.4.1

VERTICAL DISPLACEMENT X AXIS

C/A = 0, 1/24, 1/12, 1/8, 1/6

CENTRAL POINT LOAD

SIMPLE SUPPORT

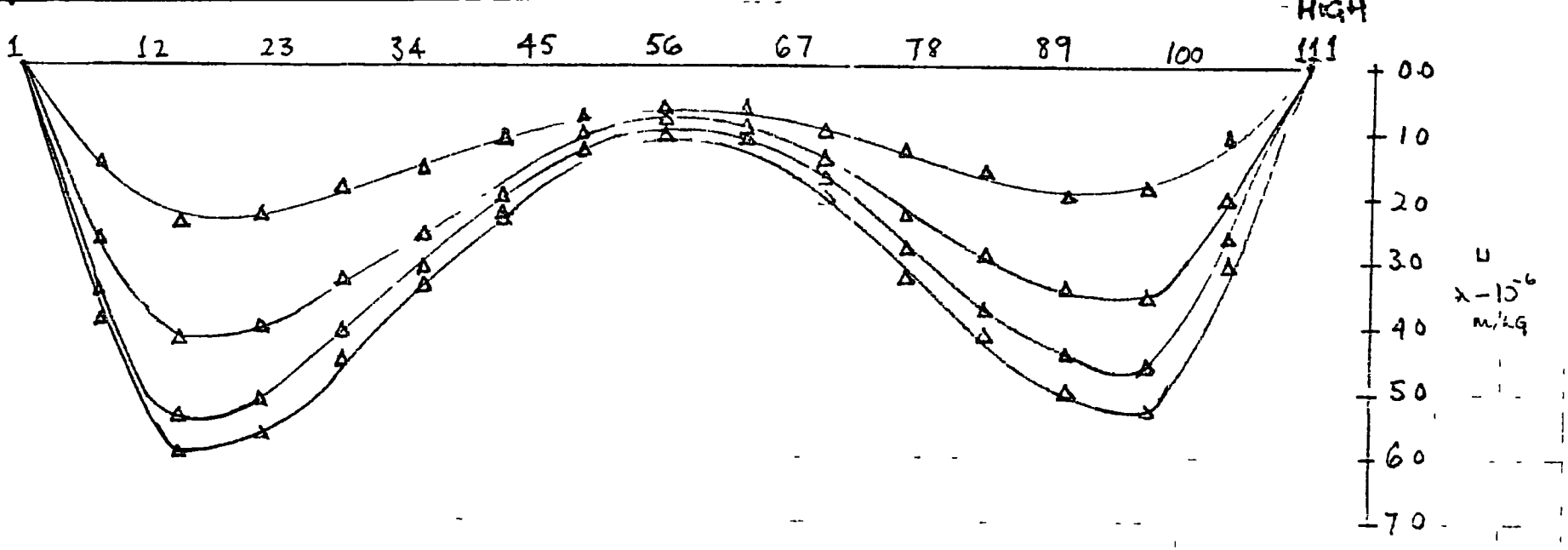

FIGURE 6.4.2

X DISPLACEMENT

C/A = 0, 1/24, 1/12, 1/8, 1/6

CENTRAL POINT LOAD

SIMPLE SUPPORT

FIGURE 6 4 3

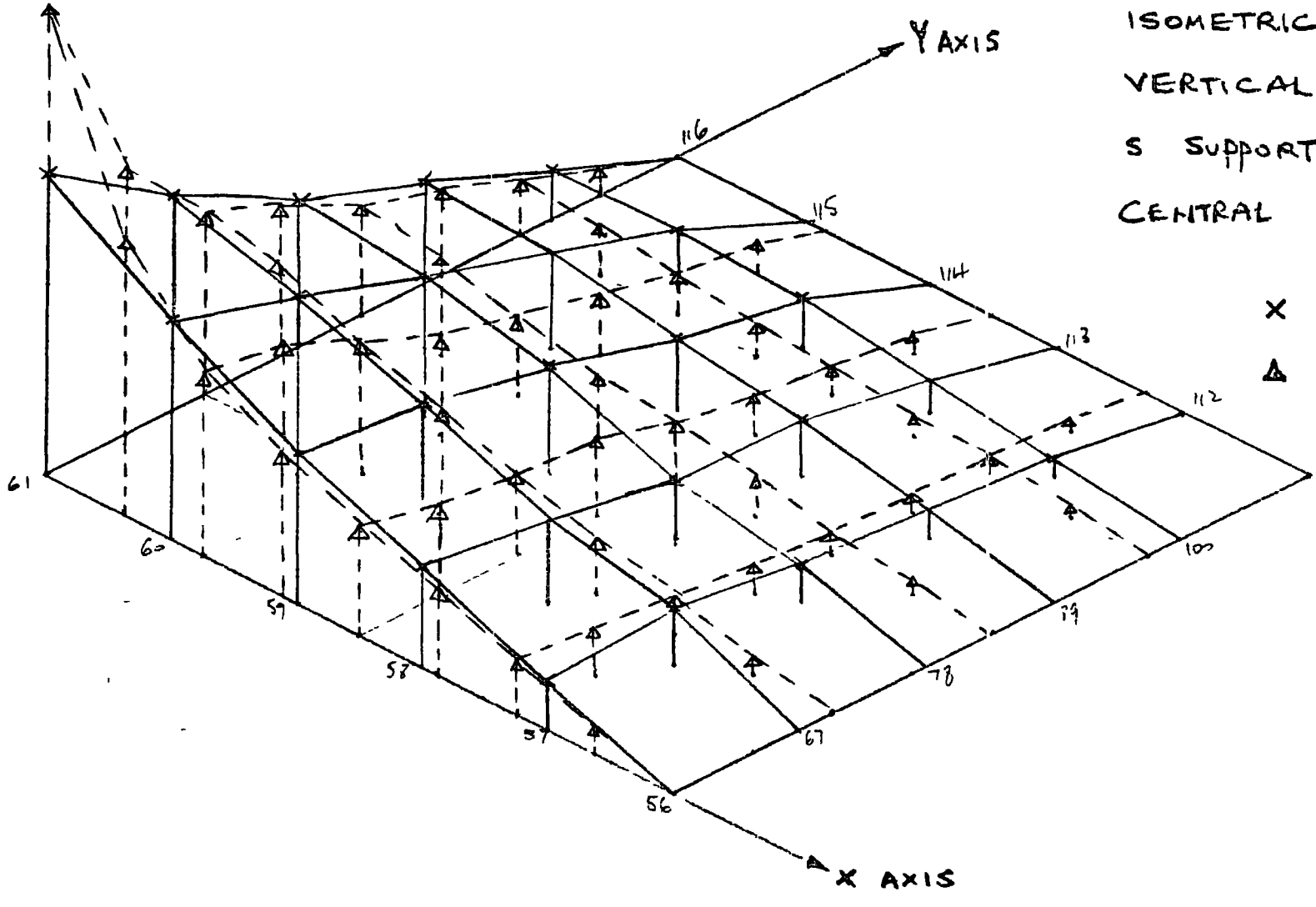

V4 FLAT PLATE C/A = 0

ISOMETRIC

VERTICAL DISPLACEMENT

S SUPPORT

CENTRAL POINT LOAD.

× EXPERIMENT

△ 8×8 FINITE ELEMENT

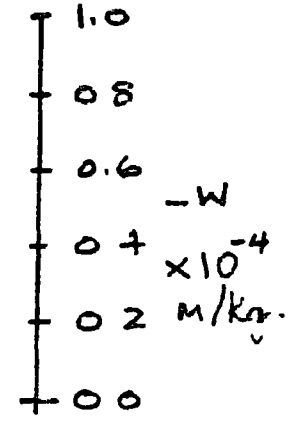

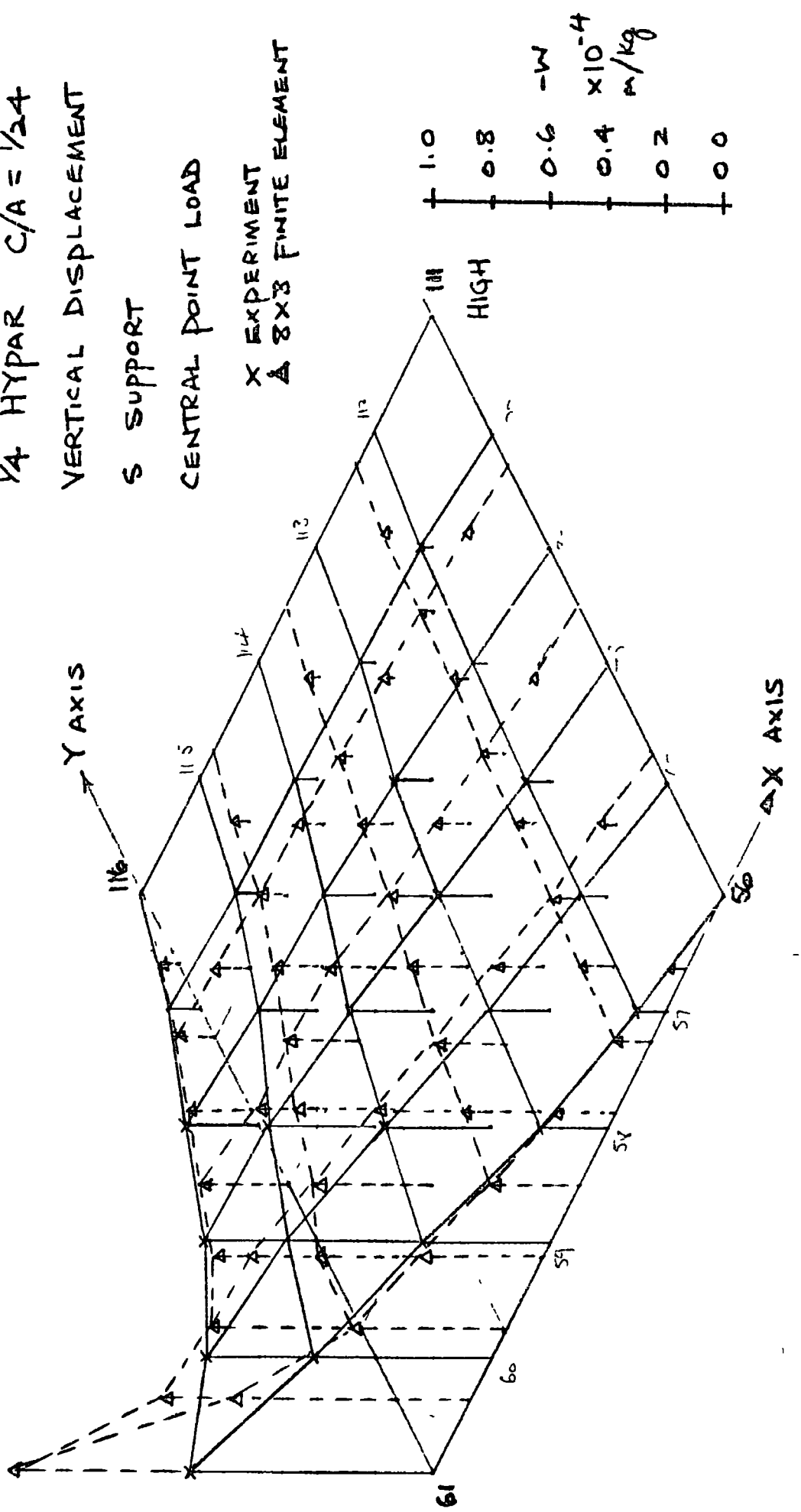
1/4 HYPAR C/A = 1/24
VERTICAL DISPLACEMENT
S SUPPORT
CENTRAL POINT LOAD
X EXPERIMENT
Δ 8X8 FINITE ELEMENT
1.0
0.8
0.6 -W
0.4 x10^-4 m/kg
0.2
0.0
HIGH
Y AXIS
ΔX AXIS
116
111
114
113
112
61
60
59
58
57
56
55

FIGURE 6.44

FIGURE 6.45

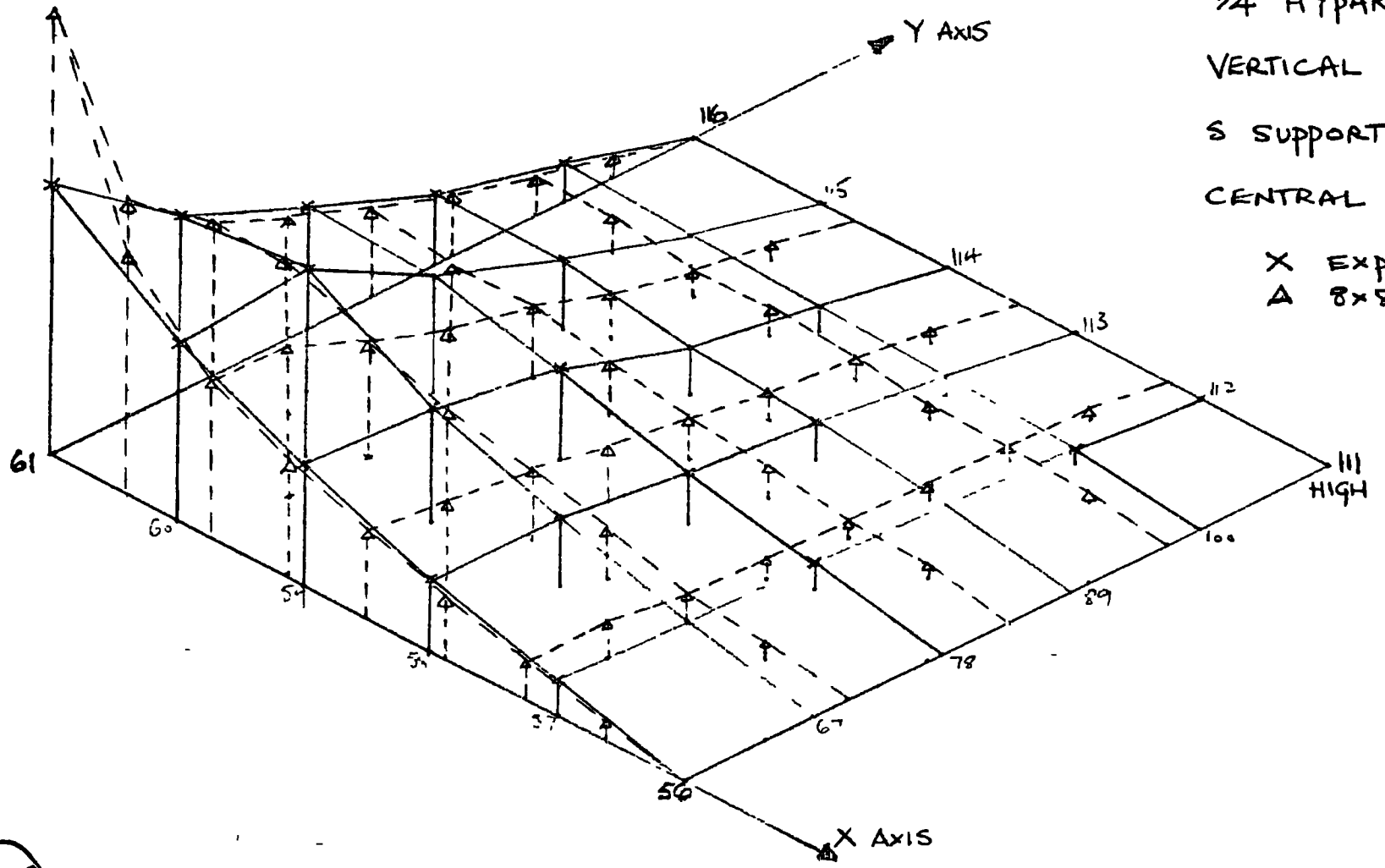

1/4 HYPAR C/A = 1/12

VERTICAL DISPLACEMENT

S SUPPORT

CENTRAL POINT LOAD

X EXPERIMENT
Δ 8×8 FINITE ELEMENT

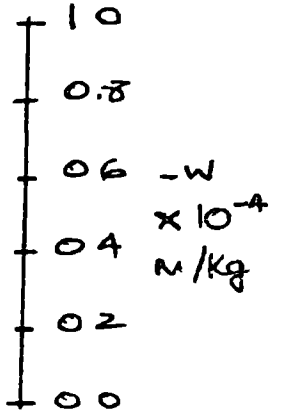

FIGURE 6 4.6

CENTRAL POINT LOAD

¼ HYPAR C/A = 1/8

ISOMETRIC

VERTICAL DISPLACEMENT

S. SUPPORT

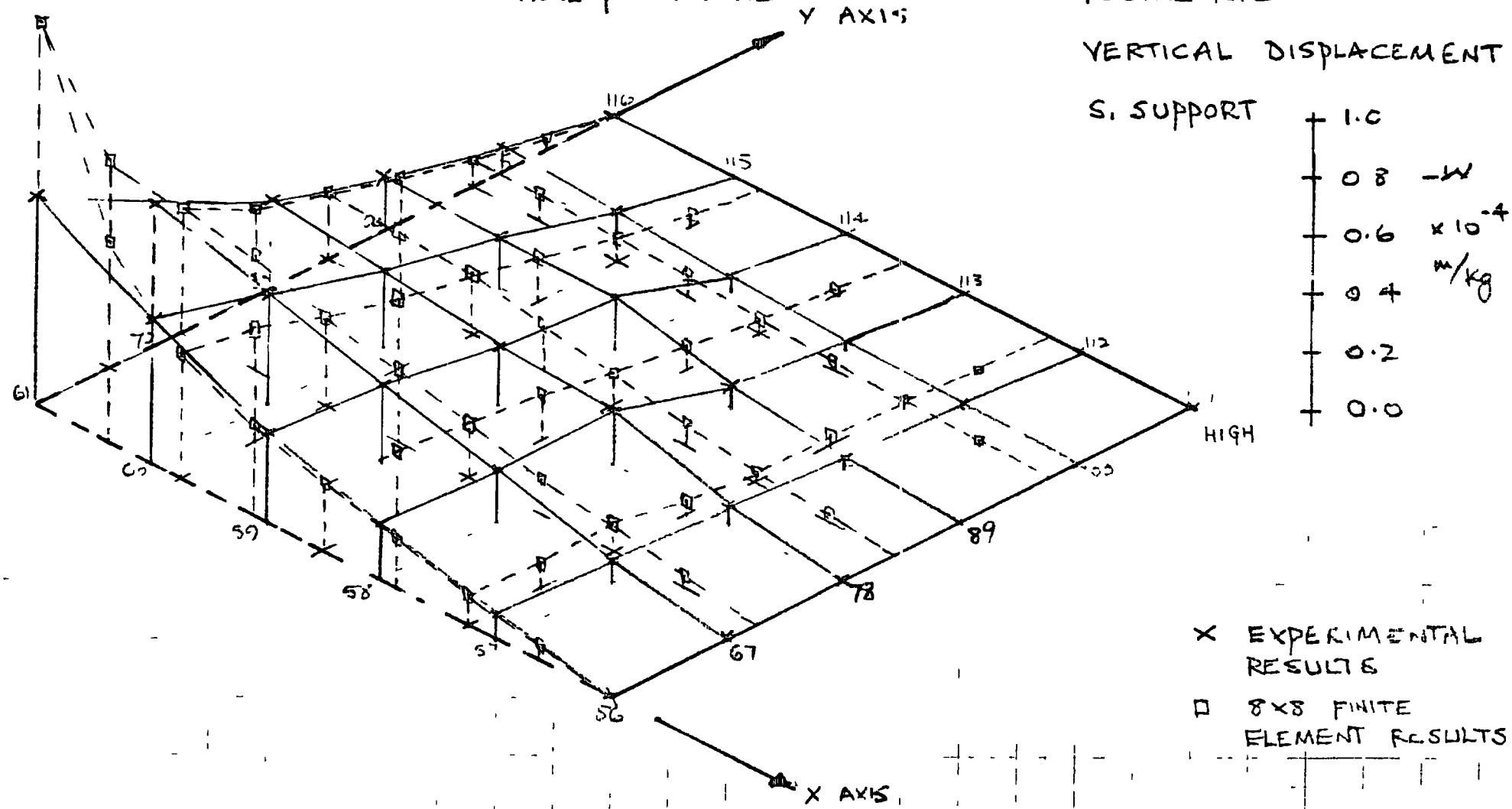

× EXPERIMENTAL RESULTS

□ 8×8 FINITE ELEMENT RESULTS

FIGURE 6 4 7

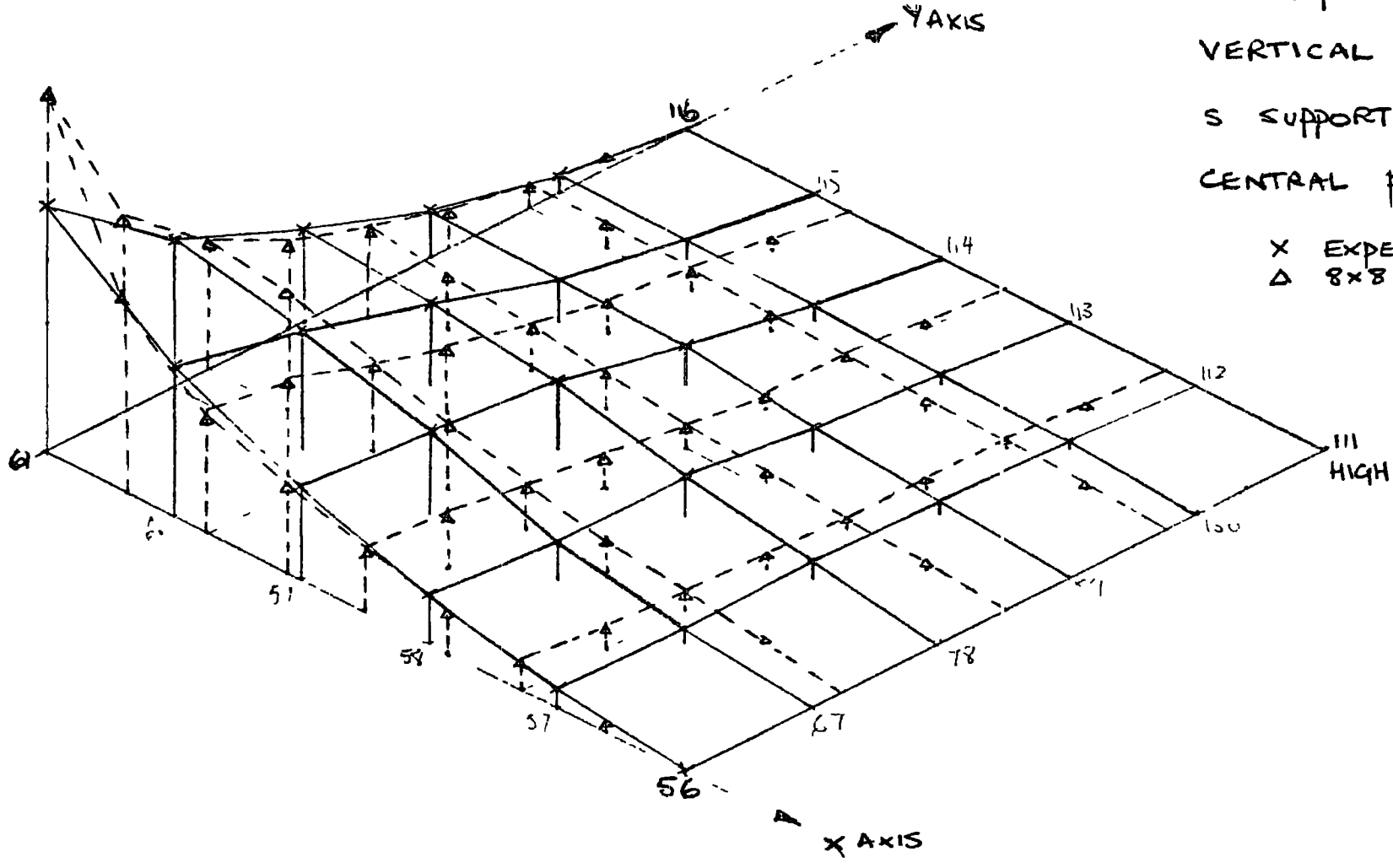

1/4 HYPAR c/a = 1/6

VERTICAL DISPLACEMENT

S SUPPORT

CENTRAL POINT LOAD

× EXPERIMENT
△ 8×8 FINITE ELEMENT

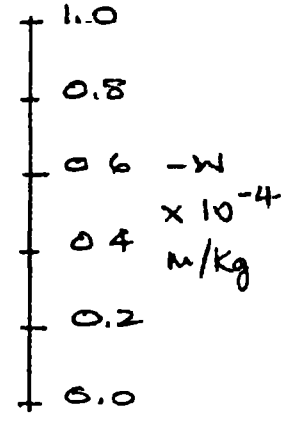

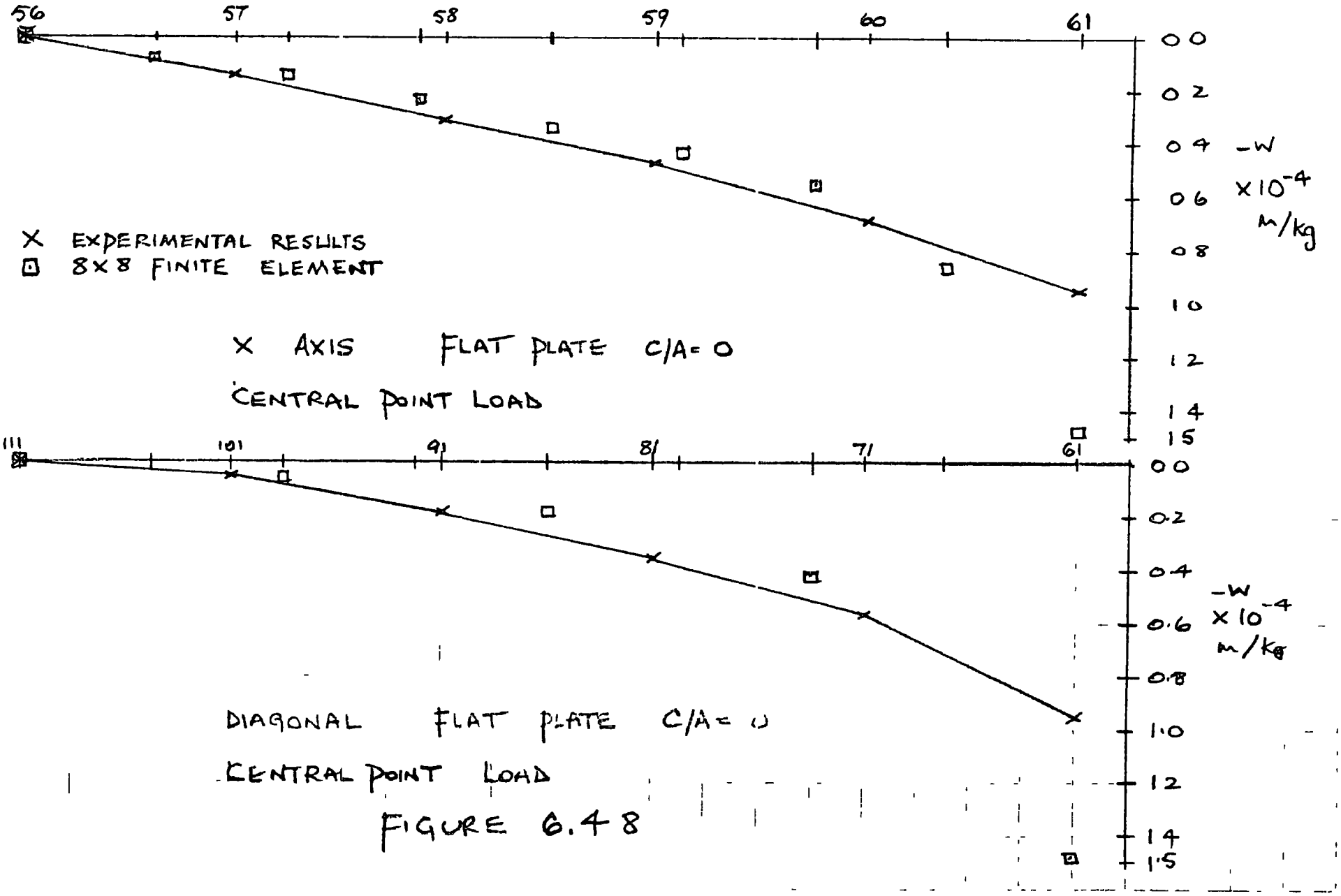
56
57
58
59
60
61
00
02
04
06
08
10
12
14
15
-W
$\times 10^{-4}$
m/kg
X EXPERIMENTAL RESULTS
8x8 FINITE ELEMENT
X AXIS FLAT PLATE C/A = 0
CENTRAL POINT LOAD
111
101
91
81
71
61
00
0.2
0.4
0.6
0.8
1.0
1.2
1.4
1.5
-W
$\times 10^{-4}$
m/kg
DIAGONAL FLAT PLATE C/A = 0
CENTRAL POINT LOAD

FIGURE 6.48

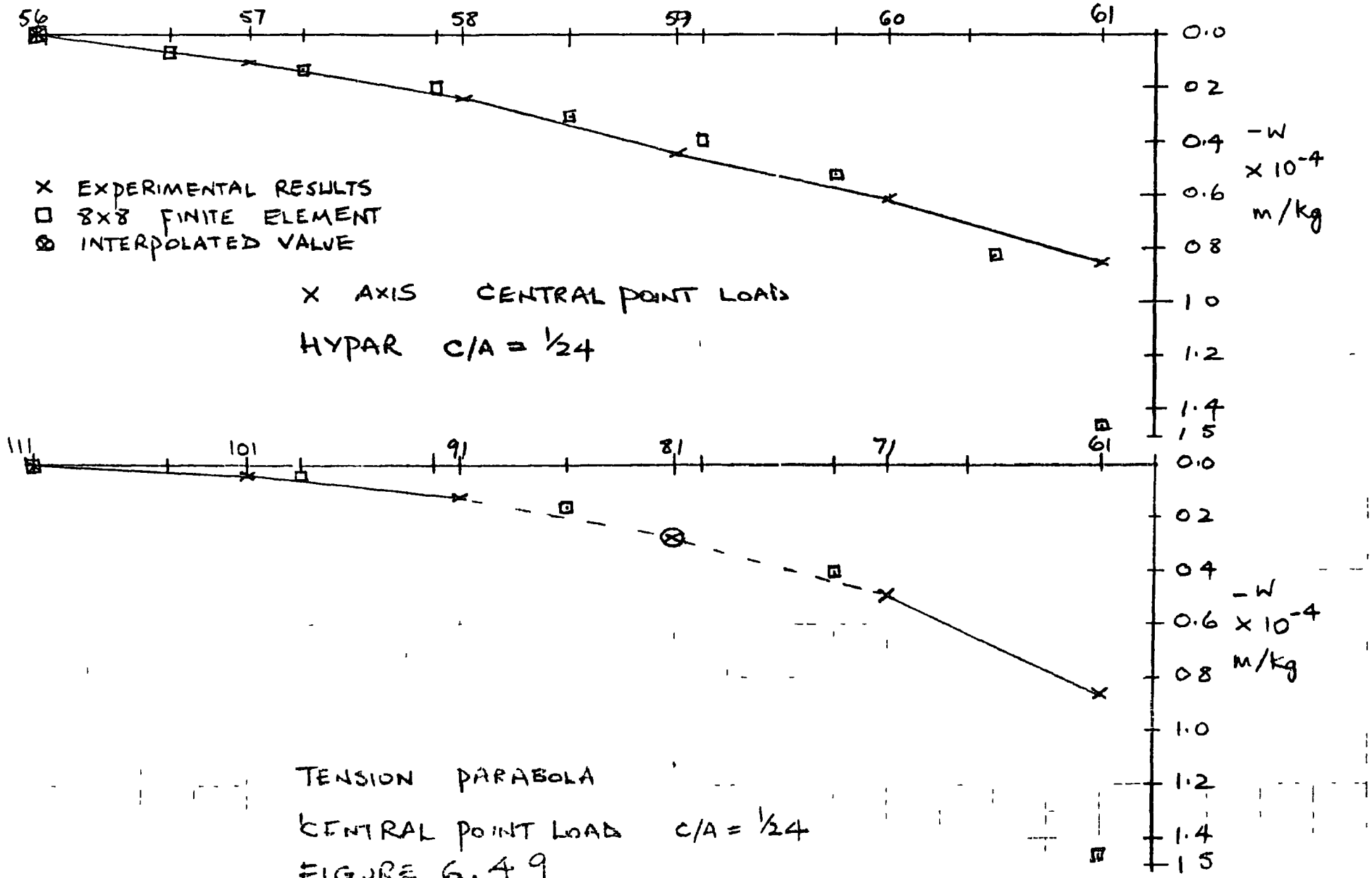
56
57
58
59
60
61
0.0
0.2
0.4
0.6
0.8
1.0
1.2
1.4
1.5
-W
x 10-4
m/kg
× EXPERIMENTAL RESULTS
□ 8x8 FINITE ELEMENT
⊗ INTERPOLATED VALUE
X AXIS CENTRAL POINT LOAD
HYPAR C/A = 1/24
111
101
91
81
71
61
0.0
0.2
0.4
0.6
0.8
1.0
1.2
1.4
1.5
-W
x 10-4
m/kg
TENSION PARABOLA
CENTRAL POINT LOAD C/A = 1/24

FIGURE 6.49

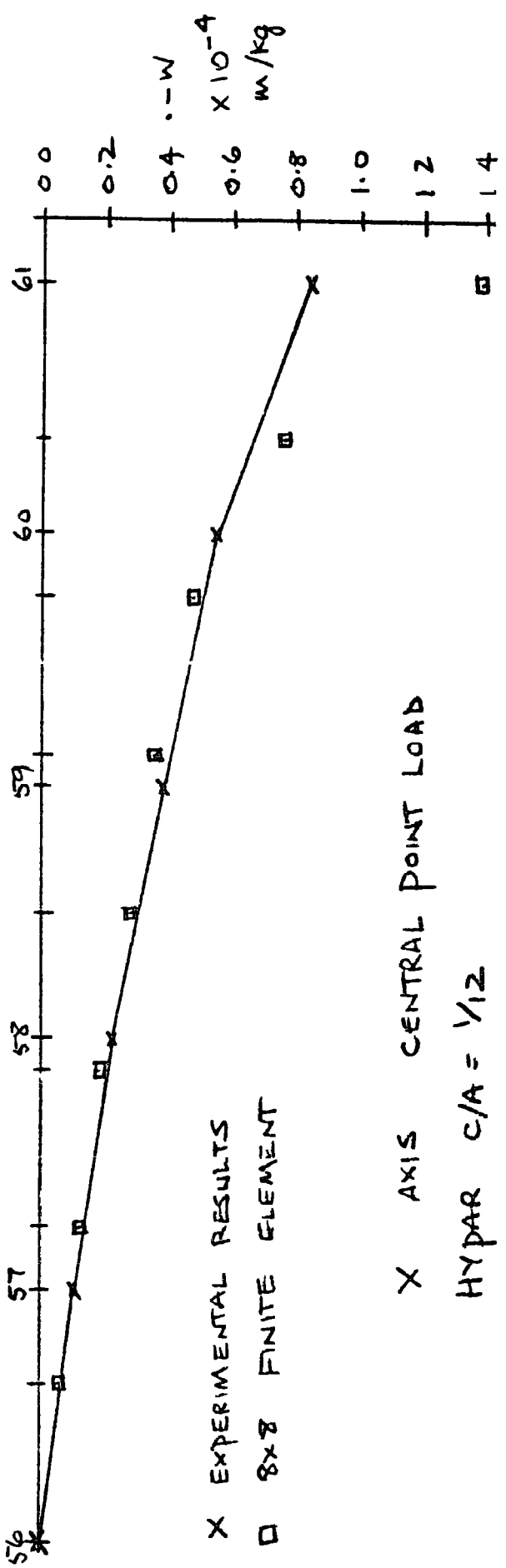
0.0
0.2
0.4
0.6
0.8
1.0
1.2
1.4
-W x10⁻⁴ m/kg
56
57
58
59
60
61
X EXPERIMENTAL RESULTS
□ 8x8 FINITE ELEMENT
X AXIS CENTRAL POINT LOAD
HYPAR C/A = 1/12

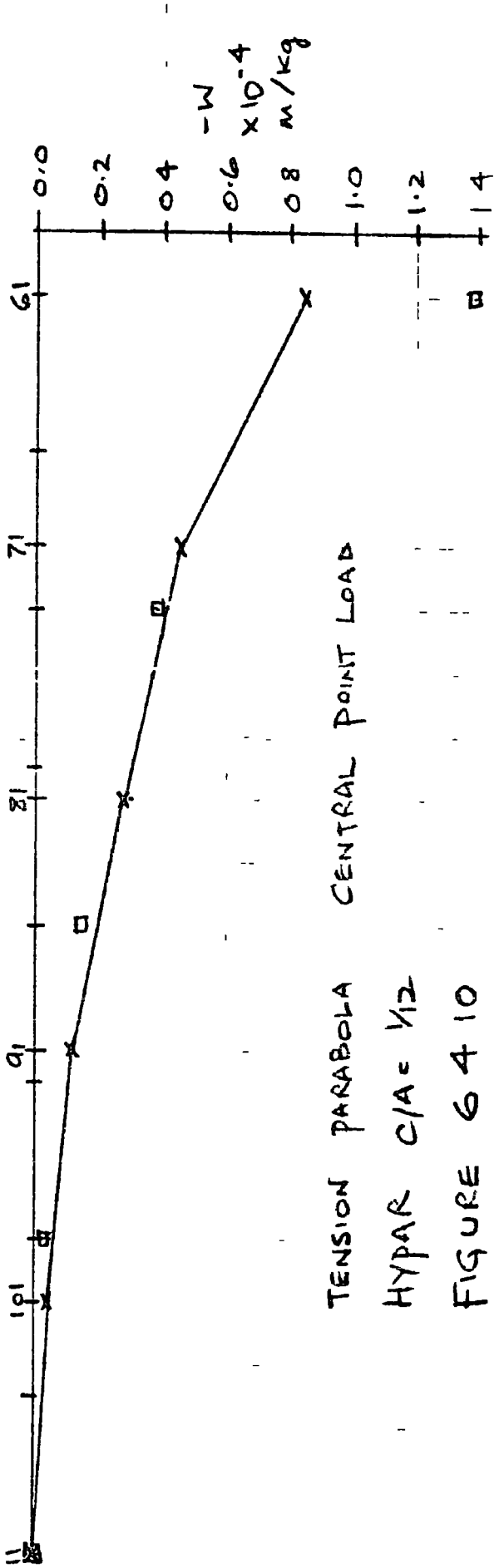
0.0
0.2
0.4
0.6
0.8
1.0
1.2
1.4
-W x10⁻⁴ m/kg
61
71
81
91
101
111
TENSION PARABOLA CENTRAL POINT LOAD
HYPAR C/A = 1/12

FIGURE 6.4.10

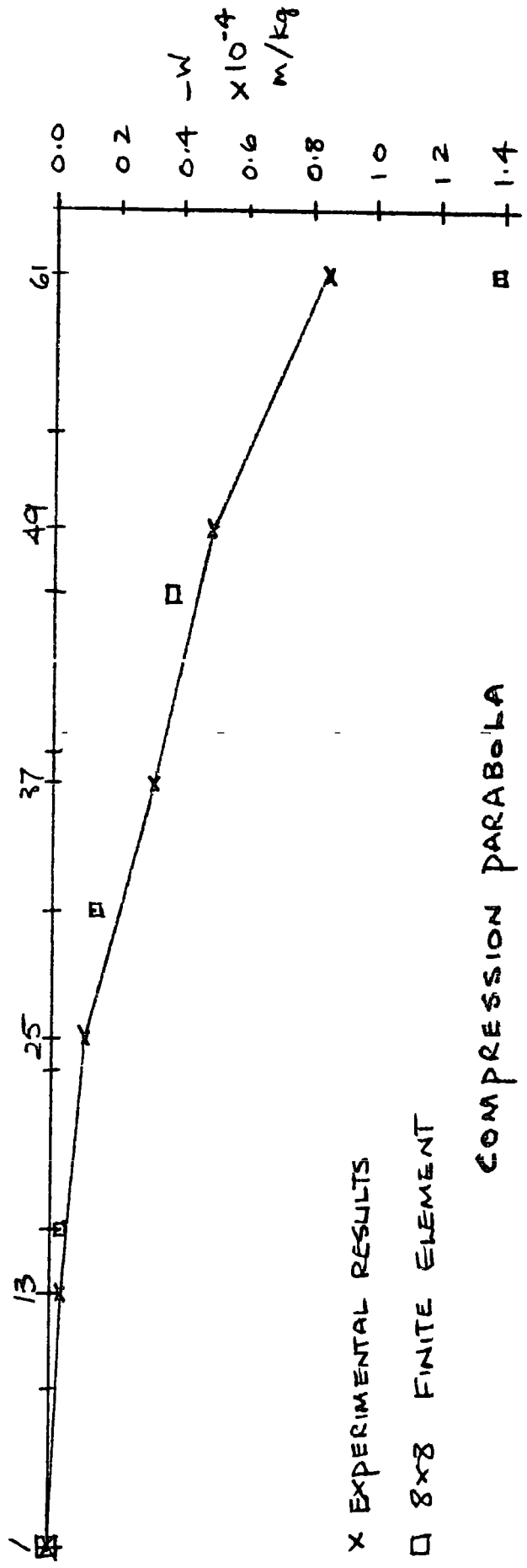

COMPRESSION PARABOLA
HYPAR C/A = 1/12
CENTRAL POINT LOAD

FIGURE 6.4 11

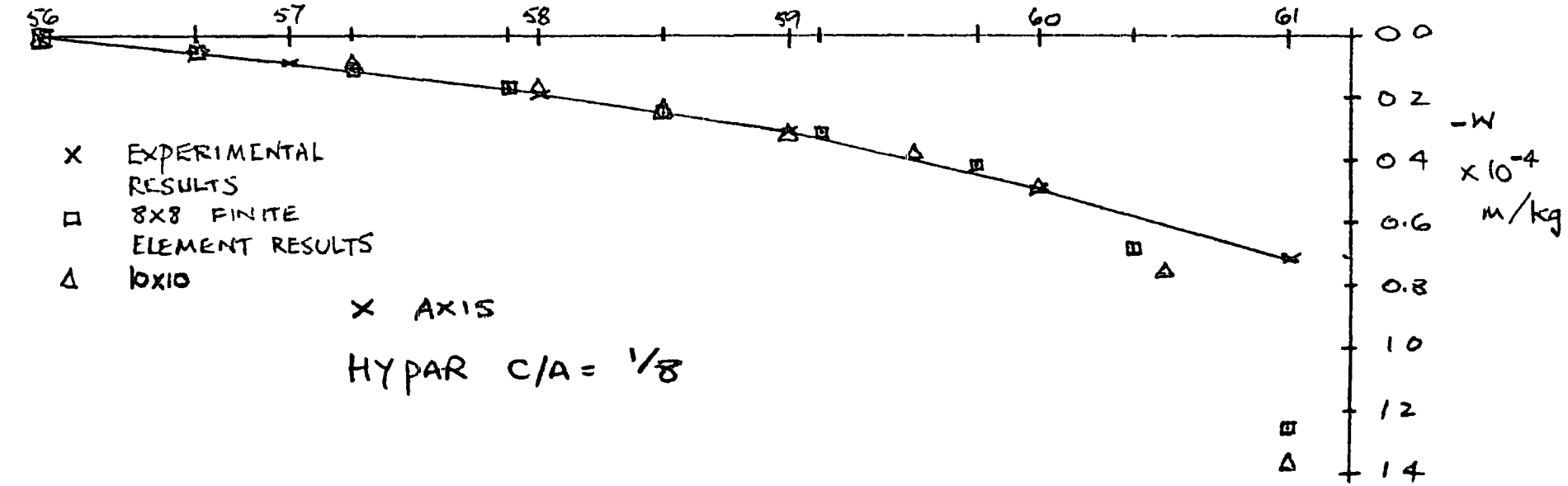

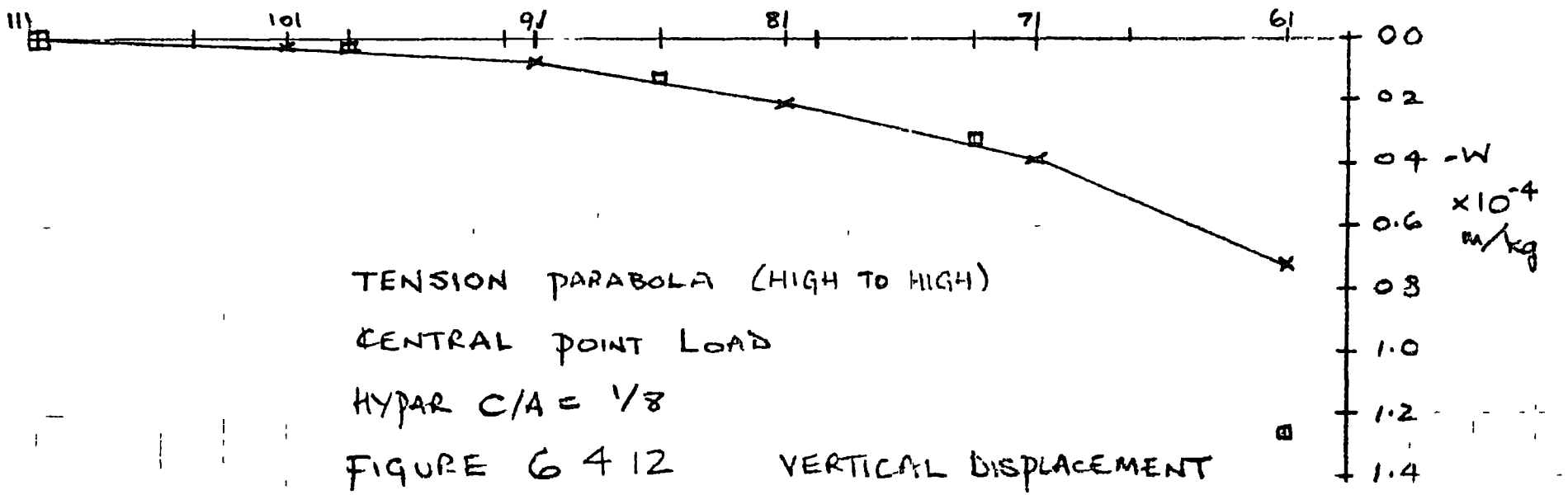

TENSION PARABOLA (HIGH TO HIGH)

CENTRAL POINT LOAD

HYPAR C/A = 1/8

FIGURE 6 4 12 VERTICAL DISPLACEMENT

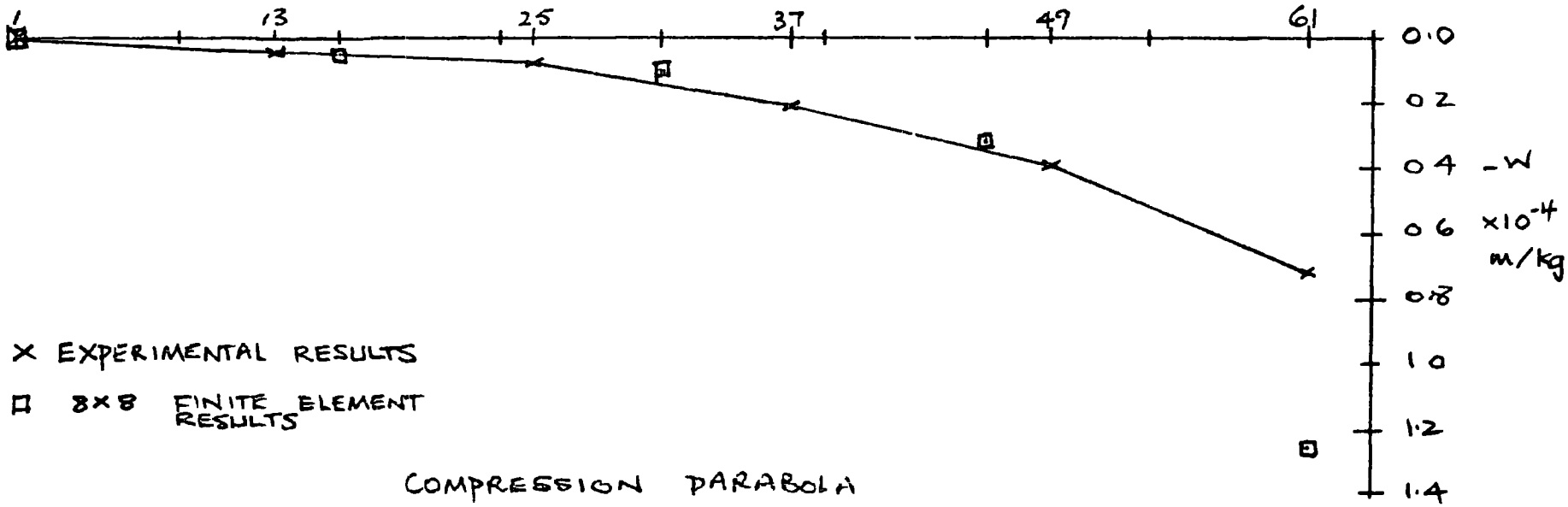

COMPRESSION PARABOLA

HYPAR C/A = 1/8

CENTRAL POINT LOAD

FIGURE 6 4.13 VERTICAL DISPLACEMENT

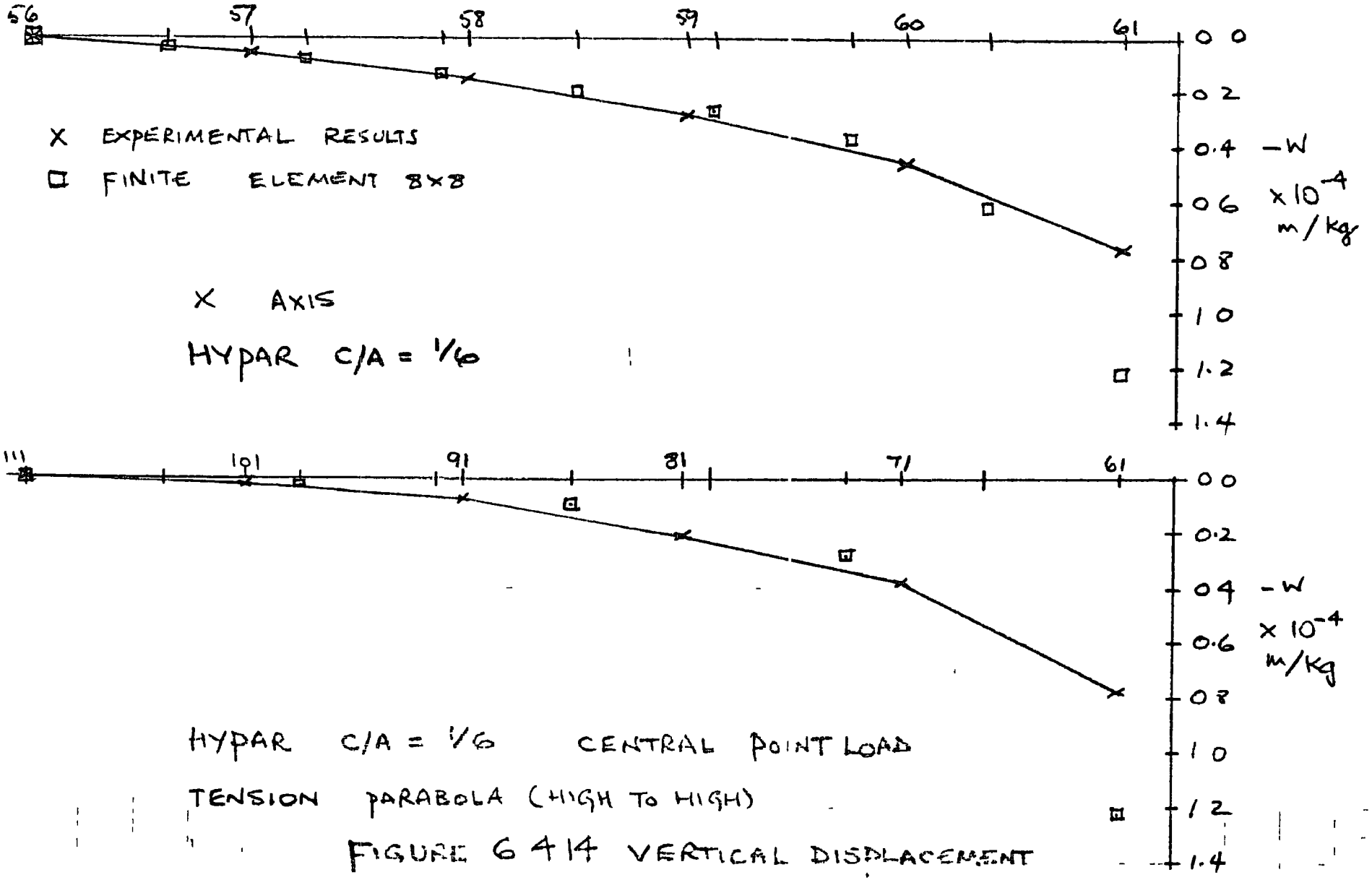

FIGURE 6 4 14 VERTICAL DISPLACEMENT

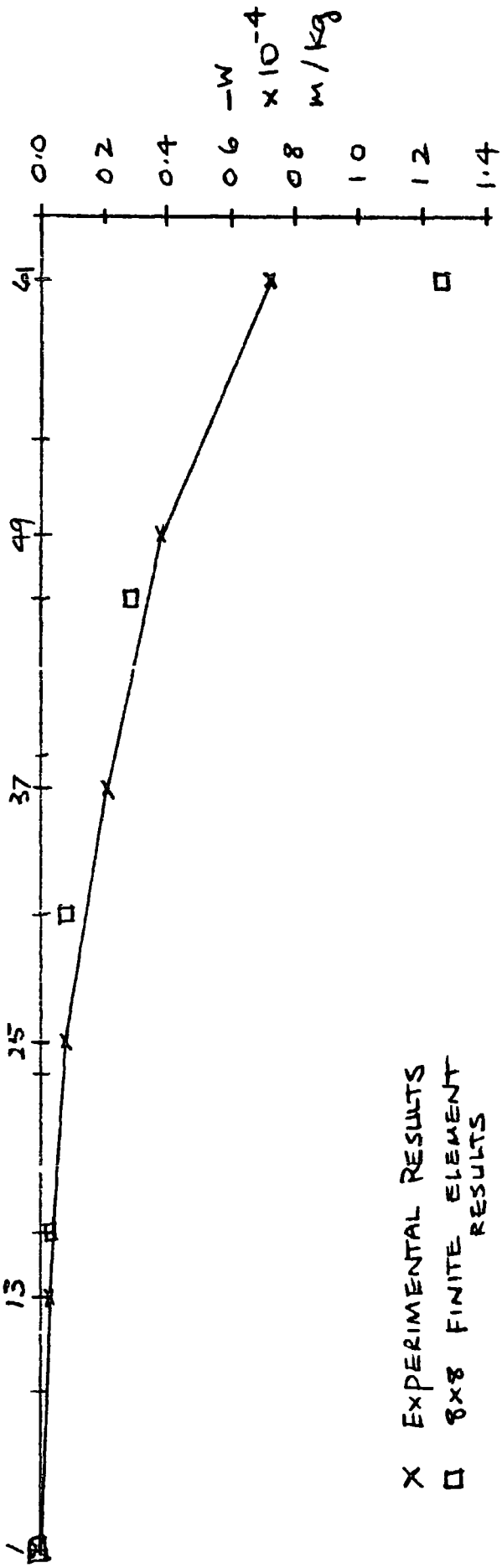
0.0
0.2
0.4
0.6
0.8
1.0
1.2
1.4
-w x 10^-4 m/kg
61
49
37
25
13
1
X EXPERIMENTAL RESULTS
□ 8x8 FINITE ELEMENT RESULTS
COMPRESSION PARABOLA
CENTRAL POINT LOAD
HYPAR c/a = 1/6
VERTICAL DISPLACEMENT

FIGURE 6.4.15

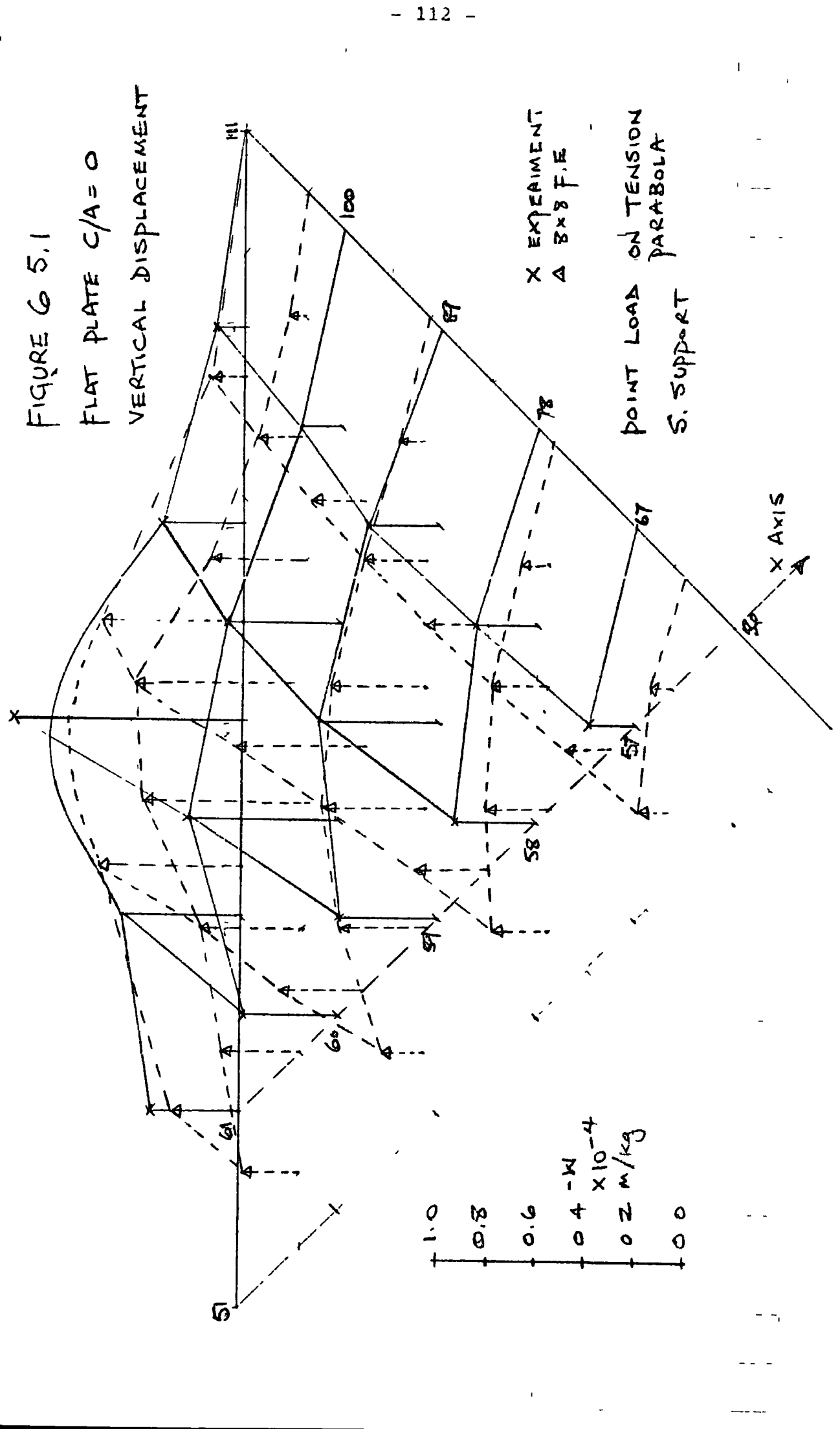
FIGURE 6 5.1
FLAT PLATE C/A = 0
VERTICAL DISPLACEMENT
X EXPERIMENT
Δ 8×8 F.E
POINT LOAD ON TENSION PARABOLA
S. SUPPORT
X AXIS
111
100
67
78
67
58
51
60
61
51
-W × 10⁻⁴ m/kg
1.0
0.8
0.6
0.4
0.2
0.0

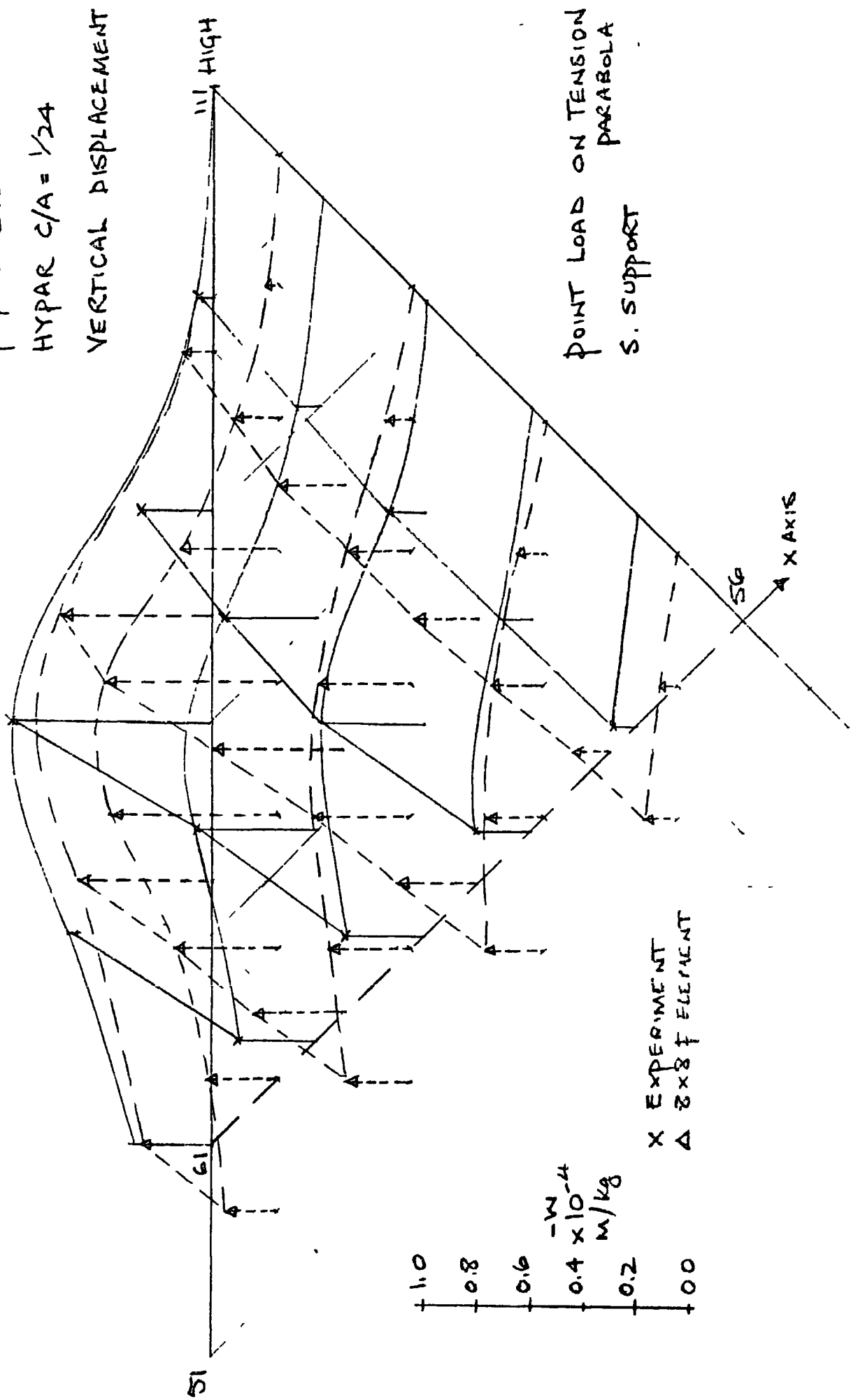
FIGURE 6.52
HYPAR C/A = 1/24
VERTICAL DISPLACEMENT
111 HIGH
POINT LOAD ON TENSION PARABOLA
S. SUPPORT
X AXIS
56
51
61
X EXPERIMENT
Δ 8×8 ℓ ELEMENT
-w
0.4 × 10⁻⁴ M/kg
1.0
0.8
0.6
0.2
00

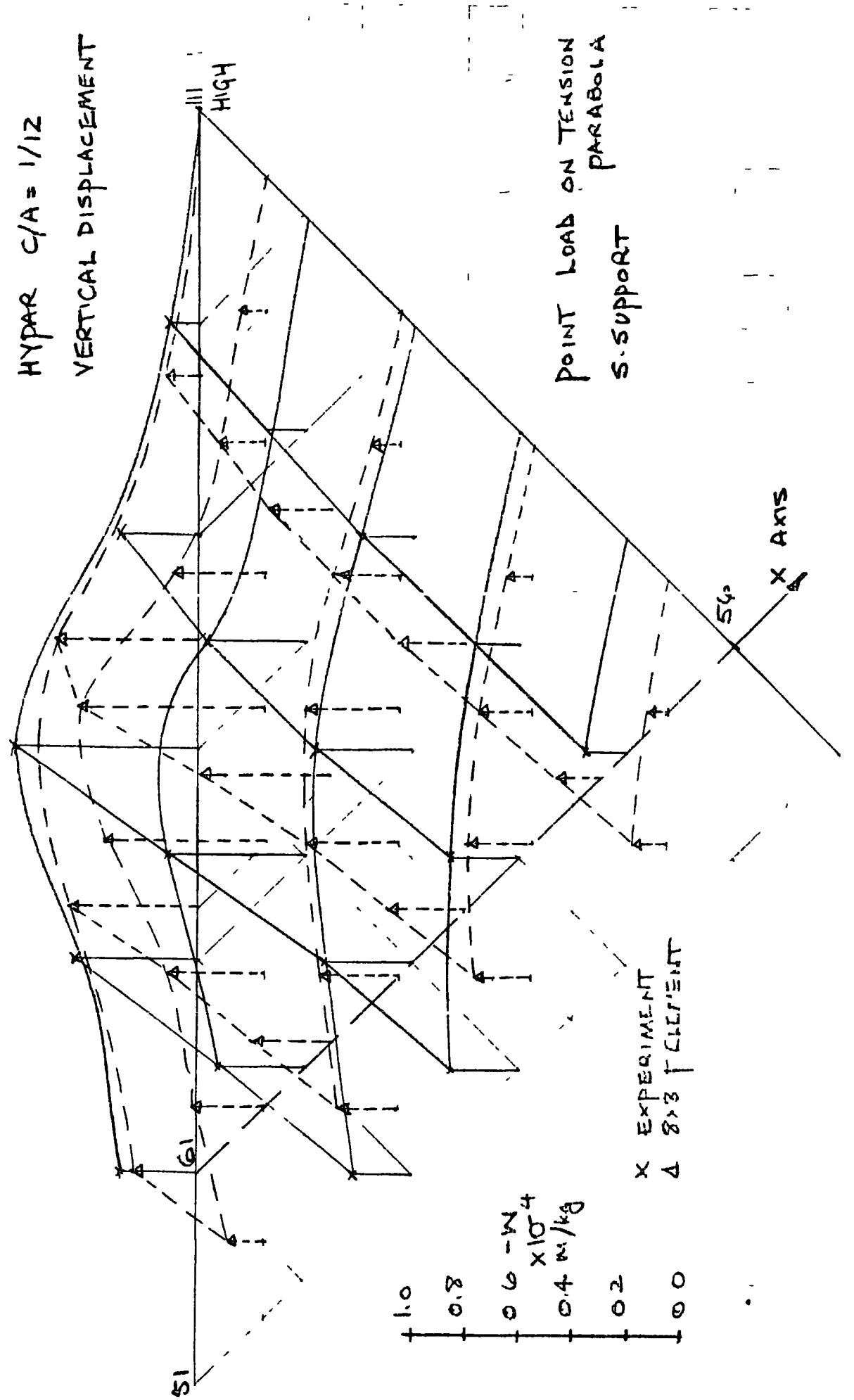
FIGURE 6.5.3
HYPAR C/A = 1/12
VERTICAL DISPLACEMENT
111
HIGH
POINT LOAD ON TENSION PARABOLA
S. SUPPORT
54
X AXIS
61
51
X EXPERIMENT
Δ 8×3 ELEMENT
1.0
0.8
0.6
0.4
0.2
0.0
-W x10^-4 m/kg

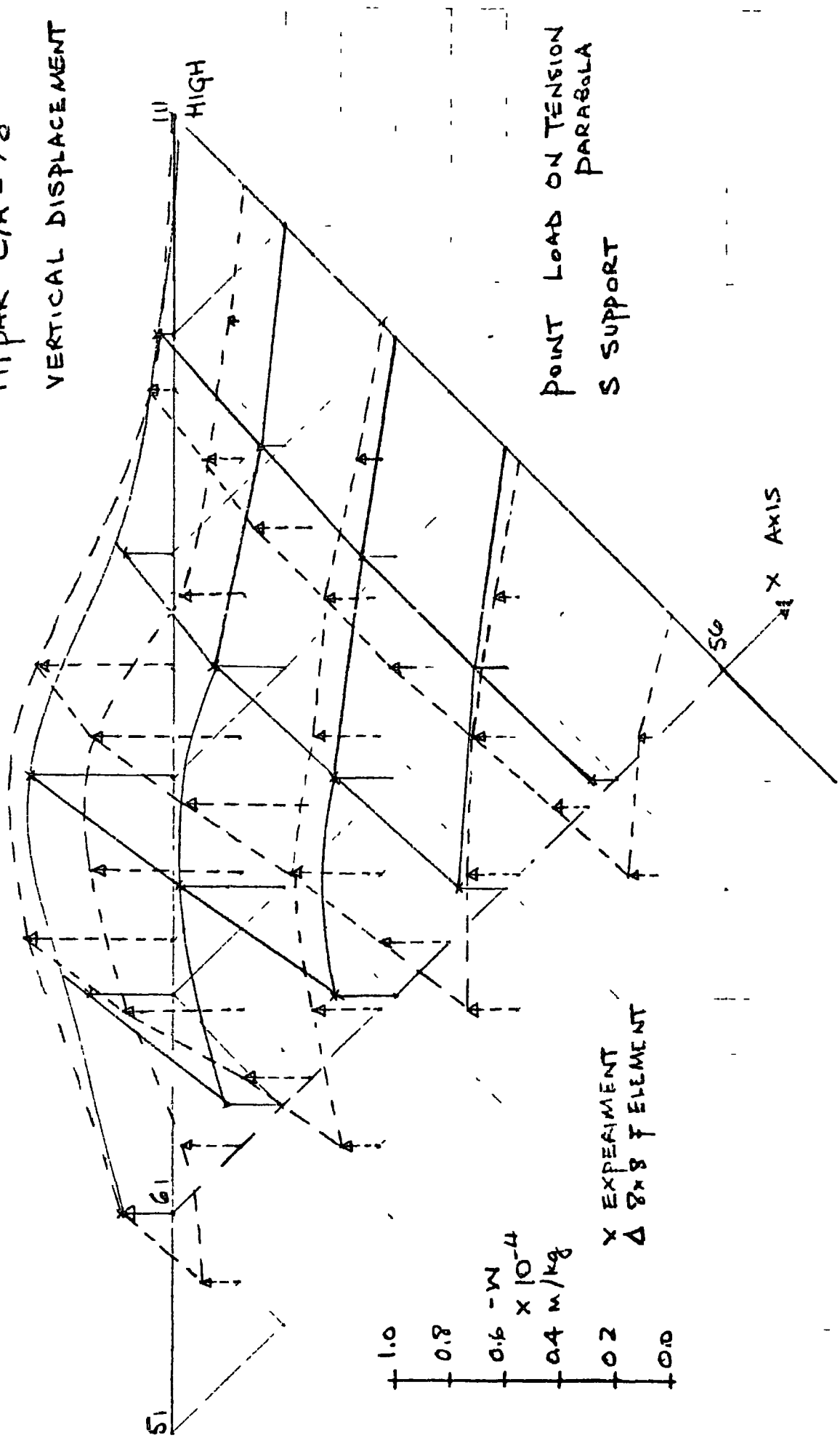

FIGURE 6.5.4
HYPAR C/A = 1/8

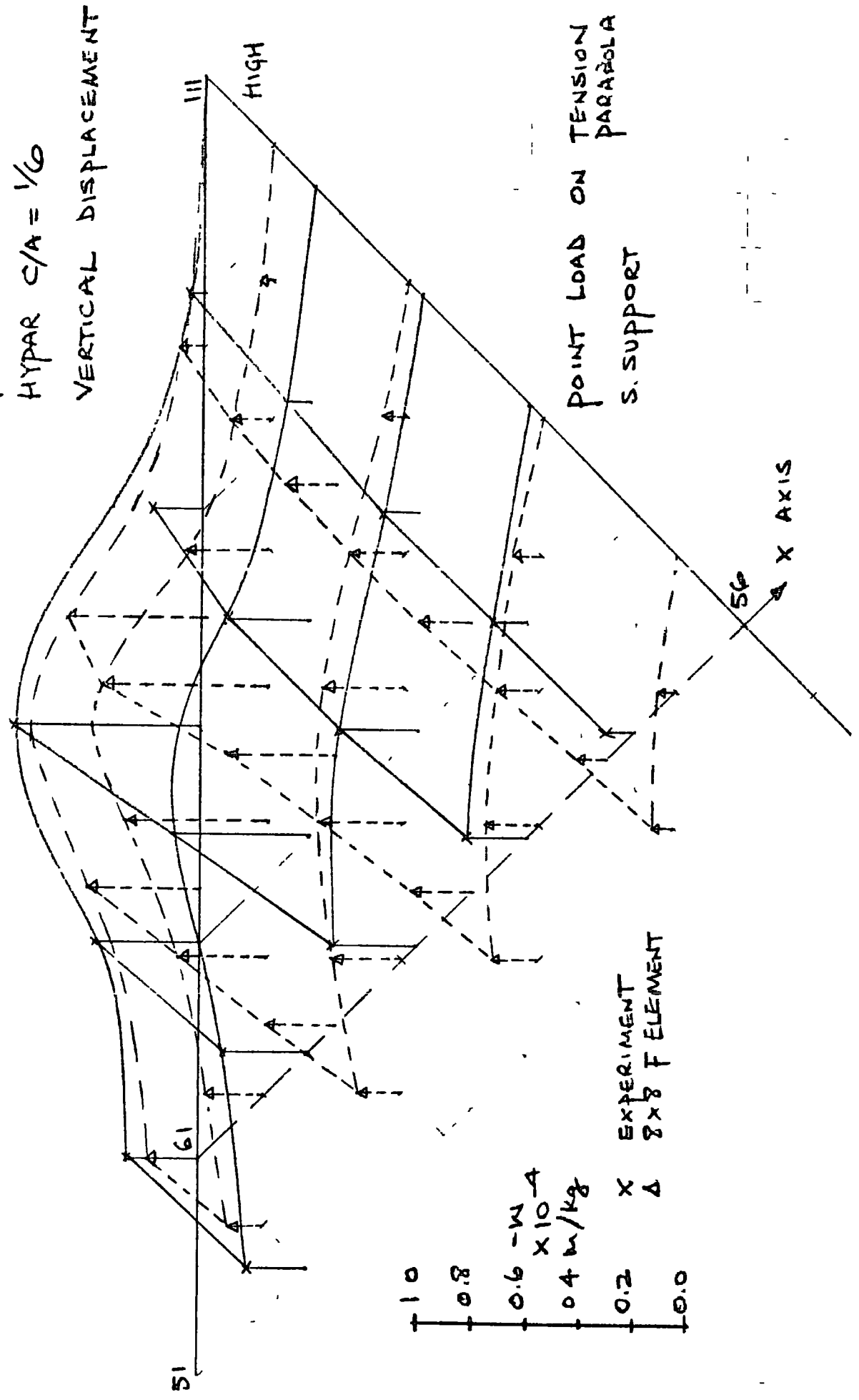
FIGURE 6 5.5
HYPAR C/A = 1/6
VERTICAL DISPLACEMENT
111
HIGH
POINT LOAD ON TENSION PARABOLA
S. SUPPORT
56
X AXIS
61
51
1.0
0.8
0.6
0.4
0.2
0.0
-W
x10^-4
m/kg
EXPERIMENT
8x8 F ELEMENT

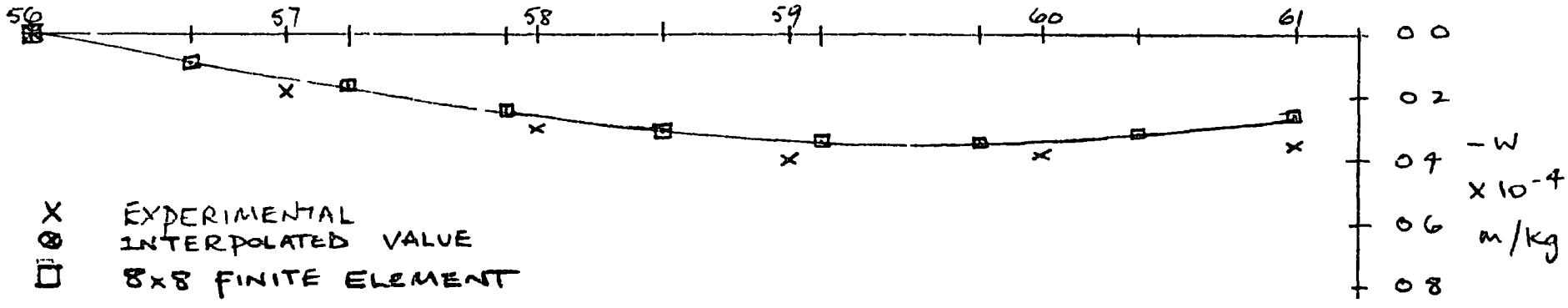

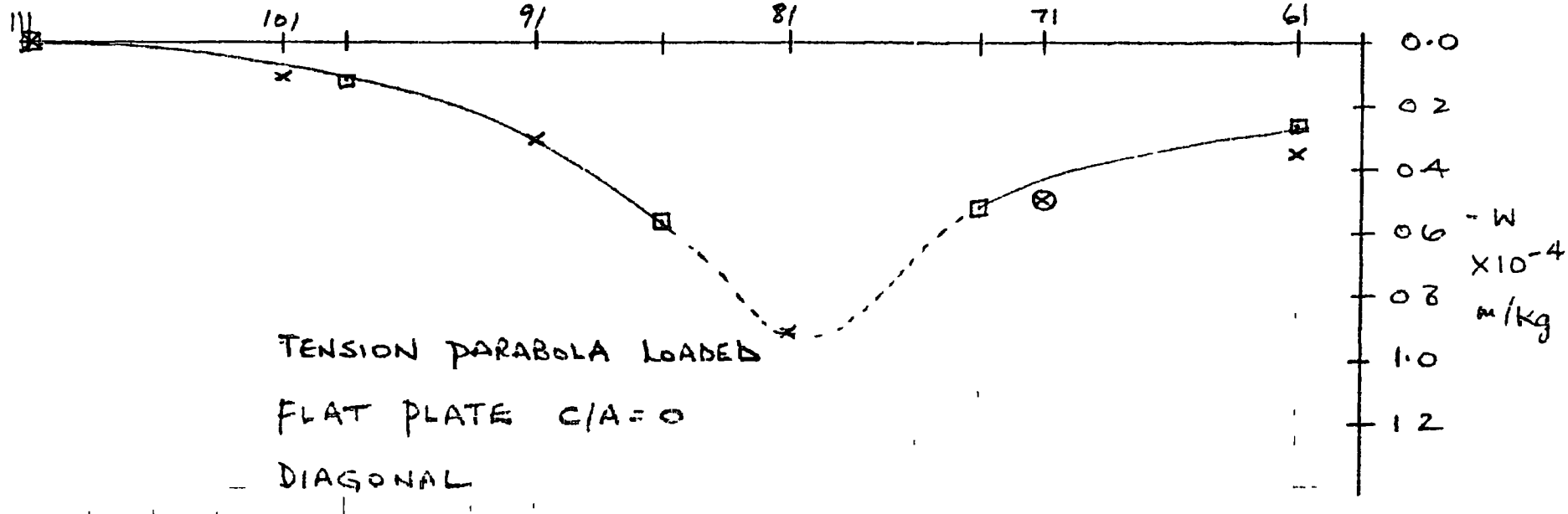

FIGURE 6.56 VERTICAL DISPLACEMENT

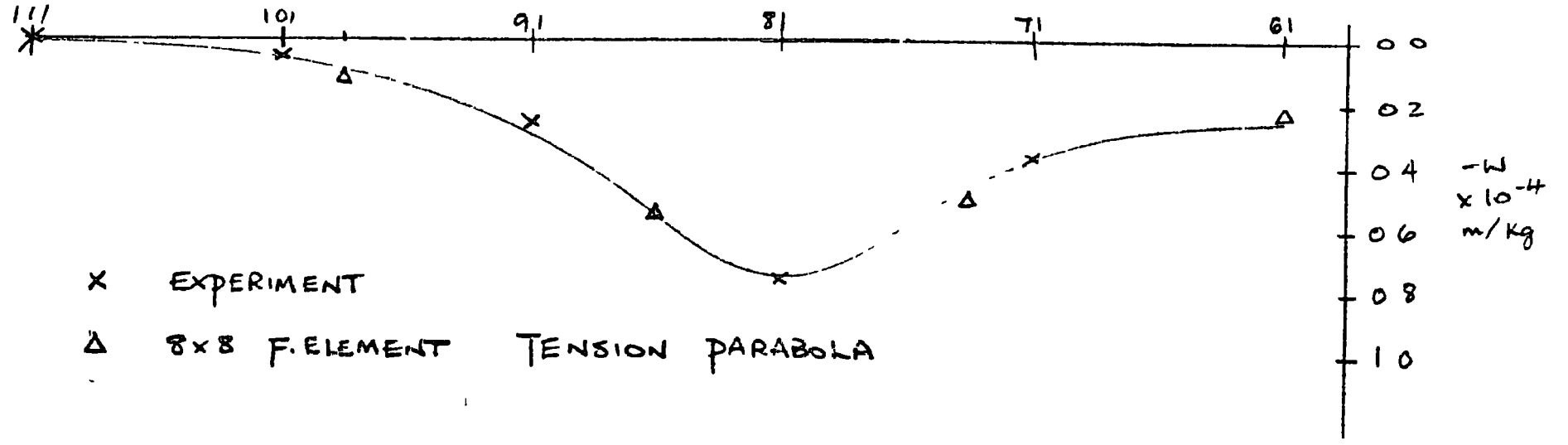

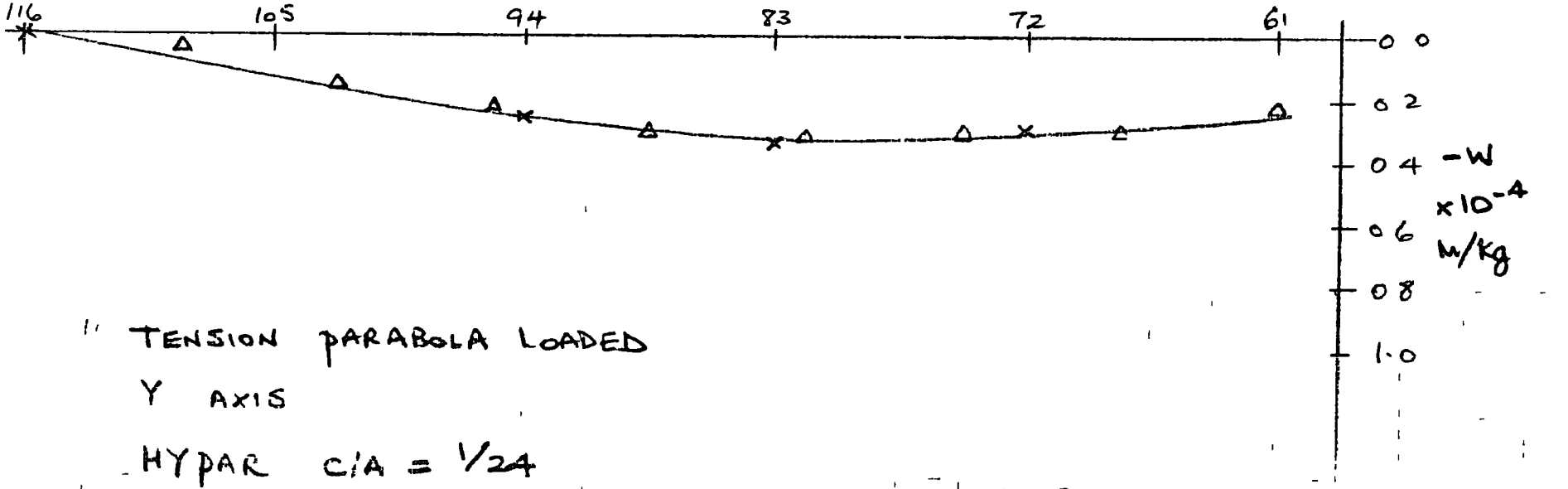

" TENSION PARABOLA LOADED
Y AXIS
HYPAR C/A = 1/24

FIGURE 6.5.7 VERTICAL DISPLACEMENT

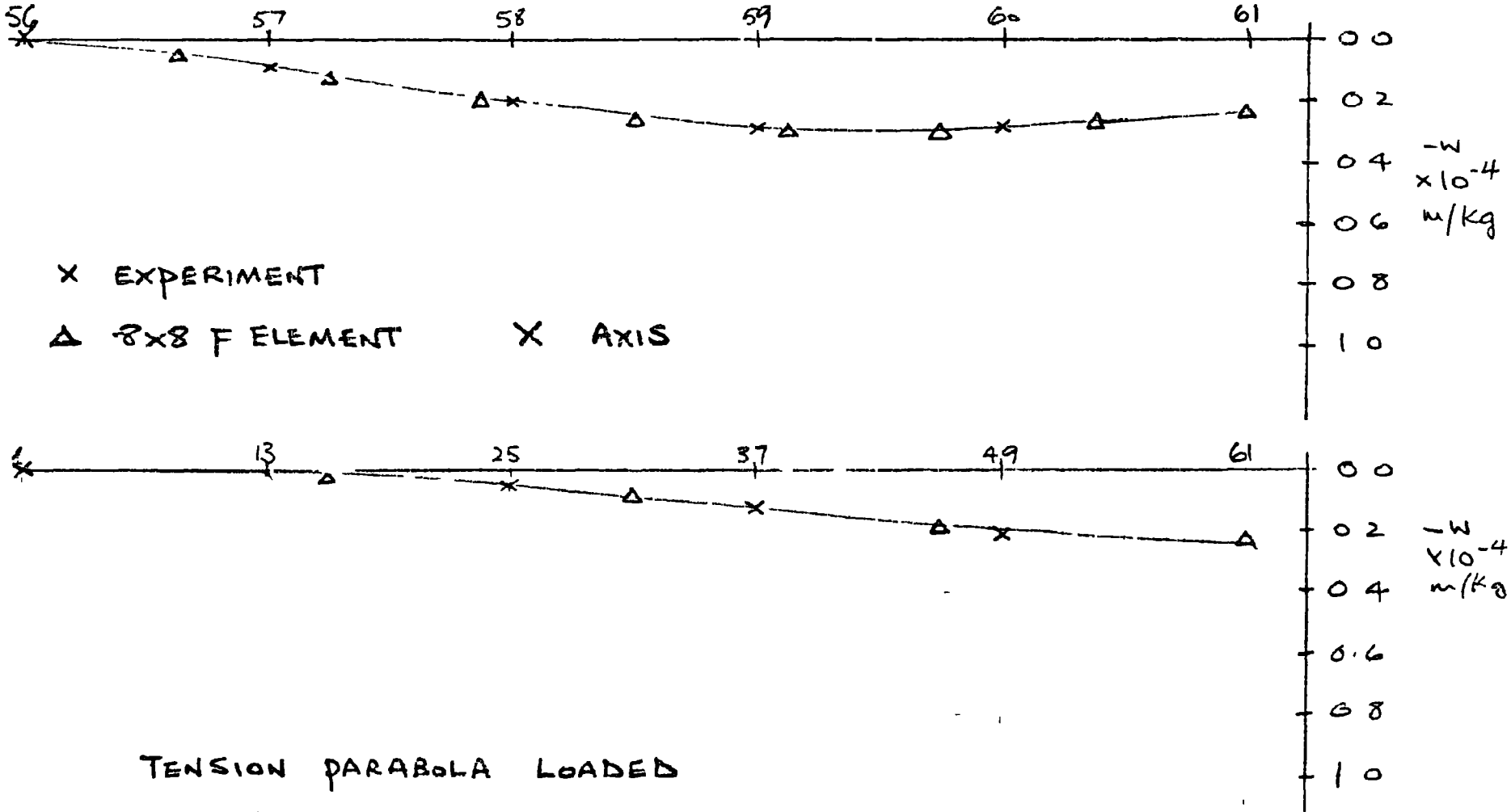

FIGURE 6.5.8 VERTICAL DISPLACEMENTS

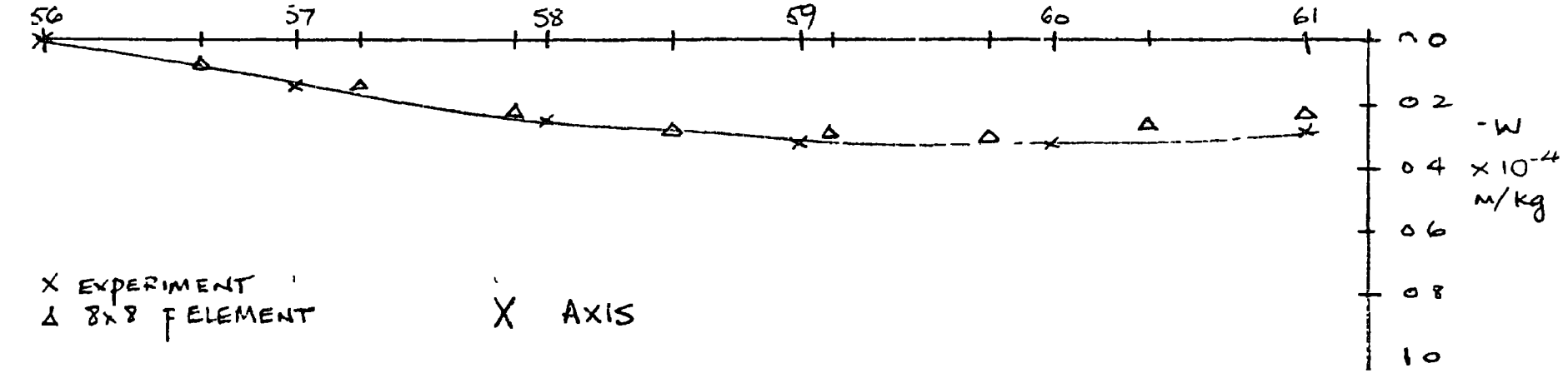

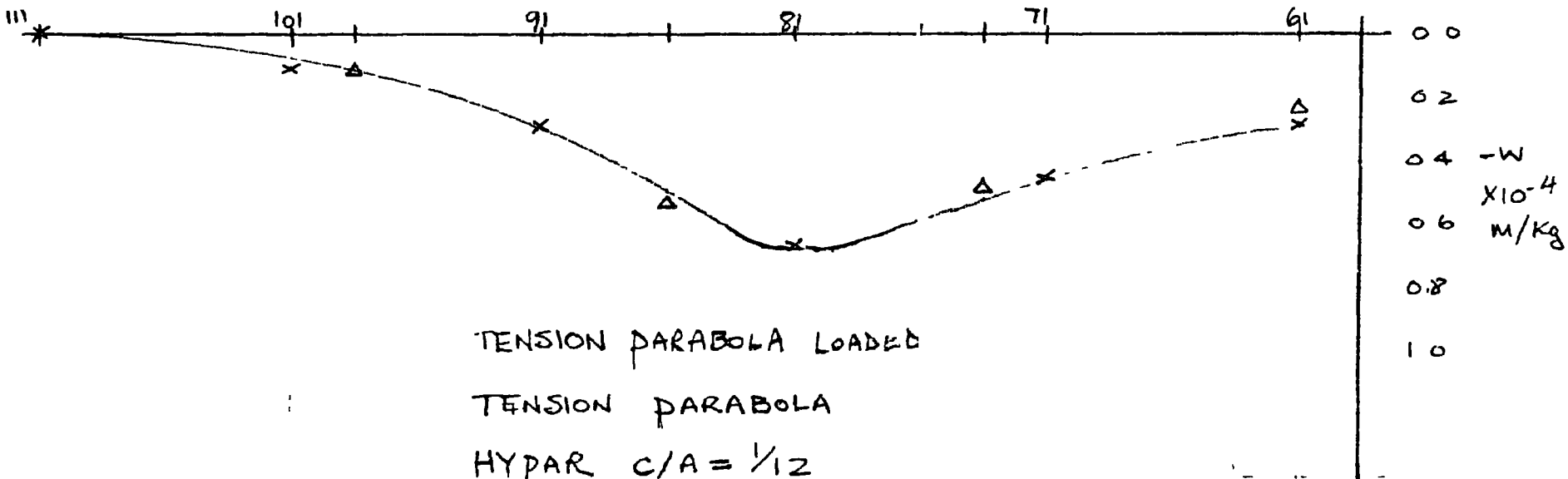

TENSION PARABOLA LOADED

TENSION PARABOLA

HYPAR c/A = 1/12

FIGURE 6 5.9

VERTICAL DISPLACEMENT

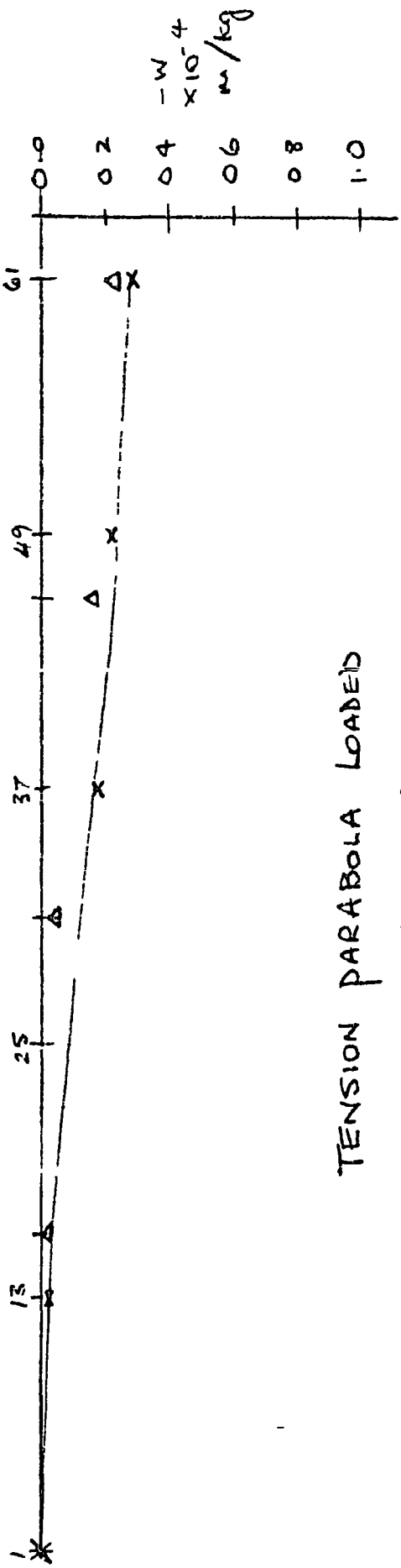

TENSION PARABOLA LOADED
COMPRESSION PARABOLA
HYPAR C/A = 1/12
FIGURE G 5.10

VERTICAL
DISPLACEMENT

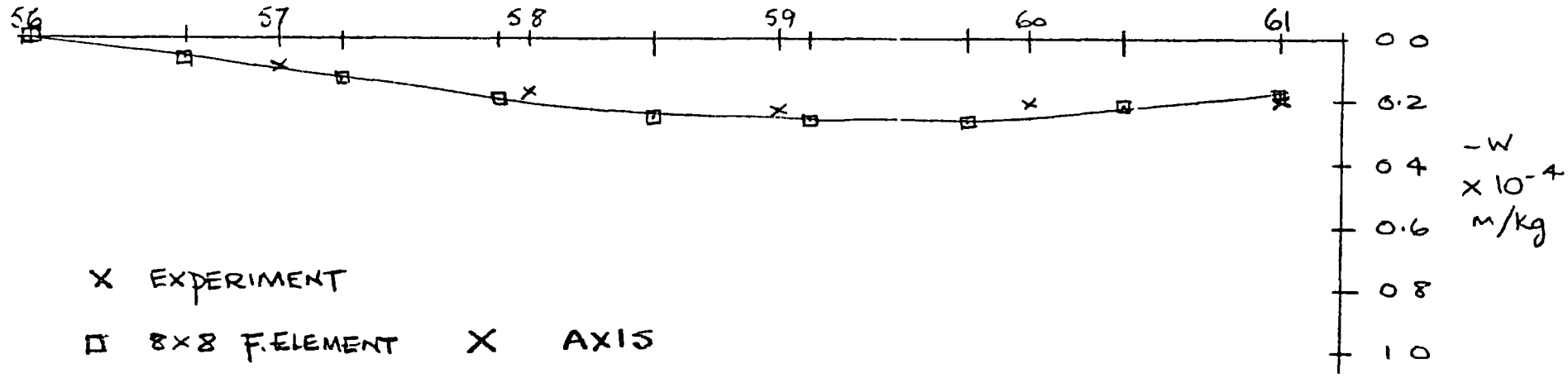

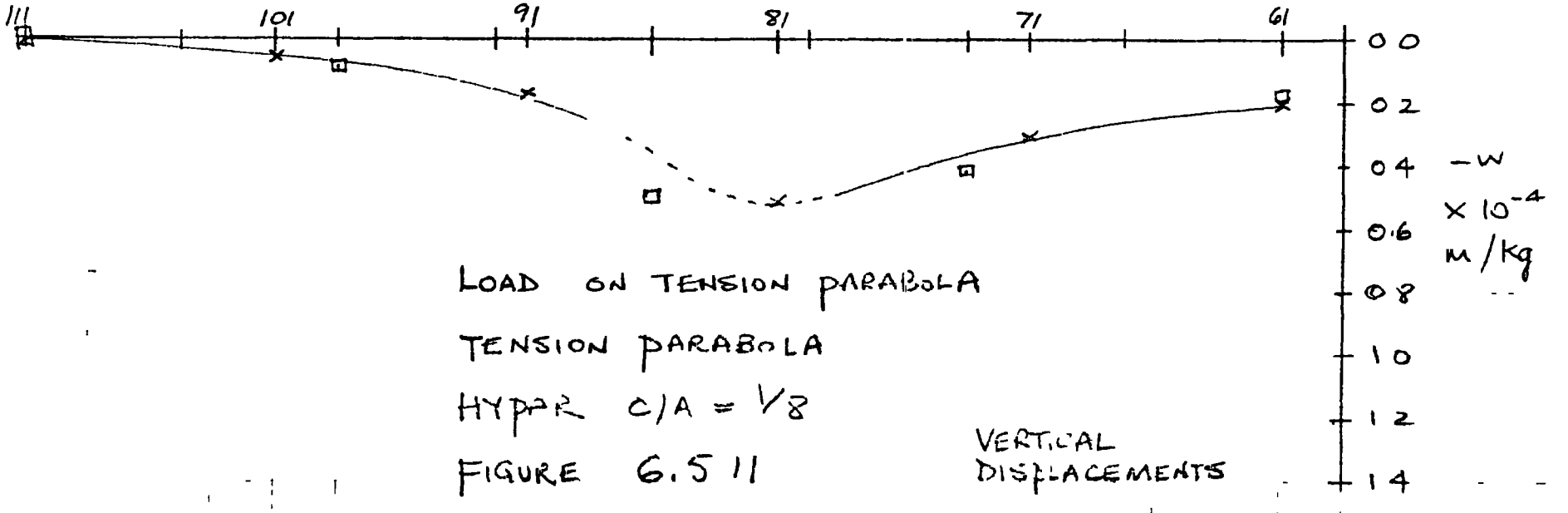

LOAD ON TENSION PARABOLA

TENSION PARABOLA

HYPR C/A = 1/8

FIGURE 6.5 11

VERTICAL DISPLACEMENTS

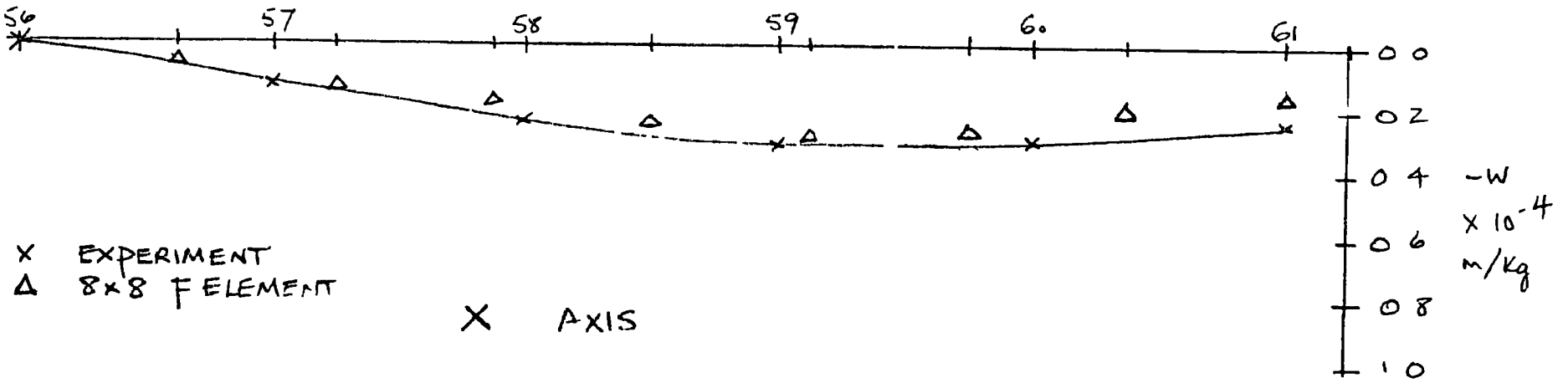

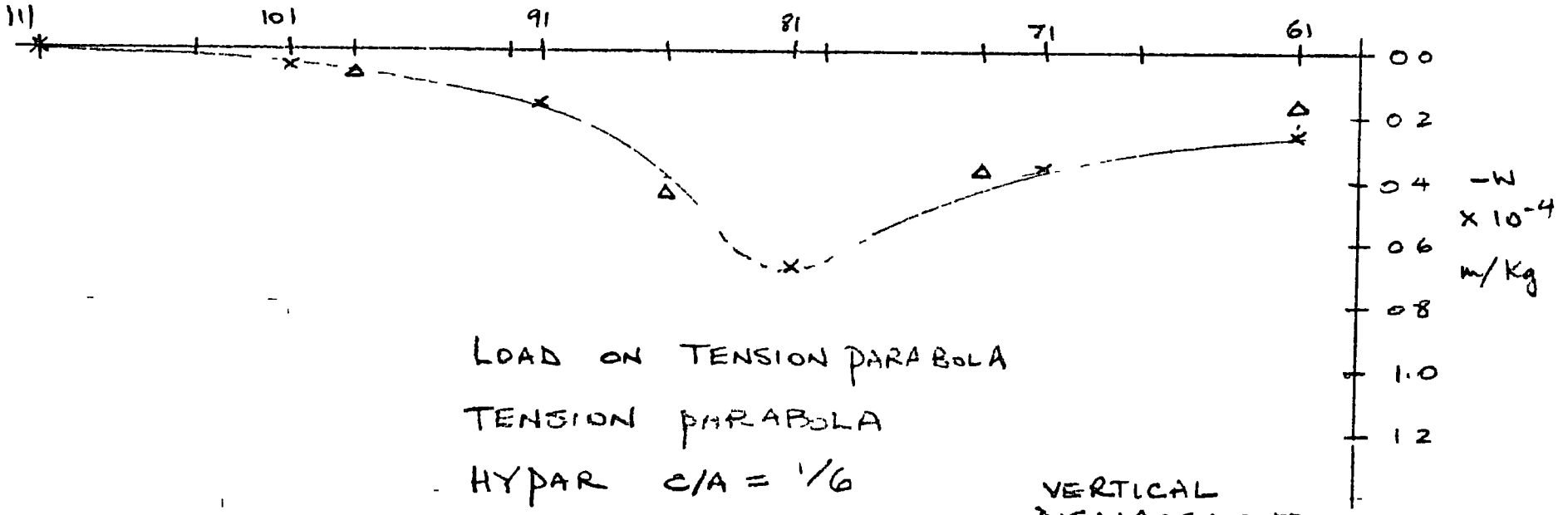

LOAD ON TENSION PARABOLA

TENSION PARABOLA

HYPAR c/A = 1/6

FIGURE 6.5 12

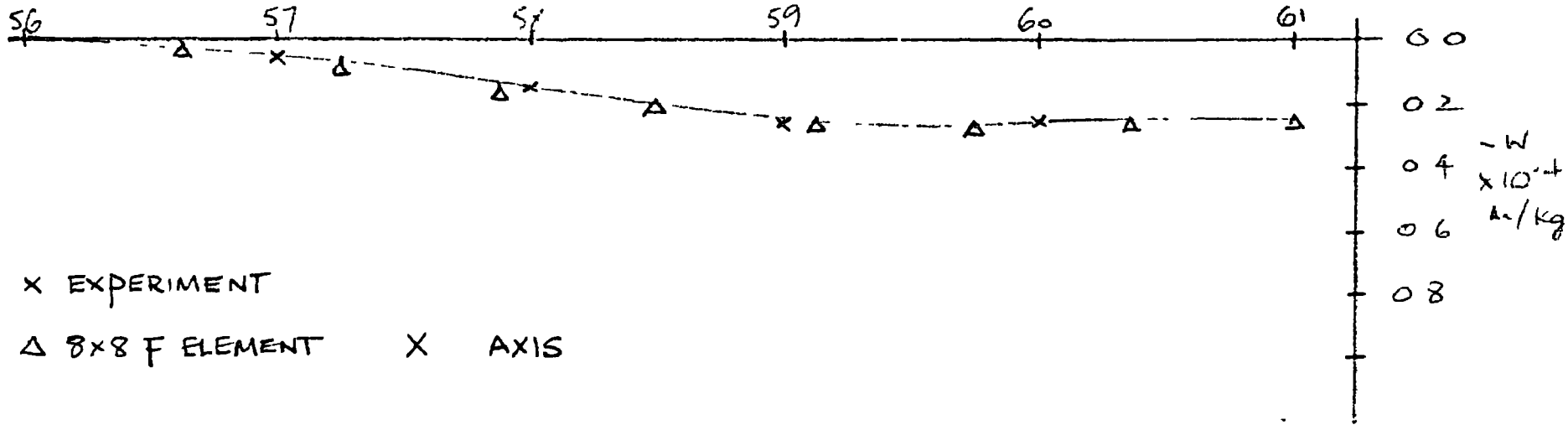

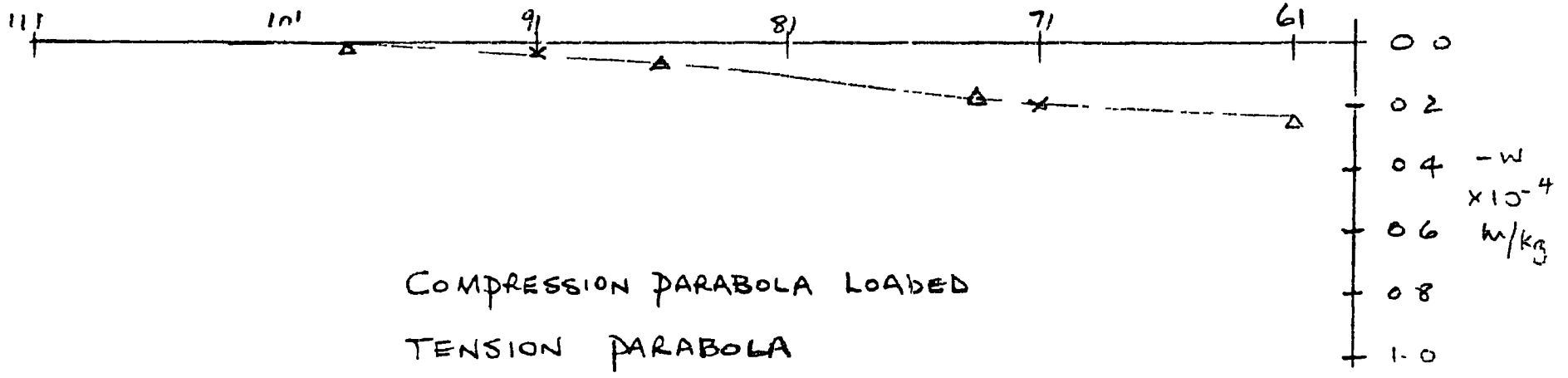

COMPRESSION PARABOLA LOADED

TENSION PARABOLA

HYPAR c/a = 1/24

FIGURE G 5.13

VERTICAL DISPLACEMENT

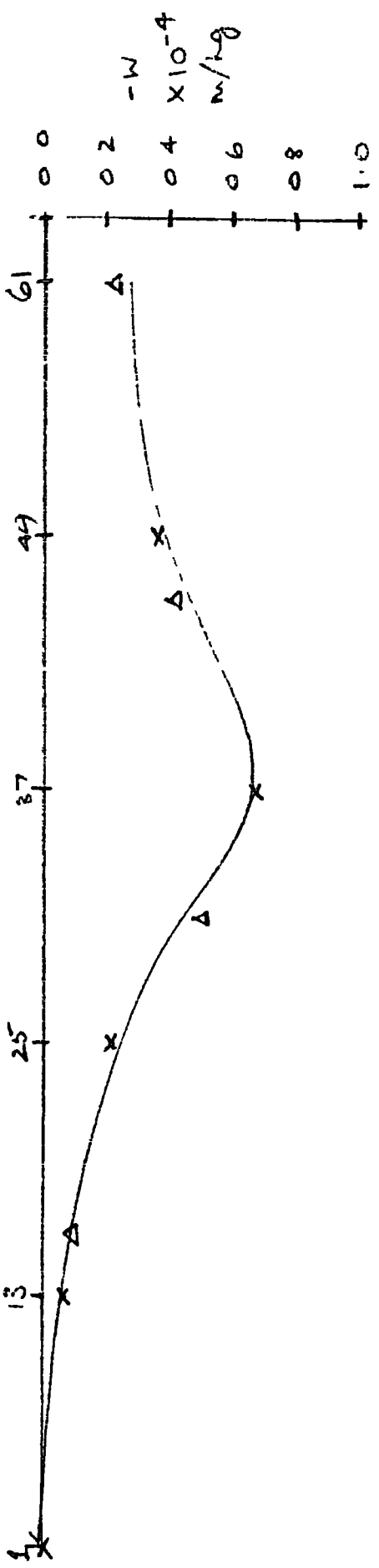

COMPRESSION PARABOLA LOADED

COMPRESSION PARABOLA

HYPAR c/a = 1/24

VERTICAL DISPLACEMENT

FIGURE 6.5.14

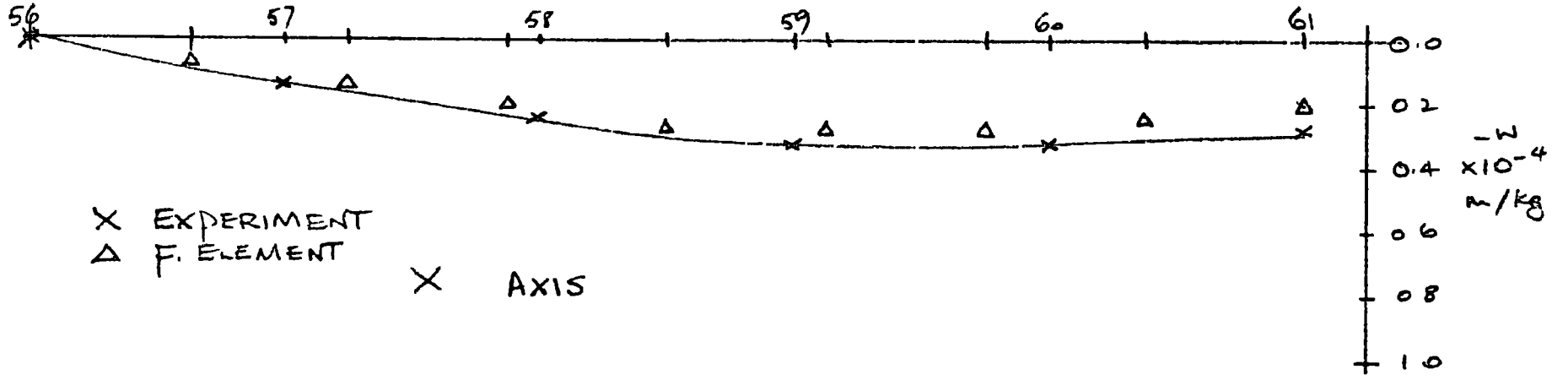

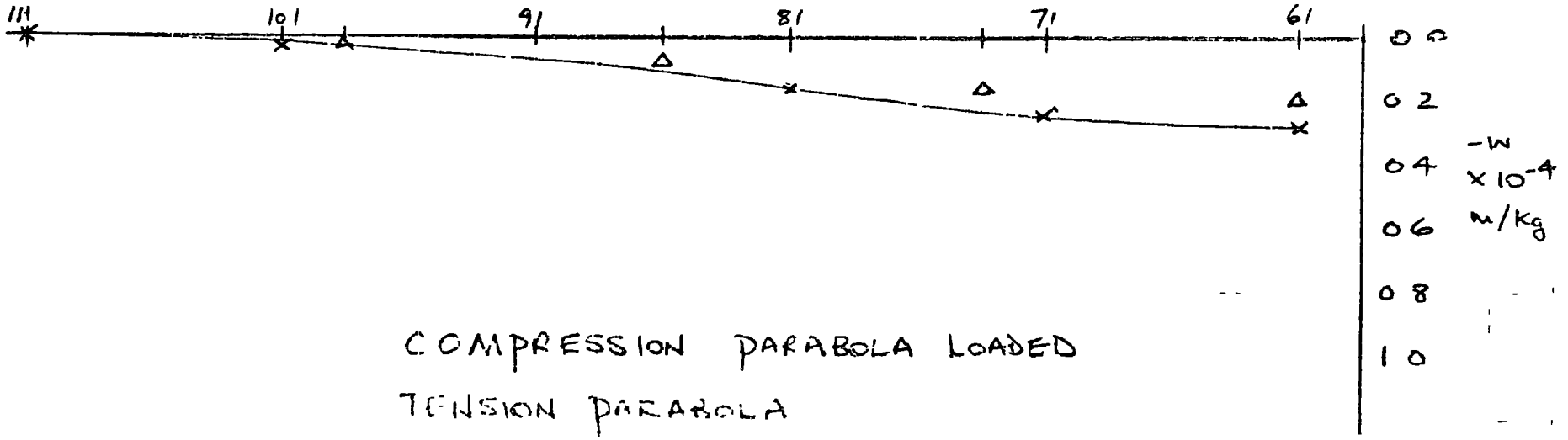

COMPRESSION PARABOLA LOADED

TENSION PARABOLA

HYPAR c/a = 1/12

FIGURE 6.5.15

VERTICAL DISPLACEMENT

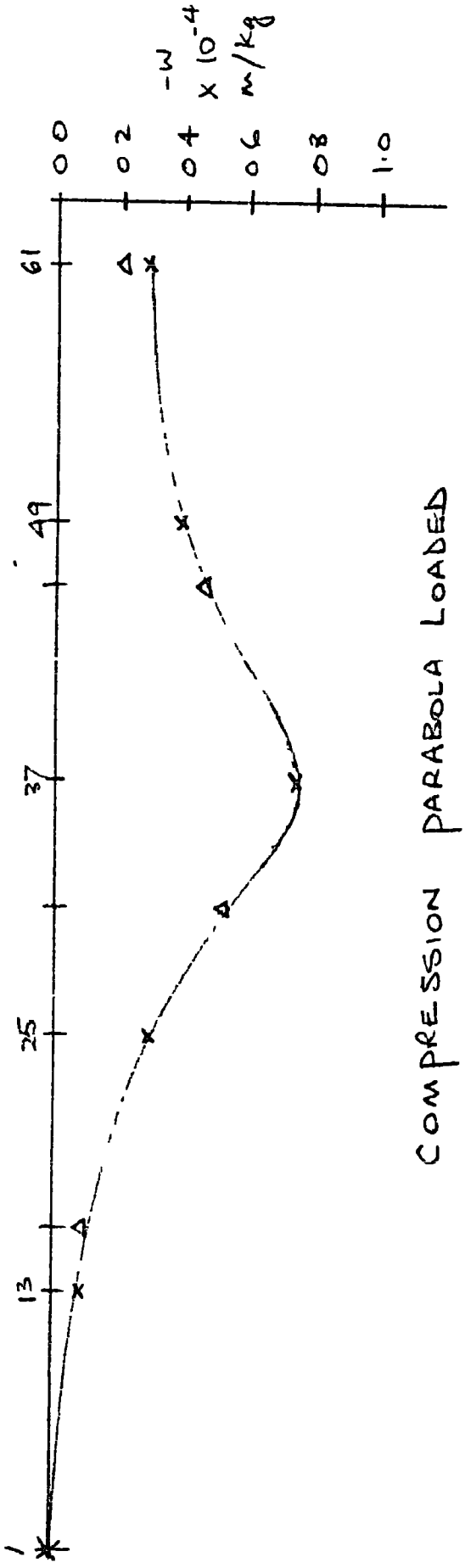

COMPRESSION PARABOLA LOADED

COMPRESSION PARABOLA

HYPAR C/A = 1/12

FIGURE 6 5.16

VERTICAL DISPLACEMENT

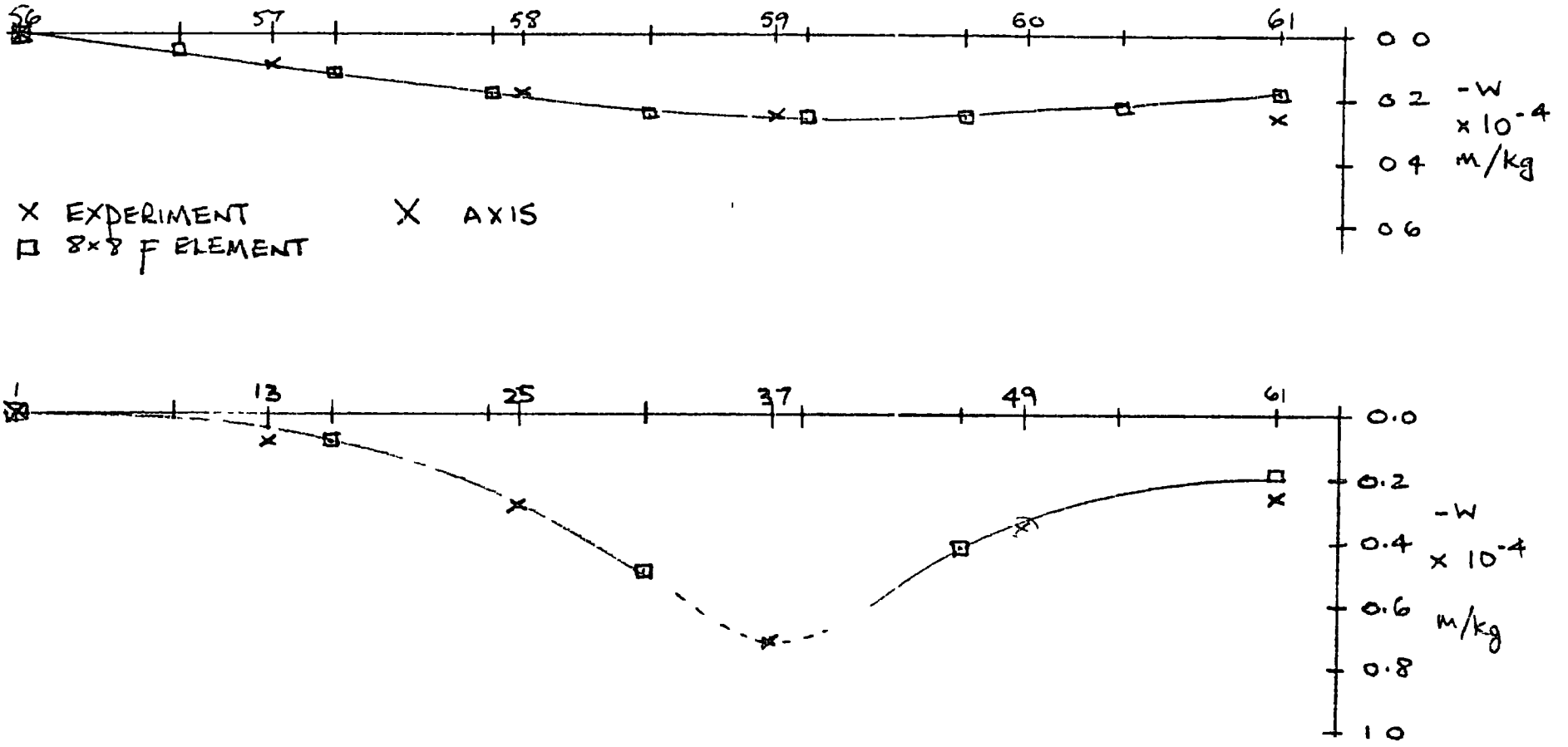

LOAD ON COMPRESSION PARABOLA

COMPRESSION PARABOLA

HYPAR C/A = 1/8

FIGURE 6 5.17

VERTICAL DISPLACEMENT

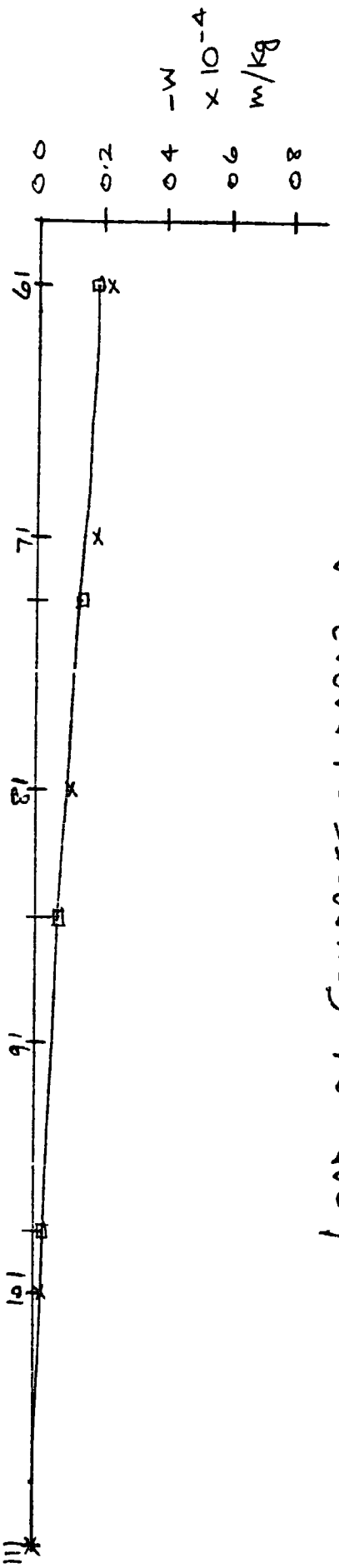

LOAD ON COMPRESSION PARABOLA

TENSION PARABOLA

HYPAR c/a = 1/8

FIGURE 6.5.18

VERTICAL DISPLACEMENT

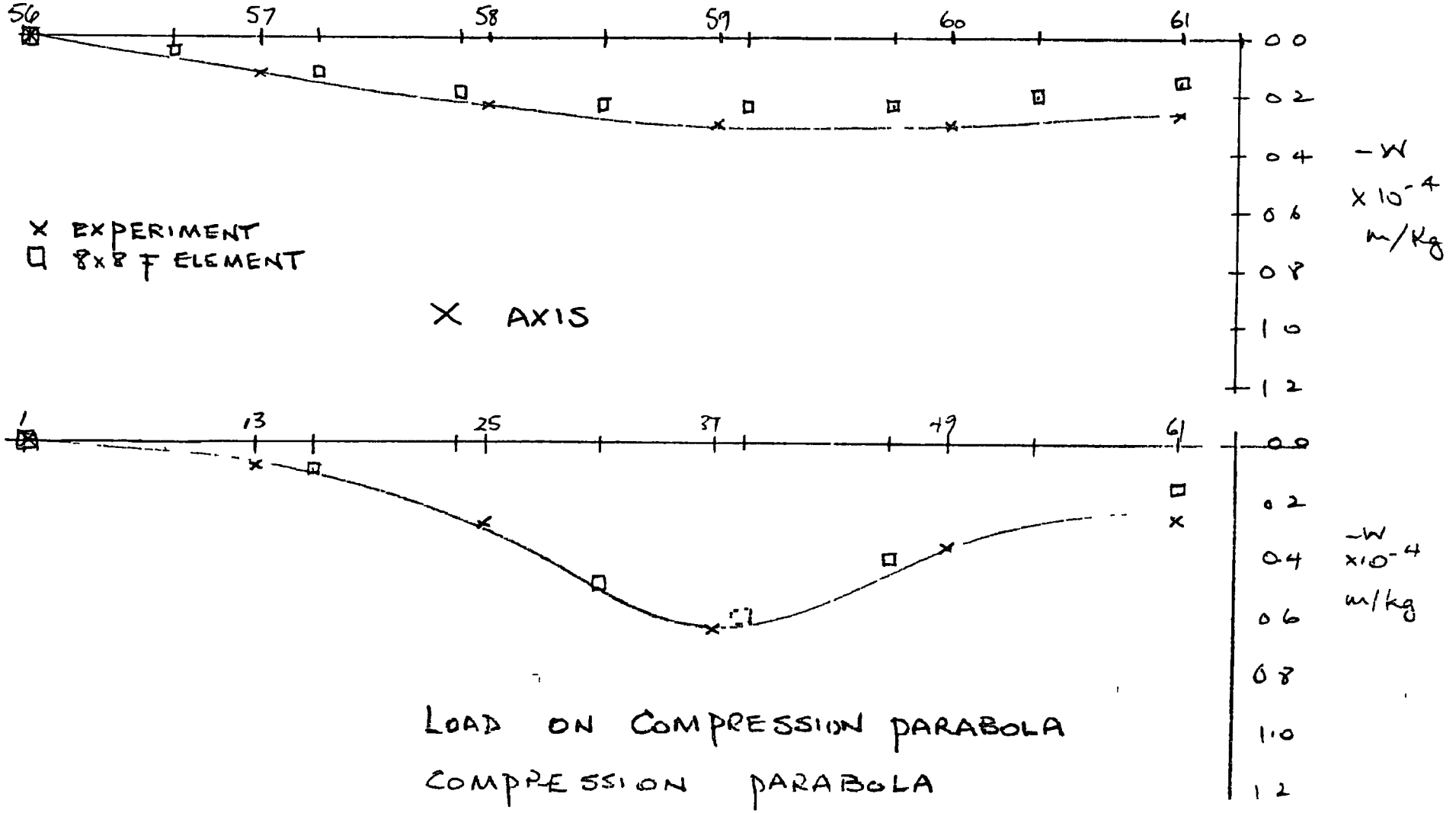

LOAD ON COMPRESSION PARABOLA

COMPRESSION PARABOLA

HYPAR C/A = 1/6

FIGURE 6.5.19

VERTICAL DISPLACEMENT

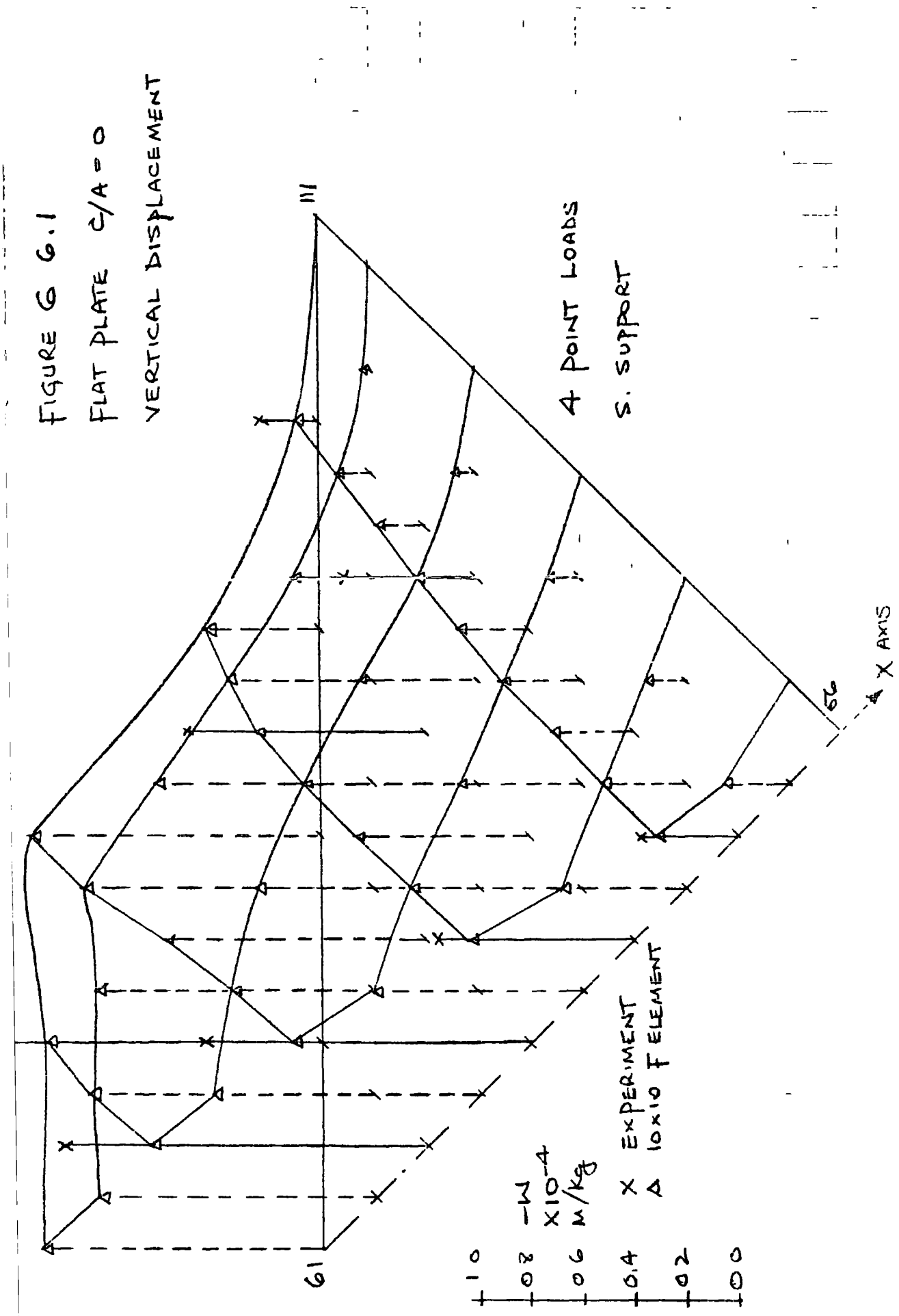
FIGURE G 6.1
FLAT PLATE c/A = 0
VERTICAL DISPLACEMENT
4 POINT LOADS
S. SUPPORT
111
61
52
X AXIS
X EXPERIMENT
Δ 10x10 F ELEMENT
-W X10-4 M/KG
1.0
0.8
0.6
0.4
0.2
0.0

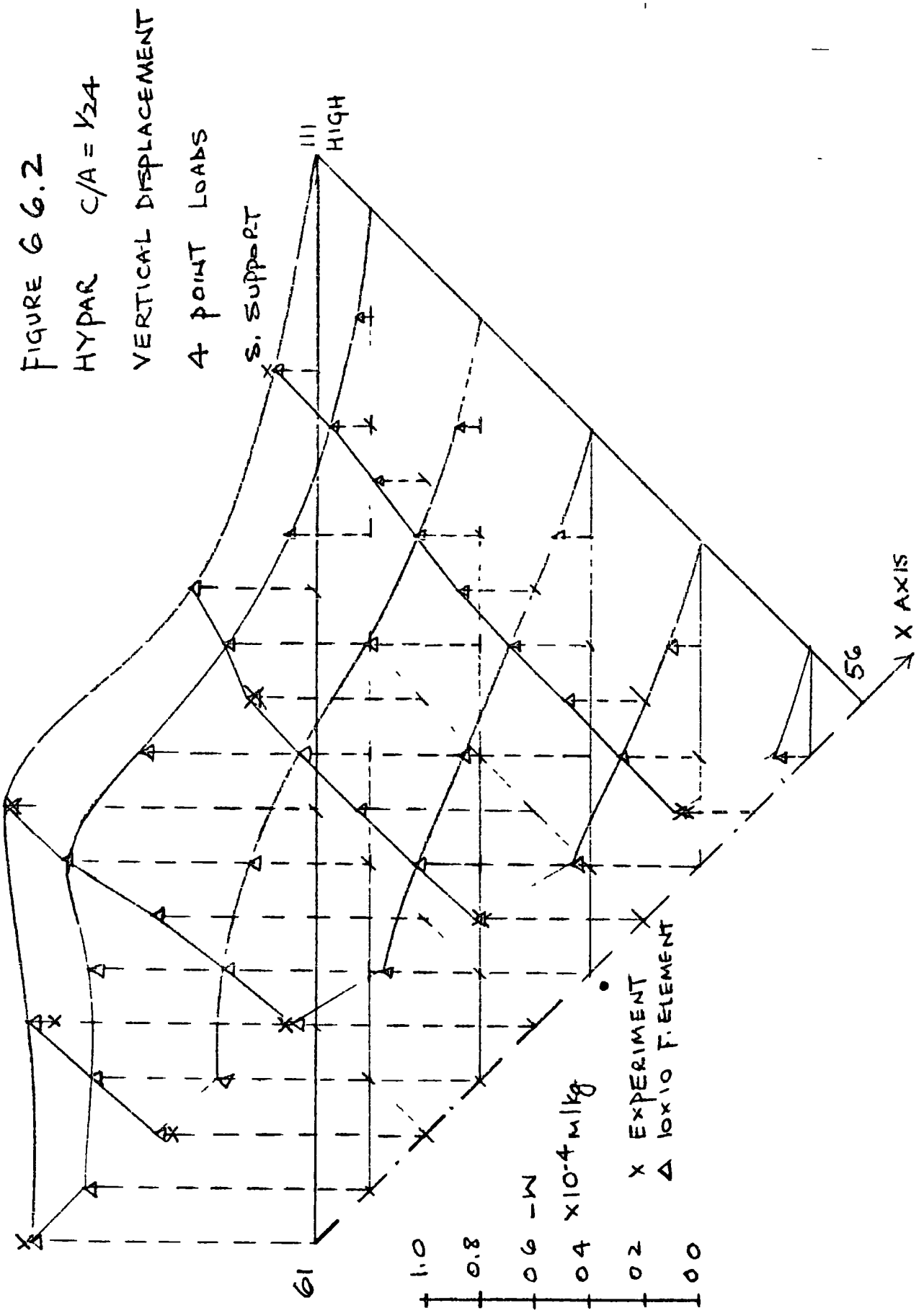
FIGURE 6 6.2
HYPAR C/A = 1/24
VERTICAL DISPLACEMENT
4 POINT LOADS
S. SUPPORT
111
HIGH
61
56
X AXIS
1.0
0.8
0.6
0.4
0.2
0.0
M - N
x10-4 m/kg
X EXPERIMENT
Δ 10x10 F.ELEMENT

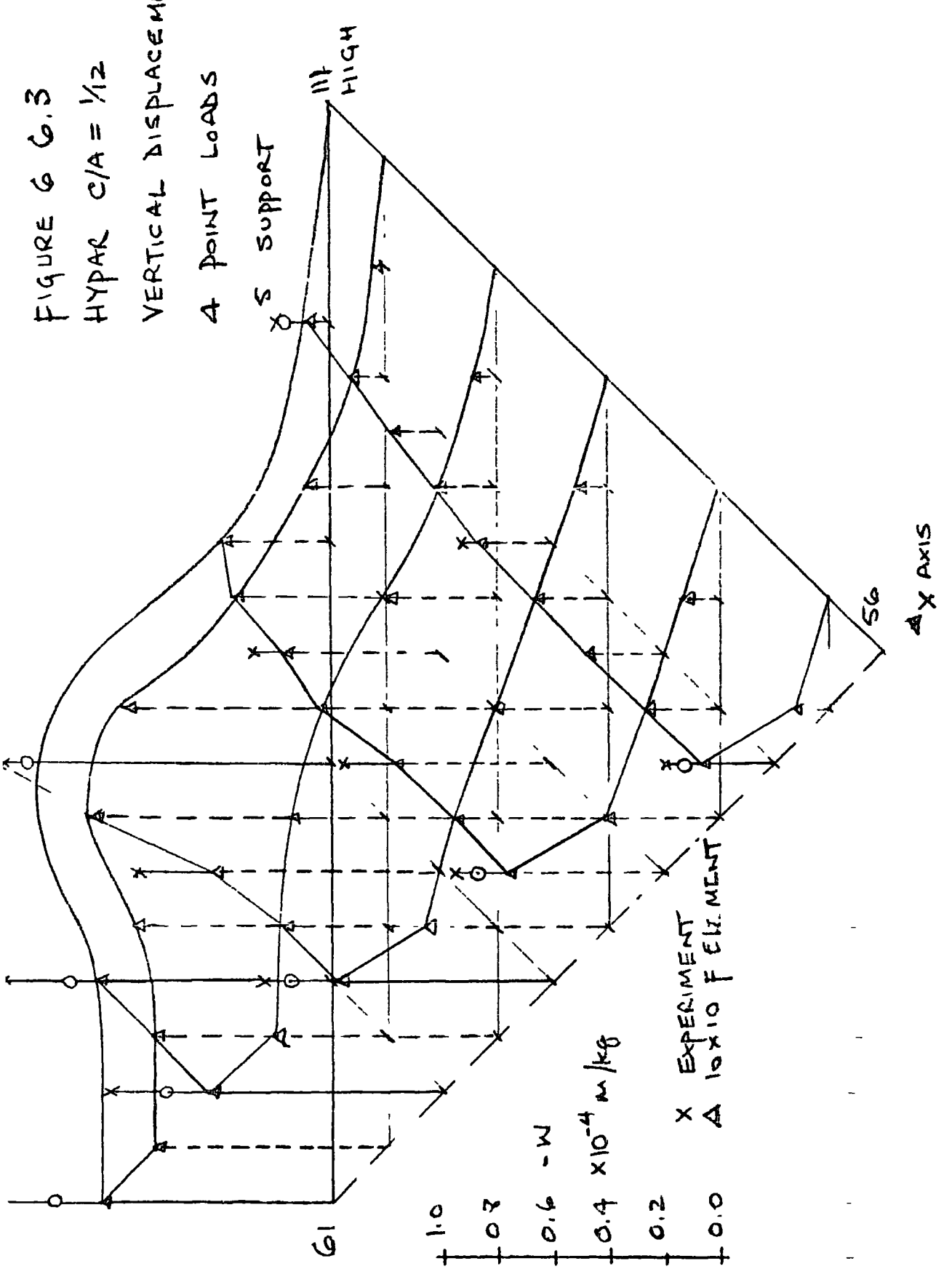
FIGURE 6 6.3
HYPAR C/A = 1/12
VERTICAL DISPLACEMENT
4 POINT LOADS
5 SUPPORT
111 HIGH
61
56
X AXIS
1.0
0.8
0.6
0.4
0.2
0.0
- W
$\times 10^{-4}$ m/kg
X EXPERIMENT
Δ 10 x 10 F ELEMENT

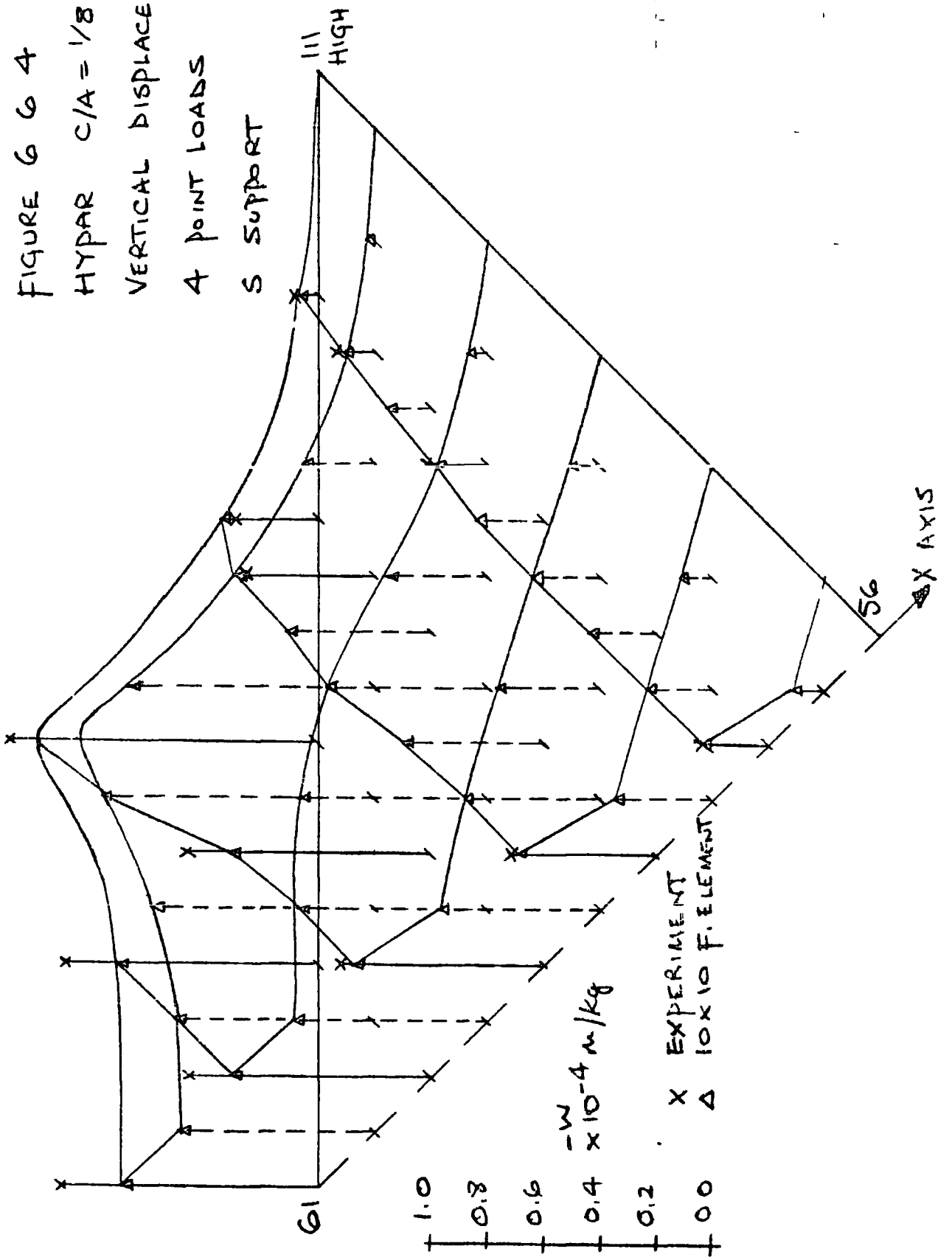

FIGURE 6 6 4
HYPAR C/A = 1/8
VERTICAL DISPLACEMENT
4 POINT LOADS
S SUPPORT

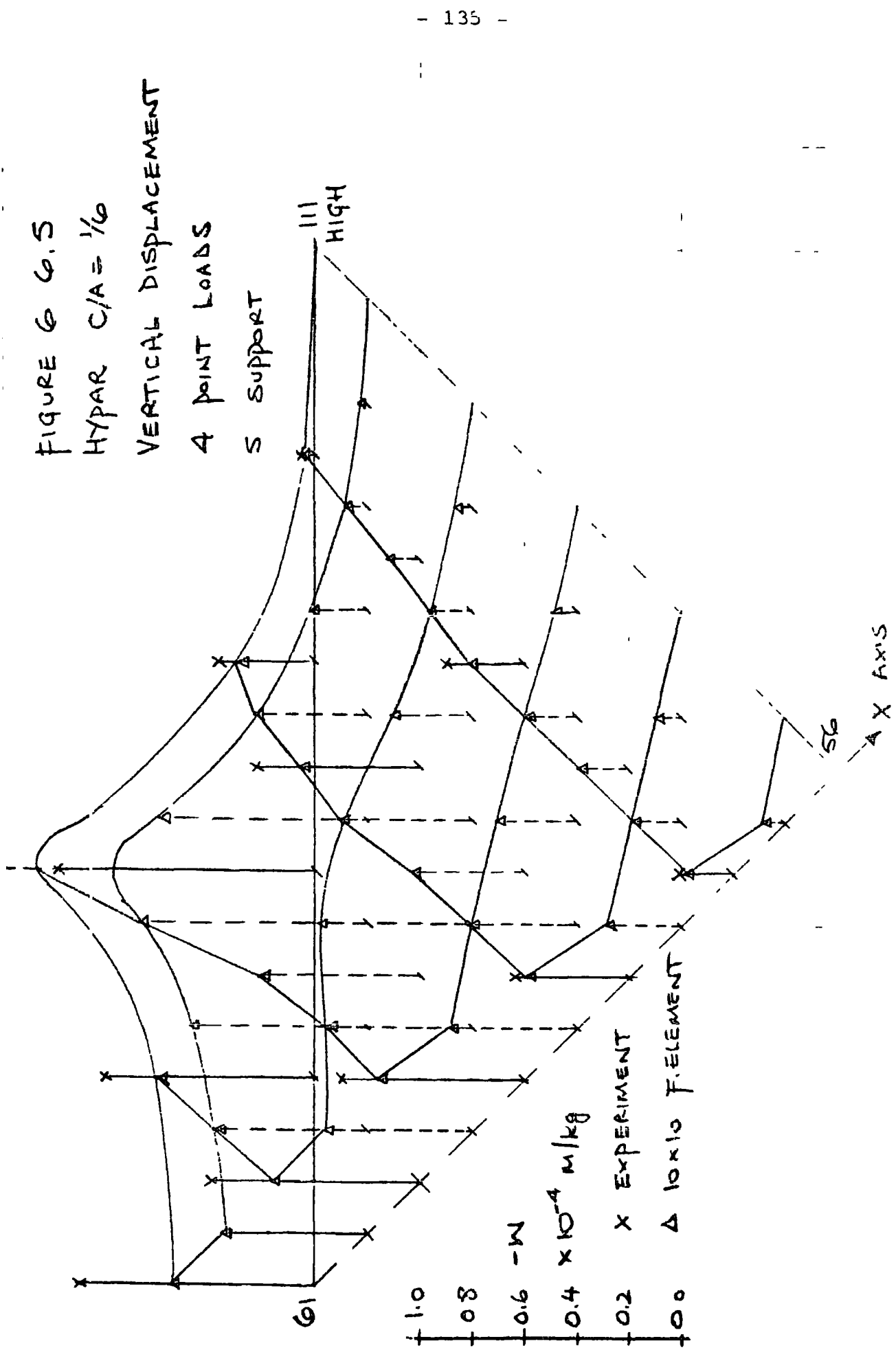
FIGURE 6 6.5
HYPAR C/A = 1/6
VERTICAL DISPLACEMENT
4 POINT LOADS
S SUPPORT
111 HIGH
61
55
X AXIS
1.0
0.8
0.6
0.4
0.2
0
-W x 10^-4 m/kg
X EXPERIMENT
Δ 10x10 F.ELEMENT

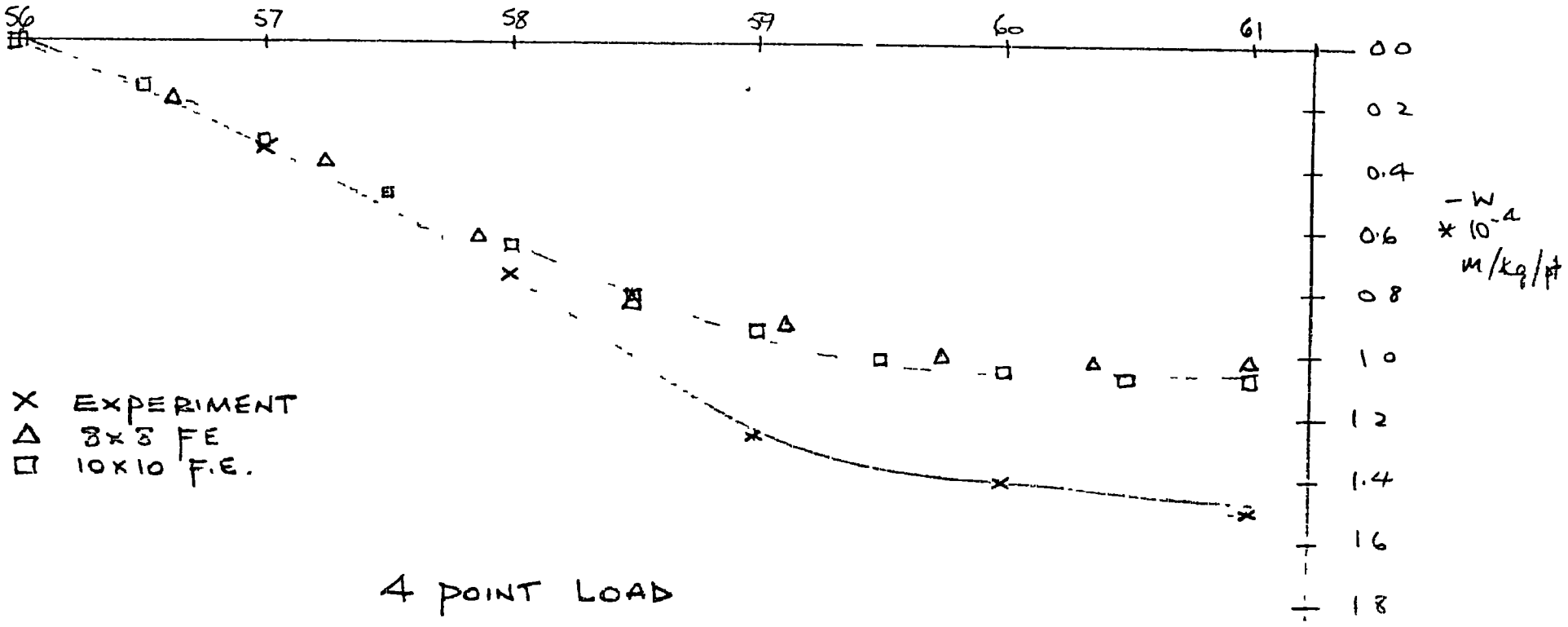

4 POINT LOAD

X AXIS

FLAT PLATE C/A = 0

FIGURE 6.6.6 VERTICAL DISPLACEMENT

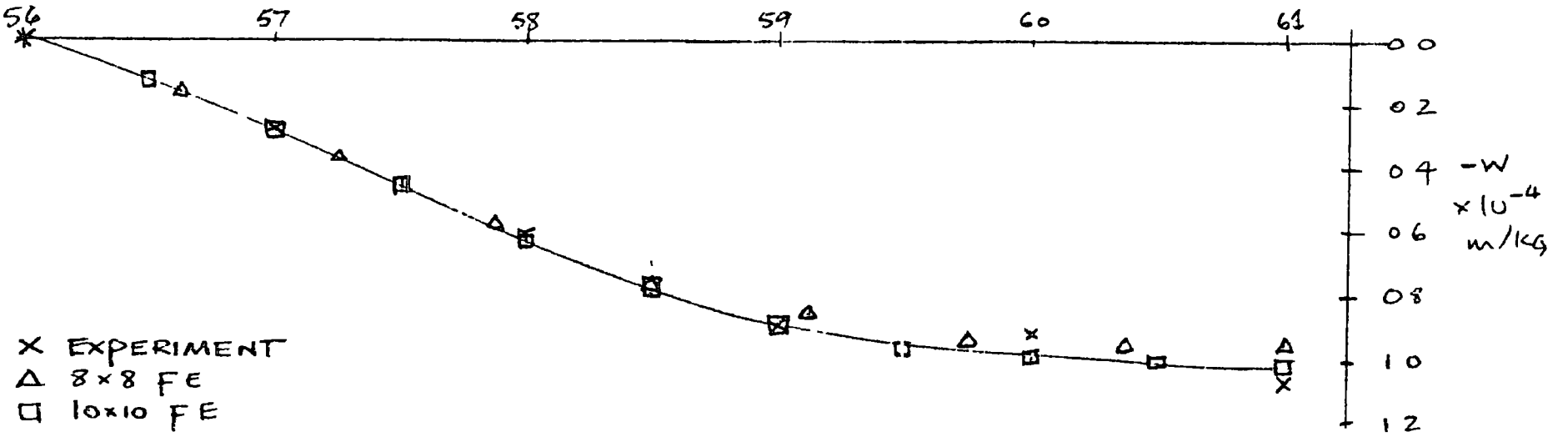

4 POINT LOAD

X AXIS

HYPAR C/A = 1/24

FIGURE 6 6.7 VERTICAL DISPLACEMENT

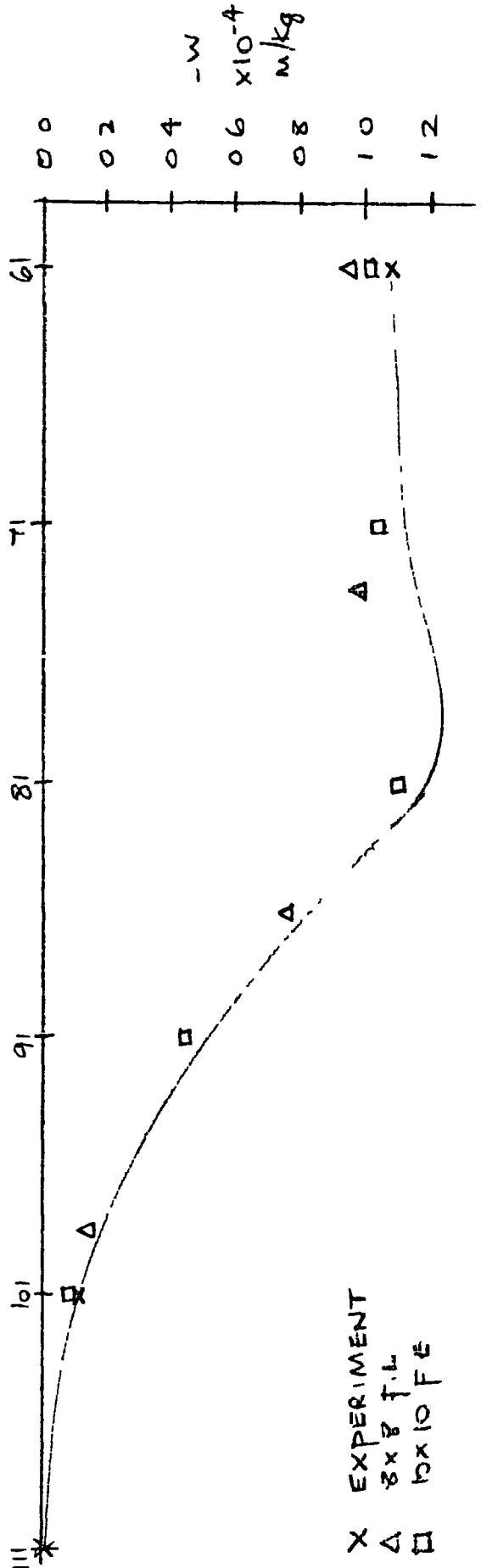

4 POINT LOAD
TENSION PARABOLA
HYPAR C/A = 1/24
FIGURE 6.6 8

VERTICAL DISPLACEMENT

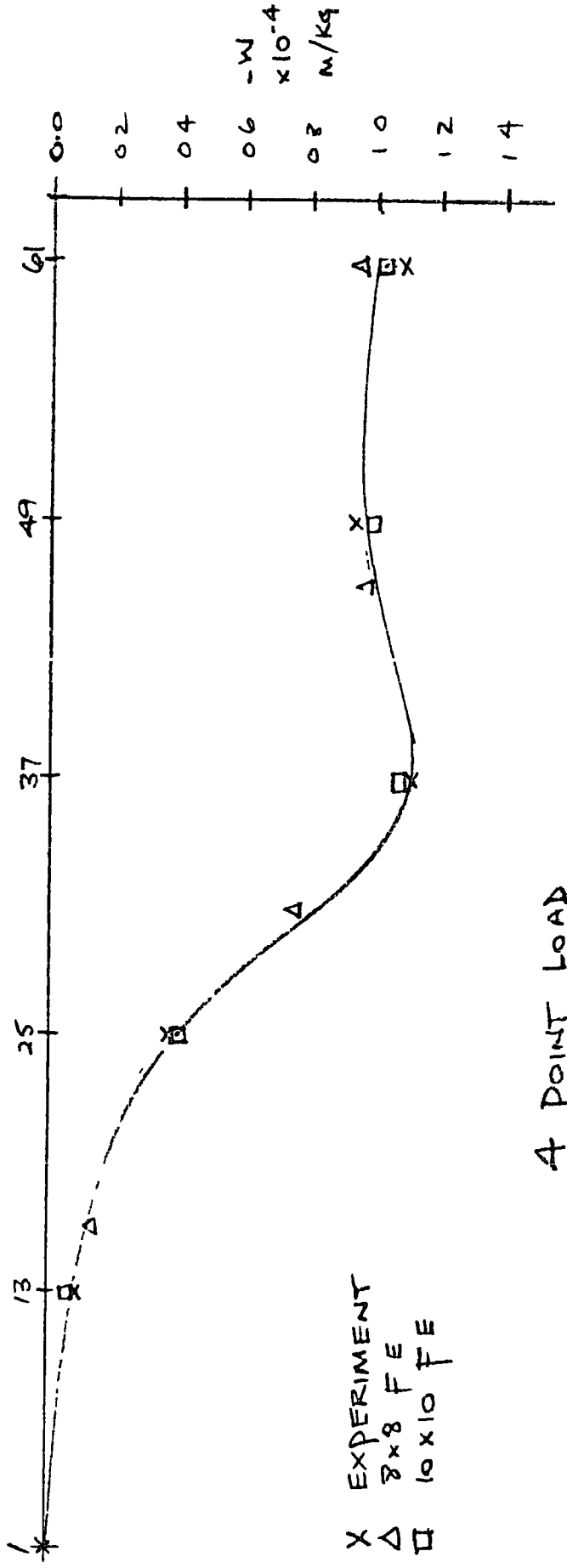

4 POINT LOAD
COMPRESSION PARABOLA
HYPAR C/A = 1/24
FIGURE 6 6 9

VERTICAL
DISPLACEMENT

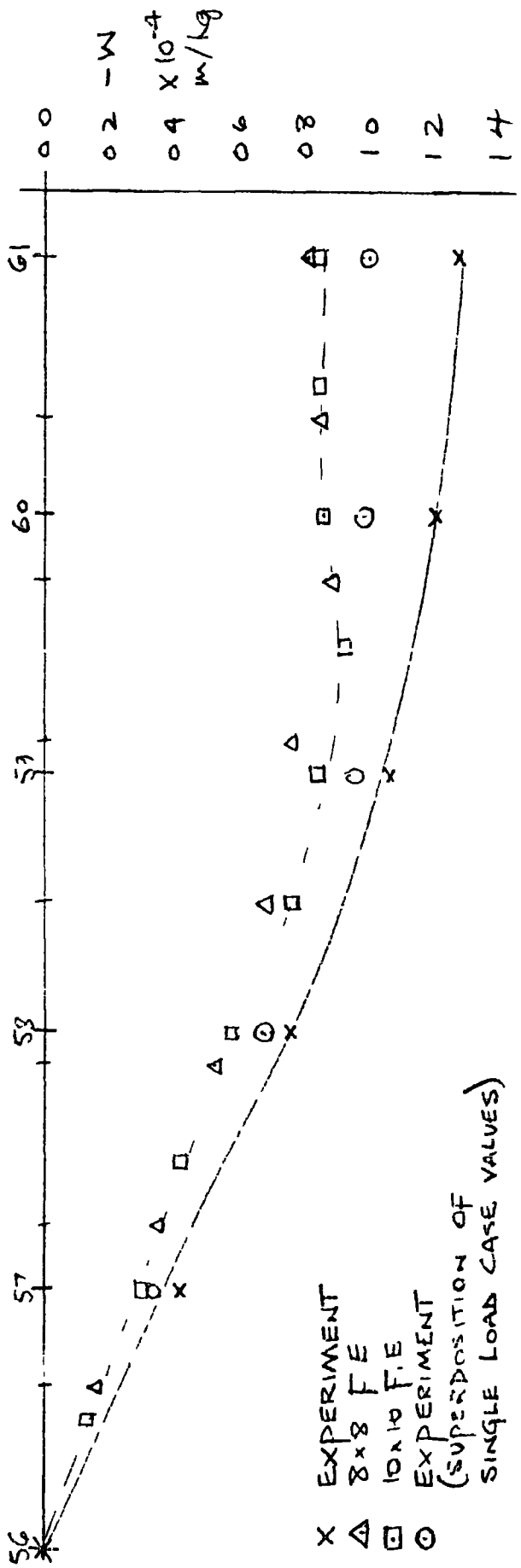

4 POINT LOAD

X AXIS

HYPAR C/A = 1/12

VERTICAL DISPLACEMENT

FIGURE 6.6.10

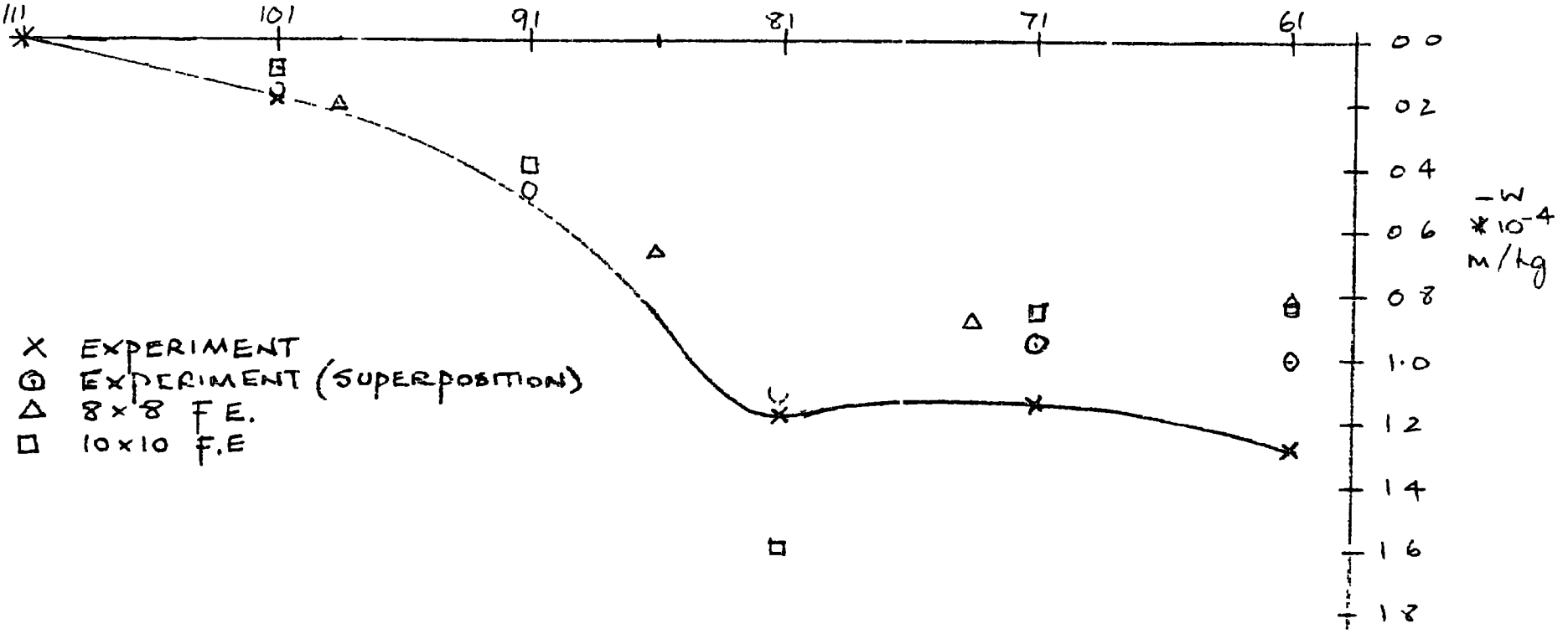

4 POINT LOAD

TENSION PARABOLA

HYPAR c/A = 1/12

FIGURE 6.6.11

VERTICAL DISPLACEMENT

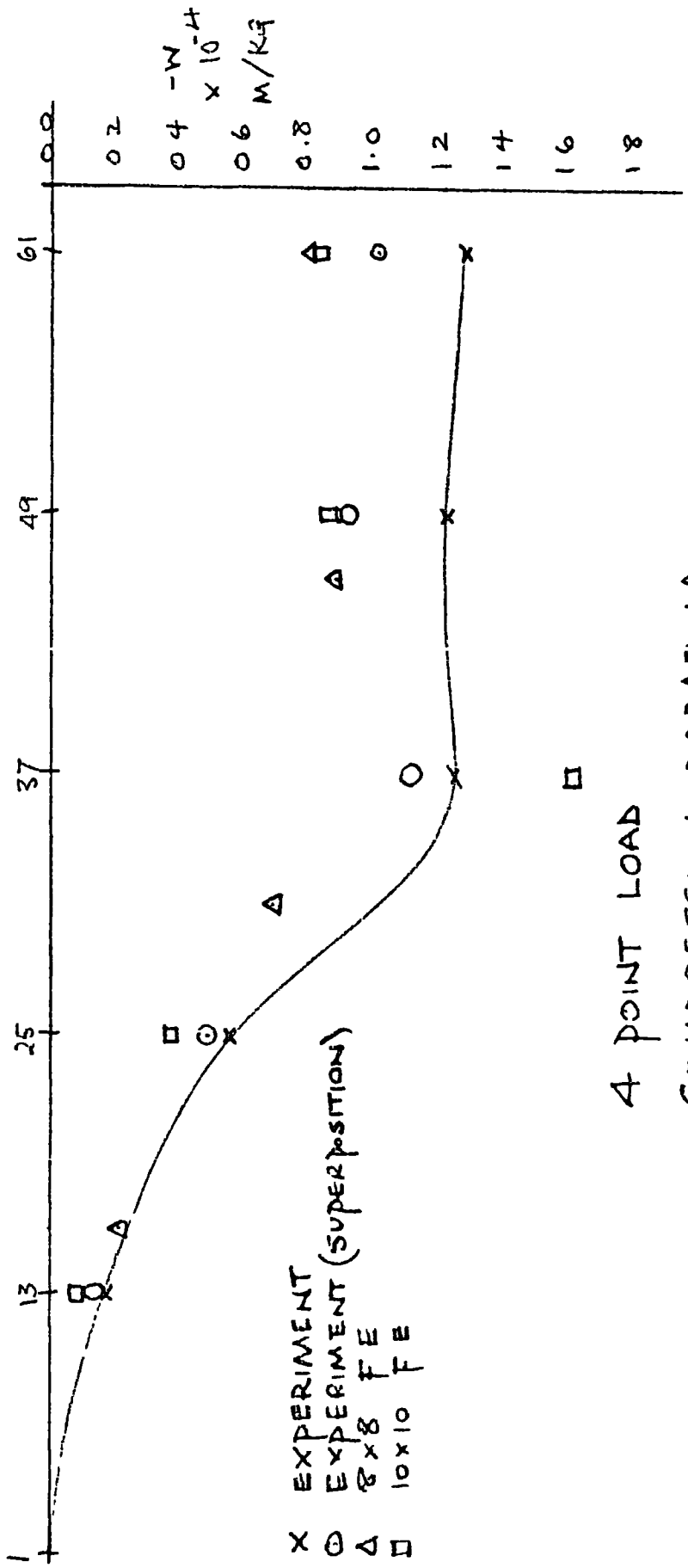

4 POINT LOAD
COMPRESSION PARABOLA
HYPAR C/A = 1/12
FIGURE 6.6 12

VERTICAL DISPLACEMENT

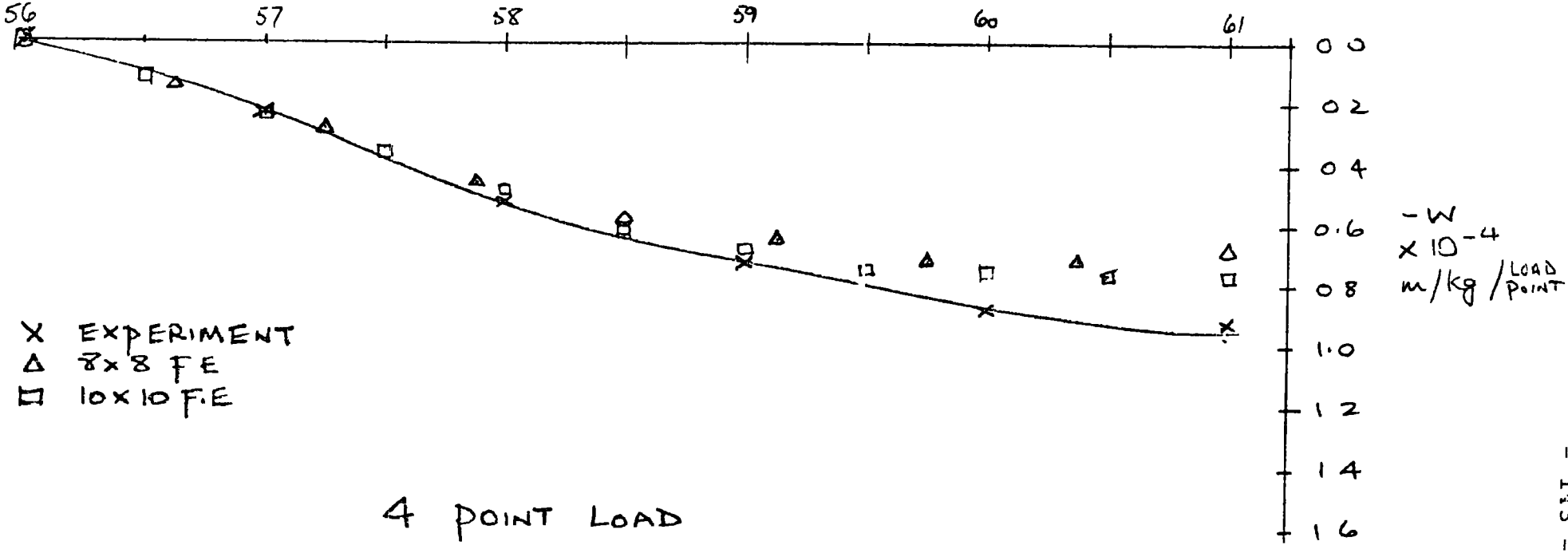

4 POINT LOAD

X AXIS

HYPAR C/A = 1/8

FIGURE 6.6.13

VERTICAL DISPLACEMENT

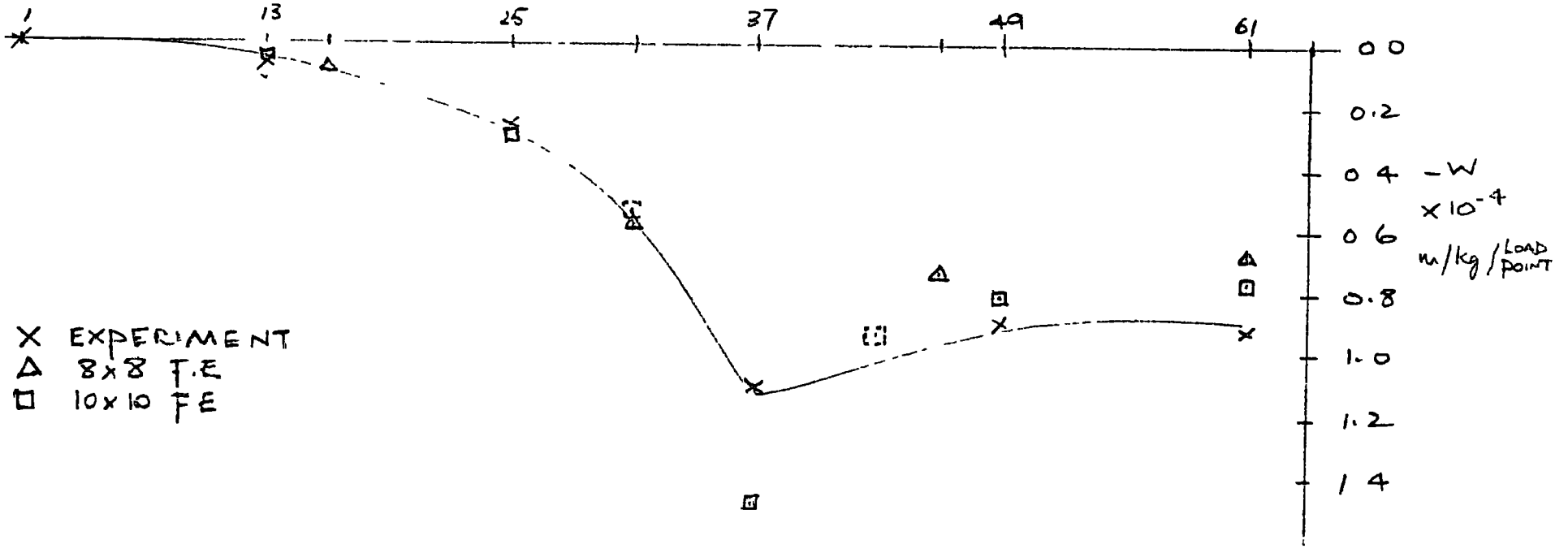

4 POINT LOAD

COMPRESSION PARABOLA

HYPAR c/a = 1/8

FIGURE 6.6 14

VERTICAL DISPLACEMENT

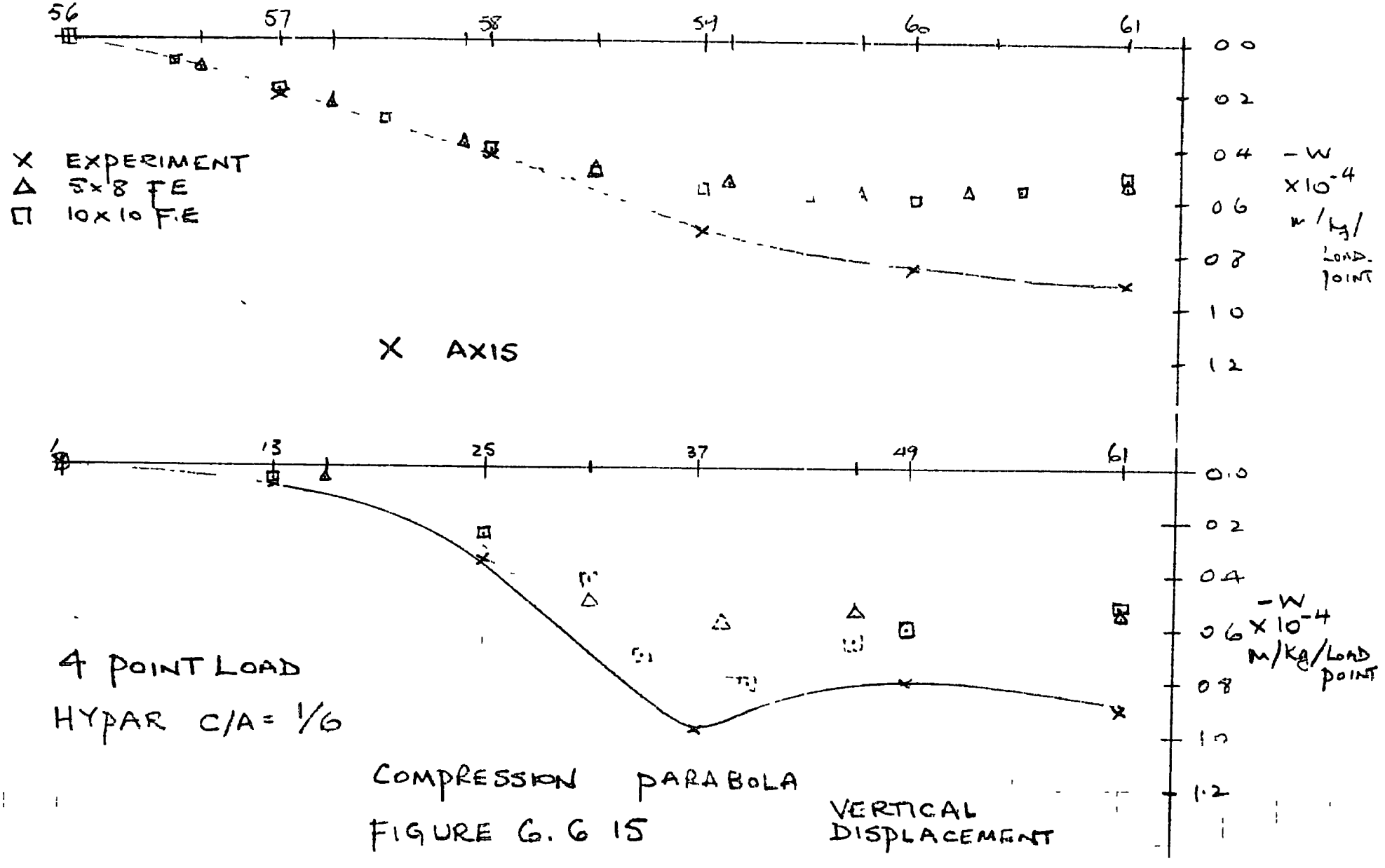
56
57
58
59
60
61
X EXPERIMENT
△ 5×8 F.E
□ 10×10 F.E
X AXIS
0.0
0.2
0.4
0.6
0.8
1.0
1.2
-W ×10⁻⁴ m/kg/ LOAD. POINT
1
13
25
37
49
61
0.0
0.2
0.4
0.6
0.8
1.0
1.2
-W ×10⁻⁴ m/kg/Load point
4 POINT LOAD
HYPAR C/A = 1/6
COMPRESSION PARABOLA
VERTICAL DISPLACEMENT

FIGURE 6.6 15

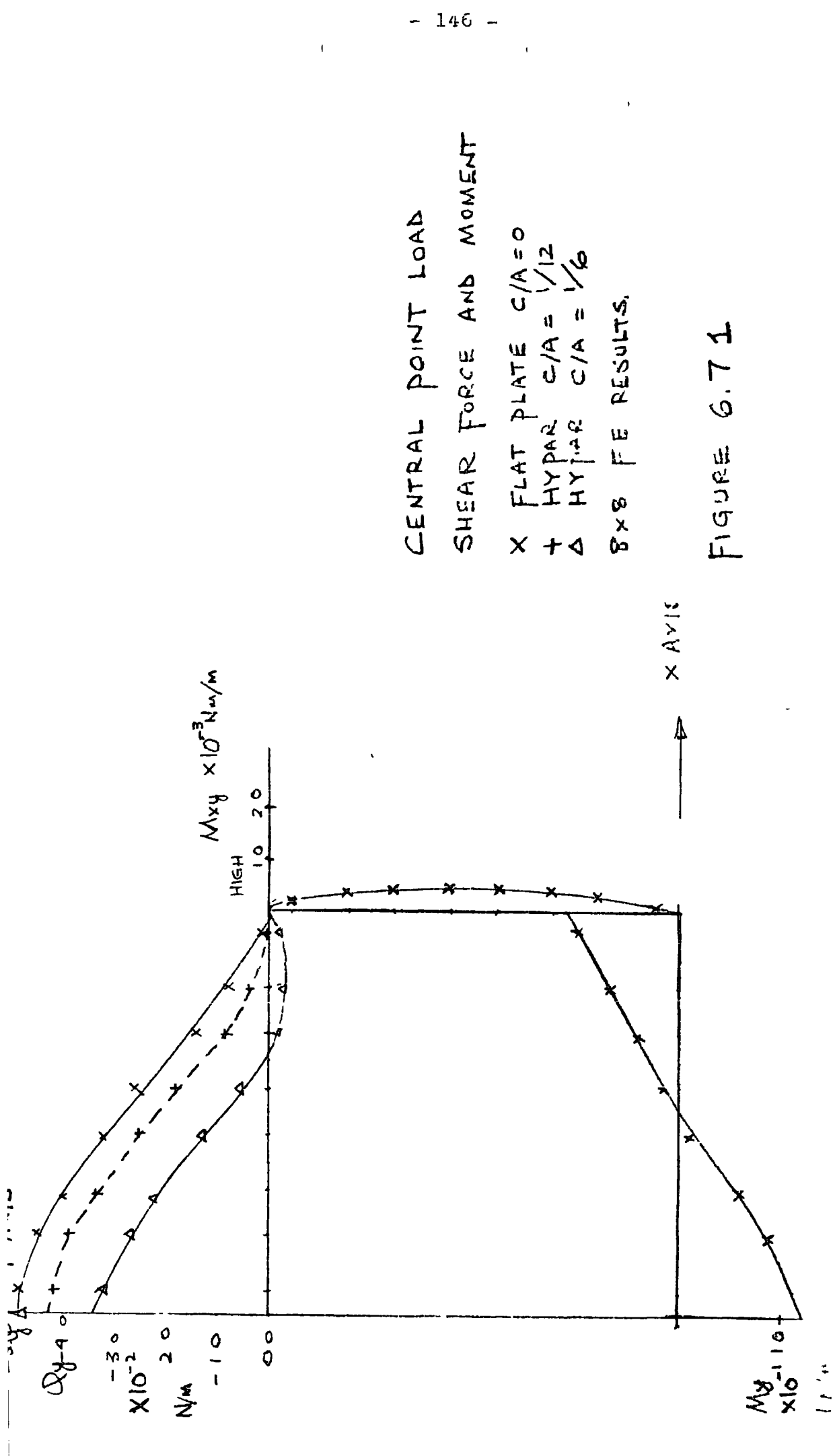
CENTRAL POINT LOAD
SHEAR FORCE AND MOMENT
X FLAT PLATE C/A = 0
+ HYPAR C/A = 1/12
Δ HYPAR C/A = 1/6
8x8 FE RESULTS.
X AXIS
Mxy x10⁻³ Nm/m
HIGH
10
20
Qy
-30
-20
-10
00
x10⁻²
Nm
My
-10
x10

FIGURE 6.71

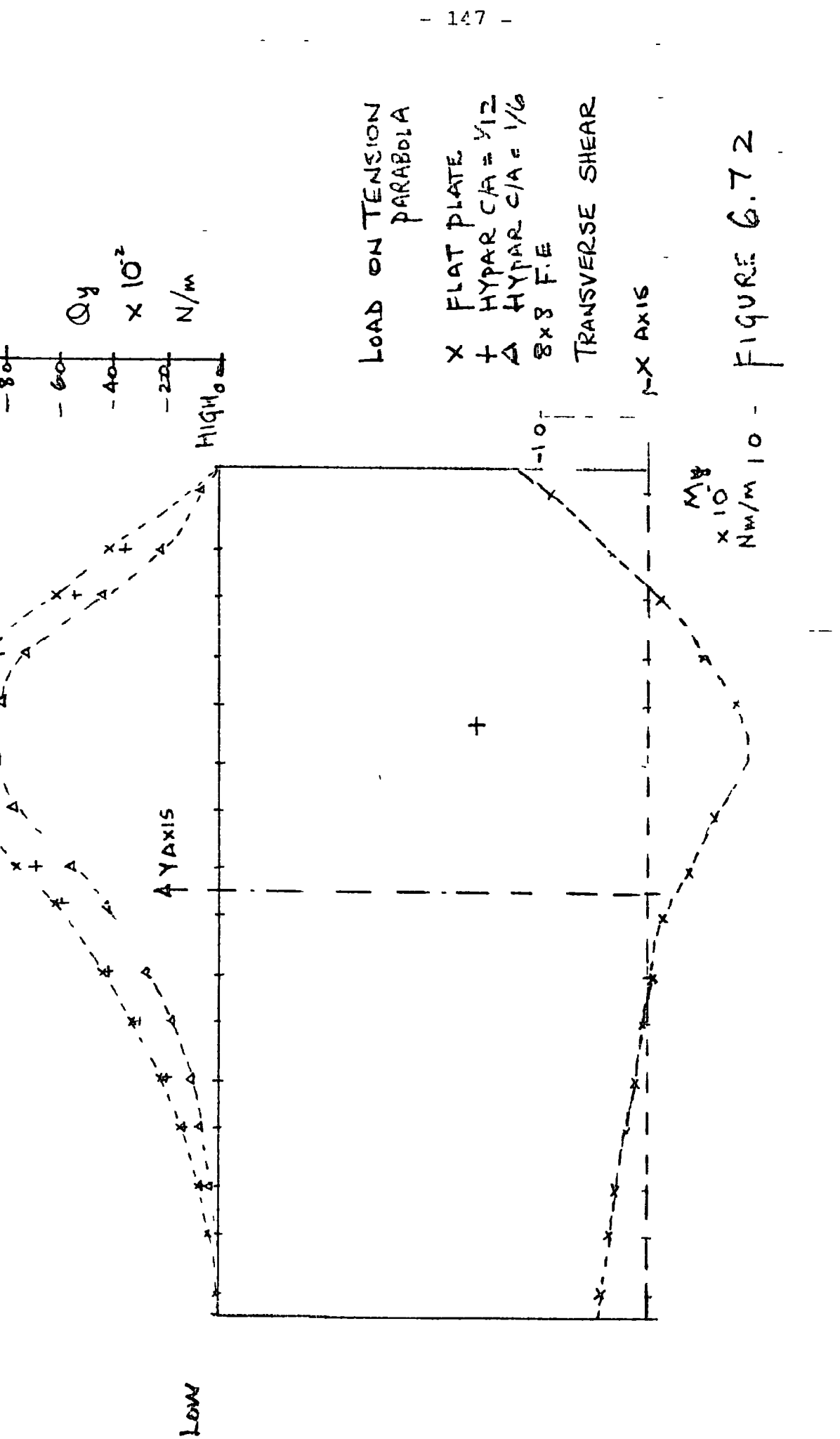
LOAD ON TENSION PARABOLA
× FLAT PLATE
+ HYPAR C/A = 1/12
Δ HYPAR C/A = 1/6
8×8 F.E
TRANSVERSE SHEAR
Qy × 10² N/m
HIGH
LOW
Y AXIS
X AXIS
Mx × 10 Nm/m

FIGURE 6.72

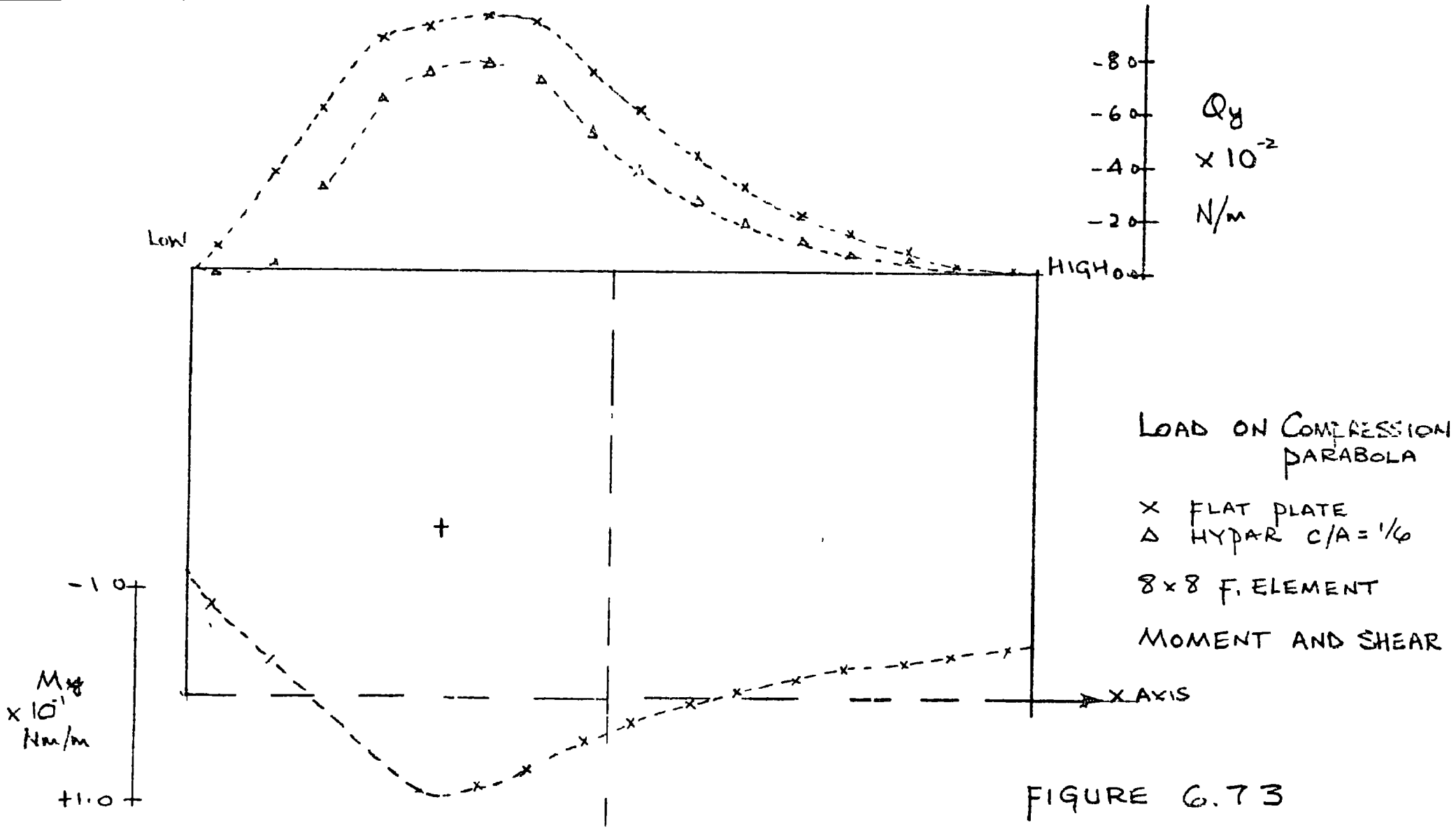
-8.0
-6.0
-4.0
-2.0
0.0
Qy
x 10^-2
N/m
LOW
HIGH
-1.0
Mxy
x 10^1
Nm/m
+1.0
X AXIS
LOAD ON COMPRESSION PARABOLA
× FLAT PLATE
Δ HYPAR C/A = 1/6
8 x 8 F. ELEMENT
MOMENT AND SHEAR

FIGURE 6.73

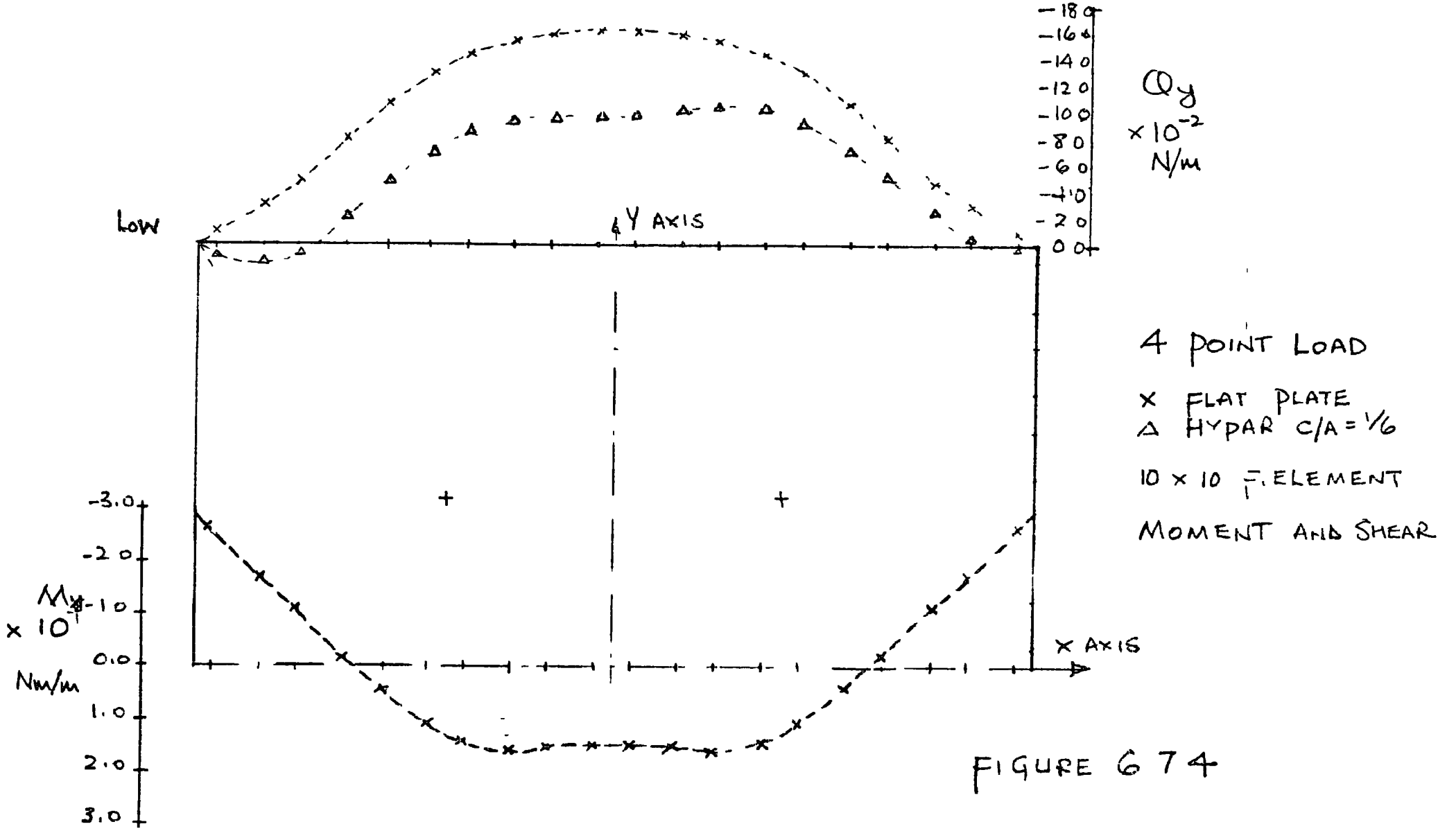
Low
Y AXIS
X AXIS
-18.0
-16.0
-14.0
-12.0
-10.0
-8.0
-6.0
-4.0
-2.0
0.0
Qy
x 10^-2
N/m
-3.0
-2.0
-1.0
0.0
1.0
2.0
3.0
Mx
x 10^1
Nm/m
4 POINT LOAD
× FLAT PLATE
△ HYPAR C/A = 1/6
10 x 10 F.ELEMENT
MOMENT AND SHEAR

FIGURE 6 7 4

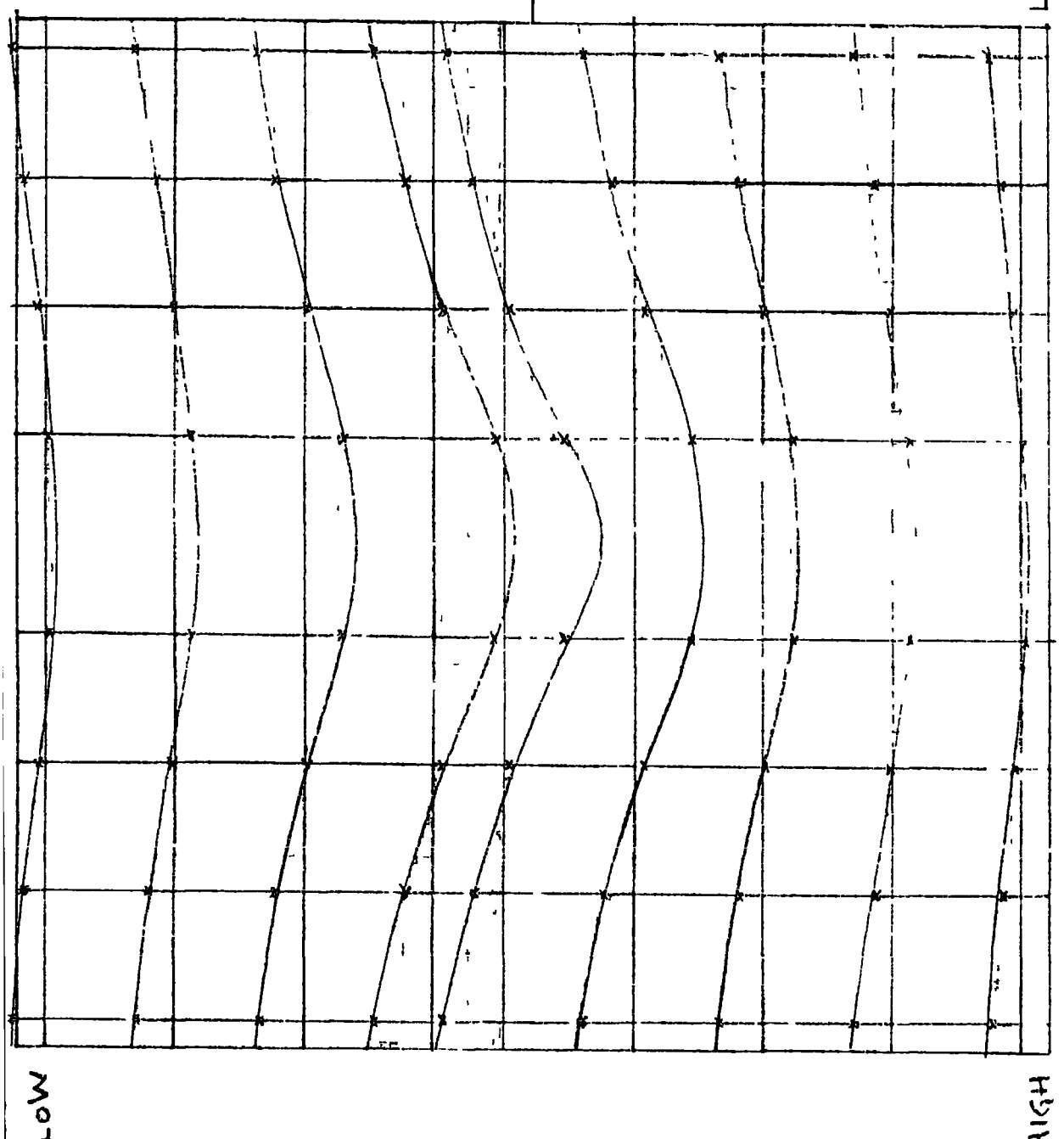

CENTRAL POINT LOAD
BENDING MOMENT M_y
FLAT PLATE

FIGURE 6.75

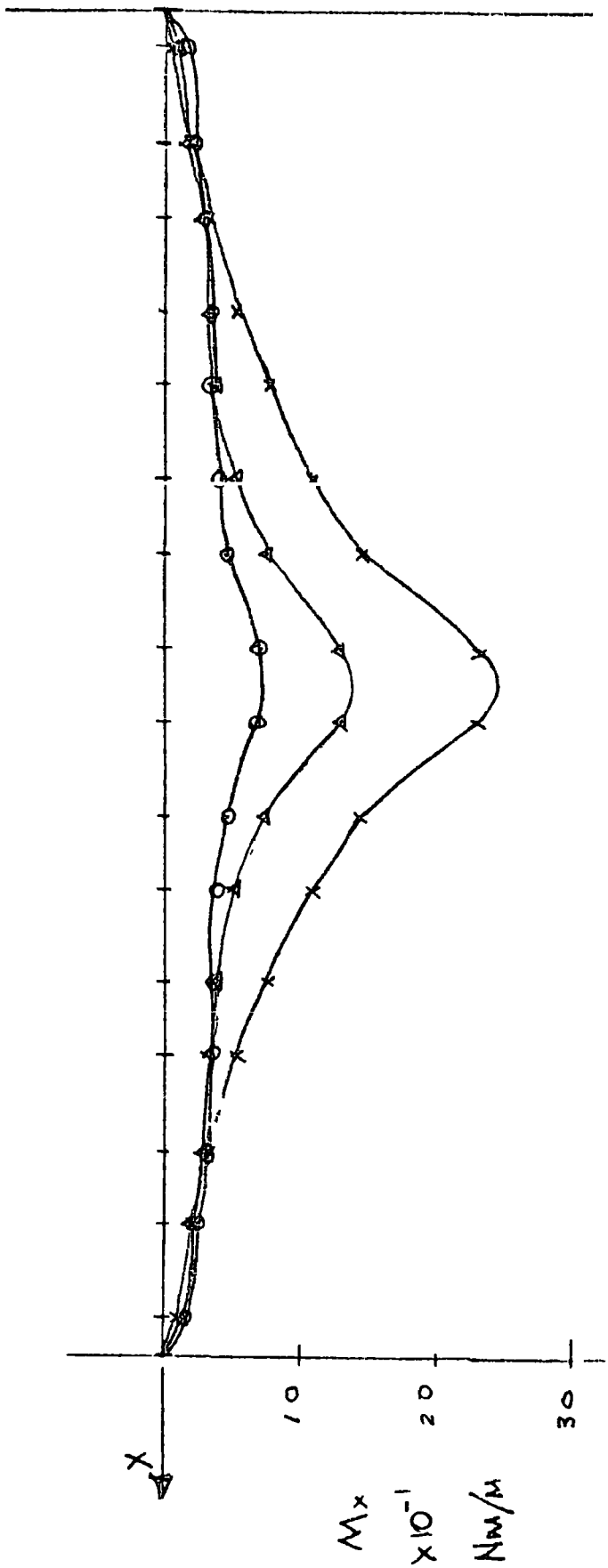

FIGURE 6 7 6

BENDING MOMENT M_x

ALONG ℄ X AXIS

CENTRAL POINT LOAD

SIMPLE SUPPORT

× FLAT PLATE C/A = 0

Δ HYPAR C/A = 1/24

○ HYPAR C/A = 1/6

8 × 3 FINITE ELEMENT

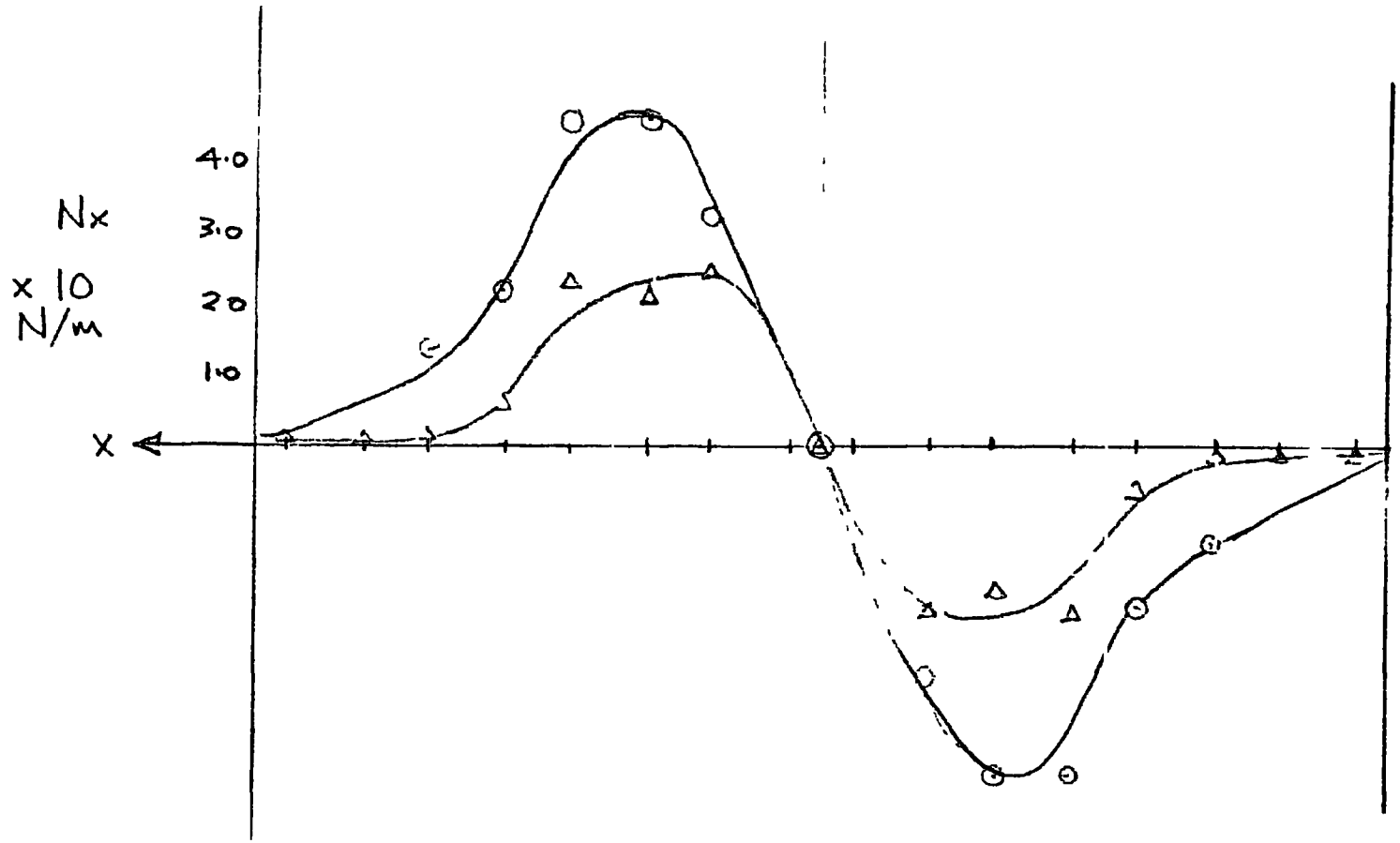

△ HYPAR C/A = 1/24

⊙ HYPAR C/A = 1/6

8 x 8 FINITE ELEMENT

FIGURE 6 77

MEMBRANE FORCE Nx

CENTRAL POINT LOAD

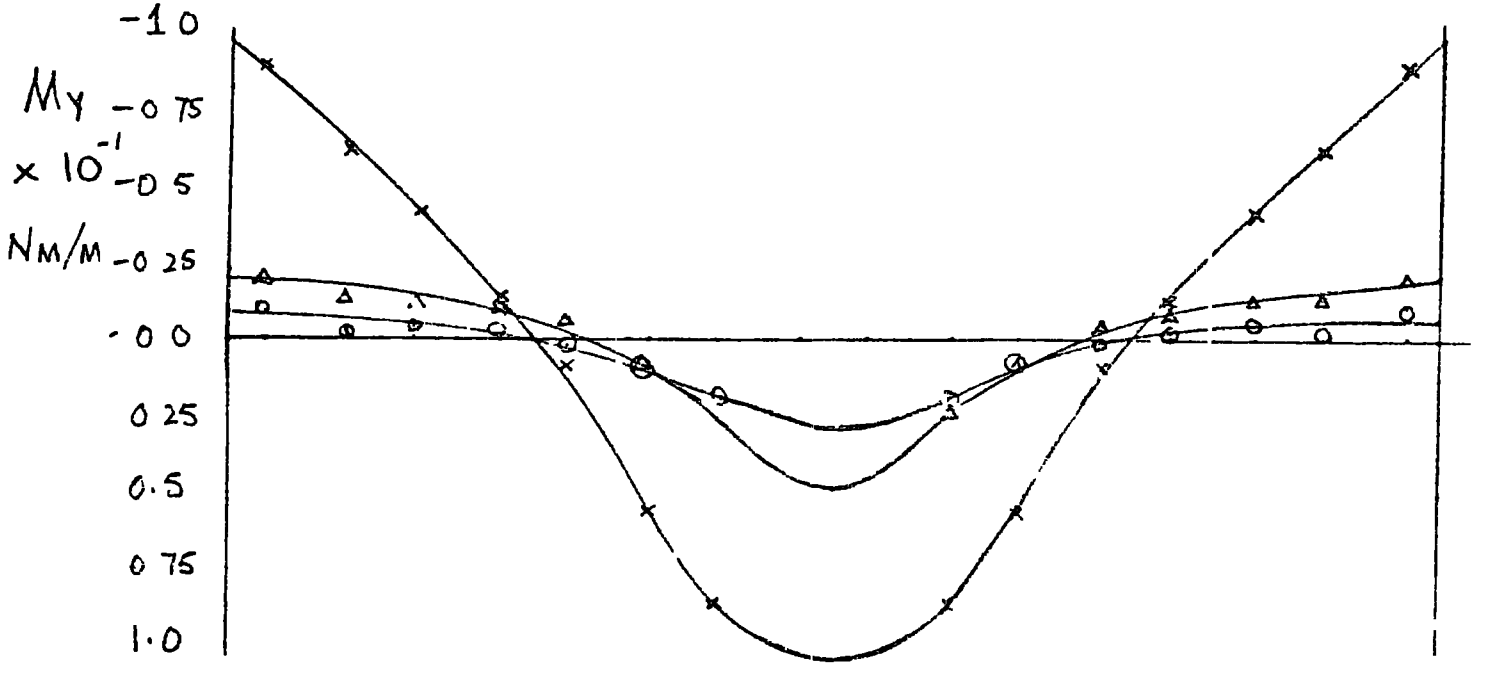

× FLAT PLATE C/A = 0
Δ HYPAR C/A = 1/24
○ HYPAR C/A = 1/6

8 × 8 FINITE ELEMENT

FIGURE 6.7.8

BENDING MOMENT My (REAL VALUES ALONG ℓ X AXIS OMITTED)

CENTRAL POINT LOAD

SIMPLE SUPPORT

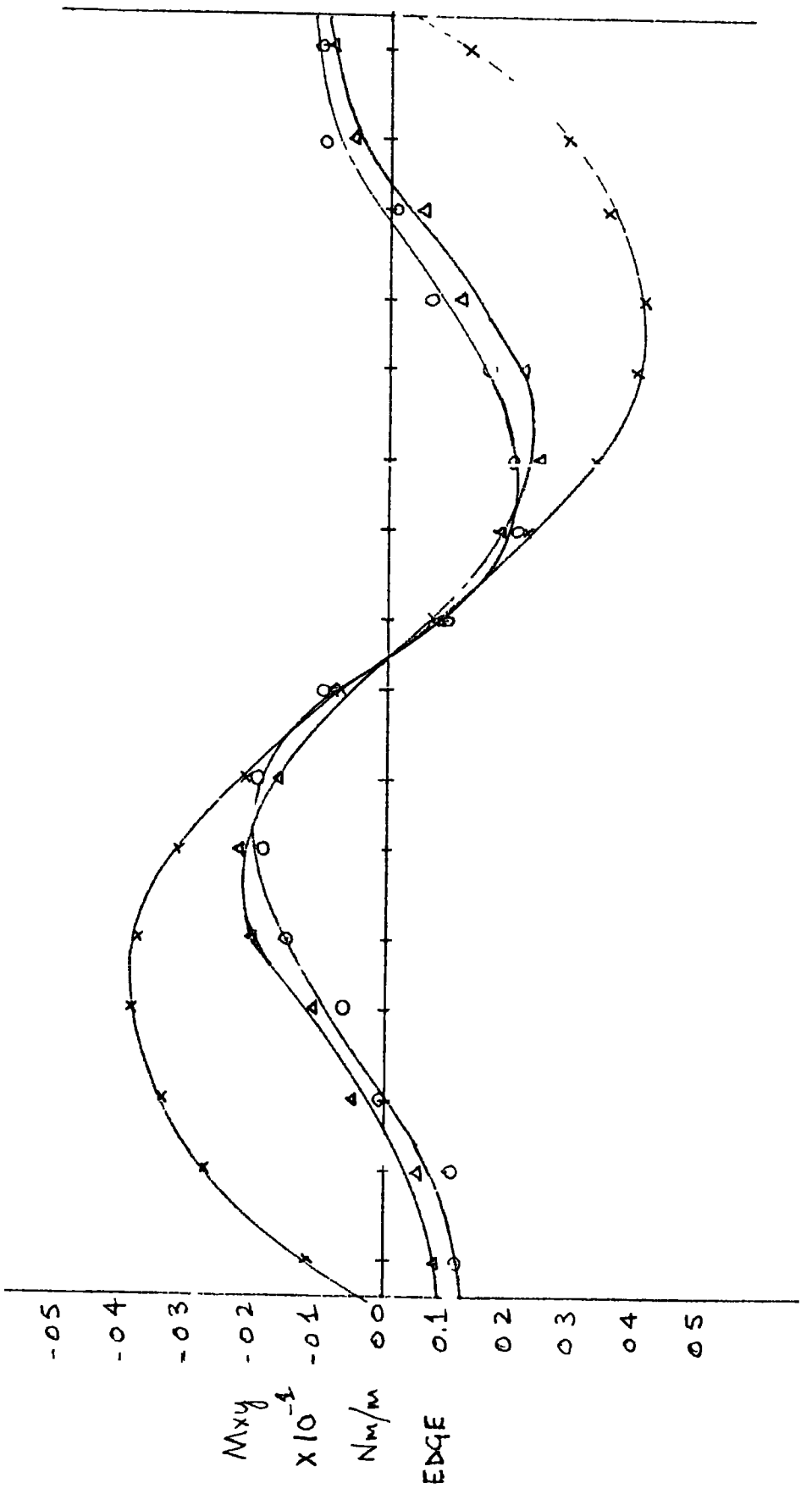

FIGURE 6 7 9

TWISTING MOMENT MxY

EDGE

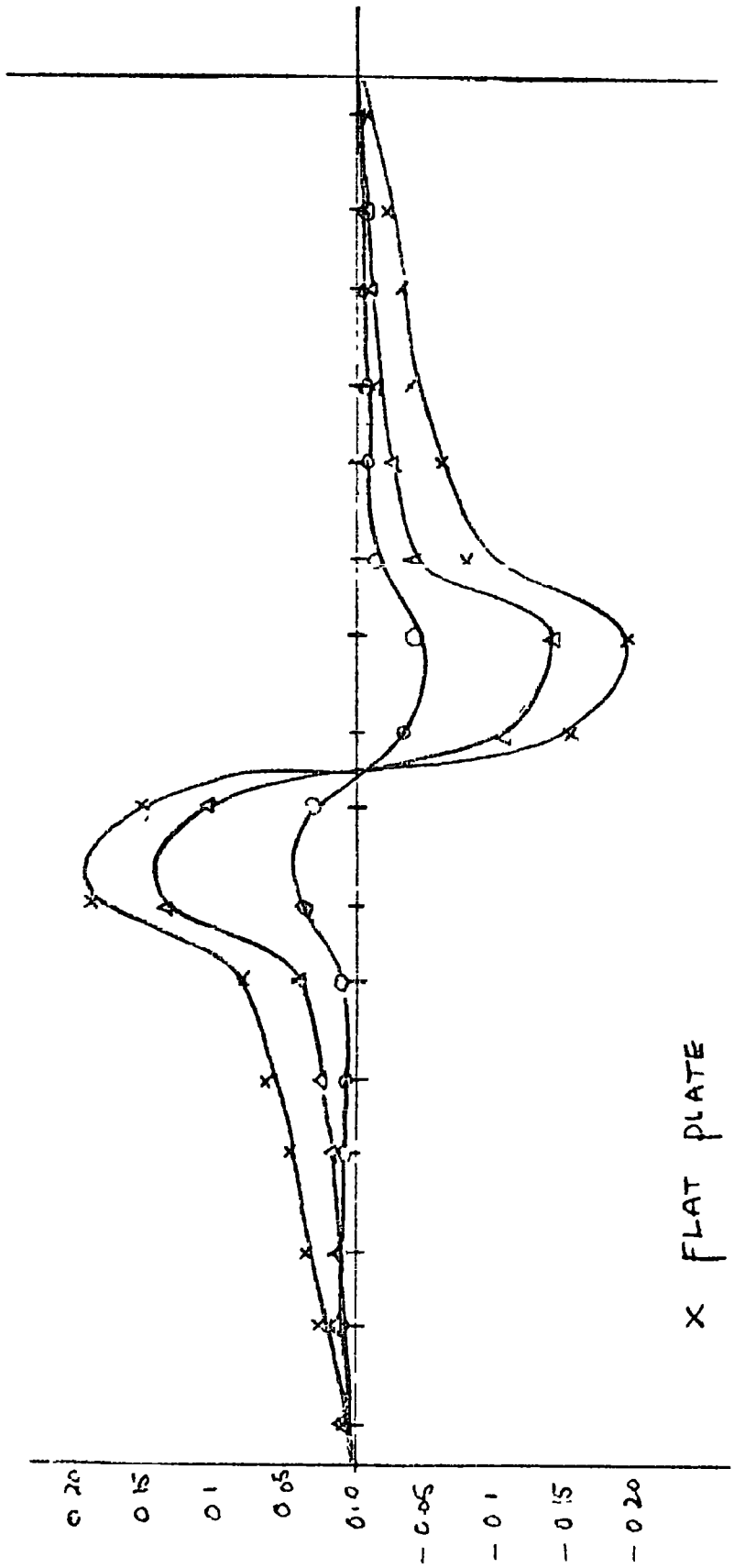

FIGURE 6 7 10
TWISTING MOMENT MXY
X AXIS

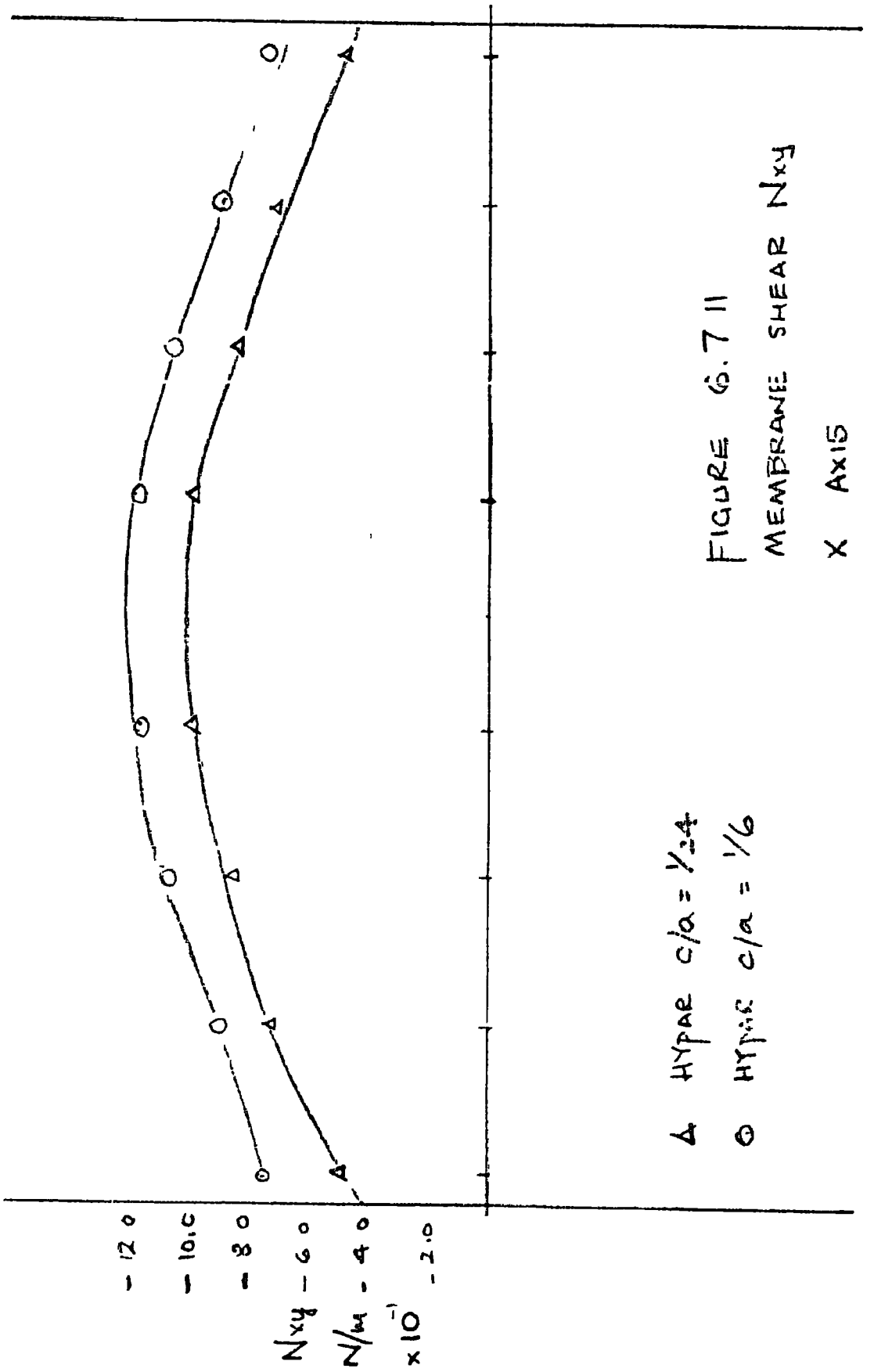

FIGURE 6.7 11
MEMBRANE SHEAR N_{xy}

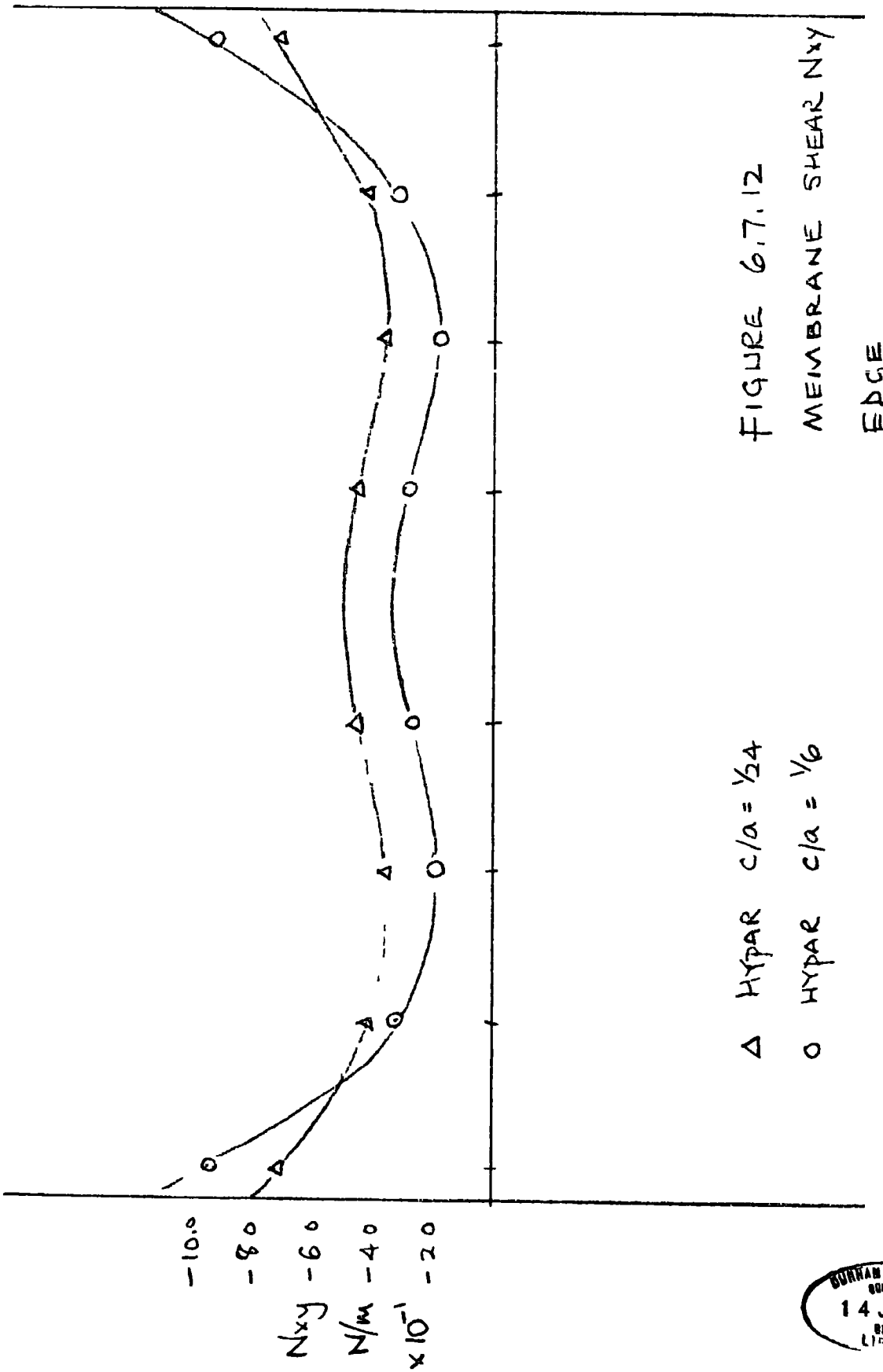

FIGURE 6.7.12
MEMBRANE SHEAR N_{xy}